NONLINEAR CHARACTERISATION OF POWER ULTRASONIC DEVICES USED IN BONE SURGERY

Andrew Charles Mathieson

A thesis for the degree of Doctor of Philosophy (PhD)

Submitted to the School of Engineering,
College of Science and Engineering,
University of Glasgow

January 2012

Abstract

Ultrasonic cutting has existed in surgery since the 1950s. However, it was not until the end of the 20^{th} century that advances in ultrasonic tool design, transduction and control allowed commercially viable ultrasonic cutting devices to enter the market. Ultrasonic surgical devices, like those in other power ultrasonic applications such as drilling and welding, require devices to be driven at high power to ensure sufficient output motion is produced to fulfil the application it is designed to perform. With the advent of novel surgical techniques surgeons require tuned ultrasonic tools which can reduce invasiveness while giving access to increasingly difficult to reach surgical sites. To fulfil the requirements of novel surgical procedures new tuned tools need to be designed. Meanwhile, it is well documented that power ultrasonic devices, whilst driven at high power, are inherently nonlinear and, if no attempt is made to understand and subsequently control these behaviours, it is likely that these devices will suffer from poor performance or even failure.

The behaviour of the commercial ultrasonic transducer used in bone surgery (Piezosurgery® Device) is dynamically characterised through finite element and experimental methods whilst operating in conjunction with a variety of tuned inserts. Finite element analysis was used to predict modal parameters as well as stress levels within the tuned devices whilst operating at elevated amplitudes of vibration, while experimental modal analysis validated predicted resonant frequencies and mode shapes between 0-80kHz. To investigate the behaviour of tuned devices at elevated vibrational amplitudes near resonance, responses were measured whilst the device was excited via the burst sine sweep method. In an attempt to provide an understanding of the effects that geometry, material selection and wavelength of tuned assemblies have on the behaviour of an ultrasonic device, tuned inserts consisting of a simple rod horn design were characterised alongside more complex cutting inserts which are used in maxillofacial and craniofacial surgery. From these results the aim will be to develop guidelines for design of tuned inserts.

Meanwhile, Langevin transducers, commonly known as sandwich or stack transducers, in their most basic form generally consist of four parts; a front mass, a back mass, a piezoceramic stack and a stud or bolt holding the parts together under a compressive pre-load. It is traditionally proposed that the piezoceramic stack is positioned at or close to the vibrational nodal point of the longitudinal mode, however, this also corresponds with the position of

highest dynamic stress. It is also well documented that piezoceramic materials possess a low linear stress threshold, therefore this research, in part, investigates whether locating the piezoceramic stack away from a position of intrinsic high stress will affect the behaviour of the device.

Through experimental characterisation it has been observed that the tuned devices under investigation exhibited; resonant frequency shifts, jump amplitudes, hysteretic behaviour as well as autoparametric vibration. The source of these behaviours have been found to stem from device geometry, but also from heating within the piezoceramic elements as well as joints with different joining torques.

Acknowledgments

Before I dwell on the amount of hard work, long hours and sometimes infuriating moments which have littered the last few years, I should recognise that the freedom of research, the new friends I have gained and generally great experiences I have had more than counter the tough and trying moments.

First and foremost, I must recognise and express my sincerest gratitude for the efforts, patience and guidance of Dr Andrea Cardoni, who in three years not only managed to drag me to two different continents but also embedded in me an enthusiasm for ultrasonics. I must also equally recognise and express gratitude of the efforts and resourcefulness of Professor Margaret Lucas, who apart from helping me cross the finish line, was an important ally in my battle with the English language.

I would like to thank the Engineering and Physical Sciences Research Council (EPSRC, grant number EP/E025811/1) for funding the project, as well as the project's industrial partner, Mectron S.p.A. At Mectron S.p.A, I would specifically like to thank Mr Niccolò Cerisola for his willingness to share his knowledge of ultrasonics as well as his keen interest and positive influence on the project.

A special acknowledgement to the Power Ultrasonics Group at the Instituto de Acustica (CSIC) of Madrid, Spain for giving me access to their laboratory facilities for making measurements taken under high-power conditions possible.

I would like to thank Dr Patrick Harkness, who apart from becoming a close friend over the last few years, (almost) always opened his door to me when I needed someone to bounce ideas off, subdue frustrations or just have a coffee with. Meanwhile, without the researchers of the Power Ultrasonics group at Glasgow, many problems would have taken longer to solve and life would have been rather solitary.

Thanks to a family friend, Janie Munroe for all the suffering she endured and patience she showed while proof reading my thesis. Finally, I would like to thank Emma, my parents, my brother Scott and my closest friends who have put up me when I have been tired or difficult and who I have not made enough time for. Without them I would never have finished.

Contents

Abstract **i**

Acknowledgments **iii**

1 Introduction **1**

1.1 Power ultrasonic devices . . . 2
1.2 Transducer transduction . . . 3
1.2.1 Magnetostriction . . . 3
1.2.2 Piezoelectricity . . . 5
1.3 Industrial applications of power ultrasonics . . . 15
1.3.1 Established power ultrasonic applications . . . 15
1.3.2 Modern power ultrasonic systems . . . 17
1.4 Ultrasonics in medical applications . . . 21
1.4.1 High intensity focused ultrasound . . . 21
1.4.2 Cataract removal . . . 22
1.4.3 Soft tissue dissection . . . 23
1.4.4 Oral prophylaxis . . . 24
1.4.5 Ultrasonic osteotomy . . . 25
1.5 Nonlinear behaviour in dynamic systems . . . 28
1.5.1 Duffing system . . . 28
1.5.2 Routes to Chaos . . . 30
1.6 Summary of work . . . 32

2 Review of Literature **33**

2.1 Historical background . . . 33
2.2 Ultrasonic transduction . . . 34
2.3 Application of ultrasonics . . . 38
2.3.1 Early years . . . 38
2.3.2 Power ultrasonics . . . 38
2.3.3 Dental and surgical applications . . . 43
2.4 Nonlinear behaviour . . . 45

3 Design and optimisation of ultrasonic devices **49**
3.1 Design of ultrasonic devices . . . 49
3.1.1 Uniform slender bar . . . 49
3.1.2 Design of piezoelectric transducer . . . 51
3.1.3 Material selection during the design of ultrasonic devices . . . 57
3.1.4 Assembly of ultrasonic devices . . . 62
3.1.5 Summary: Design of Ultrasonic devices . . . 63
3.2 Finite element analysis . . . 64
3.2.1 FE study: Mesh convergence of slender rod . . . 64
3.2.2 FE study: Mesh convergence of surgical transducer . . . 66
3.2.3 FE analysis: Piezoceramic ring . . . 68
3.2.4 Summary: Finite element analysis . . . 69
3.3 Experimental Modal Analysis . . . 70
3.3.1 Theoretical approach to vibration analysis . . . 71
3.3.2 EMA: Experimental considerations . . . 75
3.3.3 Boundary conditions . . . 77
3.3.4 Excitation of structure . . . 78
3.3.5 Collection of Data . . . 79
3.3.6 Spectrum Analysers . . . 82
3.3.7 Experimental modal analysis: Experimental setup . . . 85
3.4 FEA and EMA: comparison . . . 86
3.4.1 Modal parameters . . . 86
3.4.2 Dynamic performance . . . 88
3.5 Characterisation of medical ultrasonic devices . . . 91
3.5.1 Characterisation of scaling inserts . . . 91
3.5.2 Evolution of bone cutting device . . . 93
3.5.3 Optimisation of bone cutting devices . . . 97
3.6 Chapter Summary . . . 101

4 Characterisation of surgical devices **103**
4.1 Experimental characterisation techniques . . . 104
4.1.1 Harmonic response at constant voltage . . . 104
4.1.2 Harmonic response with constant current . . . 104
4.1.3 Harmonic response: burst excitation . . . 105
4.1.4 Burst excitation: measurement of transient response . . . 105
4.1.5 Burst excitation: measurement of steady state response . . . 106
4.2 Power harmonic characterisation: experimental setup . . . 107
4.2.1 Initial harmonic characterisation experimental setup . . . 107
4.2.2 Experimental harmonic characterisation setup developed at CSIC . . . 108

4.3 Power harmonic characterisation of ultrasonic devices . . . 110
4.3.1 Commercial surgical insert: Half wavelength assembly . . . 110
4.3.2 Commercial surgical insert: Full wavelength assemblies . . . 116
4.3.3 Custom Inserts . . . 123
4.3.4 Custom Insert: Half wavelength assemblies . . . 125
4.3.5 Custom Insert: Full wavelength assemblies . . . 131
4.3.6 Discussion of custom and commercial inserts . . . 137
4.4 Effect of temperature on ultrasonic devices . . . 142
4.4.1 Burst drive versus continuous drive . . . 142
4.4.2 Burst drive - Time delay study . . . 143
4.4.3 Discussion - Effect of temperature on ultrasonic devices . . . 145
4.5 Effect of joint tightness . . . 146
4.5.1 Characterisation of joint tightness . . . 147
4.5.2 Discussion - Effect of joint tightness . . . 149
4.6 Chapter Conclusion . . . 151

5 Characterisation of Langevin transducers 152
5.1 Transducers . . . 153
5.2 Resonant frequency and mode shape extraction . . . 154
5.2.1 Finite element and experimental modal analysis . . . 154
5.2.2 Impedance Analyser measurements . . . 156
5.2.3 Discussion . . . 159
5.3 Power harmonic characterisation . . . 160
5.3.1 Power harmonic characterisation of transducer configurations I, II & III 161
5.3.2 Harmonic responses of configurations I, II and III . . . 166
5.3.3 Discussion . . . 169
5.4 Stress in transducers . . . 171
5.4.1 Finite element model . . . 172
5.4.2 Discussion . . . 173
5.5 Chapter conclusion . . . 174

6 Conclusions 175
6.1 Correlation between FEA and EMA . . . 175
6.2 Vibrational behaviour of ultrasonic devices . . . 176
6.2.1 Influence of tuned insert on vibrational behaviour . . . 176
6.2.2 Influence of location of piezoceramic stack on transducer behaviour . . . 178
6.3 Summary of findings . . . 179
6.4 Design guidelines . . . 179

7 Future Work 181

A List of publications **182**

References **183**

List of Tables

3.1 Maximum strain and safe working limits of materials commonly used in ultrasonic tool manufacture 58
3.2 Material properties relating to toughness 59
3.3 Characteristics and applications of typical piezoceramics 60
3.4 Values of selected properties of piezoelectric materials 61
3.5 Acoustic values of materials used in tool manufacture 63
3.6 Cost of common alloys used in manufacture of ultrasonic components 63
3.7 Types of Excitation Signals 78
3.8 Predicted and measured frequencies of the tuned mode of vibration for the modified OT7 inserts 98

4.1 Mechanical quality factors and material of manufacture of full wavelength surgical assemblies 117
4.2 Longitudinal frequencies of full wavelength surgical assemblies predicted through FEA 117
4.3 Properties of rod horn material of manufacture 124
4.4 Mechanical quality factors of rod horn assemblies 124
4.5 Frequency shift and Q_m of half and full wavelength surgical assemblies 138
4.6 Amplitude of vibration and excitation voltage that amplitude jumps are first observed in tuned assemblies 140
4.7 Hysteretic widths of tuned assemblies 140

5.1 Percentage difference between resonant frequencies found through EMA and impedance analyser methods 157
5.2 Frequencies of maximum and minimum admittance of transducer configurations I, II & III 158
5.3 Values of k_{eff} for transducer configurations I, II & III 159
5.4 Values of Q_e for transducer configurations I, II & III 159
5.5 Mechanical quality factors of 1^{st} longitudinal mode of transducer configurations I, II & III 161

6.1 General guidelines for the design and the control of common nonlinear behaviours observed in ultrasonic devices 180

List of Figures

1.1 Schematic of high power ultrasonic system 2
1.2 Influence of magnetic field on strain in ferromagnetic materials 3
1.3 Positive and negative magnetostrictive effect 4
1.4 Ferromagnetic shape memory alloy domain shape 4
1.5 The piezoelectric effect represented with a single dipole 5
1.6 Relationship between piezoelectricity and pyroelectricity 6
1.7 The perovskite structure of ABO_3 crystalline material 9
1.8 Orientation of domains in ferroelectric material throughout poling process . . 10
1.9 Ferroelectric hysteresis loops during polarisation 11
1.10 Typical layout of broad and narrow-band transducers 12
1.11 Approximate equivalent circuit unloaded piezoelectric resonator 13
1.12 Approximate relationships of unloaded piezoelectric resonator 14
1.13 Ultrasonic cleaning process 15
1.14 Ultrasonic welding processes 17
1.15 Ultrasonic horns used in food cutting 18
1.16 Transducer designed to operate in a longitudinal-flexural complex mode . . . 19
1.17 Horns designed to operate in a longitudinal-torsional complex mode 19
1.18 Simplified structure of an ultrasonic motor 20
1.19 Experimental levitation and transportation setup 21
1.20 Depiction of HIFU treatment on a tumour 22
1.21 Schematic diagram of phacoemulsification 23
1.22 Soft tissue dissection 24
1.23 Ultrasonic scaling 25
1.24 Simulation of deformation of the oscillation of an ultrasonic cutting insert . . 26
1.25 Cutting with Piezosurgery® Device 26
1.26 Representative histologic photomicrographs of decalcified specimens 27
1.27 Frequency response curves for varying cubic stiffness terms 29
1.28 Depiction of nonlinear responses of dynamic systems 29
1.29 Beam containing a primary and secondary coupled structures under autoparametric behaviour 30

1.30 Depiction of period doubling route to chaos 32

3.1 Element within a slender bar 50
3.2 Basic architecture of a symmetrical prestressed Langevin transducer 51
3.3 Basic architecture of an asymmetrical prestressed Langevin transducer . . . 52
3.4 Poling direction of piezoceramic rings within a piezoceramic stack containing four active elements 53
3.5 Fatigue stress limit in piezoceramic 54
3.6 Calculation of Q factor 58
3.7 Number and type of elements to achieve convergence of resonant frequencies of slender bar 65
3.8 Number of elements required to achieve convergence upon the frequency of the 1^{st} longitudinal mode of vibration 67
3.9 Mesh design and convergence of surgical transducer 68
3.10 Thickness mode of PZT ring found through FEA 69
3.11 Revision of FE models with experimentally acquired properties 70
3.12 Theoretical route to vibration analysis 71
3.13 Single degree of freedom system 72
3.14 Example of repeated modes 74
3.15 Simplified schematic diagram of LDV 81
3.16 Different types of windowing 82
3.17 Forms of multi-sampling averaging 84
3.18 Schematic diagram of experimental modal analysis 85
3.19 Half wavelength sandwich transducer with titanium endmasses 86
3.20 Estimated endmass length with respect to acoustic impedance ratio 86
3.21 Undeformed 3D transducer geometry of transducer configuration A 87
3.22 Configuration A: Experimental FRF's and curve fitted traces found through EMA 87
3.23 Configuration B: Experimental FRF's and curve fitted traces found through EMA 88
3.24 Resonant frequencies and mode shapes of configuration A found through FEA and EMA 89
3.25 Resonant frequencies and mode shapes of configuration B found through FEA and EMA 89
3.26 Influence of application of global damping on amplitudes of vibration on FE model of configuration A 90
3.27 Response of transducers excited at $1V_{peak}$ acquired from experimental and FE methods 90
3.28 Mectron S.p.A scaling Inserts 91

3.29 S1 Insert: Mode shapes of tuned mode of vibration found through FEA/EMA 92
3.30 S2 Insert: Mode shapes of tuned mode of vibration found through FEA/EMA 92
3.31 Dynamic stress distributions in scaling inserts 93
3.32 Mectron cutting inserts 94
3.33 OT2 Insert: Mode shapes of tuned mode of vibration found through FEA/EMA 94
3.34 OT6 Insert: Mode shapes of tuned mode of vibration found through FEA/EMA 95
3.35 OT7 Insert: Mode shapes of tuned mode of vibration found through FEA/EMA 95
3.36 Dynamic stress distributions in bone cutting inserts 96
3.37 Modified OT7 cutting inserts 97
3.38 Mode shapes predicted through FEA of modified OT7 inserts 98
3.39 Mode shapes extracted from EMA of modified OT7 inserts 98
3.40 FEA - Modified OT7 insert assemblies normalised undeformed contour map of displacement 99
3.41 EMA - Modified OT7 insert assemblies normalised undeformed contour map of displacement 99
3.42 Amplitude of vibration and corresponding stress verses change in blade length 100
3.43 Normalised stress distributions in modified OT7 cutting inserts 101

4.1 Transient response method: Voltage and current waveforms 105
4.2 Burst response of current 106
4.3 Schematic of initial experimental setup 107
4.4 Thermal images of Mectron transducer with base insert 108
4.5 Schematic of CSIC experimental setup 109
4.6 Burst voltage/current signal captured from the oscilloscope 109
4.7 Transducer and OT7 insert assembly 110
4.8 Piezosurgery® base and OT7 insert 111
4.9 OT7 insert: Mode shapes of tuned mode of vibration found through FEA/EMA 111
4.10 Base insert: Mode shapes of tuned mode of vibration found through FEA/EMA 111
4.11 Vibration response of OT7 and base insert assemblies - Experimental setup 1 112
4.12 Vibration response of OT7 and base insert assemblies - Experimental setup 2 112
4.13 Comparison of resonant frequency shift found through experimental setup 1 & experimental setup 2 113
4.14 Comparison of hysteretic width found through experimental setup 1 & experimental setup 2 114
4.15 Current drawn by transducer during characterisation of OT7 and base insert assemblies - Experimental setup 2 115
4.16 Oscilloscope images captured of OT7 and base inserts near resonance 115
4.17 Photographs of half wavelength Mectron inserts 116

4.18 TLR insert with blade tip: Mode shapes of tuned mode of vibration found through EMA 118
4.19 TLR insert without blade tip: Mode shapes of tuned mode of vibration found through EMA 118
4.20 X15TR insert with blade tip: Mode shapes of tuned mode of vibration found through EMA 119
4.21 420BR insert with blade tip: Mode shapes of tuned mode of vibration found through EMA 119
4.22 Percentage difference between frequencies of longitudinal modes found through FEA and EMA 120
4.23 Vibrational response of full wavelength surgical assemblies between 2-50V_{rms} 121
4.24 Current drawn by transducer during response characterisation of full wavelength surgical assemblies 122
4.25 Nonlinear behaviour of full wavelength surgical assemblies 122
4.26 Power spectrum images captured of TLR insert with/without blade tip . . . 123
4.27 Rod horns used in the half and full wavelength assemblies 124
4.28 Half wavelength aluminium rod horn assembly: Mode shapes of longitudinal modes of vibration found through FEA/EMA 125
4.29 Half wavelength brass rod horn assembly: Mode shapes of longitudinal modes of vibration found through FEA/EMA 126
4.30 Half wavelength stainless steel rod horn assembly: Mode shapes of longitudinal modes of vibration found through FEA/EMA 127
4.31 Percentage difference between frequency of longitudinal vibration of custom half wavelength assemblies 128
4.32 Vibrational response of half wavelength assemblies between 2-50V_{rms} 129
4.33 Current drawn by transducer during response characterisation of half wavelength assemblies 130
4.34 Nonlinear behaviour of half wavelength assemblies 130
4.35 Full wavelength aluminium rod horn assembly: Mode shapes of longitudinal modes of vibration found through FEA/EMA 131
4.36 Full wavelength brass rod horn assembly: Mode shapes of longitudinal modes of vibration found through FEA/EMA 132
4.37 Full wavelength stainless steel rod horn assembly: Mode shapes of longitudinal modes of vibration found through FEA/EMA 133
4.38 Percentage difference between frequency of longitudinal vibration of full wavelength assemblies found through FEA and EMA 134
4.39 Vibrational response of full wavelength assemblies between 2-50V_{rms} 135
4.40 Current drawn by transducer during response characterisation of full wavelength assemblies 136

4.41 Nonlinear behaviour of full wavelength assemblies with respect to amplitude . 137
4.42 Effect of temperature increases in OT7 insert assembly - Experimental setup 1 142
4.43 Response of assembly containing X15TR insert 143
4.44 Nonlinear behaviour of X15TR insert with respect to amplitude 144
4.45 Nonlinear behaviour of X15TR insert with respect to excitation voltage . . . 144
4.46 Temperature measurements from surface of piezoceramic stack: X15TR Insert 145
4.47 Frequency response of the half wavelength assembly containing a brass rod horn with tight and loose joints at an excitation of $2V_{rms}$ 147
4.48 Vibrational response of half wavelength assembly contain a brass rod horn . . 147
4.49 Current drawn by transducer during nonlinear characterisation of half wavelength assembly containing a brass rod horn with tight and loose joints . . . 148
4.50 Nonlinear behaviour of half wavelength assembly containing a brass rod horn with tight and loose joints 148

5.1 Transducer Configurations 153
5.2 Configuration I: Mode shapes of 1^{st} longitudinal mode of vibration found through FEA/EMA 154
5.3 Configuration II: Mode shapes of 1^{st} longitudinal mode of vibration found through FEA/EMA 154
5.4 Configuration III: Mode shapes of 1^{st} longitudinal mode of vibration found through FEA/EMA 155
5.5 Configuration I: Mode shapes of 2^{nd} longitudinal mode of vibration found through FEA/EMA 155
5.6 Configuration II: Mode shapes of 2^{nd} longitudinal mode of vibration found through FEA/EMA 155
5.7 Configuration III: Mode shapes of 2^{nd} longitudinal mode of vibration found through FEA/EMA 155
5.8 Mode shapes of 3^{rd} longitudinal mode found through FEA 156
5.9 Admittance and impedance measurements of transducer configurations 157
5.10 Percentage difference between frequencies of longitudinal modes of vibration of transducer configurations 158
5.11 Amplitude response for 1^{st} longitudinal mode under $1V_{rms}$ excitation 160
5.12 Vibrational response of configuration I 161
5.13 Vibrational response of configuration II 162
5.14 Vibrational response of configuration III 162
5.15 Vibrational response of transducer configurations against excitation voltage . 163
5.16 Current drawn by transducer configurations 163
5.17 Resonant frequency shift versus vibrational response of transducer configurations 164

5.18 Hysteretic width and corresponding vibrational response of transducer configurations 164
5.19 Current drawn by transducer configurations against vibrational response at first longitudinal mode 165
5.20 Configuration I - Power spectrum captured from oscilloscope 166
5.21 Configuration I - Excitation of 1^{st} longitudinal mode: Response of ω_2 167
5.22 Configuration I - Response of excitation at 3^{rd} longitudinal mode of vibration 167
5.23 Configuration I - Current drawn by transducer at 3^{rd} longitudinal mode . . . 167
5.24 Configuration II - Power spectrum captured from oscilloscope 168
5.25 Configuration II - Frequency response of ω_2 168
5.26 Configuration III - Power spectrum captured from oscilloscope 169
5.27 Configuration III - Frequency response of ω_2 169
5.28 Stress contour plots of transducer configurations 172

Chapter 1

Introduction

The definition which the Oxford dictionary gives to sound is; *a vibration in an elastic medium at a frequency and intensity that is capable of being heard by the human ear*, later adding that, *The frequency of sounds lie in the range 20Hz to 20000Hz* [1]. Although the upper and lower thresholds of human hearing vary from person to person, it is readily accepted that this range represents a standardisation which the frequency thresholds of human hearing can be measured against. Sound waves outwith the audio range are often referred to as either infrasound, those which lie below the lower threshold of human hearing, or those with frequencies in excess of 20kHz which are classified as ultrasonic or ultrasound.

The field of ultrasonics encompasses a broad spectrum of industrial processes and medical procedures. These will generally fall in to two distinct groups, the first (low power ultrasonics) propagates acoustic waves through a medium that do not alter the physical properties of that medium, such as in ultrasonic nondestructive testing or medical diagnostics. The second (high power ultrasonics, also referred to as macrosonics) requires that the acoustic waves induce a permanent change in the medium that they are applied or propagated in, such as during ultrasonic cutting, ultrasonic welding and sonochemistry processes. Generally low power applications utilise frequencies in the range from hundreds of kilohertz to megahertz while high power processes usually use frequencies from the lower ultrasonic range, up to a few hundred kilohertz. Meanwhile, the acoustic intensity threshold at which low power applications becomes high power is not exact as it can depend on the properties of the medium in which the acoustic wave is propagated, however, it can be approximated between 0.1Wcm^{-2} and 1Wcm^{-2} [2–5].

This document focuses on the characterisation of high power ultrasonic devices utilised in bone surgery and for these devices carry out their designated task, they are required to be driven at elevated amplitudes (typically between 10 to 100μm). If these devices operate linearly, the signal used to excite the devices will be proportional to the output amplitude of vibration, however, it has been well documented [6–11] that power ultrasonic devices, including those used in surgery, when operated under these conditions can demonstrate

nonlinear behaviour. Nonlinear behaviour results in the output amplitude of vibration of the device being disproportional to the input excitation signal and although this can lower performance, it can also increase the likeliness of device failure. The dynamic behaviour of ultrasonic surgical devices (which contain slender geometry that minimises the evasiveness or allows the access to difficult to reach surgical sites) results increases the likelihood that they will suffer from nonlinear behaviour than ultrasonic devices which possess a more robust geometry. Therefore a combination of finite element analysis and experimental techniques has been used to characterise both linear and nonlinear behaviour of high power ultrasonic devices utilised in bone surgery with the aim that design guidelines which minimise or control nonlinear behaviour will ensue.

1.1 Power ultrasonic devices

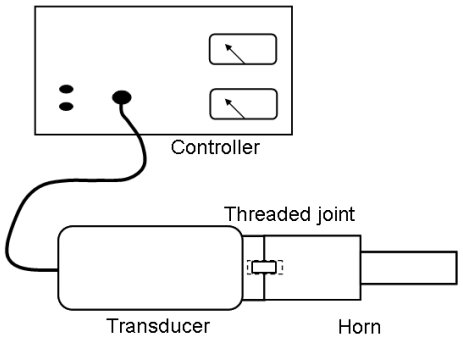

Figure 1.1: Schematic of high power ultrasonic system

Power ultrasonic devices, as seen by Figure 1.1, generally consist of two fundamental components; the generator and the transducer. The transducer converts electrical energy into mechanical energy and is often tuned to operate within a narrow frequency bandwidth. Meanwhile, the generator transforms mains power supply from a frequency of 50Hz or 60Hz to the tuned frequency of the transducer as well as altering the voltage or current to optimise operational performance. In many processes the maximum amplitude of vibration achieved by the transducer is not sufficient to drive the process (such as ultrasonic cutting or welding), therefore, the amplitude at the output face of the device can be increased by connecting a tool (often called a horn and tuned to the same resonant frequency of the transducer) designed to amplify the output amplitude of vibration. Furthermore intermediate horns can be incorporated between the tool with the working output face and the transducer to further enhance output amplitude at the working face. These processes often consist of vibrating tools with small output surface areas, optimised for high amplitude of vibration, meanwhile process such as sonochemistry, may require horns to be optimised in sightly different ways, for example, large output surface areas for enhanced acoustic transmission into a fluid. Nevertheless, the tuned horn should be machined from acoustically efficient

materials manufactured to minimise acoustic loss. Furthermore, acoustic efficiency should also be considered when joining different tuned components together so that the materials each component is manufactured from have similar acoustic properties to ensure optimal transmission of acoustic energy across the join.

1.2 Transducer transduction

The purpose of power ultrasonic transducers is to convert electrical energy at a set frequency to mechanical motion which oscillates at the same frequency as the electrical input signal. To achieve the transformation of electrical to mechanical energy, transducers contain active materials which possess either the magnetostrictive effect or the inverse piezoelectric effect. Power transducers should not be confused with measurement transducers such as accelerometers or load cells. These 'transducers', fundamentally, operate using reverse principles of that utilised in power transducers as they produce electrical signals which are proportionate to the level of vibration which they are exposed to.

1.2.1 Magnetostriction

Magnetostriction is a broadly used term which refers to the phenomenon where a material changes shape due to a change in its magnetic state. Ferromagnetic materials, such as iron, cobalt and nickel, are constructed from structures or domains (which can be imagined as ellipses, Figure 1.2) and are naturally distorted and unaligned, but critically also possess a magnetic polarity. When a magnetic field, H, is applied to the ferromagnetic material, the domains will re-orientate, aligning themselves with direction of the applied field. The stronger the field, the more defined the realignment of the domains will become until the domains have re-orientated as much as they can and saturation has been reached [12, 13].

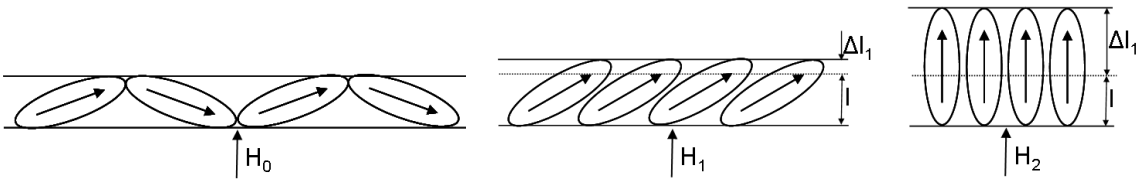

(a) No magnetic field (b) Weak magnetic field (c) Strong magnetic field

Figure 1.2: Influence of magnetic field on strain in ferromagnetic materials

Magnetostriction was first reported by Joule after observing a small, reversible change in the length of a sample of iron when a weak magnetic field was applied to it. This form of magnetostriction, in which the length of the sample changes but the volume is conserved, is known as Joule magnetostriction, however, there are also two other common types of magnetostriction: transverse magnetostriction, where the dimension of change in the sample

is perpendicular to the magnetic field, and volume magnetostriction, where the volume of the sample is not conserved when a magnetic field is applied. Joule magnetostriction is the most understood variant of magnetostriction; a ferromagnetic sample is exposed to a longitudinal magnetic field causing the sample to either expand (positive magnetostriction) or contract (negative magnetostriction) along its longitudinal axis and, as volume of the magnetostrictive material is assumed to remain constant dimensions perpendicular to the longitudinal direction will either reduce or lengthen respectively.

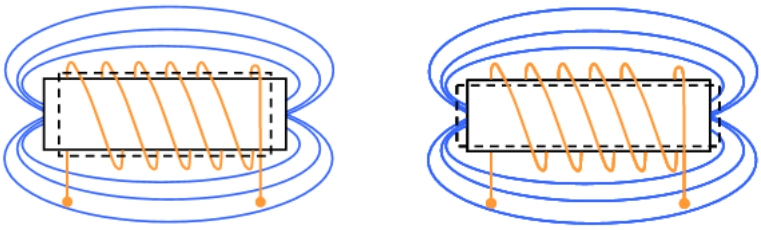

(a) Positive magnetostrictive effect (b) Negative magnetostrictive effect

Figure 1.3: Positive and negative magnetostrictive effect

Materials such as transition metals; iron, cobalt and nickel, demonstrate magnetostrictive behaviour, although the strain produced within the material before saturation is relatively small (0.01%), thus restricting the potential vibrational displacement which can be achieved. Modern magnetostrictive alloys, or 'giant magnetostrictive materials' (GMM) on the other hand can achieve strain levels in the region of 1-2%. These alloys contain rare earth metals such as Terbium (Tb) and Dysprosium (Dy) which possess large magnetostrictive properties, while, another group of materials which possess high magnetostrictive properties are 3-d transition based iron-gallium (Fe-Ga) alloys. However, the third and possibly most promising form of modern magnetostrictive materials are ferromagnetic shape memory alloys (FSMA) as they have the potential to produce strains in the region of 2-6% before saturation. To produce such large strains, FSMAs exploit the movement between a structure which naturally contains several tetragonally distorted domains (when under no magnetic field) and a structure which in the presence of a magnetic field contains a single domain, Figure 1.4 [12, 13].

(a) FSMA structure: No magnetic field (b) FSMA structure: Under magnetic field

Figure 1.4: Ferromagnetic shape memory alloy domain shape with and without magnetic field [12]

Power transducers which utilise the magnetostrictive effect to generate ultrasound

are found in both medical and industrial processes. Generally, magnetostrictive power transducers consist of stack of thin strips of a magnetostrictive material arranged in parallel as a laminate. A coil of wire is wound around the magnetostrictive stack and by passing an electrical current through the coil, a magnetic field is generated. The frequency from the electrical source should be half that of the desired operational frequency of the transducer as the magnetic field will alternate twice throughout a single cycle of a sinusoidal electrical wave inducing either the positive or negative magnetostrictive effect in the stack and thus producing an output amplitude.

1.2.2 Piezoelectricity

Materials demonstrating piezoelectricity (partly named after the Greek word *piezein* meaning to 'press' or 'pressure'), such as quartz and Rochelle salt as well as piezoceramics; barium titanate, $BaTiO_3$, and lead zirconate titanate (PZT), $PbZr_xTi_{1-x}O_3$, induce an electric charge with the application of a force [14]. Materials which demonstrate the direct effect will also exhibit the converse or inverse effect characterised by a strain being induced with the application of a potential difference, as illustrated in Figure 1.5. Although, all piezoelectric materials contain a crystalline structure, they must have the prerequisite of lacking a centre of symmetry, making them intrinsically anisotropic. Altogether there are 32 classes of crystalline structures, of which 21 lack a centre of symmetry with 20 possessing piezoelectric properties. These can be further divided into 10 crystal subgroups where each will contain an unique polar axis (an electric dipole moment or spontaneous polarisation) even in the absence of an electric field [15, 16].

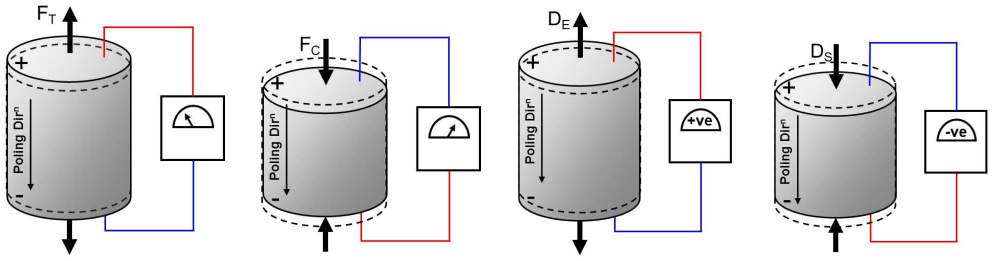

(a) Direct effect under tension (b) Direct effect under compression (c) Inverse effect under +ve PD (d) Inverse effect under -ve PD

Figure 1.5: The piezoelectric effect represented with a single dipole [17]

As well as possessing the ability to generate an electric charge with the application of stress, the crystalline structures which compose the previously mentioned 10 crystalline subgroups will also generate an electric charge when exposed to uniform heating or cooling. This phenomenon is known as pyroelectricity (also stemming from Greek, *pyr*, meaning fire). However due to the nature of the internal dipoles, some piezoelectric materials, such as quartz, will not exhibit pyroelectricity due a lack of polar axis in the unstrained

condition. Therefore, even though not all piezoelectric materials demonstrate pyroelectricity, all materials which demonstrate pyroelectric properties are inherently piezoelectric due to the crystalline symmetry conditions [15, 16, 18].

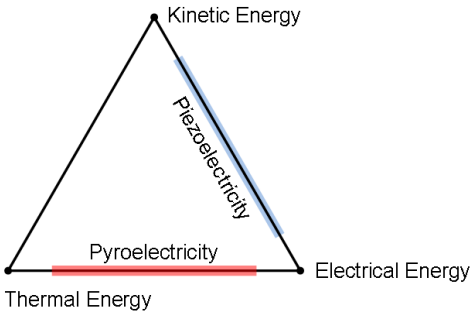

Figure 1.6: Relationship between piezoelectricity and pyroelectricity

As previously discussed, minerals (such as quartz) and inorganic compounds (piezoceramics) demonstrate piezoelectric as well as pyroelectric and ferroelectric properties, however there is also a third material classification that exhibits such properties, polymers. Polymers are composed from molecule chains of repeating structural units and the piezoelectric, pyroelectric and ferroelectric effects have been studied in natural polymers such as cellulose (structural component of the primary cell wall of green plants and is commonly used in the manufacture of paper) and collagen (protein found in animals, especially in flesh and connective tissues such as tendons) since the 1940s. However, approximately twenty years after the discovery of piezoelectric natural polymers, the piezoelectric effect was discovered in poled synthetic polymers such as polyvinylidene fluoride (PVDF) and those derived from vinylcyanide and vinyacetate or vinylideme fluoride and trifluoroethylene [19–21].

Constituent equations

Properties of piezoelectric materials consist of a coupling between mechanical and electrical variables which are related through constituent equations. Each equation is constructed from both electrical and mechanical constants (which are dependent on crystal type) and variables (which are dependent on boundary conditions), usually stress, T, or strain, S, located on one side of the equation and electric field, E, or dielectric displacement, D, on the other. To construct the constituent equation, the mechanical and electrical relationships for an unstressed non-piezoelectric material should be initially considered. The mechanical relation for a material exposed to zero electric field strength and under the application of an applied stress will produce the following strain;

$$S = sT \tag{1.1}$$

where s is the elastic compliance (inverse of stiffness or $\frac{strain}{stress}$) of the material. In crystalline

structures, the number of independent elastic compliance constants can be large, although, with increased symmetry the number reduces. Meanwhile the electric relation for the material under the influence of an electric field is;

$$D = \varepsilon E \tag{1.2}$$

where ε is the electrical permittivity (measure of the resistance encountered when forming an electric field) of the material. Four forms of linear piezoelectric equations are listed below, Equation sets 1.3 to 1.6. The first equation of each set represents the inverse piezoelectric effect while the second represents the direct piezoelectric effect for each condition. Equation set 1.3, containing E and S as independent variables, represents the specific condition of a piezoelectric material operating in a 'thickness mode' while Equation set 1.4 expresses the condition for piezoelectric material operating in a longitudinal mode where the electric field is applied transversely and E and T are independent variables [15, 16, 18, 22, 23];

$$\begin{aligned} T_i &= c_{ij}^{E} S_j - e_{mi} E_m \\ D_m &= e_{mi} S_i + \varepsilon_{mk}^{S} E_k \end{aligned} \tag{1.3}$$

$$\begin{aligned} S_i &= s_{ij}^{E} T_j + d_{mi} E_m \\ D_m &= d_{mi} T_i + \varepsilon_{mk}^{T} E_k \end{aligned} \tag{1.4}$$

$$\begin{aligned} S_i &= s_{ij}^{D} T_j + g_{mi} D_m \\ E_m &= -g_{mi} T_i + \beta_{mk}^{T} D_k \end{aligned} \tag{1.5}$$

$$\begin{aligned} T_i &= c_{ij}^{D} S_j + h_{mi} D_m \\ E_m &= -h_{mi} S_i + \beta_{mk}^{S} D_k \end{aligned} \tag{1.6}$$

The piezoelectric constants, d, g, e, and h, are third-order tensors which relate second order symmetry tensors (strain and stress) to vectors (dielectric displacement or electric field). The elastic compliance, s, and stiffness, c, constants are fourth-order symmetric tensors relating two second-order symmetric tensors and the dielectric permittivity, ε, and impermittivity, β, constants are second-order symmetric tensors relating two vectors. To simplify the notation, tensor notation can be shortened to matrix notation using the Voigt convention. Indices

written as ii in tensor form equal 11, 22 or 33, however, matrix form replaces this with a single index, $m = 1$, 2 or 3, while, mixed indices, such as $ij = 23$ or 32, 13 or 31, 12 or 21 in tensor form, are written as $m = 4$, 5 or 6 respectively. Matrix notation has been used in Equations 1.3 to 1.6 and $i, j = 1$ to 6, and $m, k = 1$ to 3 [14, 18]. The constants from Equations 1.3 to 1.6 are also interrelated as follows;

$$\begin{aligned} d_{mi} &= \varepsilon^T_{nm} g_{ni} = e_{mj} s^E_{ji} \\ g_{mi} &= \beta^T_{nm} d_{ni} = h_{mj} s^D_{ji} \\ e_{mi} &= \varepsilon^S_{nm} h_{ni} = d_{mj} c^E_{ji} \\ h_{mi} &= \beta^S_{nm} e_{ni} = g_{mj} c^D_{ji} \end{aligned} \tag{1.7}$$

Finally, superscripts D and E denoted in the elastic, piezoelectric and dielectric constants refer to boundary conditions which the piezoelectric material are kept under. Superscript D represents that the electrodes are in open circuit conditions, keeping the dielectric displacement constant, while superscript E implies short circuit conditions, or constant electric field across the piezoelectric element. Meanwhile, the dielectric permittivities, ε^S represents the material under static conditions where it behaves as if under free boundary conditions and thus under zero stress. ε^T on the other hand represents the material under dynamic conditions, when it behaves as it was under clamped boundary conditions, therefore strain within the material is zero. Both conditions are considered to be far from resonance, ε^S at a frequency far lower than the first resonant frequency while, ε^T is considered far above a resonant frequency.

Ferroelectricity

All piezoelectric and pyroelectric materials are ferroelectric. They possess at least two equilibrium orientations of spontaneous polarisation (internal dipole moment) in the absence of an electric field, while in the presence of an electric field the polarisation direction will align with the direction of the applied field. The structure of most ferroelectric materials is not constant with temperature. Above a temperature threshold known as the Curie temperature, T_c, the structural phase of the crystallites (crystals in quartz or grains in piezoceramics) will be non-ferroelectric or paraelectric. The paraelectric phase can either be piezoelectric or non-piezoelectric, although it will generally not possess polar properties.

Piezoceramic materials often possess the general chemical formula $\mathrm{A}^{2+}\mathrm{B}^{1+}\mathrm{O}_3^{2-}$ and are built from cells known as perovskite structures; a tetragonal-rhombohedral cell with a shape close to a cubic, where A usually represents a large divalent metal ion such as barium, Ba, or lead, Pb, while B often denotes a tetravalent metal ion such as titanium, Ti, or zirconium, Zr. Above the Curie temperature, the perovskite cells in a piezoceramic, such as barium

titanate, will contain a phase structure similar to that illustrated in Figure 1.7(a). The structure exhibits a simple cubic symmetry which is centrosymmetric due to the coinciding positive and negative charge sites, however, once the temperature is cooled below the Curie temperature the cell takes a slightly different shape as seen in Figure 1.7(b). The cell structure now contains a tetragonal symmetry as the positive and negative charges no longer coincide, the structure contains a natural dipole which has the ability to be reversed [15, 16, 18, 24].

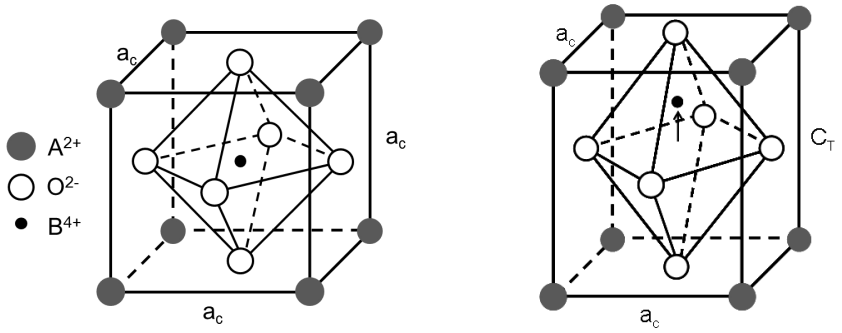

(a) Cubic cell: Paraelectric phase (b) Tetragonal cell: Ferroelectric phase

Figure 1.7: The perovskite structure of ABO_3 crystalline material [16, 18]

The dipoles within the global structure of the ferroelectric material are not randomly oriented, but aligned similarly to that of its neighbouring dipoles, known as Weiss domains. Within Weiss domains all poles are aligned producing a net polarisation, however, the direction of polarisation between neighbouring Weiss domains in the crystalline structure can vary by 90^o or 180^o giving the global effect zero net polarity. Materials such as piezoelectric ceramics possess zero polarity during the production process and at these stages do not exhibit piezoelectric or pyroelectric behaviour due the net cancelation among individual domains. However, through a process called poling, polycrystilline ferroelectric materials can be given a polar state through the application of a strong electric field whilst at an elevated temperature just below the material's Curie temperature. The process does not re-orientate the crystals or grains within the material, but reorients the polarity of the domains to that of the applied electric field. Figures 1.8(a) and 1.8(b) illustrate the random and then re-orientation of the domains in the presence of an electric field. After the removal of the electric field the remaining polarisation is known as the remanent polarisation, P_R, and is dependent on domain states. Generally the larger the number of domain states (or angles which domain walls meet at), the higher the theoretical maximum polarisation, however, in reality the polarisation is always lower. This is due to a number of reasons, from the inability of some domains to re-orientate due to the occurrence of complex sets of internal stresses to simply that some ultimately return to their original poling direction, Figure 1.8(c) [16,18,24].

Similar to piezoceramics, poled polymers, such as PVDF and those derived from vinylcyanide and vinyacetate or vinylideme fluoride and trifluoroethylene, demonstrate

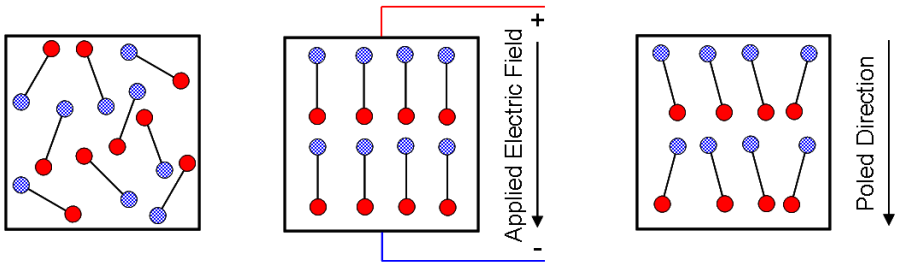

(a) Before polarisation (b) During polarisation (c) After polarisation

Figure 1.8: Orientation of domains in ferroelectric material throughout poling process [17]

tensile, thickness and shear piezoelectricity and similarly require poling. They can be poled through the application of an electric field, reorienting dipoles within the in the crystalline phases inside the lamellae and in the interfaces between the crystalline and noncrystalline phases so they have a common direction [20, 25]. However unlike piezoceramics, poled polymers possess a negative piezoelectric coefficient value, d_{33}, therefore when exposed to an electric field, the polymer will deform compressively when a piezoceramic would lengthen.

Nonlinearities in ferroelectrics

The cause of nonlinear behaviour in ferroelectrics can be traced to the application of mechanical and electrical stresses to the material and the influence they have on the domain configuration. During poling, ferroelectric materials exhibit nonlinear behaviour, due to domain wall shifting, in the form of an hysteresis loop, Figure 1.9(a). At low excitation levels, between points A-B, in Figure 1.9(a) (corresponding to a period when the ferroelectric material remains not poled), polarisation relates linearly with electric field strength. However as electric field strength rises those domains not already aligned within the field will increasingly align themselves with the applied electric field until the section B-C (Figure 1.9(a)) is reached where the domains will rapidly align themselves. This section will also demonstrate strong nonlinear behaviour until point C is reached, at which, all domains are aligned with the electric field. Further increases in electric field, section C-D, will see a return to linear behaviour however, with the reduction of electric field strength after poling, some domains will return to their original orientation. The electric field necessary to return the polarisation to zero (at point E) is called the coercive field, E_c, while the spontaneous polarisation (the polarisation in the absence of an external electric field) is extrapolated from the linear section, C-D, to an intercept with the polarisation axis. To reverse the polarisation, an electric field of opposite polarity is required to be applied to the ferroelectric for an extended period of time.

In addition to the polarisation-electric field strength hysteresis loop, switching the polarisation due to a changing electric field also induces a strain-electric field hysteresis loop, Figure 1.9(b). This differs considerably from that of the P-E hysteresis loop and

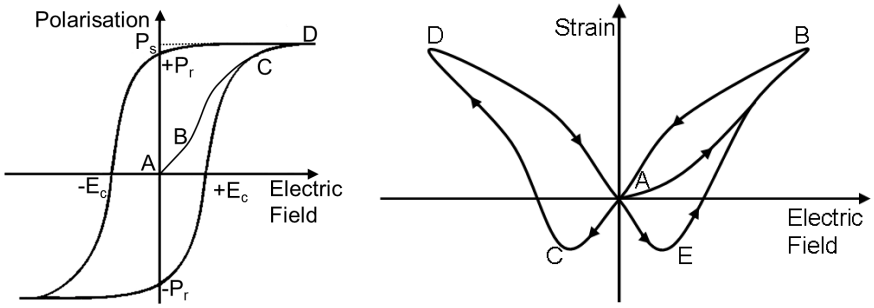

(a) Polarisation-electric field hysteresis loop

(b) Strain-electric field hysteresis loop

Figure 1.9: Ferroelectric hysteresis loops during polarisation [17, 18]

is often referred to as a 'butterfly loop' due to the shape of its outline. The region *A*-*B* in Figure 1.9(b) illustrates a typical hysteresis loop where a positive electric field is applied to a ferroelectric material which, due to the inverse piezoelectric effect, induces a positive strain, causing expansion within the material. The removal of the electric field to zero is then mirrored by the induced strain which returns to zero as well. However one cycle of an alternating electric field contains both positive and negative fields points. The negative electric field induces a negative strain along the region *A*-*C* until the electric field reaches the depoling or coercive field at point *C* where the poling direction switches and the strain becomes positive again (at D). The electric field reduces from *D*, until the electric field and strain are zero at *A*, at which the process is repeated along the path *A*-*E*-*B* [18, 24].

It should be noted that in the above cases, *P*-*E* and *S*-*E* hysteresis loops represent ideal responses that assume only 180° domain boundaries which reverse instantaneously. In reality piezoceramics contain many non-180° domains and the switch of non-180° domain walls can lead to an increase in strain, compounding strain levels generated by the piezoelectric effect. This further source of strain has been found to be strongly nonlinear and hysteretic, as well as often being the *S*-*E* relationship most commonly observed experimentally. Furthermore, the hysteresis loops, illustrated in Figure 1.9, also assume ideal microstructure and composition of the material, excluding any possible structural defects. These factors can become significant, not only influencing the behaviour and properties of the ferroelectric material, but possibly controlling it [18].

Although polarisation after poling treatments is permanent, it is possible to reverse the poling process resulting in either the partial or even total loss of the ferroelectric piezoelectric properties. Depolarisation can occur in a poled ferroelectric material when exposed to a combination of elevated electric field and high mechanical stress or heated to its Curie temperature as well as with age.

Piezoelectric ultrasonic transducers

Fundamentally, piezoelectric transducers can be grouped into two categories, those which require a broad-band response and those which require a narrow-band response. Typically broad-band transducers are those which have the ability to generate ultrasonic waves over a broad frequency spectrum (high response and sensitivity far from resonance) and are primarily used in low power applications such as medical diagnostics. On the other hand narrow-band transducers, of which Langevin or sandwich transducers are part of and are the type investigated in this thesis, are designed to produce ultrasonic waves most efficiently within a narrow frequency range (close to resonance) and are typically used in high power applications. Typical forms of each transducer, depicted in Figure 1.10, contain the same basic components, piezoelectric element(s), an acoustic backing, which encourages the generated acoustic wave to propagate in the desired direction and an acoustically efficient front or working face used to transmit the acoustic energy. However, they also contain elemental differences with respect to operation and piezoelectric materials used in their construction.

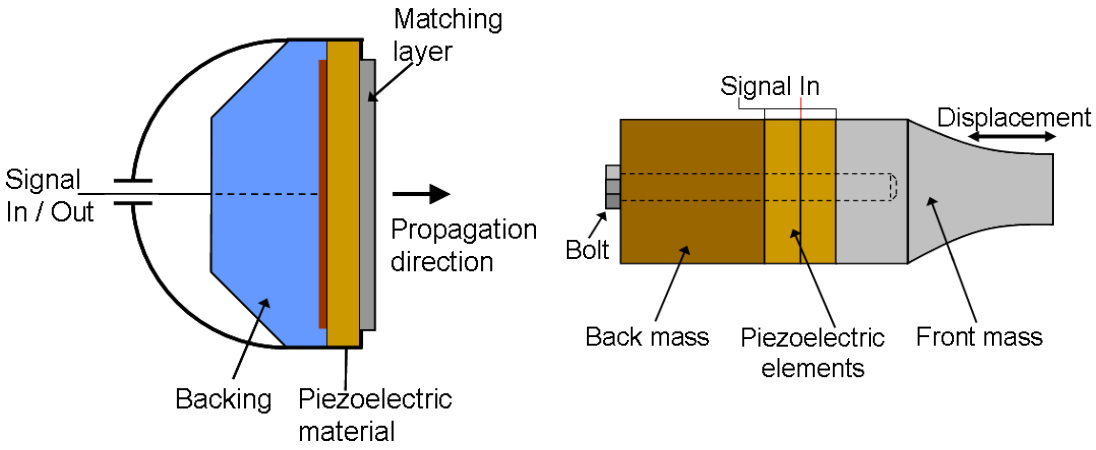

(a) Broad-band transducer

(b) High intensity narrow-band (Langevin) transducer

Figure 1.10: Typical layout of broad and narrow-band transducers [15]

Currently, the piezoelectric material most commonly used in piezoelectric ultrasonic transducers is a variant of lead zirconate titanate (PZT), however, as the operational requirements for low and high intensity transducers considerably differ, the types of PZT utilised in each transducer contain significantly different properties. The piezoceramic property, the electro-mechanical coupling factor, k_{eff}, is the measure of the effectiveness with which electrical energy is transformed into strain (and vice versa) and can be found through Equation 1.8, where f_r and f_a are the resonant and antiresonant frequencies. The piezoelectric charge constant, d, refers to the polarisation per unit of stress or strain, while permittivity, ε, and the mechanical quality factor, Q_m, indicates the level of damping. This can be controlled through the addition of small amounts of dopants. Donor doping, the addition of niobium, Nb, facilitates an increase in domain wall motion which is characterised by enhanced values

for electro-mechanical coupling, piezoelectric constants and lower permittivity values. These piezoceramics are often referred to as 'soft PZTs' and tend to be utilised in applications which require quick response times and high sensitivity, however, due to their low Q_m value heat generation can become problematic when driven at resonance. Acceptor doping, the addition of iron, Fe, manganese, Mn, or chromium, Cr, will generally pin domain walls, resulting in the reduction of domain wall movement. This leads to reductions in the values for piezoelectric and electro-mechanical coupling constants, however, crucially it significantly enhances the mechanical quality factor. These are often referred to as 'hard PZTs' and are preferred in high intensity applications where benefits gained from a value of high Q_m considerably outweigh those gained from higher d and k_{eff} properties found in soft PZTs [26, 27].

$$k_{eff} = \sqrt{\frac{(f_a^2 - f_r^2)}{f_a^2}} \tag{1.8}$$

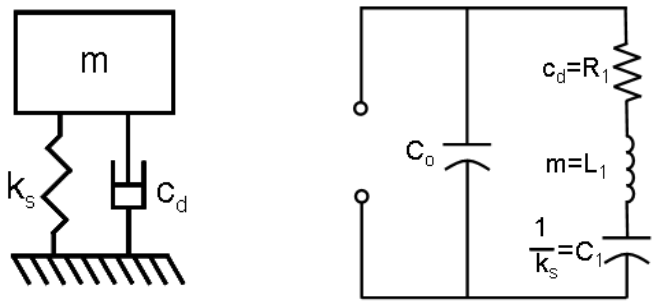

(a) 1-DoF spring-mass system with damping

(b) Equivalent circuit

Figure 1.11: Approximate equivalent circuit unloaded piezoelectric resonator [22]

To investigate the behaviour of piezoelectric transducers, the equivalent circuit approach is often employed. This method 'lumps' together physical properties of the resonator such as mass, m, stiffness, k_s, (modulus of elasticity) and loss factors, c_d, (damping) and represents them as inductance, L_1, resistance, R_1, and capacitance, C_1, while C_o represents the electrodes and cabling of the transducer. Figures 1.11 and 1.12 represent an unloaded piezoelectric resonator's behaviour close to resonance. Away from resonance, piezoelectric materials demonstrate purely capacitive behaviour, as seen in Figure 1.12(b), however, within the frequency range, between the series resonance, f_s, (point of lowest impedance or highest admittance) and parallel resonance, f_p, (point of highest impedance or lowest admittance), the piezoelectric material is inductive. Figure 1.12(d) illustrates a vector admittance diagram of a piezoelectric resonator close to resonance from which the motional admittance circle can be seen. From the diagram, it can be seen that the largest motional (series) admittance occurs at mechanical resonance, f_r, while the minimum motional admittance is located close

to parallel resonance of which both have the same zero phase angle. The maximum and minimum total admittance (frequencies at which maximum and minimum currents flow) occur at f_m and f_n respectively. In a lossless system the assumption can be made that $f_m = f_r = f_s$ and $f_n = f_a = f_p$. Furthermore, (high) power ultrasonic systems can be driven at either mechanical resonant or anti-resonant conditions, both having their advantages and disadvantages. This is further discussed in Section 3.1.2.

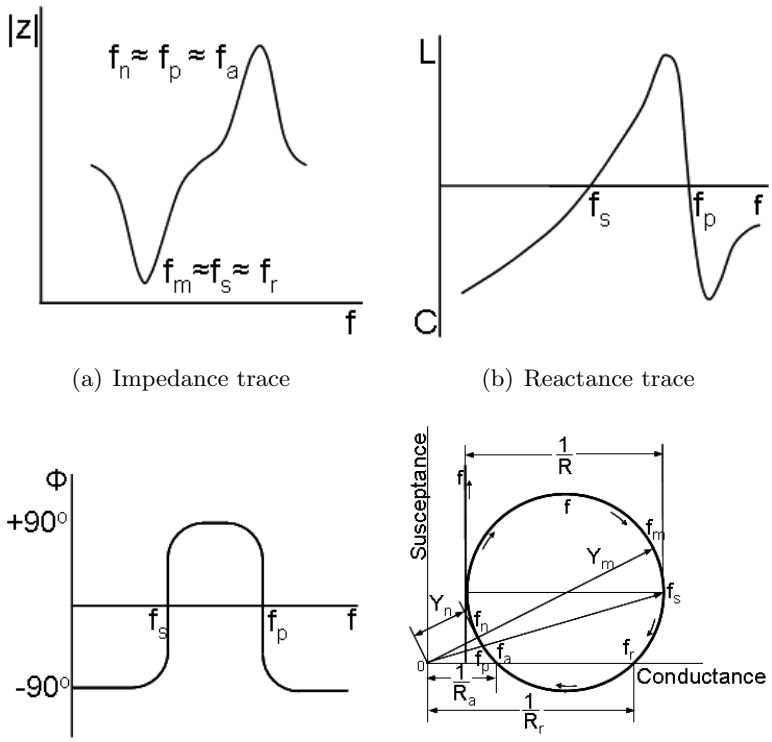

(a) Impedance trace (b) Reactance trace

(c) Phase Angle (d) Vector diagram

Figure 1.12: Approximate relationships of unloaded piezoelectric resonator [22]

1.3 Industrial applications of power ultrasonics

Established applications of high intensity ultrasound in industry, often referred to as macrosonics, are; cleaning, plastic welding, metal welding, chemical processing, plastic/metal forming and machining [2]. The use of the term 'power ultrasonics' will solely describe ultrasonic processes which utilise high intensity acoustic waves.

1.3.1 Established power ultrasonic applications

As previously mentioned, three established applications which utilise high intensity ultrasonics are cleaning, machining and welding.

Cleaning

Ultrasonic cleaning, possibly the first practical and commercially viable power ultrasonic process, dates back to the end of the 1940s and beginning of the 1950s [2, 28]. Devices range from tabletop instruments to commercial scale processes which are used primarily to remove loosely-held contaminants, degrease and descale medical and industry components throughout or after the manufacturing process, or during the assembly of a product. Figure 1.13(a) illustrates a simplified setup of an ultrasonic cleaner; a bath of cleaning fluid where high intensity ultrasound is applied via an ultrasonic transducer-horn assembly. The tuned horn has been optimised by incorporating an output face with a large cross-sectional area which enhances acoustic transmission from the vibrating horn to the liquid. The effects in the cleaning fluid which induce the removal of adhered contaminants are cavitation and acoustic micro-streaming as well as the emulsification of insoluble liquid contaminants.

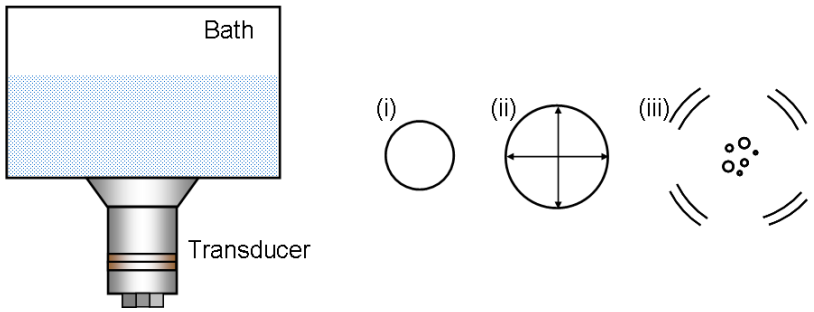

(a) Diagram of table top cleaning bath

(b) Inertial cavitation

Figure 1.13: Ultrasonic cleaning process

Several forms of cavitation exist and are possible to induce during the cleaning process. Inertial cavitation, which was observed by Lord Rayleigh, is depicted in Figure 1.13(b); (i)-(ii) represents the rapid expansion of a microbubble until (iii) where they collapse or implode violently, releasing large amounts of energy. Meanwhile, another form of cavitation, noninertial cavitation, is observed when insufficient energy is present to induce inertial

cavitation, but instead induces bubble oscillation which is of a high enough amplitude that heat and acoustic streaming are generated.

Acoustic micro-streaming is a vortex-like motion which occurs in the presence of microbubbles oscillating due to an external force. Travelling waves influence the oscillating trajectory of the microbubbles, resulting in a motion which causes a non-circulatory shearing flow in the surrounding fluid. The fluid velocity is greatest near the microbubble surface and decreases with respect to distance from the bubble surface, thus creating a velocity gradient in the region of the fluid around the bubble. It is this motion which permits the removal of contaminants from the surface of an object.

Although the general basis is similar for different types ultrasonic cleaning baths, those used in the aerospace industry require significantly higher levels of power from those used in the manufacture of electric circuitry. This is due to the ability of cavitation, especially inertial cavitation, has to erode the surface of metals, plastics and ceramics. Therefore, the level of acoustic power required for adequate cleaning should be carefully selected so that a satisfactory clean is achieved without damaging the object.

Machining

Ultrasonic machining (USM) is a mechanical material removal process first developed during the 1940s and 1950s for cutting materials with low ductility and high hardness levels, such as inorganic glasses, silicon nitride, nickel-titanium alloys and rock [29–32]. The process, now referred to as conventional ultrasonic machining, utilises an ultrasonic tool oscillating against the workpiece while a flow of an abrasive slurry is fed between the two parts. A static load forces the ultrasonic tool against the workpiece forcing the abrasive particles, generally silicon carbide or boron carbide particles suspended in a fluid, to impact against the surface of the workpiece removing material through microchipping.

Variations on the conventional methods such as rotary ultrasonic machining, where the tool rotates at speeds of $\sim$ 300rpm, or USM combined with electric discharge machining have been developed for specialised situations or to improve the general machining performance or efficiency. Generally, USM has the ability to produce complex shapes with a high quality surface finish, although this can be dependent on workpiece material and abrasive slurry used in the process [30].

Welding

Two different forms of ultrasonic welding exist, plastic and metal welding. Plastic welding relies upon a combination of thermal energy, pressure and vibrational amplitude, generally delivered at frequencies up to 90kHz, which melt the plastic at the designated point at which two parts will be joined. The process is often used instead of a mechanical fastener or glue in the manufacture of electrical goods and toys [2, 33, 34]. Figure 1.14(a) illustrates before, (i),

and after, (ii) the application of ultrasonics in the fastening of a metal part to a plastic base.

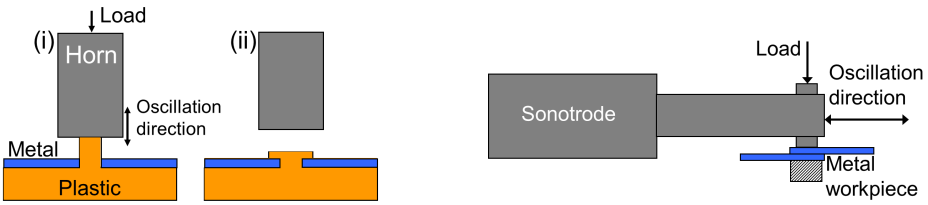

(a) Connection of a metal part to a plastic substrate

(b) Diagram of metal welding process

Figure 1.14: Ultrasonic welding processes [2, 33]

Metal welding, on the other hand, is used to bond metal plates or sheets together as in the fabrication of heat exchangers or to join contacts in electrical circuit boards. Two physical processes are utilised, macroslip and microslip. Both rely upon the ultrasonic energy being delivered tangentially while under high longitudinal force. If relatively large motions are supplied by the ultrasonic horn then macroslip (sliding) will occur which in turn produces enough frictional heat, melting a thin layer of the joining materials and bonding them together. On the other hand, if relatively small amplitudes of vibration are applied microslip will occur. This causes fretting and rapid heating, however the energy supplied is generally not enough to melt the material. Instead, the heating induces rapid diffusion between the joining materials bonding them together [2, 34, 35].

1.3.2 Modern power ultrasonic systems

Although ultrasonic processes discussed in the previous section have matured, they are still commercially viable and have continued to evolve and improve with modern technology by incorporating advancements in material science, transduction methods and electronics. Furthermore, greater understanding in component design and ultrasonics in general has enabled the efficiency of power ultrasonic devices to improve as well as being used in a variety of new applications. A few new applications and technologies which have been developed throughout the last 20 years are discussed.

Ultrasonic food cutting

Ultrasonic food cutting is currently used in commercial scale food production to reduce the size of bulk volumes of food, which have been prepared through processes such as baking or cooking, so they are suitable for distribution, handling or eating. Properties of food, such as texture and structure, can differ considerably from one product to another, for example, baked to frozen to fresh goods. These goods are also often difficult to cut by conventional methods (rotating saw or static guillotine) due to brittleness, likely to crumble or collapse because they contain differing layers of different consistences. Furthermore, if these foods

can be cut with conventional tools, damage can occur after the cut due to smearing or the product adhering to the cutting blade, which has the potential of increasing the likelihood of cutting jams and halting production [36, 37].

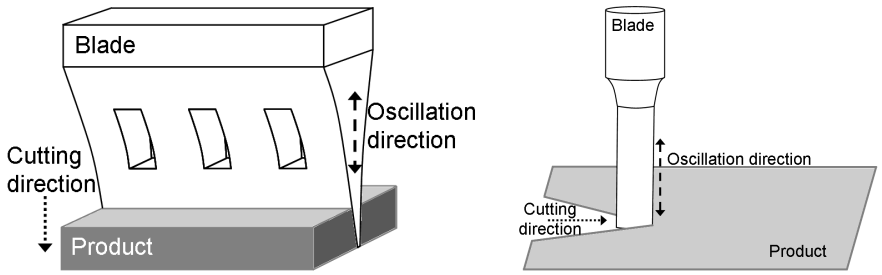

(a) Guillotine blade (b) Dagger blade

Figure 1.15: Ultrasonic horns used in food cutting

Two ultrasonic 'blade' types found commercially are illustrated in Figure 1.15. The guillotine blade is used to cut a product vertically into parts and is often used to cut products such as bakery goods in to sections, while the dagger or similar sabre blade can be used on the production line to slice wide products into multiple thinner sections. These cutting methods are not limited to food preparation and production, but are also used successfully to cut materials such as fabrics or other materials in the aerospace, automotive and packaging industries [36].

Complex vibration loci / modal coupling

Ultrasonic devices traditionally utilise a single mode of vibration, commonly the longitudinal mode. However, in processes such as ultrasonic welding and cutting, coupling multiple modes of vibration, for example combining longitudinal-bending or longitudinal-torsional modes of vibration, has shown to be advantageous in improving the performance of existing processes as well as instigating the development of new technologies [34].

Various transducer and horn designs have been developed to induce a combination of different modes. Figure 1.16(a) illustrates a Langevin transducer with two separate sets of piezoceramic elements designed to couple a longitudinal mode with a bending mode. The piezoceramic elements in Set I are complete rings and are poled in opposite directions, as in conventional transducers, and induce a longitudinal motion when an alternating current is applied to them. Set II on the other hand are constructed from two pairs of piezoceramic elements; the first pair are poled in the same direction as Set I while the second pair are poled in the opposite direction, hence, when an alternating current is applied to the piezoceramics of Set II, the elements in the first pair compress and expand 180^{o} out of phase from the second pair, inducing a flexural motion in the device [38].

Ultrasonic horns have also been developed to convert purely longitudinal oscillations to a complex mode containing multiple modes of vibration. Figure 1.17 presents two techniques

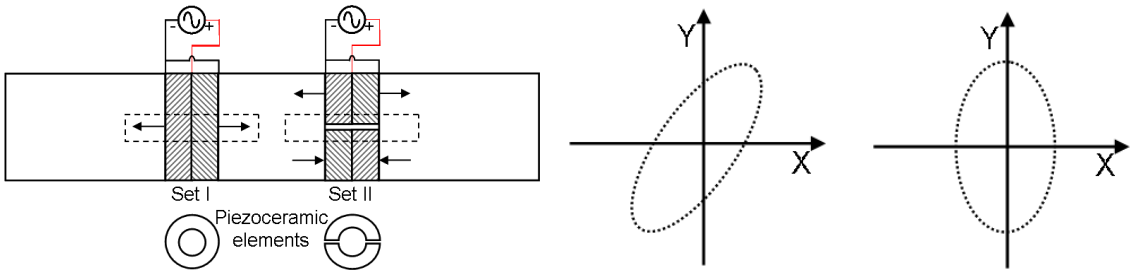

(a) Transducer architecture (b) Example of complex vibration loci at output face

Figure 1.16: Transducer designed to operate in a longitudinal-flexural complex mode [38]

for converting a purely longitudinal source to a combined longitudinal-torsional mode of vibration. The horn depicted in Figure 1.17(a) contains diagonal slots which are partially cut into the circumference of the cylinder and located near the location of highest vibrational displacement or antinode. The incident wave, marked with a solid line, is partially converted to a torsional wave when it is reflected at the free edge of the slots where it continues to the final non-slotted part with combined components of both longitudinal and torsional motions. If the system oscillates at its tuned mode of vibration, the output face of the vibrating part will oscillate with an elliptical or circular motion [34, 39]. Figure 1.17(b), on the other hand, uses a spiral grove cut in the horn (similar in shape to a conventional drill bit) to degenerate the longitudinal motion into a combination of both longitudinal and torsional motion [40].

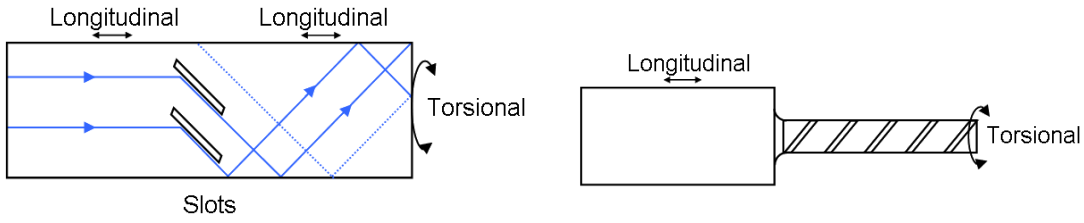

(a) Slotted horn (b) Degenerative horn

Figure 1.17: Horns designed to operate in a longitudinal-torsional complex mode [34, 39, 40]

Ultrasonic motors

Modern ultrasonic motors come in various sizes and are used in numerous applications and although they are not all utilised in high intensity ultrasound, their architecture is fundamentally similar to ultrasonic transducers, Figure 1.18. They consist of a power supply, stator (containing piezoelectric elements and a vibrator or horn to transmit the vibrational amplitude) and a slider or rotor which provides mechanical output. Generally, there are two types of ultrasonic motors; rotary and linear, although, these can be further classified by shape of the stator; rod (depicted in Figure 1.18), π-shaped, ring and cylinder. Meanwhile, the vibrational output of ultrasonic motors can either come in the form of standing or travelling

waves [41, 42].

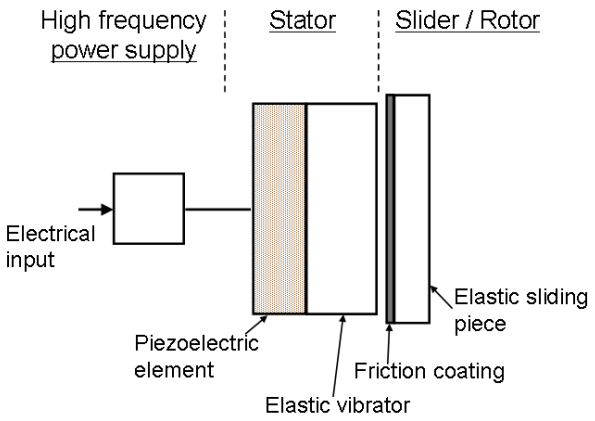

Figure 1.18: Simplified structure of an ultrasonic motor [41, 42]

Ultrasonic motors range in size from sub millimeter to a few millimeters where they are used in autofocus systems in cameras [41]. The fundamental phenomenon that allows 'frictionless movement' in these devices is known as near-field acoustic levitation (NFAL). The phenomenon relies upon acoustic radiation generating a gas squeezed film, ranging from tens to hundreds of microns, separating the vibrating surface from the planar object [43–45].

Acoustic levitation

Using similar principles as ultrasonic motors, conventional acoustic levitation can be used to levitate particles or light objects at the nodal point of a standing wave propagated in to a fluid. An evolution of this technology has led to a system which utilises NFAL to transport planar objects from one end of a vibrating plate to the other. To suspend and transport the object, flexural travelling waves are induced in a thin rectangular plate by fastening two longitudinal Langevin transducers at right angles to each end of the plate, Figure 1.19. The first transducer generates an acoustic wave at the tuned frequency of the flexural mode, vibrating it at an amplitude of 20μm, while the second transducer acts as a receiver and absorbs it. To maximise the efficiency of the absorbtion of the acoustic wave, the second transducer is connected to a load consisting of a resistance and inductance [44, 46, 47].

Although the driving setup of the flexural travelling wave in the system, depicted in Figure 1.19, is the same as in ultrasonic linear motors, two fundamental differences exist [46]:

1. The levitated planar object does not contact the vibrating plate during operation, while the slider or rotor of the ultrasonic motor does make contact with the vibrating surface.

2. The levitated object is transported from the emitting transducer towards the absorbing transducer, rather than the slider or rotor moving towards the ultrasound source as in ultrasonic motors operating in a flexural mode.

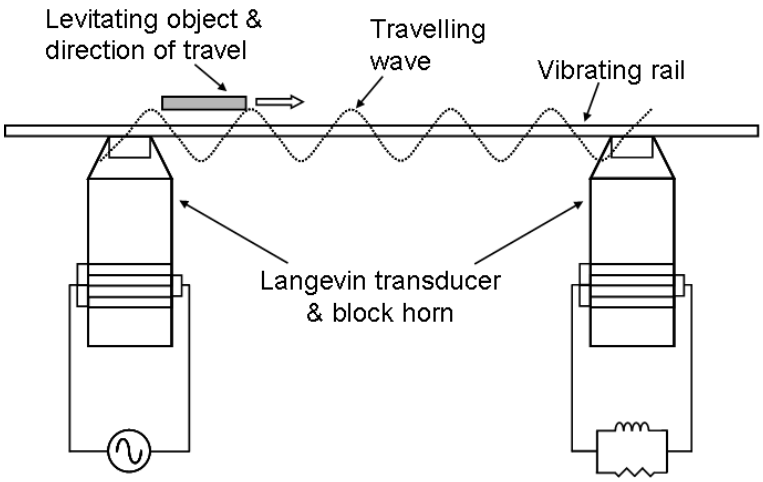

Figure 1.19: Experimental levitation and transportation setup [44, 46, 47]

Initial experimental apparatus demonstrated that a planar object of 10kg could be successfully transported along the vibrating plate. To enhance the potential transportation distance, multiple systems can be joined in series, extending the transportation distance or, to transport broader objects, multiple systems can be arranged in parallel. Despite the novelty of the technology, potential industrial applications range from the transportation of delicate planar objects, such as thin glass or silicon sheets or as use as non-contact linear bearings, [43, 44, 46, 47].

1.4 Ultrasonics in medical applications

Ultrasonics is currently used in a wide variety of medical procedures and applications. Diagnostic ultrasound, sometimes called medical sonography or ultrasonography, is an imaging technique most often associated with obstetrics, but it is also used to visualise internal organs as well as muscles and tendons. Although diagnostic ultrasound has no permanent effect on biological tissue, due to the low intensities of the ultrasound employed, applications which use power ultrasonics, on the other hand, do have a destructive capability on biological tissue.

Clinical procedures which utilise medium and high power ultrasonics range from the treatment of cancer and kidney stones to cosmetic procedures and surgical procedures such as cataract removal, thrombolysis (destruction of blood clots), hard and soft tissue dissection and dental hygiene procedures.

1.4.1 High intensity focused ultrasound

High intensity focused ultrasound, commonly referred to as HIFU, is a form of therapeutic ultrasound which uses high intensity ultrasound to rapidly heat and destroy tissue located at the focus of the acoustic beam. The primary mechanism for destroying the tissue is

coagulative necrosis (cell death by the restriction of blood or oxygen) by thermal absorption. The high intensity ultrasound can be generated and focused either by a single piezoelectric element shaped into a concave bowl or by an array of piezoelectric elements arranged into a concave shape. These transducers can produce acoustic energy in the frequency range of 0.5 to 10MHz, although most procedures are performed at around 1.5MHz with power levels of 10^3-10^4Wcm^{-2} and a focal point of a few cubic millimeters. The duration of each application of high intensity ultrasound can last between 1-30 seconds, however, considerations will ensure that sufficient absorption time is given to treat the designated area without damaging the tissue between the transducer and focal point. HIFU treatments are often used in conjunction with medical imaging techniques such as diagnostic ultrasound, CT (X-ray computed tomography) or MRI (Magnetic resonance imaging). This is often necessary to guide the HIFU treatment as tissue inhomogeneities can often distort the intended focal point [48–50].

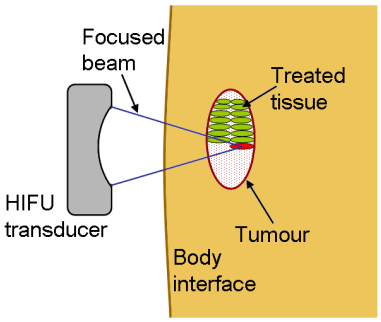

Figure 1.20: Depiction of HIFU treatment on a tumour [48]

The earliest use of HIFU was in the treatment of prostate cancer, however the process is now used in the treatment of tumours in the liver, brain and other soft organs as well as treating uterine fibroids (benign tumours which grow out from the myometrium, the smooth muscle layer, and accompanying connective tissue of the uterus), while HIFU has also been developed to stop internal bleeding in civilian trauma victims or military casualties by repairing ruptured blood vessels. Figure 1.20 illustrates how a tumour may be treated through repetitively applying the focal point to the tumour until the entire tumour has been treated. Due to the non-invasiveness of HIFU, treatments can be repeated even after the first HIFU treatment failed or was a partial success [48–50].

1.4.2 Cataract removal

A cataract is an optical opacity of the lens of the eye which can be caused by various factors such as trauma, long term exposure to ultraviolet light or old age and is generally formed due to the denaturation (loss of solubility) of the proteins contained within the lens [51]. Traditional surgical treatments of cataracts date back as far as the 1st century AD and rely upon cutting at least a 180^o incision into the cornea of the eye giving the surgeon

access to remove or displace the cataract. Unfortunately this technique, which is solely reliant on the skill of the surgeon, can often lead to complications and long recovery times. Phacoemulsification is a technique where an ultrasonic device delivers ultrasonic energy to the cataract, fragmenting and emulsifying it before it is removed via suction. A prosthetic (intraocular) lens is then placed into the empty lens capsule. An incision of 1.5 to 3mm is required to access the cataract and insert the intraocular lens. This technique is far less invasive than traditional methods, and reduces recovery time as the incision is able to selfheal [51–53].

Different ultrasonic devices have been designed to emulsify the cataract through the application of longitudinal vibrations, torsional vibrations or a combination of both [54–56]. Phacoemulsification devices generally operate at frequencies around 40kHz, although may modulate between the fundamental driven frequency and other frequencies with either lower or higher frequencies (maybe as high as 120kHz) [57].

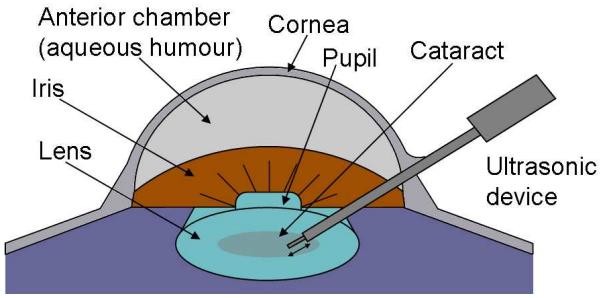

Figure 1.21: Schematic diagram of phacoemulsification

1.4.3 Soft tissue dissection

Power ultrasonic devices, such as the Harmonic Scalpel developed by Ethical, a subsidiary of Johnson and Johnson Inc, have been developed for various soft tissue dissection procedures and show some advantages, such as higher precision, over traditional dissection techniques as well as other modern devices such as laser surgery and electrosurgery (soft tissue dissection through the application of a high frequency electric current). Major disadvantages of laser surgery are the inherent danger of injury due to exposure to high intensity laser light, either through accidental activation or misguidance as well as its high cost. Meanwhile, electrosurgery possesses the danger of electrocuting either the patient (through incorrect grounding) or the surgeon. Although this disadvantage is limited to monopolar electrosurgery (where the current passes through the body to an electrode), it does not apply to bipolar electrosurgery as the current is not required to pass through the body, however this surgical technique also contains other disadvantages such as limited power and cutting ability as well as tending to damage tissue located laterally to the intended surgical site. However, the advantages of these modern techniques is that they prevent bleeding during surgery, which

improves the surgeon's vision of the operating site as well as reducing blood loss in the patient [58].

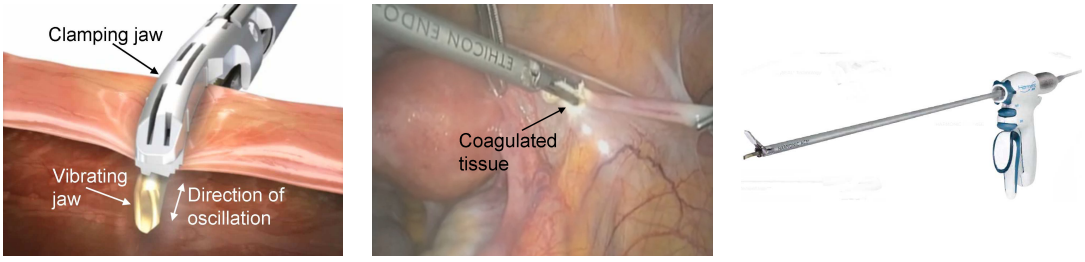

(a) Cutting mechanism (b) Coagulation of tissue (c) Ethicon Harmonic ACE® 45E

Figure 1.22: Soft tissue dissection [59, 60]

The Harmonic Scalpel vibrates longitudinally at a frequency in the region of 55.5kHz, and operates by transmitting the ultrasonic energy down a tuned rod to the cutting blade. The cutting blade oscillates longitudinally and makes up the bottom half of a set of jaws. The top jaw, which does not oscillate, is able to open and close and provides a clamping force to hold soft tissue in place during dissection. Frictional heating between the oscillating blade and dissecting tissue as well as acoustic streaming and pressure waves cause cell breakdown, transforming their shape in to a sticky coagulum that seals the blood vessels [59–61]. The surgeon, however, is required to utilise the device with care, as tissue will generally coagulate between 60°C and 80°C causing no permanent damage in the tissue, but with a tissue temperature rise above 100°C necrosis can occur [62].

1.4.4 Oral prophylaxis

Oral prophylaxis, commonly known as dental scaling, is an oral cleaning procedure carried out to remove plaque and calculus. It is also one of the earliest widespread application of power ultrasonics in healthcare, dating back to the 1950s. Plaque is a biofilm formed from microorganisms, cells that stick to one another, which form naturally within the mouth. These are harmless until they adhere to a tooth and, if not removed through good oral hygiene, start to produce acids that demineralise the tooth surface leading to cavities. If left untreated a buildup of plaque can also cause irritation of the gum around the tooth and in extreme cases may lead to gingivitis (inflammation of gum tissue), periodontal disease and tooth loss [63]. After a period of time, plaque mineralises to a hard substance known as calculus.

Traditionally, calculus was removed using non vibrating manual dental instruments, however, dental studies from the 1950s through to the 1990s showed that the utilisation of mechanical oscillations reduces the time the dentist requires to clean without causing considerable discomfort for the patient [64–68]. At present, there are two commercially available classes of vibrating scaling devices, sonic and ultrasonic scalers. Both types of

device operate through the exploitation of micrometric dynamic deformation of the working tip. Sonic scalers typically rely on motion induced by a small turbine which is incorporated within the hand-piece and is driven by pressurised air to deform the working tip at frequencies which can vary between 2.5 and 16 kHz. Meanwhile ultrasonic scalers operate at frequencies generally between 20 and 50 kHz and are currently driven through either the magnetostrictive or inverse piezoelectric effects [68, 69].

(a) Tooth anatomy (b) Ultrasonic scaling tip (c) Mectron Piezo Smart ultrasonic scaling device

Figure 1.23: Ultrasonic scaling[1]

High tip velocities of the scaling device generate temperature increases of the oscillating tip and the area under treatment. To regulate the temperature, a cooling solution is directed through the instrument and expelled, cooling both the tip and treatment area. The coolant also enhances the cleaning process by removing dislodged debris, while the presence of cavitation and micro-streaming, induced by the high tip velocity, may also improve the cleaning process by aiding in the removal of calculus and other contaminants [68, 71].

1.4.5 Ultrasonic osteotomy

Ultrasonic devices used in osteotomy (the dissection of bone tissue), as with those used in ultrasonic prophylaxis devices, exploit micrometric dynamic deformation of the cutting tip to cut the tissue. Transducers are generally tuned to generate longitudinal vibration in conjunction with a variety of different cutting inserts. Cutting inserts can be shaped to oscillate either longitudinally or in a combined longitudinal-flexural motion and can also be designed to access different surgical sites and produce different shapes of cut or surface finish.

Figure 1.24 illustrates the exaggerated motion, found through finite element analysis, of the tuned mode of vibration of an osteotomy insert connected to the Piezosurgery® Device. Developed by Mectron S.p.A [70], the Piezosurgery® Device operates in a frequency range of 24 to 36kHz and has been adopted in a variety of surgical procedures ranging from oral surgeries to maxillofacial operations such as orthognathic surgeries (correction of problems relating to the jaw and face, such as jaw re-alignment or the treatment of a cleft palate). The device has also been utilised in implantology (reconstruction of missing teeth and their

[1]Figures 1.23(b) and 1.23(c) courtesy of Mectron S.p.A [70]

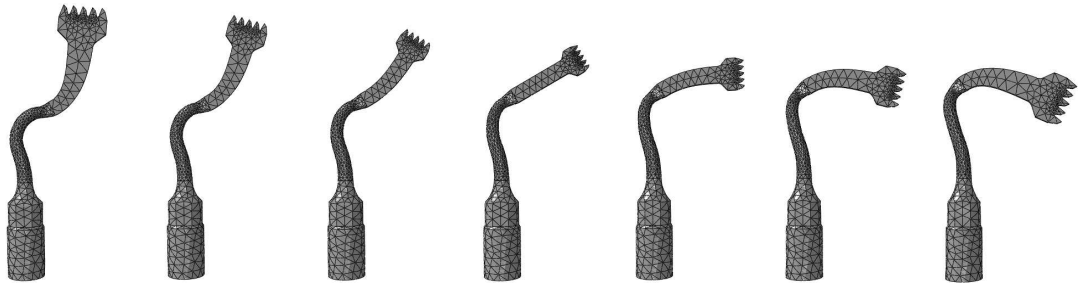

Figure 1.24: FEA simulation of deformation of half a cycle of oscillation of an ultrasonic cutting insert (OT7 Piezosurgery® Device Insert)

supporting structure), craniofacial surgery (craniofaciostenosis: the removal of the outside wall of the orbit or eye socket to access tumours) and osteotomy in the hand, foot and spine [72–74].

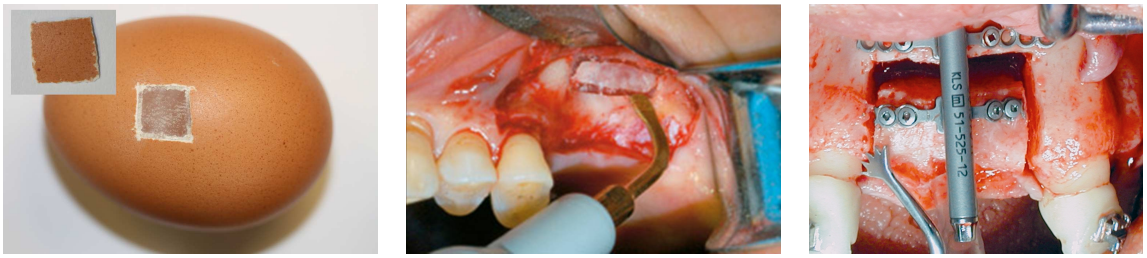

(a) Window cut in raw egg (b) Preparation of bone window (c) Osteotomy of bone section

Figure 1.25: Cutting with Piezosurgery® Device[2]

Ultrasonic devices used in osteotomy have shown to hold advantages such as high precision, less damage to both soft and hard tissues and quicker recovery times than traditional instruments such as bone burs and bone saws. Rather than macrometric rotations and oscillations as bone burs and saws use to dissect hard tissue, ultrasonic devices achieve higher precision by generating micrometric deformations which also reduces the load required to hold them in position [72,75]. However, unlike bone saws and burs which can easily damage soft tissue, the vibrations of the ultrasonic device, such as the Piezosurgery® Device, appear not to damage soft tissue. Even in an extreme scenario where the vibrating tip was held against nerve tissue, with a force larger than required to correctly use it, the micrometric vibrations failed to dissect the nerve tissue. Therefore, it can be suggested that ultrasonic devices provide higher levels of safety than bone burs and saws during osteotomy when they are located in close proximity to delicate tissue such as nerve, brain and spinal cord, which if damaged could have severe consequences for the patient [72, 75–78]. Figure 1.25(a) illustrates the precision and low loading requirements of an ultrasonic cutting device (used by an untrained operator) during cutting a window in a raw egg without piercing its internal membrane. Meanwhile Figure 1.25(b) shows part of the sinus lift procedure which is used to

[2]Figures 1.25(b) and 1.25(c) courtesy of Mectron S.p.A [70]

increase bone volume in the maxillary (upper jawbone) and is necessary to aid the successful placement of dental implants. The procedure dissects close to the Schneiderian membrane, which if ruptured can lead to heavy bleeding and postponed surgery [79]. An example of multipiece maxillary osteotomies, in which the upper jawbone is shortened or lengthened is shown in Figure 1.25(c).

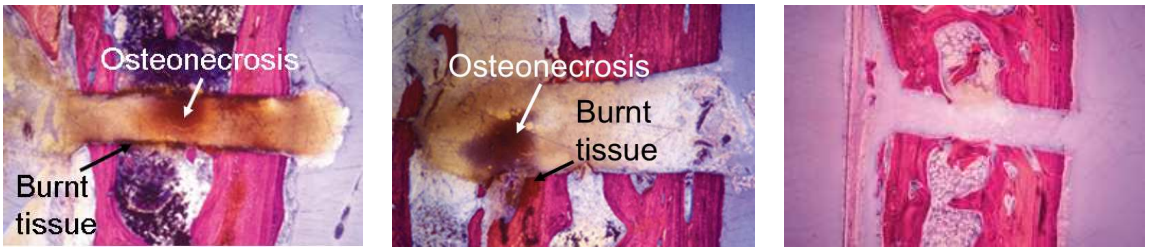

(a) Bone saw (b) Bone bur (c) Ultrasonic device (Piezosurgery® Device)

Figure 1.26: Representative histologic photomicrographs of decalcified specimens characterising the appearance of the cut edges of osteotomy incisions baseline (original magnification 2.5x, stain hematoxylineosin)[3]

A comparison of dissections made with a power ultrasonic device and traditional cutting methods is shown in Figure 1.26. It can be observed that both the ultrasonic device and bone bur produce relatively parallel edges in the cut, while the bone saw does not. This suggests that a higher cutting precision is achievable with these two devices. The absence of discolouration in the histologic photomicrograph associated with the dissection performed using the ultrasonic device conveys that osteonecrosis, the death of bone cells, has not occurred. On the other hand, prominent discolouration can be seen in the histologic photomicrographs belonging to tissue dissected by the traditional cutting techniques and depict a clear sign of osteonecrosis. Furthermore, from Figure 1.26(c) it can be observed that the edge of the dissection is untarnished as it is either white, red or pink in colour. However the dissections seen in Figures 1.26(a) and 1.26(b) clearly show that the edges of dissection are darker, indicating the presence of burnt tissue. As a result, the network of channels that have the primary function of bone vascularisation (Haversian channels) have been obstructed, and as bone healing is strictly related to the vascularisation rate, this will impact on bone regrowth and recovery time [79, 80].

[3]Figure 1.26 courtesy of Mectron S.p.A [70]

1.5 Nonlinear behaviour in dynamic systems

Linear systems, such as the system described in Figure 1.11, represent mathematical approximations of a dynamic system. Although useful, as they allow problems to be approximated with relative ease, they do not represent the actual behaviour of a real system. As linear mathematical approximations can never truly represent a real system, all systems must be described as being inherently nonlinear. The change of state of a linear system will always be proportionate to the level of energy or load applied to the system, while nonlinear systems will not always experience a proportionate change in their state, even if initially the system appears to change proportionately, as eventually a point will be reached at which the rate of change will cease being proportionate and will become disproportionate [81].

Even though every system in existence is ultimately nonlinear, linear systems often give a sufficient approximation of a system's behaviour. However there are systems which contain nonlinearities which cannot be ignored. Finding the source of nonlinear behaviour in a system through mathematical models can be difficult as the nonlinearity can stem from different origins which can be difficult to isolate as a term in mathematical models [81];

Geometrical nonlinearities generally arise from large deflections or rotations or other kinematic characteristics.

Material nonlinearities stem from the nonlinear relationship between stress and strain (force and deformation).

Physical configuration nonlinearities can be induced from the presence of another component or influence, which could be operating linearly. For example plays, stops or discontinuous couplings.

1.5.1 Duffing system

The equation of motion for a linear oscillating dynamic system can be written as Equation 1.9, where ω_o is the undamped linear natural frequency, β is the damping ratio and $\ddot{u}$, $\dot{u}$ and u are the generalised acceleration, velocity and displacement terms, respectively. However, by adding a nonlinear stiffness (cubic) term, γu^3, to the linear Equation 1.9, gives Equation 1.10 and represents a form of Duffing Equation [81, 82].

$$\ddot{u} + 2\beta\omega_o\dot{u} + \omega_o^2 u = q\cos(\Omega t) \tag{1.9}$$

$$\ddot{u} + 2\beta\omega_o\dot{u} + \omega_o^2 u + \gamma u^3 = q\cos(\Omega t) \tag{1.10}$$

Figure 1.27 depicts the influence that γ has on the cubic nonlinearity term of Equation 1.10. If γ is negative, the natural frequency of the system lowers and the frequency response

curve bends to the left. This is known as the softening effect, while the hardening effect occurs if γ is positive and the natural frequency increases and the frequency response curve bends to the right. The greater the value of γ, either negative or positive, the greater the softening or hardening effect.

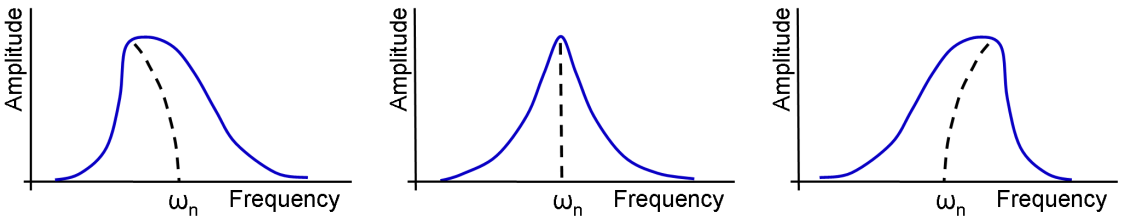

(a) Softening: $-\gamma$ (b) Linear: $\gamma = 0$ (c) Hardening: $+\gamma$

Figure 1.27: Frequency response curves for varying γ values

Dynamic systems that demonstrate Duffing-like responses often display further nonlinear behaviours such as jump phenomena and hysteresis regions. Figure 1.28(a) depicts a dynamic system exhibiting a softening response, jump phenomenon and a hysteresis region. The location of the upward jump is between points *II* and *III* while the downward jump is located between points *V* and *VI* creating a hysteresis region and bifurcation, a point at which there may be a number of solutions rather than an unique one. A system oscillating between the frequencies of the upward and downward jumps will show unstable characteristics as the amplitude of vibration alternates between high and low amplitudes of vibration. If the system is unstable enough, it can provide a route to chaotic behaviour. However, if the system is excited away from the hysteretic region, for example at points *I* and *IV*, the system will remain stable [81, 82].

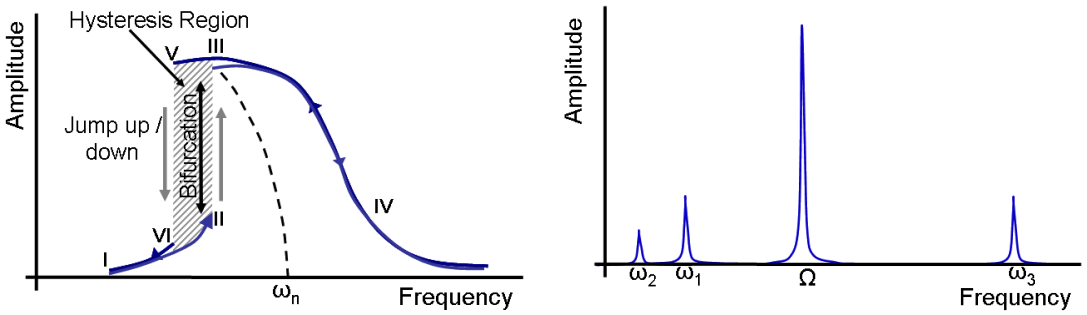

(a) Softening response with amplitude jump phenomenon and bifurcation

(b) Multiple modal responses

Figure 1.28: Depiction of nonlinear responses of dynamic systems

Another form of nonlinear behaviour, illustrated in Figure 1.28(b), and seen in dynamic systems, are modal interactions. These occur when two or more natural frequencies of a system are *commensurate* or *near commensurate*. This means that natural frequencies (ω_1, ω_2 and ω_3) are related to the excitation frequency (Ω) through simple combinations of integers

or near integers such as;

$$\Omega \approx 2\omega_1, \quad \Omega \approx 4\omega_2, \quad \Omega \approx \omega_1 + 2\omega_2, \quad \Omega \approx \frac{1}{2}\omega_3$$

and could be simultaneously excited. Systems which are excited away from resonance, but through a simple relation (or internal coupling) a mode of vibration is excited, are said to be parametric.

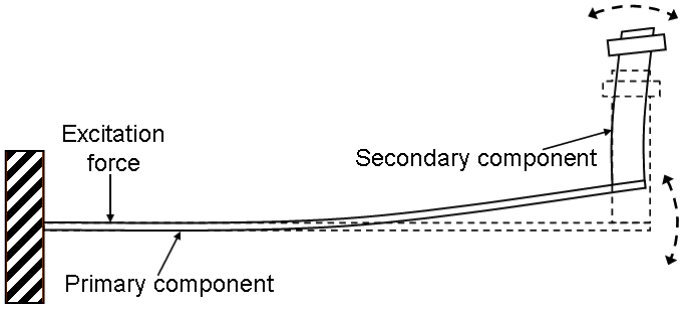

Figure 1.29: Beam containing a primary and secondary coupled structures under autoparametric behaviour [82]

Meanwhile, if a system or a structure contains two components (a primary and a secondary), such as in Figure 1.29, where the primary part is excited at a resonant frequency, Ω, it is possible for the secondary component to be parametrically excited at resonance at a different frequency, ω. If the relationship between Ω and ω is similar to those discussed above, it is said that the response of the secondary component is known as the principal parametric resonance and the structure is said to be autoparametric. In general this is characterised by a system that contains internal coupling between two or more modes of vibration as well as a coupling between the response characteristics of these modes of vibration [81, 82].

1.5.2 Routes to Chaos

Chaotic vibrations can be viewed as any other vibrational phenomenon such as resonance, harmonics or amplitude jumps. Simply described, chaotic systems demonstrate behaviour which can not be predicted to a necessary level of accuracy within a desired timescale. Although linear systems can not behave chaotically, most 'real' world systems do demonstrate a level of chaotic behaviour due to the fact that it is impossible to accurately predict their behaviour in the distant future. However, in reality it is possible to have *weakly chaotic* systems, those which it is possible to predict their behaviour with the necessary accuracy within the desired time frame, even though it is impossible to predict their behaviour in the distant future. On the other hand, *strongly chaotic* systems are those which it is not possible to predict their behaviour with any reasonable accuracy within the timescale of interest [81].

There are serval methods available for the detection of chaotic behaviour in vibrating systems; phase planes, Poincaré maps and Lyapunov exponents, however the most relevant

method for the ultrasonic devices characterised in this thesis is investigating the frequency (Fourier) spectrum of the response. The spectrum of a oscillating system is also useful for distinguishing periodic from non-periodic motion (which is always displayed as a discrete frequency spectrum) and quasi-periodic (which can be displayed as two or more incommensurate frequencies which could also contain sub and higher order harmonics and linear combinations of these) from chaotic motion (which contains a frequency response displaying a continuous broad-band spectrum with larger responses at the fundamental or dominating frequencies) [81].

Chaotic behaviour is usually only observed in a system when the system lies within particular parameter ranges. For a system to transit from regular to chaotic behaviour, the system undergoes a sequence of bifurcations, a qualitative change in a system's behaviour that occurs when the parameters of the system are varied [81], known as a *route to chaos*. There are several routes to chaotic behaviour, but some have been observed more often than others, while some routes appear to cross disciplines, demonstrating universal qualities. Routes to chaos include quasi-periodic, the transient route, the intermittency route and the period-doubling route.

The period doubling route to chaotic behaviour, Figure 1.30, is characterised by cascades of bifurcations that results in a doubling of the period of motion. In a vibrating system the motion will become chaotic once the critical parameter threshold for that system has been passed. Figure 1.30(a) illustrates a bifurcation diagram where a function, x, and the system parameter μ, is the bifurcation parameter. Initially (for values $< \mu_1$) the solution 'settles down' towards a *fixed point* which is stable, and can be known as the 'period-1' motion, however at μ_1 the fixed point splits (becomes unstable), producing two different values. This is known as period doubling. For values greater than μ_1, but less than μ_2 the solution becomes a stable period-2 motion. The solution remains stable until μ_2 at which the solution becomes unstable in preference for a stable period-4 motion after period doubling. The system will proceed the process of period doubling with smaller increments of μ until the critical value has been reached and chaotic motion will occur beyond that value.

Figure 1.30(b) depicts a general response for a system exhibiting a route to chaos. The manifestation of a subharmonic period-2 motion as discrete 'spikes' or responses on a Fourier spectrum at the driving frequency, Ω, subharmonic, $\omega = 0.5\Omega$ and the harmonics, $\omega_k = k0.5\Omega$, where k is the harmonic number. A DC response at 0Hz illustrates that the system is displaced from zero and it oscillates around a buckled position. Meanwhile, if chaotic motion has been reached, a broad-band (noisy) response will be exhibited on the Fourier spectrum, with dominating frequencies, such as Ω raising above the noise level. When detecting chaotic motion through experimental techniques, the natural noise level should be considered and must not be mistaken for a chaotic response.

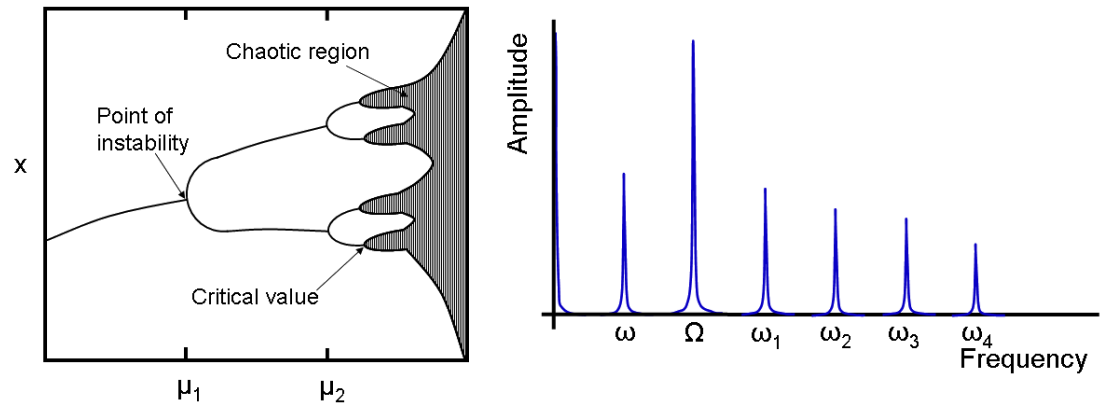

(a) Bifurcation diagram (b) Spectrum response containing period doubling

Figure 1.30: Depiction of period doubling route to chaos [81]

1.6 Summary of work

As alluded to in previous sections, the use of power ultrasonic devices developed for surgical procedures is growing. The increasing numbers of surgeons adopting ultrasonic devices in their surgical tool box has in turn increased the demand for devices which are able to be used increasingly in new procedures with more difficult to access surgical sites. Therefore, to develop novel devices with which the surgeon is able to enhance their clinical methods, both the designer and surgeon are required to work together, ensuring that each new device is optimised for the procedure it is required for.

It is also well known that ultrasonic devices are inherently nonlinear. Some sources of nonlinear behaviour are known, and can be successfully controlled. However, with the requirement of newer even more complex device designs, it is increasingly important to understand that if nonlinear behaviour becomes detrimental to its performance, through reduced efficiency or failure, how this can be designed out of the device and controlled.

The work presented in this document uses finite element analysis to investigate resonant frequencies and modes of vibration of current and prototype surgical devices while experimental methods are used to validate these models. The accuracy between resonant frequencies predicted through finite element models and those experimentally measured are investigated, and reasons of varying levels of accuracy between finite element and experimental methods are discussed.

Experimental methods to characterise ultrasonic devices at high amplitudes of vibration are discussed. One method was used to investigate the influence that joint tightness, heating of piezoceramic elements, geometry and material selection of tuned inserts has on the behaviour of ultrasonic devices. Finally, an investigation studies the influence that the location of the piezoceramic stack has on the behaviour of Langevin transducers is discussed.

Chapter 2

Review of Literature

2.1 Historical background

The study of acoustics, of which ultrasonics or ultrasound is a branch, finds its roots in ancient Greek and Roman times. Pythagoras (6^{th} century BC), according to legend, is thought to have investigated why some sounds when put together are pleasant to the ear, while others are not. Although various methods have been suggested in literature of how Pythagoras investigated this problem (most common suggestions involve vibrating strings of different lengths), ultimately, he has been accredited as a pioneering character in the understanding and development of the seven-tone diatonic scale used in modern music. Meanwhile, a few hundred years later, Aristotle (384-322BC) correctly hypothesized that acoustic waves travel through air by the motion of molecules colliding with one another, however, it was not until Galileo (1564-1642) furthering the work of Pythagoras that modern acoustics was born [83].

By the second half of the 17^{th} century (1681) the relationship between frequency and pitch had been established through an instrument developed by Hooke (also known for the law of elasticity). Although this instrument was possibly the forerunner for one of the first ultrasonic generators, the concept that frequencies of sound exist above that of human hearing was still unheralded. The first recorded 'near miss', suggesting the possibility of the existence of sounds within the ultrasonic range, was unwittingly proposed by Spallanzani when attempting to explain the method by which bats hunt and navigate when flying in the dark. This work led him to hypothesize in 1794 that bats had an unknown 'sixth' sense, however, after correspondence with the Swiss zoologist Jurine, his opinion altered and by 1798 the men correctly concluded that bats used their ears in direction finding. This conclusion was dismissed by the wider science community, resulting that bat echolocation lay undiscovered throughout the whole of the 19^{th} century and the first third of the 20^{th} century. It was not until 1938 that Pierce and Griffin finally established that some bats emit sound in the ultrasonic frequency range but it was not until the 1940s that it was established that bats used echolocation for navigation and hunting [28, 84, 85].

The first reasonably accurate measurement of the speed of sound in air (within 1% of today's standards) was made at the Paris Academy in 1738. However, it took until the 19th century to first accurately measure the speed of sound in a solid, when Biot measured the speed of sound in an iron rod in 1808. Furthermore, it was not until 1826 that Colladon and Sturm accurately measured the speed of sound in water after carrying out an experiment which involved ringing a bell in Lake Geneva.

By the 1800s the existence of frequencies outwith the range of human hearing had been accepted and investigations measuring the hearing threshold of human as well as that of animals had been instigated. In 1830 French physicist and medical doctor Savart used a toothed wheel to produce sounds with a range of frequencies up to and in excess of 20kHz in an attempt to determine the pitch limit and audibility thresholds of humans. Meanwhile, high frequency whistles were also invented during the 1800s and although developed by various scientists, the most well known of these whistles, and often also referred to as the birth of ultrasonics, was developed in 1883 by Galton to investigate the audio threshold of humans and animals. A more thorough study investigating the audio threshold of human hearing was published by instrument maker Keonig in 1899, using his own tuning forks which could produce frequencies from 16Hz to 90kHz. Keonig is also known for inventing the wave siren in 1867. Developed throughout the 19th and early 20th centuries sirens gave scientists the ability to study various phenomena in acoustics such as pitch discrimination and beats.

Strutt (3rd Baron Rayleigh) originally published *The Theory of Sound, volumes I and II* in 1877 and 1878 respectively (although extended publications of the volumes were printed in 1894 and 1896), and these are still considered to be the leading and possibly the most important works published on acoustics. They explored previous discoveries in acoustics and optics which are fundamental to wave propagation while Strutt also added his own discoveries. Furthermore, Strutt completed other research on atomisation, surface (or Rayliegh) waves, molecular acoustics, radiation pressure as well as cavitation, all having a direct influence on ultrasonics throughout the following decades [28, 85–87].

2.2 Ultrasonic transduction

Although Galton's whistle is often seen as the birth of ultrasonics, the technological beginning of ultrasonics commenced with the accidental discovery of the direct piezoelectric effect in crystals such as quartz and Rochelle salt in 1880 by Pierre and Jacques Curie when attempting to determine the relationship between the pyroelectric phenomenon and crystal symmetry [15, 28, 85]. Although the Curie's did not suggest the presence of the opposite effect, the converse or inverse piezoelectric effect, a year later fellow French physicist Lippmann theoretically proposed its existence in the presence of the direct effect, and this was promptly validated by the Curie's [88].

The first technological application of ultrasonics, a device for submarine detection, is

most associated with Langevin. Langevin, who obtained his PhD from Pierre Curie, received a proposal from Russian electrical engineer Chilowsky outlining a method of submarine detection using the process of echolocation, shortly after the outbreak of the first world war. The idea took inspiration from British meteorologist Richardson's patent (issued in the aftermath of the Titanic disaster) for methods of large obstacle avoidance, as well as a device developed by Fessenden, a Canadian born American engineer. Fessenden's device, a low frequency oscillator (named the Fessenden oscillator) was used in underwater depth measurements and was operational in naval ships prior to the Titanic disaster. Initially, the use of the inverse piezoelectric effect was ruled out to generate ultrasound due to the inherent low tensile strength of quartz, the most reliable piezoelectric crystal available at the time. However, after some advancements in the preparation of quartz crystals, they were used in the generation of ultrasound. The first quartz transducer consisted of a single quartz crystal embedded in wax, however, Langevin later conceived a transducer design which consisted of a mosaic or array of quartz crystals cemented between two steel plates. This development, now referred to as the sandwich or Langevin transducer, enhanced the level of radiated acoustic energy by improving coupling between the transducer and water as well as dropping its resonant frequency to 50kHz. Despite advances made during the design and development of the ultrasonic echo ranging device, an operational instrument arrived too late for the war effort, nonetheless, it is seen as an important step for the future technological advances in ultrasonics [15, 28, 85, 87, 89].

Ultrasonics research continued in the 1920s, although a slightly different application was developed during this time. The piezoelectric or crystal resonator was developed by Cady, Pierce, van Dyke, and Nicolson (somewhat independently and with a little hostility) after the realisation that a crystal such as quartz vibrating at resonance produces an electrical signal with a very precise, stable frequency. These characteristics were found to be suited for use in radio broadcasting, and were used in stabilisation of transmitted and received signals [28, 88]. Presently, crystal oscillators are used in modern devices such as wrist watches and electronics circuitry as counters. However, critically for the development of power ultrasonics, from this stemmed the discovery that near mechanical resonance, a piezoelectric material, such as quartz, behaves as a simple electric resonator shunted by a capacitance. This knowledge allowed Dye of the National Physical Laboratory and van Dyke of Wesleyan University, Connecticut, to independently derive the equivalent circuit of a piezoelectric oscillator, a theoretical technique used in the design and development of ultrasonic devices [28, 88, 90].

Although early developments in ultrasonics utilised the inverse piezoelectric effect, this is not the sole mechanism for generating ultrasonic waves. Magnetostriction was discovered almost 40 years earlier than the piezoelectric effect, in 1842 by Joule. Published in 1847, his report summarised his findings that a ferromagnetic material (an iron rod) will alter its shape when exposed to a magnetic field. However, the first reported use of the magnetostrictive effect in ultrasonics came almost 80 years after its discovery, in 1928 when Pierce and

Vincent independently invented the magnetostrictive oscillator [91,92]. Throughout the 1930s magnetostrictive transducers were further developed using a combination of nickel-iron and cobalt-iron alloys as ferromagnetic materials and by the end of the 1930s and beginning of the 1940s, these transducers were found to be more robust, less expensive and better suited to low ultrasonic frequencies than corresponding piezoelectric transducers. Hence, during the 1940s magnetostrictive transducers generally replaced piezoelectric transducers, especially in applications such as sonar [13, 28, 93].

When ferroelectricity was discovered in 1921, only two ferroelectric materials were known to exist; Rochelle salt and variants of potassium dihydrogen phosphate (KDP) [41]. However, in the early 1940s groups working independently in the United States and the former USSR discovered a significantly high dielectric effect in barium titanate oxide. A synthetic ferroelectric, this ceramic requires poling through the application of a strong electric field just below its Curie point of 120°C. The first barium titanate transducer was seen in 1947, becoming popular due to the relatively low cost of barium titanate (when compared to quartz), as well as being able to be synthetically manufactured into different shapes. Furthermore, transducers could be constructed from relatively large volumes of the material (shaped as cylindrical tubes or rectangular blocks) which gave them the ability to produce large output amplitudes [87, 94, 95]. However, as with quartz and other single crystal piezoelectric materials, barium titanate has low tensile strength and is difficult to bond to other materials used in the construction of Langevin transducers. The solution to both problems, first patented in 1955 by Miller, was to fasten the two endmasses together under a compressive load with a bolt or stud with the piezoceramic material sandwiched in the middle. Although Miller was not the first to apply a pre-load to piezoelectric material (pre-load was used in an accelerometer three years earlier) the pre-load increased the tensile strength of the ceramic by offsetting tensile loading with compressive [28, 94].

Barium titanate was widely used in ultrasonic transducers until the introduction of lead zirconate titanate, commonly known as PZT, in 1957. PZT possesses many favourable properties which supersede those of barium titanate such as higher poled stability and superior mechanical properties [15, 87, 95, 96]. First developed by Shirane and Sawaguchi of the Tokyo Institute of Technology, the discovery that PZT possessed strong piezoelectric properties once poled was proposed by Jaffe, Roth and Marzullo in 1955 [22, 87, 93]. The magnitude of the ferroelectric moment as well as its high Curie temperature allows variations in the chemical or thermal treatments, permitting the alteration of some physical properties of the ceramic whilst the fundamental piezoelectric effect remains strong. Slight differences in chemical composition or pretreatment result in *soft* or *hard* piezoceramics which are currently individually tailored for use in different ultrasonic applications [22].

As from July 2006, European Union (EU) legislation stated that whenever possible, instruments or devices containing hazardous materials (of which lead is one) should replace or substitute the hazardous material with a safe or safer material. This directive is an attempt

to deal with Europe's increasing levels of technological waste. Although exemptions are made to this legislation, in cases where it is scientifically or technically impractical to replace the hazardous material, it is reviewed at least every four years, which means that continuous progression is required to ensure that manufacturers are able to adapt before their product is affected by a change in legislation [97,98]. PZT ceramics contain lead, a hazardous material, but it is not just the disposal of devices and instruments containing PZT which are seen as the problem. Lead oxide (PbO) is released to the environment during the sintering and calcination processes during manufacture as well as when the material is machined.

Although research is currently ongoing to attempt to find lead-free alternatives to PZT and other lead based piezoelectric materials, this research is not completely new. Investigations during the 1950s and 1970s considered the removal of lead from piezoelectric materials, although it was concluded that better performance with alternatives could not be found. Current attempts to replace lead are investigating piezoelectric materials with components of sodium, potassium and niobate, KNNs, or piezoelectric materials based on bismuth with sodium and titanate, BNTs, or potassium and titanate (or related materials), BKTs. Currently, lead-free piezoceramics cannot reproduce the properties of present day lead based piezoceramics such as PZT, however, with the discovery of high piezoelectric response in relaxor-ferroelectric single crystals, such as $Pb(Zn_{\frac{1}{3}}Nb_{\frac{2}{3}})O_3$-$PbTiO_3$ and $Pb(Mg_{\frac{1}{3}}Nb_{\frac{2}{3}}O)$-$PbTiO_3$, investigations are now running in parallel with those for PZT, searching for lead-free high performance single crystals [98]. It should be noted that single crystal piezoelectric materials have improved bandwidth, sensitivity and source level as well as higher efficiency and are therefore most suited for use in transducers used in applications which require these properties, such as medical diagnostics [41, 98, 99].

Developments made throughout the 1950s, 1960s and 1970s in modern piezoceramics did not end the use of magnetostrictive materials in ultrasonic applications. The discovery of giant magnetostrictive materials during the 1960s by Clark *et al* demonstrated that under cryogenic conditions rare earth metals, Terbium, Tb, and Dysprosium, Dy, exhibit strain levels three times that of nickel or other known ferromagnetic materials. Studies throughout the following decade further investigated rare earth metals, compounding them with transition metals with the aim of producing an alloy which could achieve high strains at more practical temperatures. The resultant compound produced in 1974 was $Tb_{0.3}Dy_{0.7}Fe_{0.2}$, commonly known as Terfenol-D, which has the ability to produce high strain levels when exposed to a relatively small magnetic field at room temperature. By 1987 sophisticated crystal control technology was developed which stabilised the magnetostriction effect in such materials so that a 0.15% strain could be produced [12,13,41]. However, during the mid-1990s a new class of magnetostrictive materials was discovered. Magnetic shape memory, MSM, alloys or ferromagnetic shape memory alloys, FSMA, such as N_2MnGa where found to have the ability to produce extremely large strains, in the region of $2 - 6\%$ [12, 100].

Although two different transduction methods have been discussed, piezoelectric ceramics

are currently the favoured transduction technology utilised in many power ultrasonic applications. However, it should be stressed that applications such as dental hygiene (dental scaling) utilise both transduction methods. The future for magnetostrictive and piezoelectric materials will not solely depend on their performance but will also be influenced by future legislation.

2.3 Application of ultrasonics

2.3.1 Early years

While developing a system to detect submarines through echolocation, Langevin observed that small fish located directly in the ultrasound field were killed, while it could also induce severe pain in humans. These observations where the first to document the potential destructive capability and biological effect of high intensity ultrasound. Among those who observed Langevin's work in France during wartime was an American, Wood. Once back in the United States and after setting up a laboratory with wartime acquaintance, Loomis, they investigated whether Langevin's observations offered a wider scope to the science and engineering community [28]. The resulting paper published in 1927 and titled *The Physical and Biological Effects of High-frequency Sound-waves of Great Intensity* reports the considerable number of experimental observations made. Areas of power ultrasonics investigated range from; pressure generated from acoustic radiation, the formation of emulsions and fogs, the influence on the rate of chemical reactions and the biological effects of high intensity ultrasound, including the destruction of red blood cells and death of small fish and frogs. A less unfortunate outcome for mice was reported; *Mice are less sensitive, a twenty-minute exposure not resulting in death, and though at the end of the treatment the animal was barely able to move, the recovery was fairly rapid.* Nevertheless, possibly the most significant area investigated, with reference to power ultrasonic applications, was the observation that acoustic energy could be transmitted through an oscillating glass rod with enough amplitude that it cuts or etches a material [101].

Before the publication of Wood and Loomis's 1927 paper, very few publications reported upon high intensity ultrasound, however, in the following twelve years paper at least 150 related research papers were released. Many investigated the effect of ultrasonics on emulsification and dispersion, the mechanism of coagulation and biological effects, but crucially the majority referenced work that first emerged from Wood and Loomis's laboratory, illustrating the importance of the broad scope of work completed there [28, 102].

2.3.2 Power ultrasonics

Between the late 1920s and 1940s, the majority of research in ultrasonics concentrated on applications such as sonar, ultrasonic NDT and the effect of high intensity acoustic waves

on different media and biological tissue and cells. However, the second half of the 1940s and beginning of the 1950s saw an increasing interest in power ultrasonic applications which used a tuned resonator to deliver vibrational energy to a medium, inducing permanent physical change in it. By the 1970s, several ultrasonic processes were commercially viable. A group of review papers titled *Macrosonics in Industry* published between 1972 and 1977 [2, 29, 35, 103, 104] as well as an extensive paper by Shoh published in 1975 [105], discuss in detail the industrial processes of ultrasonic cleaning, chemical processing machining, plastic and metal welding.

Component design

The development of ultrasonic devices from laboratory prototype to viable industrial processes, such as ultrasonic machining and welding, may not have been possible without reliable stepped and tapered half-wavelength horns which are designed to amplify vibrational amplitude. The first analytical and numerical solutions for designing half-wavelength stepped and tapered horns were published in the 1950s. Balamuth presented solutions and guidelines for the design of such horns or 'mechanical impedance transformers', concluding that stepped horns provided the largest vibrational amplitude gain, however, Balamuth's solutions did not consider lateral deformation induced by Poisson's effect, therefore it also concluded that to ensure the predicted behaviour of the horns corresponded to their actual behaviour, the diameter of the horn cross-sectional area should be kept below a quarter wavelength [106]. Similar work was published by Merkulov in 1957. Merkulov reported that in analytical and experimental analyses of tapered horns, catenoidal horns achieved considerably greater amplitude amplification, although, achievable amplitude gain was limited by the strain limit of the horn material [107]. Merkulov, along with Kharitonov, published further work in 1959 [108] describing an analytical design process as well as experimental data of more complex horns with higher amplitude gains than the horns discussed in the 1957 paper. These consisted of 'sectional' concentrators which were located within the resonator where the input and output cross-sectional areas differed. Although good correlation was seen between analytical and experimental values of amplitude gain, Merkulov and Kharitonov observed that the shape of the amplifying section could significantly affect the difference between the predicted and experimental value of the resonant frequency.

Although, Balamuth, Merkulov and Kharitonov's techniques attempted to set 'ground rules' for the design of ultrasonic horns, they relied on the designer initially estimating the optimal horn profile and dimensions before calculating whether the maximum stress during operation would exceed the maximum stress of the material used to manufacture it. If the operational stress within the horn exceeded the upper stress limit of the material, the design process would need to be repeated until a satisfactory operational stress value was achieved, something not straightforward before the advent of PCs. A paper published in 1965 by

Eisner and Seager, although the work was completed in 1957, tackled the problem from a different perspective. They reported a numerical approach which initially considered horn requirements, such as the maximum amplitude and frequency, rather than starting with an estimated horn profile which may not be suitable. By considering the mechanical properties of the material used, a horn profile could be obtained which optimised the requirements while ensuring that the maximum stress would not exceed the maximum permissible stress of the horn material.

Amza and Drimer's 1976 paper also discussed the design as well as material choice (titanium, duraluminium and austenitic non-corrosive steel among a few stated) of tapered horns. They reported that deviations exist between calculated frequencies of the longitudinal mode of vibration and those found experimentally in ultrasonic devices containing conical, exponential, and catenoidal horns. They suggested a modification to the expressions used to calculate the dimensions of tapered horns through altering the vibration distribution and the position of the nodal point by incorporating a length correction factor. This allowed a reduction in the deviation between the calculated and measured tuned frequency, however, Amza and Drimer warned that the correction factor could be dwarfed, rendering it meaningless, if a thick coating was applied to the surface of the working face of the horn.

Stepped and tapered horns are used in a wide range of power ultrasonic devices, however, these are not always the most efficient horns to use in ultrasonic processes. Processes such as plastic welding require ultrasonic energy to be applied over a wide area, enabling large uniform joins to be constructed in a single application of acoustic energy and pressure. Horns with wide cross-sectional areas, where at least one dimension of the output face has a length similar to the tuned length, are often called block horns. These where first discussed in literature during the 1960s [109], one of the earliest publications illustrating a block horn design was reported in Shoh's review on ultrasonic welding, although no specific design details were given [33]. Shoh's paper discusses the use of block horns with large output surfaces being commercially used during the 1970s, however, the presence of literature describing the design or application of these horns at this time appears to be limited, possibly an attempt by manufacturers for design confidentiality. Nevertheless, Derks's PhD thesis, *The design of ultrasonic resonators with wide output cross-sections* [109], published in 1984 discusses in detail the design principles for block horns of various shapes and sizes through finite element modelling, while also validating his theoretical predictions with experimental work. The paper in 1986 by Adachi *et al* followed on from Derks's thesis, attempting to achieve a set of rules to simplify the design of block horns where uniform amplitude was required across its radiating face. Although Adachi achieved sufficient uniformity through carefully controlling the dimensions and separation of a number of slots cut into the block, his technique did not have the ability to conclude whether an optimal design for amplitude uniformity had been reached [110].

O'Shea's paper published in 1991 used a similar finite element approach to Adachi to

design block horns, discussing the effect of geometric variables such as slot dimensions. However, unlike Adachi, O'Shea also concluded that not only modal parameters of the tuned resonant frequency needed to be considered but also those of neighbouring modal parameters to understand their potential influence on the tuned mode. A finite element study, published in 1993 by Koike and Ueha, further investigated the performance of welding block horns. Unlike previous FE analyses, Koike and Ueha investigated the transient response of the full assembly of the ultrasonic device, including both the Langevin transducer and block horn in their model, with the aim of determining whether transient stresses were the causes for tool failure during unloaded conditions [111]. The authors concluded that transient behaviour was not the cause of unloaded failure, however, they achieved relatively close correlation between simulated and measured values for the transient behaviour, while also demonstrating an attempt to increase the complexity of computer based finite element analysis.

Chapman and Lucas reported a resonant frequency analysis of a cylindrical radial mode horn used in metal forming through a combination of finite element analysis, experimental modal analysis (using accelerometers) and electronic speckle pattern interferometry (ESPI), a non-contact optical measurement technique. Measuring the radial horn's modal characteristics allowed the horn to be successfully redesigned, shifting neighbouring resonant frequencies away from the operational frequency, hence reducing the possibility of modal coupling with the tuned frequency of vibration [112]. This paper illustrates the transition towards modern design practices, the validation of finite element models with non-contact measurements instruments, such as those using optical methods.

Although block horns with wide output surfaces were initially developed for ultrasonic plastic welding, similar techniques have been used to design guillotine blades used in the food cutting industry. In order to achieve a satisfactory cut, a uniform amplitude of vibration is required, while controlling maximum stress concentrations helps to prevent blade failure [36]. However, another, but slightly different, use of block horns was described in Derks's thesis, where it was used as an intermediate component to drive multiple smaller resonating tools. Apart from increasing efficiency in manufacturing processes, such as plastic spot welding, by increasing the number of welds that can be completed in one action, increasing the number of smaller tools which can be driven by a single transducer can lower the initial setup and run cost of the devices as fewer transducers and control systems (components which make up the bulk cost in ultrasonic systems) are required.

One area of ultrasonics where multiple smaller tools used in conjunction with a block horn driven by a single transducer can be advantageous is ultrasonic cutting. During the 1980s and early 1990s industrial research, culminating in a number of patents, discussed the design and application of multiple blade systems. However, unforseen complexities and regular failures of these prototype devices restrained their commercial viability [36,113,114]. A decade or so later Cardoni [9], and Cardoni and Lucas [115–117], reported the use of multiple blade devices in the cutting of food. Through characterisation of these devices, using both finite element

analysis and experimental methods, the main sources of failure were identified and redesign of the block horn and cutting blades led to improvements in performance and reliability.

Utilisation of composite modes of vibration

The first power ultrasonic devices, developed in the 1950s, only made use of the longitudinal mode of vibration. However, in his 1964 patent, Mason reported upon an ultrasonic transducer which may enhance applications such as ultrasonic drilling, machining and welding by developing a torsional mode of vibration [118]. As mentioned by Cardoni [9] and Shuyu [119] this work was further discussed by Rozenberg, who in 1969 investigated the development of a transducer which converted part of the longitudinal motion to torsional motion, hence producing a composite longitudinal-torsional mode of vibration. However, the construction of the transducer proved to be problematic while the transducer also suffered from low conversion efficiency between the modes of vibration.

More recently, literature has been published on devices which induce compound modes of vibration. The combination of longitudinal and torsional modes of vibration is possible either through transducer architecture (multiple sets of piezoceramics poled differently) or horn geometry (incorporation of slots or a spiral cut) and these are used in applications such as plastic and metal welding to improve weld strength and increase the thickness of materials which can be welded [39,120]. The combination of longitudinal and torsional modes of vibration is also utilised in ultrasonic devices used in eye surgery, where the compound mode enhances the emulsification of the lens of the eye during cataract surgery [54–56], and in ultrasonic drills where improvements can be made to cutting performance [40, 121]. Meanwhile, ultrasonic devices which combine longitudinal and flexural modes of vibration, again either through transducer architecture or horn geometric features, are used in a broad range of applications, from ultrasonic assisted polishing to bone surgery and dental hygiene [38, 122–124].

Ultrasonic motors are another ultrasonic technology which utilise the combination of multiple modes of vibration. Originally developed in 1973 by Barth at IBM, the motor consisted of two tuned horns, each driven by an individual piezoelectric resonator, located either side of a rotor. Both horns are in contact with the rotor and when one horn is driven by its piezoelectric resonator, the rotor is driven in one direction, while when the other horn is driven the rotor is driven in the opposite direction. Although this motor was ultimately not useful due to mechanical degradation of the piezoelectric material induced by elevated operational temperatures, subsequent successful designs use the same principle. The 1980s saw the need for precise and quiet positioners, which gave some impetus to the development of ultrasonic motors [41]. In the last twenty years standing wave ultrasonic motors operating in a composite longitudinal-torsional mode of vibration has been reported [125–128], while others have been developed to produce a composite longitudinal-flexural mode of vibration [41,129].

Meanwhile, another type of ultrasonic motor has been developed to exploit the phenomenon of near field acoustic levitation (NFAL). Publications dating from the 1970s, report upon the ability to levitate small particles, even whilst they change state (solid to liquid or vice versa) [130, 131]. To transport objects using NFAL travelling wave motors are required. Travelling wave motors have the same architecture as multi-mode standing wave motors, however, instead of the multiple standing waves being produced in phase, travelling wave motors generate two different standing waves 90^{o} out of phase, hence producing a travelling wave [41]. Research carried out at the Tokyo Institute of Technology during the 1990s and the first decade of the 21st century has contributed significantly towards the development of travelling wave motors and non-contact transportation using NFAL. Travelling wave motors have been incorporated in devices which can lift planar objects of a mass of up to 10kg with the ability to transport them, linearly, along a path of several hundred millimeters [43,44,46].

2.3.3 Dental and surgical applications

Power ultrasonics was first introduced in dentistry in 1952 when Catuna used an industrial ultrasonic drilling machine to cut cavities in extracted teeth [132]. First patented by Lewis Balamuth in 1945 [30], and reported upon in 1951 [31, 32], the industrial device was originally designed to cut hard and brittle materials such as tungsten carbide, glass and ceramics. Cutting was achieved through the application of high intensity ultrasound to an abrasive slurry on the surface of the work piece, which gradually ground it away. Catuna and Balamuth's innovative use of a novel industrial device and subsequent trials lead to the development of a specialised dental device that operated on the same principles as its industrial counterpart [65, 133]. However, even though many surgical benefits over conventional air powered drills were promised by this ultrasonic device, the requirement for an abrasive paste restricted the view of the dental operator while its high cost may have hampered its overall success.

The first application of ultrasonics in the periodontal treatment of oral prophylaxis was reported by Zinner in 1955 [134]. Initial trials of early ultrasonic scalers produced favourable results over hand instruments, reducing procedure time, patient discomfort and damage to soft tissue surrounding the tooth. Despite these findings strengthening the case for the adoption of ultrasonic devices for routine prophylaxis treatment, it was also found they could potentially scratch the root surface and dentine of the tooth if applied to the tooth surface with a large force. However, it should be recognised that applying the vibrating device with large levels of force to the tooth surface is unnecessary and illustrates an incorrect use of the device. Apart from damaging tissue, the application of high pressures also reduces vibrational amplitude of the ultrasonic device reducing its performance [64, 66].

Parallel to the studies on dental scaling, investigations into the potential use of ultrasonic instruments in bone cutting procedures were undertaken during the 1950s. Although the

very first devices, such as those reported by Balamuth, relied on an abrasive slurry, towards the end of the 1950s Richman discussed the use of an ultrasonic device in dentistry which operated without slurry [135], applying the device to various endodontic treatments such as root planning. However, the use of ultrasonic devices in endodontics was significantly improved twenty years later by Martin through the application of a biological agent enhancing microorganism eradication, during root cleaning and disinfection [136, 137].

A few years after Richman, Mararow [138] and McFall *et al* [139] also reported upon the use of ultrasonic devices directly cutting bone tissue without the requirement of an abrasive slurry. These novel bone cutting trials utilising ultrasonics during the 1950s and 1960s, whether they required an abrasive slurry or not, discussed the advantages and disadvantages of ultrasonic devices when compared to traditional bone burs or saws. Richman reported that in 32 clinical cases where an ultrasonic device was used to plan alveolar bone (bone surround the tooth), healing was uneventful without postoperative complications [135]. Richman also noted increased patient acceptance of the ultrasonic method after a reduction in patient discomfort from the postoperative site, an observation independently made by Postle during the same year [140]. Reports throughout the following decades further discussed advantages and disadvantages of ultrasonic osteotomy. However, even though Mararow [138] indicated that the ultrasonic devices could inhibit bone healing, further studies by McFall *et al* [139] and Horton *et al* [80] reported little difference between recovery times between traditional and ultrasonic devices. Aro *et al* [141] concurred with McFall *et al* and Horton *et al*, although finding that initial healing was slower in bone cut ultrasonically.

Comparisons between studies investigating the performance of ultrasonic devices with oscillating burs or saws during the 1970s and early 1980s are often difficult to directly compare due to the differences in the ultrasonic devices as well as the location and type of bone dissected. The use of cooling fluid is discussed in these studies, although not always providing a consistent opinion as to whether it should be used in operation or not. Aro *et al* [141] reported that in 1974 Polyakov *et al* stated that the temperature of the cutting site with an ultrasonic saw without the presence of a cooling fluid did not exceed 78°C, however, the value that Picht *et al* reported in 1977 was considerably higher at 150°C. Picht *et al* also reported that during bone dissection with a bone saw, the temperature reached 60°C, however with coolant the temperature of bone during cutting with both the ultrasonic device and bone reached 40°C. From this study Picht *et al* illustrated that without cooling fluids ultrasonic devices had the potential to raise the temperature of bone higher than traditional bone saws, however the presence of cooling made temperature increases comparable. Picht *et al* therefore derived the same conclusions as McFall *et al* [139] and Horton *et al* [80] that cooling fluid was necessary during ultrasonic cutting.

Many modern ultrasonic bone cutting devices deliver a fluid, generally through an internal channel located through the handpiece of the ultrasonic device, to an outlet positioned near the cutting blade and cutting site. This aims to cool both the cutting blade and surgical

site, thus preventing necrosis, and to assist the removal of tissue debris from the tool-tissue interface, keeping the site clear for the surgeon to view while also removing any swarf which, through frictional heating, could burn and damage the edge of the dissection [5, 80, 142]. Studies have shown greater promotion of osteoblast (cells responsible for bone formation) in dissected regions without osteonecrosis and burnt swarf. This is probably due to intact and unblocked Haversian channels (or canals), which allow oxidation and communication between the dissected area and sites that produce osteoblasts, to permit the cells and proteins necessary for recovery to reach the dissected regions quicker than if they were damaged through osteonecrosis or blocked with burnt debris [72, 73, 80, 143].

Although ultrasonic oral prophylaxis had become a mainstream periodontic treatment by the 1990s, the use of ultrasonics in osteotomy and osteoplasty (the repair of bone) had not progressed from experimental instruments and trials. The success of dental scaling devices may be partly due to the development from early scaling tips, which were bulky, to slender tips capable of accessing hard to reach areas. However, the ability to manufacture slender and reliable inserts is also important for the control of tissue heating during osteotomy [62]. It was not until 2001 that the first commercial ultrasonic device specifically designed for bone cutting applications entered the market. Known as the Piezosurgery® Device, this system built upon ultrasonic scaler technology and was developed through a collaboration between of a maxillofacial surgeon, Vercellotti, and Italian company Mectron S.p.A [72, 123]. Possibly two important factors can account for the instrument's success; the collaboration between the surgeon and the engineering company, and advancements in transducer control electronics. The partnership between the surgeon and the design company allowed the product to be developed with direct influence from the user. This ensured that the device would be practical (early attempts at bone cutting devices were difficult to use and cumbersome) and more likely to be accepted by the surgeon [141, 144, 145]. Meanwhile, during operation, the application of different pressures by the surgeon, the presence of cooling fluid and heating within the piezoceramics elements due to extended use are factors which could cause the device's resonant frequency to change. This could lead to difficulties in tracking it the resonant frequency, however advances in modern electronics has allowed this to be adequately solved. The application of a 50kHz pulse every 10ns to the excitation frequency of the Piezosurgery® Device transducer is a novel design feature which assists the device to efficiently cut bone efficiently [70].

2.4 Nonlinear behaviour

As discussed in Section 1.5, nonlinear behaviour in a dynamic system can stem from several origins and this is no different with power ultrasonic devices. Geometric, material and physical nonlinearities in power ultrasonic devices have all been investigated and reported upon, although some more thoroughly than others.

From the first use of piezoceramics such as barium titanate and PZT in ultrasonic devices during the 1950s, reports of piezoceramics behaving nonlinearly when excited above a linear threshold had been reported [146]. The electromechanical characteristics of piezoelectric materials, such as the piezoelectric charge constant, d, found by Berlincourt *et al* [22] and Berlincourt and Jaffe [95] are correct when the materials lie within their linear region. This linear region is considered to be under low levels of vibration (strain) or stress, at frequencies considerably lower than resonant ($f \leq 1000$Hz). However, piezoceramics in power ultrasonic devices are very rarely driven under these conditions. To achieve sufficient amplitudes of vibration they are required to be driven close to resonance, hence, an extensive amount of literature is available on the characterisation of nonlinear behaviour of piezoceramics under these driving conditions [6–8, 26, 27, 146–162]. This literature also reports that electromechanical loss factors, the mechanical loss factor, Q_m^{-1}, and dielectric loss factor, δ, originate from deformation within the piezoceramic material and are both intrinsic (deformation of the lattice within each ferroelectric domain) and extrinsic (elastic deformation of non-180^o domain walls). Furthermore, it has been found that the loss factors are also dependent on electric field strength and temperature [27, 149, 150, 156, 159]. The elastic, dielectric and piezoelectric terms have also been found to be temperature dependent, although they are not as sensitive to elevated amplitudes of vibrational as the loss factors [6, 7, 158].

Before the 1990s many research studies were experimentally characterising piezoceramics utilising methods such as the constant current method (discussed Section in 4.1.2), which excited piezoceramics at high levels of amplitude and induced a significant level of heating. Hagemann [148] and Beige [150] reported the detrimental effect that heating has on both dielectric and mechanical losses as well as changing the elastic, dielectric and piezoelectric terms. An experimental measurement system (discussed in Section 4.1.4) which isolates the effect of high amplitudes of vibration from that of electric field strength and temperature increases in piezoceramics was developed by Umeda *el al* [163].

Nonlinear behaviour observed in piezoceramic elements driven under high levels of vibration, such as mechanical loss (leading to amplitude saturation), frequency softening, frequency hysteretic regions, amplitude jumps and generations of harmonics, have all been observed in piezoelectric transducers [164, 165]. However, the incorporation of nonlinear terms in simulations of piezoelectric transducers which accurately model nonlinear behaviour under operational conditions has proven difficult. Guyomar *et al* [164] and Uchino *et al* [165] both measured the response of Langevin transducers, and then theoretically simulated or modelled the behaviour they measured through analytical methods (expanding piezoelectric second order constitutive equations) or equivalent circuit method respectively. Meanwhile, reports published within the last few years by Blackburn and Cain [166, 167] and Guyomar *et al* [168] have discussed the limitations and difficulties of modelling nonlinearities in ultrasonic systems. Although analytical and computer simulations have advanced over the last few decades, previous theoretical approaches of modelling or simulating piezoceramic

elements or ultrasonic devices through incorporating measured nonlinear properties into linear solutions requires refinement. To improve simulation or modelling of nonlinear behaviour in piezoceramics or ultrasonic devices, Guyomar *et al* cited that novel and more complex methods of modelling dielectric nonlinear terms must be developed. Guyomar *et al* also stated that the nonlinear terms of non-piezoelectric materials within the ultrasonic device (materials which the endmass and tool are manufactured from) also require incorporation in to the simulation or model.

As with piezoceramic materials, non-piezoelectric materials used in power ultrasonic transducers and tuned tools also exhibit nonlinear behaviour when exposed to high levels of strain or elevated temperatures. Mason [169,170] reported that the mechanical loss (Q_m^{-1}) of a titanium alloy (Ti6Al4V) was independent of frequency and temperature at low strain levels during elastic deformation. However, as the strain level increased to anelastic deformation (where stress and strain have no definite relationship) Q_m^{-1} becomes dependant on these conditions and increases until a critical point, at which a steep rise occurs in Q_m^{-1} and component failure will become likely. Mason also noted that treatment such as annealing significantly increased the mechanical quality factor due to the pinning of dislocation loops. Previously strained samples, on the other hand, allow freer dislocation motion, reducing the stiffness of the material and, in turn, exhibiting frequency softening characteristics at lower amplitudes of vibration than the freshly annealed samples. Puškár [171], Kuz'menko [172] and Campos-Pozuelo and Gallego-Juàrez [173, 174] experimentally investigated the critical strain level for steel, aluminium and titanium alloys respectively, determining strain values which these materials can reach before critical increases in Q_m^{-1}.

The majority of ultrasonic devices are constructed from multiple components, often consisting of a transducer, booster horn and working tool. As previously discussed, the materials which these components are manufactured from display nonlinear behaviour when exposed to an amplitude of vibration above their linear threshold. However, it is also known that nonlinear behaviour can be induced from physical configurations in dynamic systems [81]. A short study in the available literature highlights that devices used in processes ranging from ultrasonic food cutting [36,115,116,175–177], rock drilling [178], and ultrasonic bonding [179], as well as devices designed to propagate high intensity acoustic waves in to gasses [10, 180], all can suffer from nonlinear behaviour, having a detrimental effect on their performance. Unstable driving conditions caused by various nonlinear behaviours; shift in tuned resonant frequency (either softening or hardening effect), amplitude jump and frequency hysteresis or modal interactions, all have been observed in power ultrasonic devices constructed from an assembly of tuned components. Although these nonlinear behaviours can stem from nonlinear material terms, physical dimension as well as component configuration can also seriously influence whether these behaviours occur or not. To predict the occurrence of certain nonlinear behaviours can be difficult with linear analytical or finite element models.

Nevertheless, the most common approach to dealing with nonlinear behaviour in

ultrasonic devices is to redesign the geometry until the unwanted behaviour disappears [9,180]. To improve the efficiency of the design and development of power ultrasonic devices, research is required to understand the effects of complex geometry, device manufacture and material selection on the behaviour of such devices.

Chapter 3

Design and optimisation of ultrasonic devices

Research into improving the design, testing and working lifespan of ultrasonic components has considerably increased since the 1950s. Developments in computing over the last 20 years has led to the development of commercial FE codes which, apart from being user friendly, allow the quick and relatively cost effective analysis of ultrasonic components. This has also enhanced experimental capabilities as programmes and hardware of increased complexity has improved data collection increasing the quantity of data which can be collected over increasingly shorter periods of time. Throughout this chapter design criteria of elementary tuned components and transducers as well as fundamental finite element analysis (FEA) and experimental modal analysis (EMA) processes will be discussed. This leads to an investigation of optimisation of a device currently utilised in bone surgery.

3.1 Design of ultrasonic devices

Modern applications which employ power ultrasonics, for example surgery, often require that tuned assemblies possess complex geometries. This can be for several reasons; to allow tool access to confined or difficult to reach areas and/or to take advantage of oscillation motions achieved through coupling multiple modes of vibration. Although not an extensive list, it highlights the necessity to the design process of finite element modelling to ensure that the device is correctly tuned and optimally designed. However to design basic structures, or to give an initial starting point for FE models, it is possible to use simple analytical solutions to predict modal parameters.

3.1.1 Uniform slender bar

To solve the analytical solution for a slender bar (a bar whose the diameter is considerably smaller than its length) of constant cross-sectional area, A, and uniform density, ρ, when

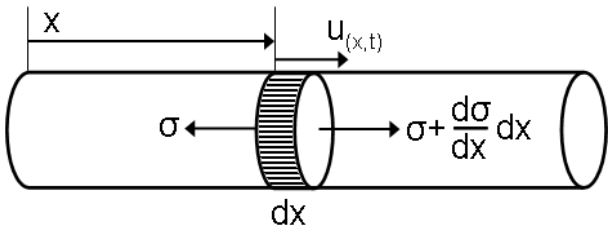

Figure 3.1: Element within a slender bar

exposed to a dynamically changing stress field, $\sigma(x,t)$, Newton's second law of motion can be applied to an element within the bar (Figure 3.1), dx, giving Equation 3.1, where the longitudinal displacement is $u(x,t)$ [181].

$$-\sigma A + (\sigma + \frac{\partial \sigma}{\partial x} dx) = \rho A dx \frac{\partial^2 u}{\partial t^2} \tag{3.1}$$

The longitudinal strain, $\varepsilon = \frac{\partial \sigma}{\partial x}$, when incorporated into Hooke's law (assuming that the rod behaves elastically) gives $\sigma = E\frac{\partial \sigma}{\partial x}$ and once substituted in to Equation 3.1 gives the wave equation;

$$E\frac{\partial^2 u}{\partial x^2} = \rho \frac{\partial^2 u}{\partial t^2} \tag{3.2}$$

The speed of sound through a rod (wave velocity) is given by;

$$c = \sqrt{\frac{E}{\rho}} \tag{3.3}$$

and incorporating it into Equation 3.2 gives;

$$\frac{\partial^2 u}{\partial t^2} = c^2 \frac{\partial^2 u}{\partial x^2} \tag{3.4}$$

To obtain the natural frequencies of the slender rod, the method of separation of variables is used to solve the partial differential equation, finding the general solution. Assuming a solution in the form of $u(x,t) = y(x)z(t)$ and substituting in Equation 3.4 reveals the following expression;

$$c^2 \frac{1}{y}\frac{d^2 y}{dx^2} = \frac{1}{z}\frac{d^2 z}{dt^2} \tag{3.5}$$

As the righthand side of Equation 3.5 is independent from the left, the function of x requires to be equal to a function of t for all x and t. Hence, to allow this a constant, $-\omega^2$, (separation constant) will be introduced;

$$\frac{d^2 y}{dx^2} + \frac{\omega^2}{c} = 0 \tag{3.6}$$

$$\frac{d^2z}{dt^2} + \omega^2 = 0 \tag{3.7}$$

This gives the general solution for u(x,t) where A, B, C and D are dependent on boundary conditions and k is material stiffness;

$$u(x,t) = (A\cos kx + B\sin kx)(C\cos \omega t + D\sin \omega t) \tag{3.8}$$

To solve the general solution, boundary conditions (Equation 3.9) must be applied. If it is assumed that the rod is under free-free conditions (the ends of the rod experience stress free mounting conditions) then only time-independent solutions of Equation 3.8 must be considered.

$$\begin{aligned} \frac{du}{dx} &= 0 \\ x &= 0, l \end{aligned} \tag{3.9}$$

Application of the free-free boundary conditions to the time-independent solutions of Equation 3.8 lead to both $B = 0$ and $\sin kL = 0$, and result in the resonant frequency, n, of a slender rod of fixed length l being expressed as;

$$f_n = \frac{n}{2l}\sqrt{\frac{E}{\rho}} \tag{3.10}$$

Equation 3.10 is only reliable when used with slender bars whose diameter is considerably smaller than length, l ($< \frac{1}{\lambda}$), and when applied to lower order modes.

3.1.2 Design of piezoelectric transducer

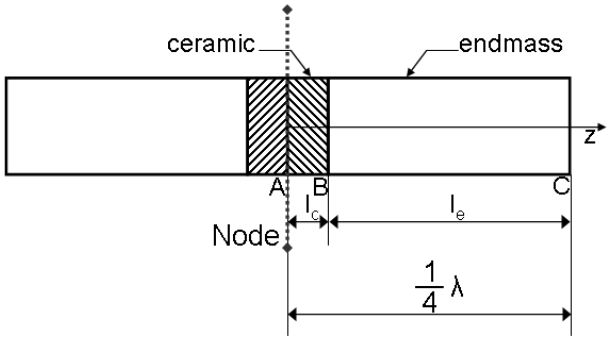

Figure 3.2: Basic architecture of a symmetrical prestressed Langevin transducer [94]

The Langevin transducer in its most basic concept consists of a piezoceramic stack sandwiched between two endmasses. As previously discussed, piezoceramic materials are considerably stronger under compression than in tension, therefore to improve the assembly it is usually

held under compression through a tensile bolt. If it is assumed, as in Figure 3.2, that the transducer is under free-free boundary conditions and the nodal plane divides the piezoceramics centrally, then each half of the transducer can be independently investigated as a quarter wavelength ($\frac{1}{4}\lambda$) section. Equation 3.11 considers the propagation of a stress wave through the piezoceramic and endmass materials and by applying resonant boundary conditions at either end, A and C, and velocity and force-continuity at the material discontinuity, B, the relationship between the resonant frequency, impedance ratio ($\frac{Z_c}{Z_e}$) and the lengths of the piezoceramic element and endmasses can be sought.

$$\frac{Z_e}{Z_c}\tan\theta_e \tan\theta_c = 1 \tag{3.11}$$

Z_c and Z_e are the acoustic impedances of the piezoceramic element and endmass respectively;

$$Z_c = \rho_c v_c A_c,\ Z_e = \rho_e v_e A_e;\ \theta_c = \frac{\omega_c}{v_c},\ \theta_e = \frac{\omega_e}{v_e}$$

while ρ, v and A are the density, speed of sound and cross-sectional area of the respective material, and ω is the tuned frequency with the relationship; $f = 2\pi\omega$. Equation 3.11 can not be directly used to derive the resonant frequency of the transducer, but can be used to fix an unknown dimension such as cross-sectional area or length. However, by finding the solution to Equation 3.11 equal to 1, an approximation of ω may be given [94].

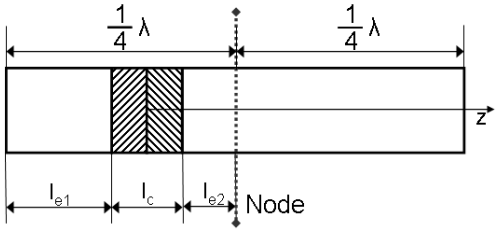

Figure 3.3: Basic architecture of an asymmetrical prestressed Langevin transducer [94]

In many transducer assemblies it is necessary to position the piezoceramic stack away from the nodal position, for example the incorporation of a support flange, so any adverse damping effect caused by a grounded point can be minimised. Figure 3.3 illustrates an asymmetrical transducer in free-free boundary conditions. Again each quarter wavelength section can be investigated separately using Equation 3.12;

$$\frac{Z_{e1}}{Z_c}\tan\theta_c \tan\theta_{e1} + \frac{Z_{e1}}{Z_{e2}}\tan\theta_{e2}\tan\theta_{e1} + \frac{Z_c}{Z_{e2}}\tan\theta_{e2}\tan\theta_c = 1 \tag{3.12}$$

Assembly of transducers

As previously stated Langevin transducers are typically constructed from piezoelectric elements sandwiched between two endmasses with a bolt holding the stack together under a compressive load. The active elements used in power ultrasonic transducers are conventionally

piezoceramic elements and generally come in the geometric form of a ring, however discs and plates are also frequently used. Piezoceramic elements are often prepared through processes such as screen printing or plating by which a thin layer (3μm to 10μm thick) of an electrical conductive material such as gold, silver, chromium or nickel is deposited on to the surface. Depending on the application of the elements, leads can be soldered straight to the prepared surface of the piezoceramic. In the assembly of Langevin transducers it is common to incorporate thin copper discs or electrically conductive mesh or epoxy between oppositely poled piezoceramic elements and connected in parallel to the power source, Figure 3.4 [15, 99].

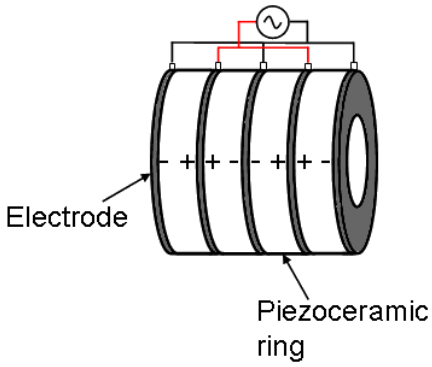

Figure 3.4: Poling direction of piezoceramic rings within a piezoceramic stack containing four active elements

The type of piezoelectric material selected for use within a ultrasonic transducer is largely dependent on the application it will be employed. However, this is not the only consideration, as the geometry of the piezoceramic element can also have a significant influence on the performance of the transducer with factors such as the thickness, diameter and number of elements being carefully considered. Optimising the thickness of the piezoceramic used within the stack of a Langevin transducer can be important as the thinner the piezoceramic element is, the better the electric field uniformity, the higher the effective electromechanical coupling coefficient and lower its impedance (higher the flow of current and hence amplitude for a given driving voltage). However, reducing the thickness of the piezoceramic element, increases the number of elements within the defined stack length which in turn increases the cost of manufacturing the transducer as well as increasing the capacitive value. Increasing the number of piezoceramic elements in the stack can also lead to inefficiency due to mechanical losses (caused through increasing the number of join interfaces) and drive problems, as too many elements can induce phase shifts among the elements causing them to counteract one another's oscillations. On the other hand thicker piezoceramic elements reduce the complexity of the transducer, hence reducing manufacturing cost as well as the mechanical losses (reduction in the number of join interfaces). However, thicker elements will also lead to a less uniform electric field at a given voltage whilst also increasing the impedance and internal

heating [182–184]. Therefore a trade off between using many thinner piezoelectric elements and fewer thicker elements should be sought to achieve optimal performance. Furthermore, properties such as Q_m and admittance of the piezoceramic material can vary considerably from batch to batch, therefore, to ensure high performance and quality of the piezoceramic stack each individual element should be investigated and carefully selected [185, 186].

Heat generation within the piezoceramic stack of power ultrasonic transducers is a well documented problem which can have a detrimental effect on the performance of the piezoceramic element [154]. Active and passive systems can be used to encourage the circulation of air around the piezoceramic stack, promoting cooling through convection, while electrodes can be used as cooling fins to improved heat dissipation [94]. The electrode thickness can also be considered with regards to heat dissipation from the piezoceramics, as increasing the thickness of the electrode will increase their mass and provide a more efficient heat sink for the piezoceramics. However, increasing electrode thickness also can have a damaging effect on the mechanical quality factor and effective electromechanical coupling coefficient [183]. Therefore a comprise must be made between the adverse effect on performance by heating and electrode thickness.

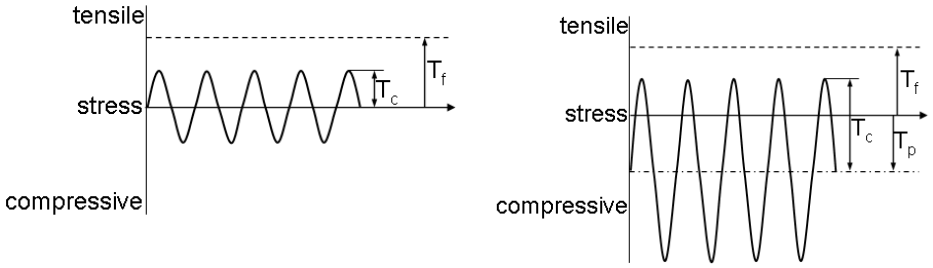

(a) Without prestress (b) With prestress

Figure 3.5: Fatigue stress limit in piezoceramic [99, 187]

As discussed previously, the compressive strength of piezoceramic elements is much greater (greater than 7×) than under tensional loading [188]. To utilise the relative strength in compression, Langevin transducers are held under a pre-stress or load which offsets tensile stress for compressive. Figure 3.5 depicts that a piezoceramic under pre-stress, can achieve higher maximum tensile stress, T_c, before exceeding its dynamic fatigue limit, T_f, than without. Pre-load is traditionally applied in a Langevin transducers by clamping the transducer together through a single central or a number of peripheral studs or bolts. A central stud or bolt is usually preferred as it delivers better compressive uniformity within the stack, however whether a single central stud or bolt or several peripheral are used, stud or bolt material selection should consider static and dynamic stress as well as fatigue loading. It is advantageous for the stud or bolt to be fine threaded as well as having a close fit with the opposite female thread. This increases the coefficient of friction between the two threaded parts and reduces the likelihood of the stud or bolt from loosening during operation.

However a novel wire bonding transducer design has been proposed by DeAngelis which disposes of the tensile bolt altogether and proposes enhanced stress uniformity across the ceramic [184, 186]. The piezoceramic stack is positioned in a cavity within the transducer body while, to apply pre-load, a wedge-like shaped object is forced in to the rear of the cavity compressing the stack together. Meanwhile, the pre-load is largely dependent on the individual transducer and materials used within it, however it is clearly an important design consideration to ensure optimal transducer performance. Insufficient pre-loading will result in high impedance, low fatigue life and lower than expected resonant frequency, while excessive pre-loading can cause piezoceramic depoling, tensile bolt failure and higher than expected resonant frequency. Typical pre-load values of transducers range from 20MPa to 80MPa [94,186,187,189–191] however to ensure the most efficient and reliable transducer, it is crucial that the pre-load value is optimised. Finally, the stud or bolt is generally covered with an electrically insulating sleeve before transducer assembly which prevents the possibility of short circuit during operation.

Driving conditions of power transducers

Ultrasonic power transducers are generally driven at a tuned frequency which lies within a narrow frequency bandwidth. Mechanical motion is induced in piezoceramic transducers by utilising the inverse piezoelectric effect to induce strain; the frequency and amplitude of the electrical signal, at its most basic a sine wave of constant amplitude, will ultimately dictate the frequency and amplitude the transducer oscillates at. The amplitude of the electrical signal will generally be controlled so it will either have an amplitude of constant voltage or constant current. Although it is less complicated to drive an ultrasonic device under constant voltage than constant current, many manufactures of ultrasonic systems favour controlling the electrical signal through constant current. This is due to the fact that transducer vibrational amplitude is proportional to the current drawn, thus allowing stable vibrational driving amplitude even when the device is under load and elevated power consumption.

The resonant conditions which the piezoelectric devices can be driven at can also vary. Systems driven with a constant electric field, under electrical short circuit conditions (electrical resonance), will require a power supply which can deliver an electrical signal with high current and low voltage. Furthermore, devices driven under these conditions will also experience heating within the piezoelectric elements which will generally become problematic after a period of time of activity. Hirose *et al* [192] reported that under resonance drive losses within the piezoceramics can be derived from Gibbs free energy expression;

$$G = -\frac{1}{2}PE - \frac{1}{2}ST \tag{3.13}$$

where P is polarisation, E, S and T are the electric field, strain and stress. Losses, W, in piezoceramics can be expressed whilst under constant electric field as;

$$W = \frac{1}{2}\varepsilon E^2 \tan\delta + \frac{1}{2}sT^2 \tan\phi + \frac{1}{2}(\frac{d^2}{s}E^2 \tan\theta) + \frac{1}{2}(\frac{d^2}{\varepsilon}T^2 \tan\theta) \tag{3.14}$$

and four loss terms are represented in Equation 3.14. The first term represents the dielectric loss, the second the mechanical loss while the third and fourth represent electro-mechanical losses with reference to *S-E* hysteresis loop and *P-T* hysteresis loop, both having the loss angle ω, respectively. Whilst driving under mechanical resonant conditions, the domain wall is able to move with relative ease due to the fairly large *S-E* hysteresis loop, however, as previously discussed, the electro-mechanical loss within the piezoceramic does not behave linearly, as at elevated amplitude levels it is significantly higher than under lower levels.

An alternative method of driving piezoelectric devices is open circuit conditions or at electrical anti-resonance (constant electric displacement, D). To drive a piezoelectric device under this condition requires the electrical signal to have low current with a high voltage to achieve comparable vibrational amplitudes to those seen in short circuit conditions where the opposite conditions are required. Driving under open circuit conditions can also be seen as advantageous, as the current consumption of the transducer is lower and therefore standard and relatively inexpensive power transformers can be utilised in the system design as the capacity to supply and protect users from high currents is reduced. Meanwhile, further advantages of driving under open circuit conditions have also been recognised such as lower losses (less heat generation) as well as a higher mechanical quality factor [42, 165]. Losses in piezoelectric elements while driven under open circuit conditions are expressed in Equation 3.15, where D is almost equal to P;

$$W = \frac{1}{2}\varepsilon P^2 \tan\delta + \frac{1}{2}sT^2 \tan\phi + \frac{1}{2}(\frac{d^2}{s\varepsilon^2}P^2 \tan(\theta-\delta)) + \frac{1}{2}(\frac{d^2}{\varepsilon}T^2 \tan(\theta-\delta)) \tag{3.15}$$

It is evident that each term in Equation 3.15 corresponds with each of those in Equation 3.14, although in the former expression the third and fourth terms approach zero as $\theta \approx \delta$ and the permittivity of the ceramic is considerably larger than the permittivity of air ($\varepsilon >> \varepsilon_o$). Furthermore, when piezoceramics are driven with constant electric displacement, the hysteresis loop between S and D (or P) is relatively small, indicating that the domain moves with relative difficultly. Therefore, it is suggested that piezoceramics display lower losses when driven at elevated amplitudes at antiresonance than at resonance [192].

3.1.3 Material selection during the design of ultrasonic devices

Although previously briefly discussed, there are several considerations which should be addressed during the selection of materials for use in ultrasonic devices.

Low acoustic attenuation

As an acoustic wave propagates through a medium, its intensity reduces further it travels from its source. Two causes of energy loss from the wave during propagation are scattering (the reflection of the sound wave to directions other than its original propagation direction) and absorption (the transformation of sound energy in to heat through internal friction), while the combined effect of the two is known as attenuation. Equation 3.16 expresses the decay of amplitude of a wave;

$$A = A_0 e^{-\alpha x} \tag{3.16}$$

A_0 is the initial amplitude of the propagated wave, A is the reduced amplitude of the wave after the wave has travelled a distance x from an initial location. Meanwhile, the attenuation coefficient, α, is the property which characterises how easy or difficult an acoustic wave can propagate through a medium and has the dimensions of nepers/length, where a neper is a dimensionless quantity.

Alternatively, it is possible to consider energy loss within the wave in terms as amplitude loss per cycle. The logarithmic decrement, δ, of an acoustic wave measures the rate at which the amplitude of the wave reduces and can be expressed as;

$$\delta = ln \frac{A_n}{A_{n+1}} \tag{3.17}$$

and hence in this case, $\delta = \alpha x$. The losses within the system can be characterised by the following expression;

$$\delta = \frac{\text{energy dissipated in one period}}{2\pi \times \text{ energy stored}} \tag{3.18}$$

Equation 3.18 in turn represents the reciprocal of the quality factor, Q;

$$Q = \frac{\omega}{2\alpha} = \frac{f_r}{f_2 - f_1} \tag{3.19}$$

where ω is the angular excitation frequency. To calculate the quality factor from experimentally gathered data, f_1 and f_2 are the frequencies which correspond with the value of $\sqrt{2}$ of the maximum amplitude at the resonant frequency, f_r. Hence, the lower the value of α, the lower the material losses and the higher the Q-factor. It also be noted that the Q-factor is also dependent on the width of the curve, the larger the value of Δf (where $\Delta f = f_2 - f_1$), lower its value. The quality factor differs from material to material, relatively

light alloys such as aluminium, magnesium and titanium exhibit lower losses than 'heavier' ones such as lead tine and tungsten.

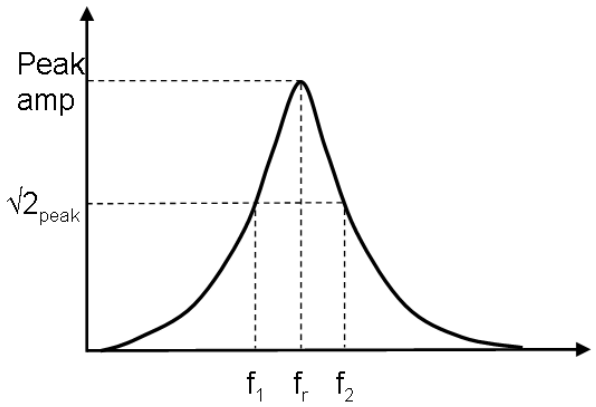

Figure 3.6: Calculation of Q factor

Dynamic stress limit

Under operational conditions ultrasonic components experience cyclical tensile stresses. These are dependent on tool shape, vibration amplitude and material properties (such as Young's modulus), however, to ensure an acceptable factor of safety in ultrasonic tools, the ultimate tensile strength of the material should be 30% higher than the maximum stress experienced within the tool during operation [62]. Materials, with working limits tested at around 23kHz at 23°C, often used in the manufacture of ultrasonic components can be seen in Table 3.1. The value of limiting strain is the threshold above which acoustic attenuation rapidly increases due to changes within the material which also prompts the onset of fatigue failure. Values of the limiting strain and maximum stress without failure are given for room temperature, and as reported in literature these values are not independent of temperature as an increase in temperature of even 20°C will see a large decrease in these values [172,174,193].

Material	Limiting strain	Maximum stress without risk of failure
Ti6%Al4%V	2.2×10^{-3}	200MPa
Duraluminium	2.4×10^{-4}	30MPa

Table 3.1: Maximum strain and safe working limits of materials commonly used in ultrasonic tool manufacture (samples tested at approximately 23kHz and 23°C) [174]

Material inertness and resistance to wear

To ensure resonating tools used in ultrasonic applications experience a prolonged lifespan, the materials which they are manufactured from should be resistant to wear and corrosion

while being chemically inert while exposed to operational conditions. Tools used in ultrasonic machining, drilling and cutting experience material wear and corrosion due to interactions at the surface between the workpiece and the tool. It has been reported that wear is dependent on several factors; the ultrasonic process, previous tool wear, and material of manufacture (both tool and workpiece) [194]. Ultimately, tool wear causes reduction in tool length which can alter the its tuned characteristics sufficiently enough to detune the ultrasonic device, reducing its vibratory performance and possible tool failure.

Materials that display physical properties which are desirable for low wear generally exhibit high fracture toughness as well as high hardness, however, materials which exhibit high levels of hardness, but are also brittle, will generally not possess a high resistance to wear [195]. Meanwhile, horns which operate submerged or exposed to a fluid, either in liquid or gaseous states, especially if the fluid is at elevated pressure, temperature or both and has either a particularly high or low pH number, should be machined from materials which lie close to the top of the cathodic side of the galvanic series. Although specific environmental conditions will slightly alter the order of the galvanic series, it is generally accepted that titanium alloys and to a lesser extent, stainless steel alloys (containing molybdenum) are generally least susceptible to corrosion, whilst aluminium alloys generally are highly susceptible to corrosion.

Material	Yield Strength (MPa)	Ultimate Tensile Strength (MPa)	Hardness (Brinell)	Fracture Toughness ($MPam^{\frac{1}{2}}$)
Ti6%Al4%V	830	960	334	55-75
Duraluminium	190-470	190-500	115-135	26-44
316 Stainless steel	210-240	460-860	160-190	16-19
Tungsten Alloys[1]	723.9	896.3	287-333	7-19

Table 3.2: Material properties relating to toughness: Given at approximately 23°C (values may alter under different treatment processes) [196–199]

Piezoelectric element

The active parts, which convert electrical energy in to mechanical motion, of the Langevin transducer are piezoelectric elements. Initially single crystals such as quartz or Rochelle salt were utilised in the generation of ultrasonics, however the advent of piezoceramics such as barium titanate, $BaTiO_3$, then latterly lead zirconate titanate, PZT, signalled a significant increase in development of piezoelectric materials. Desirable characteristics of any piezoceramic are chemical stability and strength, however, further requirements will fundamentally depend upon the specific application of the transducer as well as the environmental conditions which the piezoceramic will operate in. Typical piezoceramics, applications and general characteristics can be seen in Table 3.3 whilst archetypal properties

[1] Tungsten Class I: 89-91%W

of common piezoceramics are presented in Table 3.4.

Lead zirconate titanates, PZT, are heavily utilised in ultrasonic transducers due to their strong piezoelectric effect and high Curie points. However, as Tables 3.3 and 3.4 demonstrate, a slight difference in chemical composition of titanium and zirconium as well as minor additions of dopants can strongly influence the properties of PZT to such a level that PZT-4 and PZT-8 possess widely different characteristics from PZT-5. Power ultrasonic devices, due to their driving conditions of high electrical field and high strain as well as low losses, will almost certainly require properties which hard piezoceramics, such as PZT-4 and PZT-8 and their variants, possess.

Material	Physical characteristics	Applications
PZT-4	A hard piezoceramic with high resistance to depolarization, high coupling, high permittivity & low dielectric losses under high electric drive.	High power / high radiating transducers uses, e.g. Power ultrasonic transducers & sonar.
PZT-5A	A soft piezoceramic with high resistivity at elevated temperatures, high sensitivity, and high time stability	NDT, hydrophones & medical diagnostics.
PZT-8	A hard piezoceramic similar to PZT-4, but has lower dielectric and mechanical losses under high electric drive. It is suited for applications requiring higher power handling capability than is capable with PZT-4.	High power / high radiating transducers uses, e.g. Power ultrasonic transducers.
$Pb(NBO_3)_2$	Although pure $Pb(NBO_3)_2$ is extremely fragile, $Pb(NBO_3)_2$ based ceramics possess a high Curie temperature, high spontaneous polarization and high longitudinal coupling factors as well as low permittivity and mechanical Q factor.	Arrays for NDT & medical diagnostics.
Barium titanate	Low Curie temperature.	Ultrasonic transducers (measurement) & microphones.
PMNT-28	Single crystal with increased coupling, displacement and improved bandwidth, sensitivity and source level as well as higher resistance to applied strain than conventional PZTs.	Diagnostic medical applications & actuators.
PVDF	Piezoelectric polymer/copolymer group with high sensitivity (up to x10 over PZT-5H) and as well as possessing good dimensional stability, chemical inertness and closely matches water acoustically. Low Curie temperature.	Diagnostic medical applications, hydrophones, microphones, accelerometers & passive infrared sensors

Table 3.3: Characteristics and applications of typical piezoceramics [15, 188, 190, 200, 201]

Property	Symbol	Units	PZTs 4	PZTs 5A	PZTs 8	Niobate $Pb(NbO_3)_2$	Single crystal PMNT-28	Barium titanate	Polymer PVDF
Density	ρ	$\frac{kg}{m^3}$	7500-7800	1700-1875	7500-7800	6000	8100	5700	1780
Quality	Q_m		500-750	60-80	1000-1600	11	65	300	
factor	Q_e		250	50	250	100		100	
Elastic	s_{33}^D	$10^{-12}\frac{m^2}{N}$	7.76-7.9	9.46-15.0	8.0-10.8	21.8	10-14	7.1	
compliance	s_{33}^E		15.0-16.8	17.2-18.8	13.0-15.7	25.4		9.5	
	s_{11}^E		11.6-13.3	16.4-16.7	10.9-11.7			9.1	
Elastic	c_{33}^D	$10^{10}\frac{N}{m^2}$	12.6-15.9	5.3-14.7	11.8-12.4			17.1	
stiffness	c_{33}^E		6.6-11.5	10.6-11.1	7.4-16.1		25-30	14.6	
	c_{11}^E		5.7-13.9	6.1-12.1	8.7-13.7			15.0	
Coupling	k_{33}		0.68-0.71	0.67-0.72	0.64-0.71	0.38	0.85-0.88	0.50	
factors	k_{31}		0.33-0.35	0.34-0.37	0.29-0.31		0.42	-0.045	
	k_p		0.56-0.62	0.60-0.66	0.51-0.55	-0.07	0.86	-0.36	
Dielectric	$\varepsilon_{33}^T/\varepsilon_0$		1200-1470	1700-1875	975-1250	225		1700	
constants	$\varepsilon_{33}^s/\varepsilon_0$		635-1475	830	580	190		1260	
Piezoelectric	d_{33}	$\frac{pC}{N}$	285-350	374-460	225-280	85	1200-2000	190	-30 to -34
constants	d_{31}		-135 to -122	-195 to -171	-104 to -78	-9	-370	-78	6-22
	d_{15}		495-511	550-585	294-333			260	
Curie point		°C	300-330	360-370	300	570	125-140	115	75-110

Table 3.4: Values of selected properties piezoelectric materials [15, 22, 95, 188, 200, 201]

3.1.4 Assembly of ultrasonic devices

Power ultrasonic devices are typically constructed from more than one component and for ease of assembly and disassembly they are generally fastened together using threaded joints. As with assembling a transducer under pre-load, the torque with which the components are joined together is critical as incorrect tightness within the join can have a significant effect on the performance of the device.

Another factor which significantly influences device performance is whether two components joined in series are acoustically matched. Fundamentally, longitudinal acoustic waves travel through an anisotropic medium at a speed (Equation 3.3) which is directly dependent on its properties of stiffness and density. When the wave reaches a boundary between two media the wave will be both transmitted across it as well as reflected back into the medium from which it came. The closer the acoustical matching of media, the higher the transmission rate of the acoustic wave, which is desirable for efficient ultrasonic devices. The acoustical impedance, Z, of a medium can be found from the following expression where ρ and c are the density and speed of sound within the medium;

$$Z = \rho c \tag{3.20}$$

The amount of reflection or transmission of an acoustic wave at a boundary between two anisotropic media can be evaluated through reflection and transmission coefficients which are governed by an acoustic impedance parameter, $(\rho\nu)^{\frac{1}{2}}$, where ν is the phase velocity. The reflection coefficient, R, at a boundary between two media, I and II, can be attained through the following expression [14];

$$R = \frac{(\rho\nu)_{II} - (\rho\nu)_I}{(\rho\nu)_{II} + (\rho\nu)_I} \tag{3.21}$$

In the design of ultrasonic transducers, it is standard to manufacture the front and rear endmasses from materials of different densities. This encourages greater vibrational amplitude at the radiating face or output face of the transducer as well as improving acoustic matching to the load or the adjoined tuned component [15, 187]. To achieve maximum acoustic wave transmission between the piezoceramic stack and the front endmass (radiating endmass) the following expression should be satisfied to optimise endmass material selection;

$$Z_c = \sqrt{Z_f Z_b} \tag{3.22}$$

where Z_c, Z_f and Z_b are the acoustic impedances of the ceramic, front and back endmasses. Typical transducer configurations are assembled with relatively light alloys such as aluminium or titanium as a front endmass, whilst the rear endmass will usually be manufactured from heavier materials such as steel, brass or tungsten alloys. Therefore transducer configurations such as duraluminium-PZT-tungsten or titanium-PZT-steel are common. Applying material

properties from Table 3.5 to the expression $\sqrt{Z_f Z_b}$ gives the values of $31.82 \times 10^6 \text{kgm}^{-2}\text{s}^{-1}$ and $35.12 \times 10^6 \text{kgm}^{-2}\text{s}^{-1}$ for the transducer configurations duraluminium-PZT-tungsten and titanium-PZT-steel respectively. These are close to the value of acoustic impedance of PZT-4a, with a particular close match occurring between PZT-4a and the titanium-PZT-steel configuration. Furthermore, if multiple component assemblies are constructed, then each component connected in series should be as closely matched acoustically as possible to ensure maximum transmission between join boundaries and minimal loss.

Material	Density (kgm^{-3})	Young's Modulus (GPa)	Speed of sound (ms^{-1})	Acoustic Impedance ($\text{kgm}^{-2}\text{s}^{-1}$)
PZT-4a	7500-7800		4600	34.50×10^6
Ti6%Al4%V	4420	105-120	7135	31.54×10^6
Duraluminium	2700	73	5200	14.04×10^6
316 Stainless steel	7970	193	4920	39.21×10^6
Tungsten Alloys[2]	16850-17250	305	4229	72.11×10^6

Table 3.5: Acoustic values of materials used in tool manufacture: Given at approximately 23°C (values may alter under different treatment processes) [196–199]

3.1.5 Summary: Design of Ultrasonic devices

Criteria for the design and assembly of ultrasonic transducers, tools and ultrasonic systems containing multiple parts has been investigated. Correct material selection for transducer or horn/tool manufacture is critical to ensure optimal performance and acceptable lifespan of the ultrasonic device. However, financial and economic factors will influence the design process, with materials and design being ultimately selected on the merit of cost versus benefits which may be gained.

Material	Cost $\frac{£}{m}$
Grade 5 Titanium (Ti6%Al4%V)	225.00
Duraluminium[3]	40.00
316 Stainless steel	80.00

Table 3.6: Cost per metre (rod= $\phi 40mm$) of common alloys used in manufacture of ultrasonic components [202]

[2] Tungsten Class I: 89-91%W

[3] Aluminium of similar properties to duraluminium

3.2 Finite element analysis

Finite element analysis (FEA) uses a process of numerical analysis that breaks a system in to discrete parts (elements) in order to solve or simulate problems with the aim of obtaining approximate solutions or estimates. Each element possesses governing equations, equations that determine the solution for a system, while boundary conditions are applied to elements to simulate as best as possible real conditions. The vertex of each element is known as a 'node' and these construct a grid of points forming a mesh.

Although FEA was initially developed to obtain approximate solutions of vibrating systems before the advent of computers, the use of FEA in analysis, design and product refinement has developed in parallel with advances in computing power to an extent that present day FE codes can provide results of such accuracy and precision that the duration required for prototype testing can be diminished to testing a single prototype concept or process. Large organisations may develop specialised code for analysis of their specific problems, however commercial codes are readily available within the market place.

Even though FE analysis has greatly advanced during the last decades, limitations still exist when attempting to simulate the 'real world'. FE models often contain 'perfect' material properties or boundary conditions, while the system in reality will often contain flaws or imperfections to these. Therefore FE solutions are classified as approximations, although the level of inaccuracy within the approximation can be minimised by inputting properties or conditions that most simulate the real system.

The commercial multi-disciplinary code Abaqus v6.9-1 has been utilised to investigate linear dynamic behaviour of ultrasonic devices; simulating modal behaviour, stress analysis and vibrational amplitudes.

3.2.1 FE study: Mesh convergence of slender rod

The frequency of the 1st longitudinal mode of a slender bar was found through analytical methods (Equation 3.10) and through using the FE code Abaqus v6.9-1. The slender bar of dimensions; $\phi = 54$mm and $l = 108$mm, consisting of stainless steel 316 (properties can be found in Table 4.3), of which the 1st longitudinal mode was estimated at 22928Hz using Equation 3.10.

The structure of the slender bar was modelled in the FE software as a number of finite 'elements' which apply physical properties such as thickness, density or Young's modulus to the geometry of the bar and are interconnected through points or 'nodes'. Abaqus v6.9-1 offers three types of element; tetrahedral (C3D15), wedge (C3D10M) and hexahedral (C3D20R), with two different geometric orders, first or second order. First order elements, use linear interpolation to approximate the solution whilst second order elements, use quadratic interpolation. However when investigating modal behaviour of vibrating systems, quadratic elements should always be used to ensure real mode shapes are predicted. To predict modal

parameters, the geometry of the slender bar was assumed to be under free conditions and the Eigensolver used was the Lanczos algorithm.

Once a structure contains elements, the size and number of elements used can significantly influence the accuracy and solve time of the FE simulation. If too few elements are used, the run time will be relatively short, but inaccurate results will be produced, while too fine a mesh could result in a relatively long solve time. Often mesh density will differ across a structure; parts of interest will contain a finer mesh while areas of little interest will contain a courser mesh density. In order to assess if the number of elements contained in the mesh used to model the slender bar is high enough, mesh density with respect to resonant frequency convergence has been investigated.

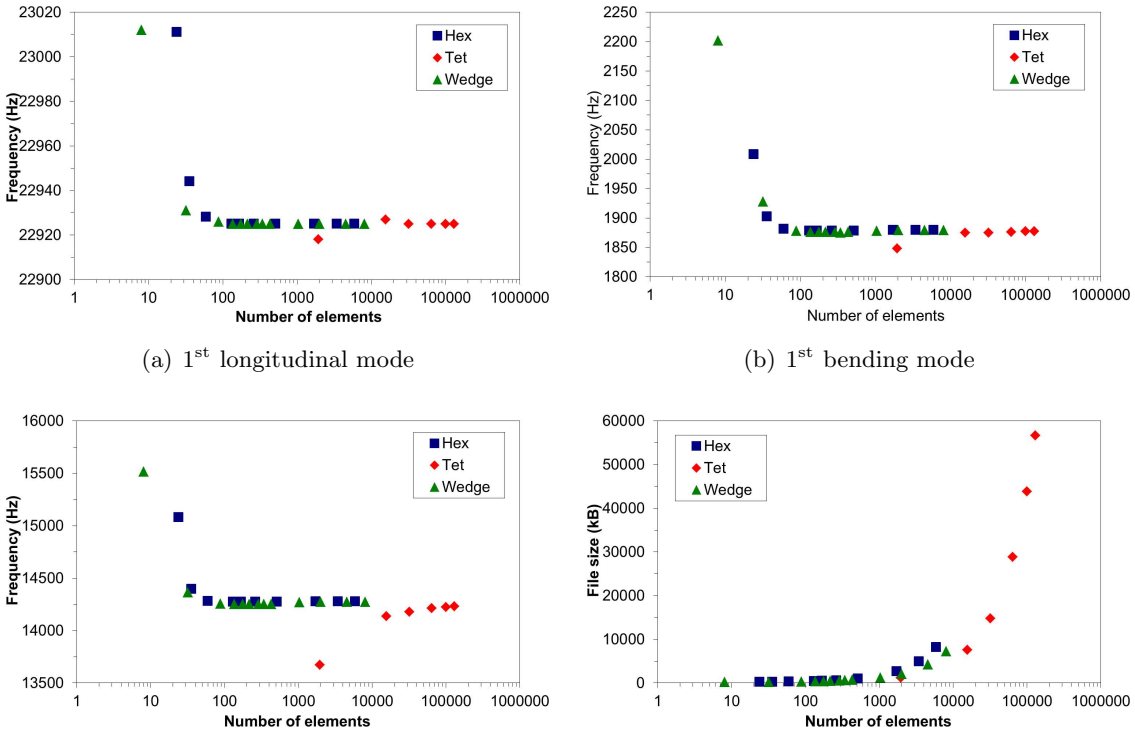

(a) 1st longitudinal mode

(b) 1st bending mode

(c) 1st torsional mode

(d) Output file size

Figure 3.7: Number and type of elements to achieve convergence of resonant frequencies of slender bar

To study the accuracy of each element type, each type was independently employed within the geometry of the slender rod. This culminated in all element types, although only once a suitable number of elements had been employed within the model, predicting a common frequency for the 1st longitudinal frequency at 22925Hz. When compared with the frequency of the longitudinal mode estimated through Equation 3.10, it can be recognised that good correlation was achieved with the FE model as a difference of 3Hz or percentage difference of 0.013% was attained. However, it can also be observed from Figure 3.7(a) that employing the tetrahedral element required a significantly higher number

of elements than wedge and hexahedral to derive the common prediction. To ensure an acceptable level of accuracy, models comprising of wedge and hexahedral elements required the bar to contain approximately 130 elements, corresponding to approximately 34 and 22 elements per wavelength axially respectively. However, the model using tetrahedral elements required approximately 32800 elements, corresponding to 240 elements per wavelength axially. Furthermore, it can be observed from Figure 3.7(d) that the greater the number of elements used in the geometry of the rod the larger the output file produced by the solver. To achieve an acceptable level of accuracy, output files containing geometry comprising of wedge and hexahedral elements were 349kB and 383kB whilst on the other hand the output file comprising of tetrahedral elements was 15044kB.

Figures 3.7(b) and 3.7(c) plot frequency convergence upon a common frequency for the 1^{st} bending and torsional modes. It can be observed that wedge and hexahedral elements will converge on a common frequency of the 1^{st} bending mode when the mesh contains approximately 130 elements, while the model containing tetrahedral elements required approximately 32800 elements. Meanwhile, the number of elements required to converge on a common frequency for the 1^{st} torsional mode depends upon the individual element. Using hexahedral elements required approximately 130 elements, which contained 4 elements across the diameter of the rod, while a structure containing wedge elements required approximately 2000 elements, although also containing 4 elements across the diameter of the bar. Meanwhile, geometry containing up to 101000 tetrahedral elements did not converge upon a common frequency for the 1^{st} torsional mode of vibration.

3.2.2 FE study: Mesh convergence of surgical transducer

To investigate whether the mesh density used to mesh components that construct an ultrasonic device, a half wavelength transducer designed by Mectron S.p.A and utilised in dentistry and bone surgery, a mesh convergence study was carried out for each component before modelling the assembled device.

Due to the complex geometry of the front and back mass, two different element types were incorporated during meshing, although the majority of the elements are hexahedral elements, to avoid misshaped or corrupt (hexahedral) elements at features such as fillets, bevels or rounded edges, wedge elements were utilised. From Figure 3.8 it can be seen that the number of elements required to achieve convergence upon the 1^{st} longitudinal mode of vibration was 7536, 3136, 5456 and 640 elements, corresponding with 106, 52, 188 and 8 elements per wavelength for the frontmass, backmass, bolt and ring, respectively.

Nevertheless, these components do not oscillate independently, but are assembled together to form a ultrasonic transducer. To investigate the influence that mesh density has the tuned (longitudinal) frequency and surrounding resonant frequencies, a mesh convergence study was completed for the assembled transducer. Figure 3.9(a) illustrates the transducer geometry

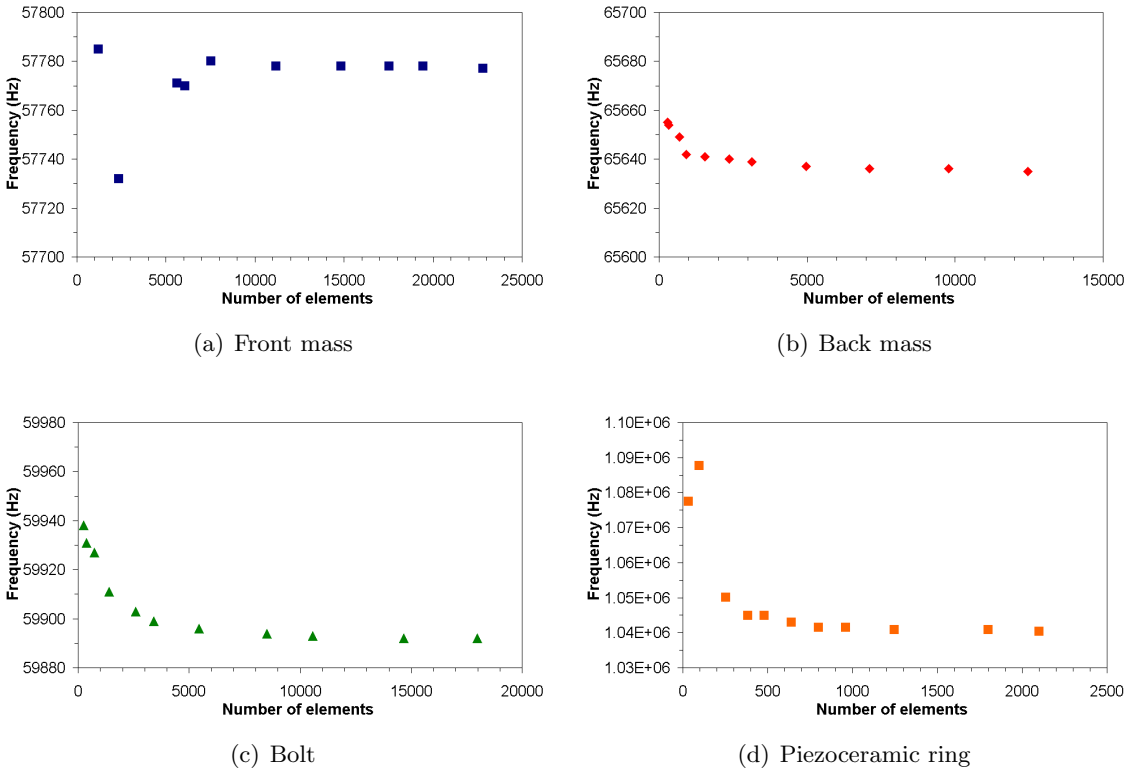

(a) Front mass

(b) Back mass

(c) Bolt

(d) Piezoceramic ring

Figure 3.8: Number of elements required to achieve convergence upon the frequency of the 1st longitudinal mode of vibration

containing three different mesh densities; (i) contains 832 elements, while (ii) and (iii) contain 10946 and 35880 elements. Figures 3.9(c) to 3.9(d) illustrate the number of elements used to construct the geometry of the transducer and their convergence upon frequencies of the 1st longitudinal mode of vibration and two neighbouring modes of vibration, the 3rd torsional and 5th bending modes. To achieve convergence upon a common frequency, the 1st longitudinal mode required the least number of elements, while the 5th bending mode required the most.

Therefore to achieve convergence upon the 1st longitudinal mode, the 3rd torsional and 5th bending mode of vibration, the model should contain approximately 10000 elements, corresponding to approximately 194 elements per wavelength. If the number of elements required for each individual component to converge upon their respective 1st longitudinal frequencies is summed, the number of elements is approximately 18688. This suggests that a coarser mesh could be used in each transducer component when incorporated in to an assembly rather than when each part is investigated individually.

Figures 3.9(b) to 3.9(d) illustrate that a finer mesh density is required to accurately predict higher order modes than lower order modes (partly due to increased nodal points), while it could also be observed that lower order longitudinal modes neighbour other higher order (bending or torsional) modes. Therefore, to safeguard from phenomena such as modal coupling, it is important that the finite element mesh should be dense enough to predict

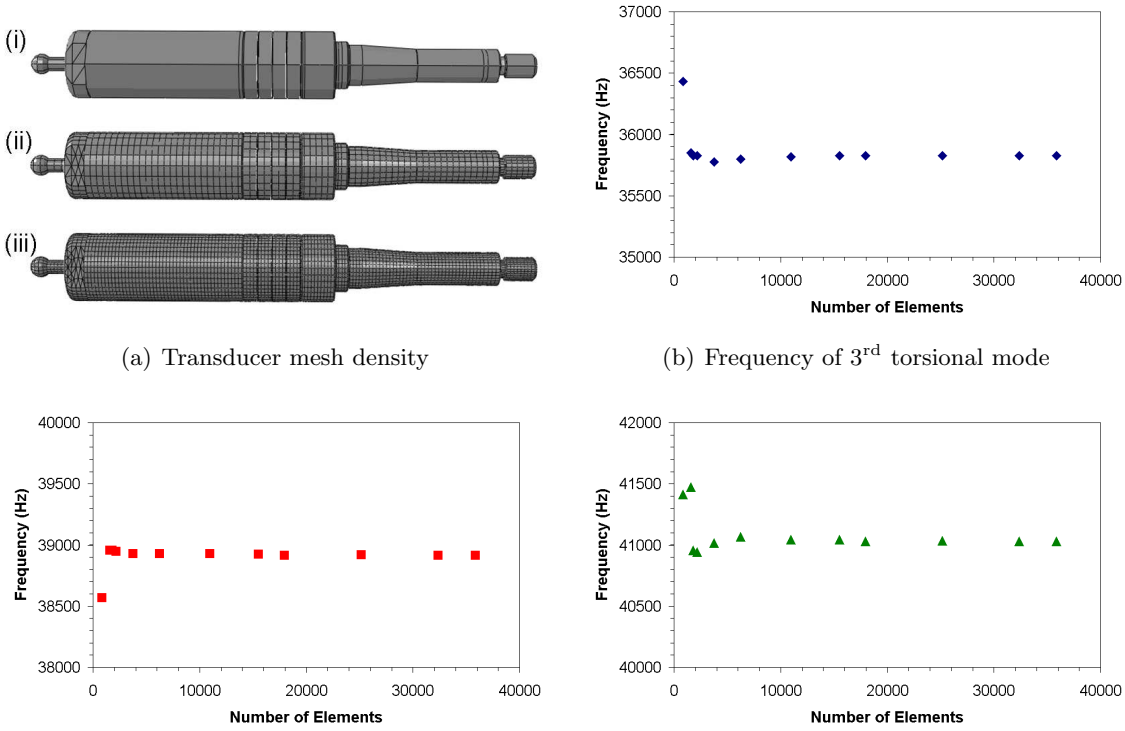

(a) Transducer mesh density

(b) Frequency of 3rd torsional mode

(c) Frequency of 1st longitudinal mode

(d) Frequency of 5th bending mode

Figure 3.9: Mesh design and convergence of surgical transducer

accurately both the tuned mode of vibration and higher other order modes which may lie within close proximity of the tuned mode.

3.2.3 FE analysis: Piezoceramic ring

Assuming lossless conditions and neglecting coupling with width vibrations, Equation 3.23 can be used to estimate the thickness mode of a single piezoceramic ring at 1.056MHz where; f_t is the frequency of the thickness mode, t is the thickness of the piezoceramic ring, and c_{33} is the elastic constant in the thickness direction, [41, 203].

$$f_t = \frac{1}{2t}\sqrt{\frac{c_{33}}{\rho}} \tag{3.23}$$

Again the commercial FE code Abaqus v6.9-1 was used to model the PZT ring and to extract modal parameters. The ring was assumed to contain free boundary conditions and was constructed from 20 node quadratic elements (C3D20R); the Eigensolver used was the Lanczos algorithm. The thickness mode was predicted at 1.067MHz (Figure 3.10(a)) through FEA, giving a percentage difference between the approximation calculated using Equation 3.23 and the FE model of 1.01%, although this value is strongly dependent on the values selected from the range of possible values of c_{33} and ρ. To further study the characteristics of the ring, a potential difference of $0.5V_{peak}$ was applied across the faces of the piezoceramic

ring through boundary conditions in the FE model to simulate the inverse piezoelectric effect. The steady-state dynamic step ultimately performs a frequency sweep between frequencies of interest, providing a steady state harmonic excitation at each frequency step. During this step the piezoceramic ring was constructed from a 20 node quadratic piezoelectric element (C3D20RE) and excited between 1-1.14MHz, Figure 3.10(b).

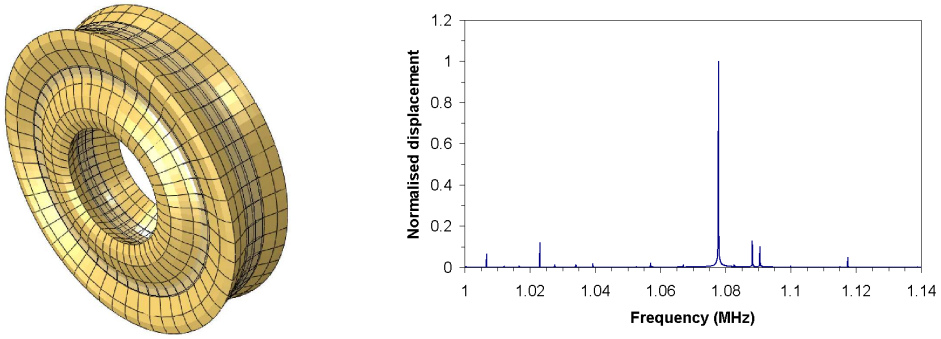

(a) Thickness mode: 1.067MHz (b) Frequency spectrum

Figure 3.10: Thickness mode of PZT ring found through FEA

3.2.4 Summary: Finite element analysis

Good correlation was seen to exist between the 1st longitudinal and thickness modes of a slender bar and piezoceramic ring estimated through analytical methods and predicted through finite element analysis. Three different models, using three different types of element, were used to model the slender bar with all predicting a common longitudinal frequency. However, to reach the common frequency many more tetrahedral elements were required than either wedge or hexahedral elements, meaning that to achieve a common frequency the output files of the models containing the tetrahedral elements are larger, thus increasing solve time. Again, the model containing the tetrahedral elements required many more elements to converge upon a common frequency for the 1st bending mode than hexahedral or wedge elements. Furthermore, when predicting the 1st longitudinal mode, within the range of testing, the model containing tetrahedral elements ultimately did not converge upon a frequency at all. Hence, it should be advised that to minimise output file size and solve time, whilst also accurately predicting resonant frequencies, wedge and hexahedral elements should be used in preference to tetrahedral. Meanwhile, when assessing mesh density of ultrasonic devices, it was observed that 'meshing' (the process of mesh generation) should be completed and assessed once the device has been assembled rather than investigating individual components. This is due to the findings in Section 3.2.2 that found convergence upon the tuned frequency (1st longitudinal) of an ultrasonic transducer required less elements than if the number of element required to achieve convergence upon the 1st longitudinal for each individual component were summed. Finally, when considering mesh density for the

assembled transducer, the mesh should be fine enough to predict modes of higher orders which neighbour the tuned frequency, thus reducing the likelihood of unwanted phenomena such as modal coupling.

3.3 Experimental Modal Analysis

Experimental Modal Analysis (EMA) is a powerful experimental process which accurately estimates modal parameters of vibrating structures. Also called resonance testing or mechanical impedance methods, experimental modal analysis is often performed for a number of reasons, from troubleshooting and vibration avoidance to validation and revising finite element models as well as being utilised in nondestructive evaluations of possible new design modifications. During the design process it can be difficult to predict properties such as damping of a structure or component through theoretical or finite element models due to features such as complex geometry, boundary conditions or loading conditions. However, once modal properties have been found experimentally, it is possible to then incorporate it into the model. A general flow chart as seen in Figure 3.11 utilises the method of revising simulations or FE modes once initial experiments have been completed.

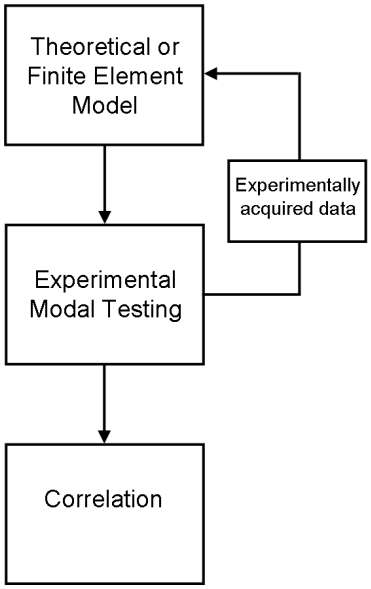

Figure 3.11: Revision of FE models with experimentally acquired properties

Although a great deal of modal testing is used to improve computer models and simulations, the principles behind experimental modal testing are decades old. The need for modal testing grew from the need to understand vibrational behaviour of aircraft structure, specifically predicting the occurrence of wing flutter. Wing flutter is a form of dynamic aeroelasticity, a phenomenon that couples aerodynamic forces with a structure's natural mode of vibration. The result is often the production of rapid periodic motions which lead to poor performance and ultimately part failure. Aeroelastic flutter is not exclusive to aircraft

structures as the well documented collapse of the Tacoma Narrows bridge in 1940, Tacoma WA, USA, demonstrates.

The first recorded incident of wing flutter occurred in 1916 in a twin engine biplane. Early attempts to control the phenomenon involved changes to the mass and stiffness properties of wing components, it was not until the mid 1930s that the first in-flight flutter experiment was devised by B. Von Schlippe at the aero manufacturer Junkers. The experiment involved studying the amplitude of vibration during flight against aircraft's airspeed and although it was successful with many aircraft, the experiment was relatively primitive and far from flawless [204].

An important achievement in modal testing was reported in 1947 by Kennedy and Pancu [205]. Kennedy and Pancu proposed a purely theoretical method for accurately determining the natural frequencies and damping of a vibrating structure. This method was still being used almost twenty years later when Bishop and Gladwell [206] discussed the state of the art methods and approaches of modal analysis of the time. Their conclusion stressed that more experimental work had to be carried out as the problem of calculating damping was not fully understood, but that the Kennedy and Pancu method was still the best method at the time to use to calculate modal parameters.

However, the advent of microelectronics in the 1970s heralded the establishment of modern techniques of experimental modal analysis through the development of measurement transducers and digital analysers [207]. These technological developments gave engineers and scientists the ability to test with more accuracy as well as being able to test applications of increased complexity, and thus led to a considerable increase in published literature relating to the theory and practice of modal testing since the 1970s.

3.3.1 Theoretical approach to vibration analysis

The theoretical approach to experimental modal analysis as described by Ewins [208] states that there are three main components, Figure 3.12.

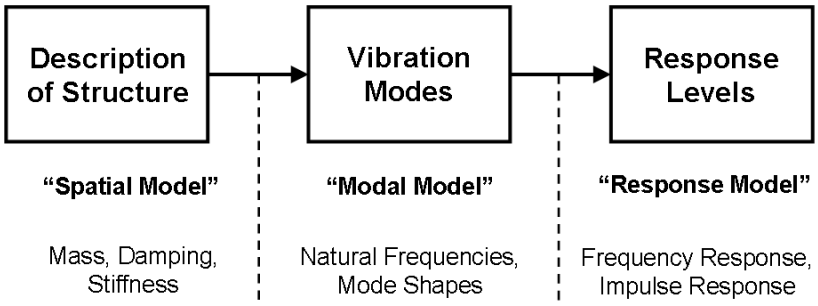

Figure 3.12: Theoretical route to vibration analysis [208]

The process begins with the Spatial Model, which describes the physical properties of the structure, such as its mass, stiffness and damping. The natural frequencies, modal damping

and mode shapes (under free vibration) are generally extracted in the next section which is described as the Modal Model while the final section in the process is referred as the Response Model and analyses how the vibrating structure will respond under external excitation conditions. Response amplitudes and frequency response functions defining the structures motions under specific excitations are calculated at this stage.

Single degree of freedom systems

In an attempt to understand how a structure vibrates, it is imperative to understand how the most basic of structures vibrates. A single degree of freedom (SDoF) system may not realistically represent any actual vibrating structures, but it is possible to build upon a SDoF system through linear superposition to generate a more complex multiple degree of freedom (MDoF) system. The basic model and equation of motion are given by Figure 3.13 and Equation 3.24 where; $m\ddot{x}$ is the inertial force of the structure, $c\dot{x}$ is the damping force of the structure and kx is the stiffness of the structure, while $f(t)$ and $x(t)$ are general time-varying force and displacement response quantities of the structure [181, 208, 209].

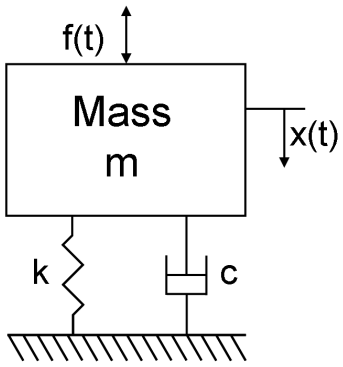

Figure 3.13: Single degree of freedom system

$$m\ddot{x} + c\dot{x} + kx = f(t) \tag{3.24}$$

Under free vibration, $f(t) = 0$, the Spatial Model is used to describe conditions, as no force is applied to the structure, Equation 3.25;

$$m\ddot{x} + c\dot{x} + kx = 0 \tag{3.25}$$

Giving the general trial solution as;

$$x(t) = X(t)e^{st} \tag{3.26}$$

where s is complex ($j\omega$). For a solution to exist, Equation 3.27, must be satisfied.

$$ms^2 + cs + k = 0 \tag{3.27}$$

Initial steps to solving Equation 3.27 gives;

$$\begin{aligned} s_{1,2} &= -\frac{c}{2m}\psi\frac{\sqrt{c^2-4km}}{2m} \\ &= -\overline{\omega_0}\zeta \pm \overline{\omega_0}\sqrt{1-\zeta^2} \end{aligned} \tag{3.28}$$

where;

$$\overline{\omega_0}^2 = \frac{k}{m} \tag{3.29}$$

$$\zeta = \frac{c}{c_0} = \frac{c}{2\sqrt{km}} \tag{3.30}$$

The solution for the modal model is therefore given by;

$$\begin{aligned} x(t) &= Xe^{-\overline{\omega_0}\zeta t}e^{i(\overline{\omega_0}\sqrt{1-\zeta^2})t} \\ &= Xe^{-at}e^{i\acute{\omega_0}t} \end{aligned} \tag{3.31}$$

As the solution is complex it is made from the imaginary part which is the frequency of oscillation, $\acute{\omega_0} = \overline{\omega_0}\sqrt{1-\zeta^2}$, and the real part which is the decay of the amplitude of the oscillation, caused by a damping rate, $a = \zeta\overline{\omega_0}$. Finally, to find the Response Model a forced response term ($f(t) = Fe^{i\omega t}$) must be introduced allowing the assumption that $x(t) = Xe^{(i\omega t)}$ and gives the equation of motion;

$$(-\omega^2 m + i\omega c + k)Xe^{i\omega t} = Fe^{i\omega t} \tag{3.32}$$

By reorganising Equation 3.32 the receptance frequency response function can be found;

$$H(\omega) = \alpha(\omega) = \frac{1}{(k-\omega^2 m) + i(\omega c)} \tag{3.33}$$

Types of FRFs

As mentioned above, the frequency response function was found using the ratio between response displacement, $X(t)$, and harmonic force, $F(t)$. However it is equally correct to calculate the frequency response function using the velocity, $V(t)$, or acceleration response, $A(t)$.

Receptance $\alpha(\omega) = \frac{X(t)}{F(t)}$

Mobility $Y(\omega) = \frac{V(t)}{F(t)}$

Inertance $A(\omega) = \frac{A(t)}{F(t)}$

It is also possible to define the frequency response function as the inverse to receptance, mobility and inertance, although in general notation it is common practice to state any standard Fourier response function as $H(\omega)$ and the inverse as $Z(\omega)$.

Dynamic Stiffness $\frac{F(t)}{X(t)}$

Mechanical Impedance $\frac{F(t)}{V(t)}$

Apparent Mass $\frac{F(t)}{A(t)}$

Repeated modes

Repeated modes, also commonly known as multiple modes, arise when more than one mode of vibration exists at a single frequency. They often exist in structures with a degree of symmetry and are especially prone in axisymmetric structures such as rods, beams or discs.

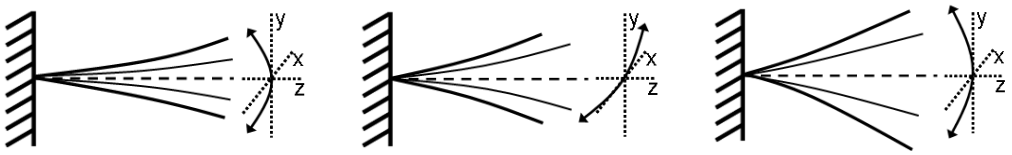

(a) Motion in Y-Z plane (b) Motion in X-Z plane (c) Motion in X-Y plane

Figure 3.14: Example of repeated modes [208]

Figure 3.14 demonstrates repeated modes in an axisymmetric cantilevered structure fixed at one end. The motion of the 1st bending mode of the bar can be seen in Figure 3.14(a) where the vibrational motion is solely within the Y-Z plane, however there is also the possibility that at the same frequency the mode could oscillate solely in the X-Z plane as seen in Figure 3.14(b). As there are multiple directions which the bar could oscillate in at the same frequency, a third vibrational solution exists where the bar vibrates in a combination of these directions, resulting in an oblique mode. Frequency analysis of a structure using finite element analysis will often find repeated or multiple modes although it is common that these are not exactly at the same frequency.

Complex modes

Complex modes are modes at which a point on a structure vibrates at an amplitude and phase unique to other points on the structure throughout the vibration cycle. This has the consequence that different points on a structure will neither reach their equilibrium position nor their extremes of motion simultaneously. Visually the mode shape appears as a traveling wave, with no stationary nodal points. This compares to a normal, sometimes called a real, mode shape which visually animated has defined nodal points and in which a standing wave can be recognised.

It is important to understand the origins of complex modes so that if one is found during modal testing it can be quickly established whether the mode is genuine, or if it is the result of poor measurements. The source of complex modes can vary; even though complex modes can appear in even the simplest of structures, their appearance is not trivial. Complex modes will only appear if the damping distribution of a structure is nonproportional. In practice this situation is widespread due to the nature of damping surrounding the joint of two components. A single component will generally experience proportional damping, usually called Rayleigh damping, however at the location of a joint interface between two components the damping will be concentrated and thus disproportionately distributed throughout the overall structure, although, this is not enough for complex modes to exist as other factors must be involved as well. One of these factors can be the closeness of two different modes, although there are 'conditions' that must be adhered to before this can become a factor. Generally for complex modes to exist, two modes should be separated by only a few hertz and the damping ratio must be 5 or more, however, if the damping ratio is below 5 then the modes will no longer be classified as close. Furthermore, the presence of repeated modes increases the possibility of the occurrence of complex modes.

3.3.2 EMA: Experimental considerations

Ultimately, vibration measurement can be broken into two experimental categories;

i Free vibration

ii Forced vibration

Free vibration is a technique which measures the response of the natural vibration of the structure without any applied excitation. This method is often used when studying extremely large structures such as bridges, or as the step before forced vibration measurements are used in a forced vibration analysis, and will yield the natural frequencies and damping factor of the structure.

On the other hand forced vibration is a technique which applies a motion (forcing function $f(t)$) to the structure of interest. The excitation can be applied to the structure through a number of different techniques ranging from a hammer to a electromagnetic shaker, while during modal testing of ultrasonic devices, the piezoelectric transducer is used to convert the excitation signal to a mechanical motion. The type of excitation applied will depend on the specific conditions of the experiment, however a list of excitation methods can be seen in Table 3.7. Modal parameters yielded through forced vibration include frequency response function (FRF), which is the ratio of amplitude response to force input, and from this the damping, natural frequencies and mode shapes can be extracted.

Generally, experimental equipment will comprise a signal generator, which feeds the excitation signal into a power amplifier before it is input to the exciter, which is used to

vibrate the test structure. To measure the force which is transmitted to the test structure, a force transducer can be used and an accelerometer or laser vibrometer used to measure the response of the test structure. The acquired signals are often amplified through conditioning amplifiers before being collected and analysed through data acquisition hardware interfaced to a PC. To visualise the vibrational response of a whole structure, multiple measurements are required to be recorded from a grid of points covering the surface or surfaces of the vibrating structure.

The density of the grid points should be sufficient to ensure that it is possible to identify every mode shape within the test range as if the design of the gird is too coarse, the possibility of identifying higher order mode shapes and locating all their nodal points reduces. Furthermore, other experimental parameters (ranging from boundary conditions, excitation of the structure and data collection) can also influence the precision and accuracy of resonant frequencies and mode shapes acquired through EMA, although these are further discussed in the following sections. A schematic diagram of the experimental modal analysis setup used throughout this document can be seen in Figure 3.18.

Repeatability and consistency of experimental results

For quality assurance and test validity it is important that several parts of the experiment are checked before each individual measurement is recorded throughout the duration of an EMA. This ensures that the highest possible quality of data is obtained from the equipment and methods used [208].

Signal quality The strength and clarity of the measurement signal is vital to ensure good data acquisition and minimise noise. Signal quality can be optimised through the proper selection of measurement equipment and by using it within the correct operational range.

Signal fidelity A valid measurement cannot be taken unless the measurement signal represents the actual motion of the structure. Although obvious, it is easy to assume that measurements imply one motion while actually representing another, for example, a 1D accelerometer or LDV measuring only the vertical component of a torsional or twisting motion, while the lateral components remain unmeasured.

Measurement repeatability This carried out to ensure that the same output reading is measured whilst under the same conditions. Causes of non-repeatable results can stem from inconsistences in test set-up of software and / or boundary conditions of the test piece.

Measurement reliability Reliability requires that identical measurements are taken under unaltered conditions. Factors which can produce non-reliable results range from

measurements taken from test equipment has not reached operating temperature or has been calibrated before use.

Measurement data consistency and reciprocity Measurements taken from one point of a vibrating structure should give consistent modal parameters, such as resonant frequencies and damping, with those found at a different point on the same structure. In an ideal system these parameters will match perfectly, however it is accepted that in a real system this may not be the case. If individual points on the structure are measured one at a time and sequentially, data found at each of these points can be inconsistent with the previous measurement. This more often than not stems from; properties of the structure changing throughout the measurement process (such as variations in temperature or the consequence of continually being vibrated) or changes in test setup conditions (such as changes in local mass or stiffness). Therefore, in an attempt to reduce the influence of these factors it is suggested that once an EMA has been started, it should be completed in one attempt.

3.3.3 Boundary conditions

Possibly the most fundamental decision made during planning an experimental modal analysis is how to prepare the boundary conditions of the test structure. Poor decisions at this stage will significantly affect the outcome of the experiment, potentially causing poor experimental results. Initial boundary condition choices are either 'free' or 'grounded'. A structure under free boundary conditions is in an ideal state, as it is not fixed at any point to ground and is theoretically 'floating' in space. On the other hand grounded conditions state that the structure is connected to a fixed point in space. In reality, when planning boundary conditions, compromises are likely to be necessary however a number of options are available for a test piece.

Unrestrained supports Under real experimental situations true 'free' conditions are not achievable, although by suspending or supporting structures by soft springs (such as elastic or sponge) it is possible to imitate, as closely as possible, free conditions. To reduce the effect of the supports the structure should always be held at normal to the direction of motion and if suspended, points of support should be located as close as possible to the node points.

Grounded supports If grounded, the structure under measurement will be rigidly fastened to base which will not vibrate. This experimental condition can either be used for structures which cannot be suspended (large power station components or large civil engineering structures) or those that operational conditions will be more closely represented, such as turbine blades from aero engines.

Supported insitu The substructure or component is connected to another part or to the global structure and the attachment is not rigid.

3.3.4 Excitation of structure

The signals which can be used to excite a structure during modal testing are numerous and can differ considerably. Table 3.7 presents three main types, with different variations of each. The requirements of the individual test will inform which method of excitation is used.

Periodic	**Transient**	**Random**
Stepped Sine	Burst Sine	True Random
Slow Sine Sweep	Burst Random	White Noise
Periodic	Chirp (Rapid Sine Sweep)	Narrow Band Random
Pseudo Random	Impulse	
Periodic Random		

Table 3.7: Types of Excitation Signals

The signals commonly used to excite ultrasonic devices during modal testing are swept sine and true random. The calculation of modal parameters using a swept sine wave was discussed in Section 3.3.1, however the calculation of modal parameters when the excitation signal is a random signal requires a different approach. The response of a structure under periodic steady-state vibration can be identically related to the excitation signal at the same period, Equation 3.33, however, the response structure under random excitation can not be entirely related to the excitation signal for the same period. Therefore to calculate the spectral densities of a random signal the signal analyser must estimate them.

$$S_{xx}(\omega) = |H(\omega)|^2 . S_{ff}(\omega) \tag{3.34}$$

$$S_{fx}(\omega) = H(\omega) . S_{ff}(\omega) \tag{3.35}$$

$$S_{xx}(\omega) = H(\omega) . S_{xf}(\omega) \tag{3.36}$$

Equations 3.34, 3.35 and 3.36 relate the spectral density properties of the excitation and response amplitude of a structure under random vibration. $S_{xx}(\omega)$ and $S_{ff}(\omega)$ are the autospectra of the response and excitation signals while $S_{fx}(\omega)$ is the cross spectrum of the two, and $H(\omega)$ is the frequency response function linking the response and excitation quantities x, and f. To calculate an estimate of the frequency response function Equation 3.35 can be reorganised to the following:

$$H_1(\omega) = \frac{S_{fx}(\omega)}{S_{ff}(\omega)} \tag{3.37}$$

As the parameters cannot be measured exactly over a finite length of time, it is necessary to validate $H_1(\omega)$ using a second estimate, $H_2(\omega)$, which is found by reorganising Equation

3.34.

$$H_2(\omega) = \frac{S_{xx}(\omega)}{S_{xf}(\omega)} \tag{3.38}$$

In theory $H_1(\omega)$ and $H_2(\omega)$ should be equal, however in reality, as they are calculated from different quantities and therefore will produce different results. To visualise the consistency between $H_1(\omega)$ and $H_2(\omega)$, the coherence function, γ^2, is introduced, Equation 3.39.

$$\gamma^2 = \frac{H_1(\omega)}{H_2(\omega)} \tag{3.39}$$

If $H_1(\omega)$ and $H_2(\omega)$ match then coherence will equal 1 otherwise it will be between zero and 1. Reasons for this can vary; imperfect measurements, noise and poor experimental boundary conditions, but as the vibrating structure approaches resonance and antiresonance it is also possible that the forcing function, $S_{ff}(\omega)$, and the response signal, $S_{xx}(\omega)$, will also be between zero and 1. Although it should be noted that poor coherence does not automatically mean poor FRF estimates, but may imply that more signal averaging is required (Section 3.3.6). Finally, poor coherence will occur if the structure exhibits nonlinear behaviour [208, 210].

3.3.5 Collection of Data

There are various methods of measuring amplitude responses of vibrating structures, categorising them into two main groups, contact and non-contact. Traditional contact vibration measurement instruments include force transducers, accelerometers and impedance heads, whilst non-contact methods include laser Doppler vibrometers, techniques using ultrahigh speed cameras and speckle interferometry.

Piezoelectric measurement transducers

Measurement transducers in their simplest form contain a piezoelectric element, such as quartz, sandwiched between two springs. Once the transducer is subjected to vibration, stress is applied to the piezoelectric element and the resultant strain within the element generates an electric charge through the direct piezoelectric effect. To quantify measurements, strain within the element is proportional to the amplitude of vibration and therefore after calibration, the generated charge is proportional to a known amplitude of vibration.

Force Transducer Also commonly known as a load cell, they are the simplest form of piezoelectric transducer. As the force transducer experiences an applied load the force applied across the piezoelectric material will generate a charge which is proportional to the force.

Accelerometer These are slightly more complex than force transducers as within the accelerometer a seismic mass is used to apply stress to the piezoelectric material. If the seismic mass moves exactly in phase with the vibrating structure the output of the accelerometer will be proportional to its acceleration.

Impedance Heads These are a combination of both force transducers and accelerometers located within the same casing. This gives the ability to measure both force and acceleration at the same point and therefore find the mechanical impedance of the measured structure.

During vibration measurements care should be taken to ensure that location of the piezoelectric transducers ensures that all natural frequencies are located in the experimental range. Finally, it is also important that the mass of the transducer or method of attachment does not change the modal parameters of the structure under test.

Optical methods

Optical methods are non-contact, hence hold a key advantage over contact methods of measurement in that they are non-invasive and do not change any properties of the vibrating structure. This is crucial when measuring the vibration behaviour of slender ultrasonic devices such as those discussed in later sections. Unlike the vibration measurement of large and heavy structures such as ones found in power stations or bridges, the attachment of even the smallest of accelerometer will alter the dynamics of the ultrasonic device and consequently give inaccurate results.

Laser Doppler vibrometers

There are two key principles to laser Doppler vibrometers (LDV), the Doppler effect, named after the Austrian physicist Christian Doppler, and interferometry. The LDV usually generates the laser beam through a helium neon laser, Figure 3.15, splitting the beam creating a reference and a measurement beam. The measurement beam is directed towards a vibrating surface where it is reflected back, collected and merged with the reference beam. The resultant intensity is not solely the addition of the two beams, but is modulated according to Equation 3.40, where I_1 and I_2 are light intensities from the respective beams, while r_1 and r_2 are the path lengths of the light (r_2 is the path of the reference beam and therefore should remain constant) [211].

$$I_{TOT} = I_1 + I_2 + 2\sqrt{I_1 I_2 \frac{\cos 2\pi (r_1 - r_2)}{\lambda}} \tag{3.40}$$

The combined measurement and reference beams, possess different wavelengths due to the Doppler effect, are directed into the detector where they will generate a dark and

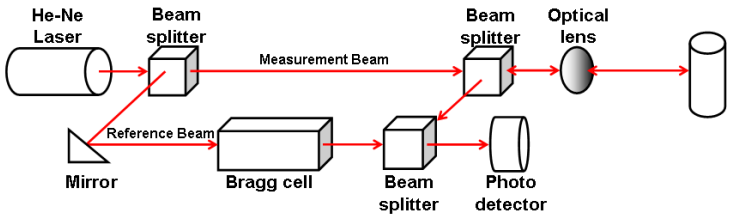

Figure 3.15: Simplified schematic diagram of LDV [211]

bright (fringe) pattern on the interferometer. One dark / bright cycle represents a target displacement of one half of the wavelength of light used in the LDV and, as the pattern changes with the modulation of the measurement frequency, the change in the interferometer pattern is therefore directly proportional to the velocity of vibration of the target. The interference pattern generated by the vibrating target is the same whether it is flexing away or towards the LDV. To be able to determine the direction in which the target is vibrating, a Bragg cell is incorporated in to the setup. The Bragg cell shifts the frequency of the reference beam so that even when the target is at rest there is modulation of the fringe pattern. By moving the target towards the LDV, the fringe modulation is reduced while moving it away from the LDV increases the frequency of modulation. Various LDVs are available, however the majority incorporate at least one of following features;

1D LDV Measures the out of plane velocity response at a single point on a vibrating surface.

3D LDV Measures three mutually orthogonal components of the vibration response of a single point. This is achieved by using three independent beams, one which measures out of plane components and two in plane components, that converge to a focus on the vibrating surface.

Scanning LDVs Scanning vibrometers, either 1D or 3D, can be programmed to automatically measure a grid of points on a vibrating surface. This can be a useful time saver as once programmed the system will automatically move from one measurement point to the next.

Using a Laser Doppler Vibrometer

As with any scientific equipment, laser Doppler vibrometers only produce accurate results if the experiment is set up correctly and is properly thought through, otherwise there is a high probability that problems will arise and result in inaccurate readings. If measurements of multiple points are to be prepared, then a clear line of sight should be ensured from the LDV to each measurement point before the experiment is started, thus guaranteeing that the structure will not require to be moved, allowing constant boundary conditions to be assured. The surface of the structure should also be prepared to ensure that adequate light is reflected back to the interferometer. The structure should be clean, but not overly

polished as this can cause a scattering of the laser beam resulting in insufficient light returning to the interferometer. However if the metallic surface is thoroughly cleaned then lightly prepared with fine grade glass paper, the surface finish should allow sufficient reflection of the measurement beam.

3.3.6 Spectrum Analysers

Throughout data collection it is important that the experimental setup is optimised to ensure that measurements are recorded efficiently, correctly and with validity. Generally, a spectrum analyser is used to extract and display the frequency response function by collecting the (analogue) measurement signals, digitising them (in a A-D converter) and then displaying them on an inbuilt screen or monitor. The signal is recorded as a set of discrete values, N, spaced through a period of time, T, and is assumed to be periodic so that a finite Fourier transform is calculated. Features of the spectrum analyser can differ, such as the sampling rate and resolution of the frequency spectrum. For all experimental modal tests discussed in this thesis, the sample frequency of the spectrum analyser is 204.8kHz and the number of spectral lines used is 51200, giving a resolution over the frequency range of 0-80kHz of 1.56Hz.

As spectrum analysers only use a finite period to calculate the Fourier transform, problems can directly arise from coupling this with the assumption of periodicity. This is known as leakage and can indicate multiple frequencies when in reality there is only one. To reduce the undesirable effects related to spectral leaking, windowing is a solution. Windowing imposes a prescribed profile onto the time domain signal prior to the Fourier transform calculation [207].

Windowing

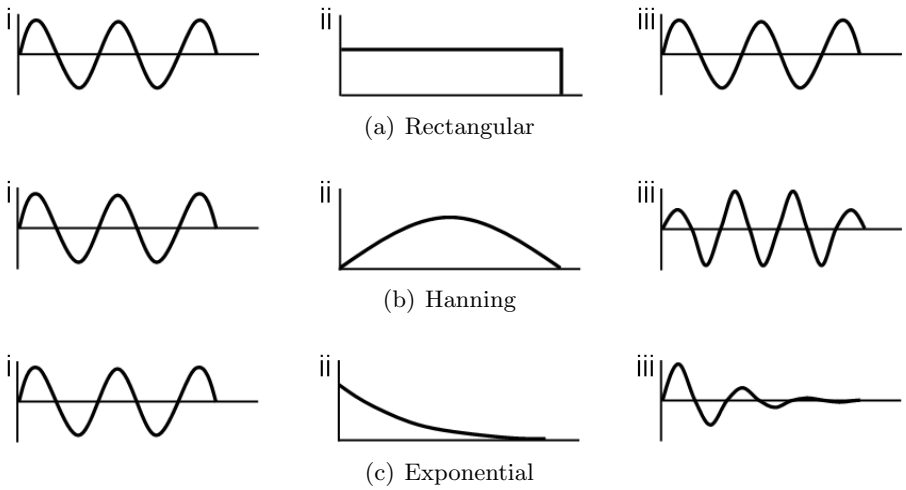

Figure 3.16: Different types of windowing - (i)Input time domain signal, (ii)Window, (iii)Output signal [181, 208]

Figure 3.16 depicts the effect that three different windowing techniques have on a time domain signal. The rectangular window, also known as the Dirichlet window, is the simplest form of windowing and is illustrated in Figure 3.16(a). This windowing technique does not modify the signal but 'gates' it, giving the impression that the signal is of finite length. Rectangular windows should only be used in tests where the signal is periodic, nearly periodic or where the signal will be an exact fit for the window length thus preventing the occurrence of any signal discontinuities. The Hanning window is commonly used for continuous signals such as steady state periodic or random, Figure 3.16(b). Hanning windows are part of the $cos^{\alpha}(X)$ family of windows and depend upon a parameter α, which is usually an integer. As α's value increases the smoothness of the window and trace also increases, hence reducing the number of 'sidebands' which may surround a response appearing in the frequency spectrum. The final window, depicted in Figure 3.16(c) is the exponential window. It is generally used in transient vibration applications, such as impulse tests, where the most significant data is concentrated in the initial section of the measurement. This prevents the suppression of the initial data which would occur if either the rectangular or Hanning windows were used.

Averaging

A requirement of processing signals, especially in the case of random excitation, is averaging. This is necessary for random signals as it is impossible to compute Fourier transforms directly from the signal, but instead they are found from estimates of the spectral densities and correlation functions which are used to characterise the system. In the averaging process a number of individual records will be compared and averaged according to the specific technique such as peak hold, exponential and linear. Averaging ensures that the results obtained are both statistically reliable and that random noise is removed from the signals.

Overlap Correlation

As discussed in Section 3.3.6, Fourier transforms are calculated using samples of discrete values spaced through periods of time. If the samples are recorded sequentially (rectangular window) parts of the sample, generally at the boundaries between two samples, will be ignored due to containing low values, providing the possibility that potentially important data could be left out of the analysis. To counter this it is possible to start sampling before the previous record has finished, thus avoiding any loss or discontinuity of data, Figure 3.17. This also has the benefit that, for the same number of records, the length of time needed to acquire the data is reduced compared to sequentially acquired records. However, the data does not have the same statistical properties as if the records where acquired sequentially as there is a possibility that data points from one record could appear in the following record.

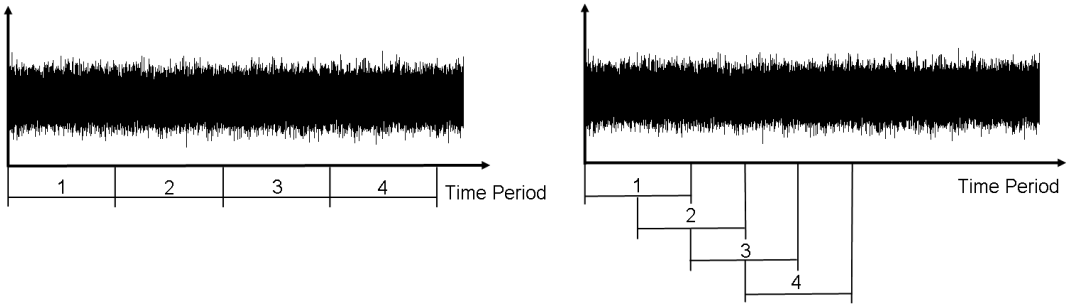

(a) Sequentially (b) Overlap

Figure 3.17: Forms of multi-sampling averaging [208]

Modal Extraction

Once experimental data has been collected, the next step in modal testing is to extract the modal parameters; natural frequencies, damping and residues (mode shape components) for each mode of vibration within the frequency range of interest. Each grid point will provide an individual frequency response function for each measurement direction. A device capable of measuring solely out of plane measurements, i.e. 1D LDV, will produce one FRF per point, while a 3D LDV which can measure both in and out of plane will produce three FRFs per point. Curve fitting of the FRFs is used to extract the modal parameters from the experimental data by forming a single theoretical FRF from the experimental data, [181,208,212]. The following steps give the order at which modal parameters can be extracted [212];

i Determine the number of modes within a small frequency range

ii Estimate the frequency and damping for the modes within the frequency range

iii Estimate the modal residues for the modes by use of frequency and damping estimates

iv Modal parameters are saved in a mode shape table

To ensure the optimal estimated result, each of the above steps require the selection of the best suited algorithm. A key consideration would initially depend upon whether the measurement system is SISO (single input single output) or MIMO (multiple input multiple output). Further considerations also depend upon individual experiments such as; the hardware used to record the vibrational response, the density of resonance frequencies and whether FRF data has slight variations in individual resonance frequencies or not. Due to the number of options open to the user during curve fitting, it may not always be obvious which method is best suited. It is therefore suggested that modal parameters are found using different curve fitting methods and that mode animations of the structure are compared to judge whether the optimal method has been used [181, 208, 212].

3.3.7 Experimental modal analysis: Experimental setup

The schematic of the equipment used during all experimental modal analyses discussed of ultrasonic devices in this thesis can be seen in Figure 3.18. The tuned devices were excited between 0 and 80 kHz using a random excitation signal created at low power by a function generator built into the data acquisition hardware that has a sample rate of 204.8kHz and 51200 spectral lines with resolution of 1.56Hz for measurements taken within the 0-80kHz range, Data Physics Quattro [210]. Due to the nature of the ultrasonic devices measured, random excitation was most suited and produced superior FRFs than a system excited through a swept sine signal. It is possible that this may be due to the slender geometry of the devices and their tendency for the frequency spectrum to contain a dense number of resonant frequencies. However, it has been observed that swept sine excitation may be useful for exciting bulkier structures where the frequency spectrum is often less dense and the resonant frequencies more widely separated.

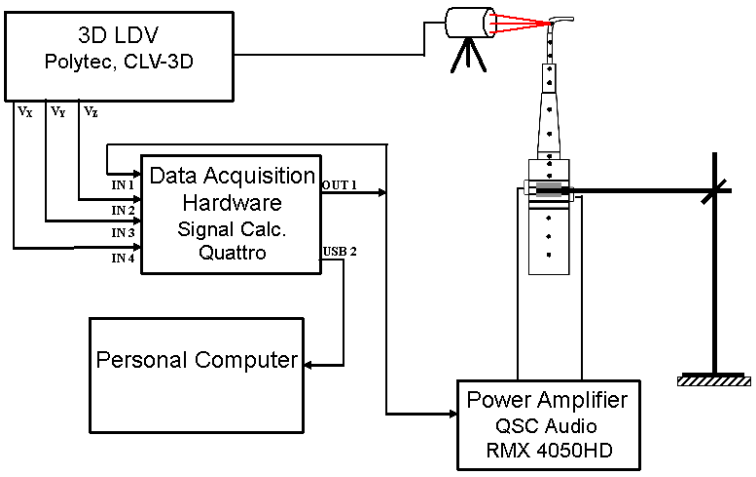

Figure 3.18: Schematic diagram of experimental modal analysis

The vibration velocities were measured over a grid of points on the ultrasonic device using a 3D laser Doppler vibrometer (Polytec, 3D CLV-3D). The detected frequency response functions were subsequently recorded on a standard desktop PC using Signal Calc ACE data acquisition software, Data Physics Corp. Collected data was imported to specialised modal extraction software ME'ScopeVES, Vibrant Technology Inc, where the curve fitting process was completed and mode shapes extracted.

3.4 FEA and EMA: comparison

3.4.1 Modal parameters

To ensure that the resonant frequencies and mode shapes predicted through finite element analysis are consistent with those found through experimental modal analysis, two half wavelength transducers were modelled through FEA and analysed through EMA. Transducer A, seen in Figure 3.19(a), consists of a piezoceramic stack sandwiched between two titanium endmasses of equal lengths, while Transducer B, Figure 3.19(b), also consists of a piezoceramic stack, approximately 8mm in length, between two titanium endmasses, although of different lengths (ratios of $\frac{1}{4}$ and $\frac{3}{4}$). The overall length of the transducers are approximately 87mm and 83mm, respectively. Both have a diameter of 10mm and were tuned to oscillate in the 1^{st} longitudinal mode at approximately 28.6kHz.

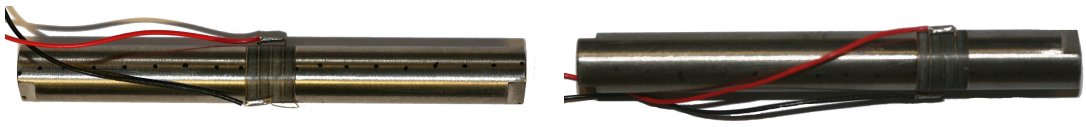

(a) Configuration A (b) Configuration B

Figure 3.19: Half wavelength sandwich transducer with titanium endmasses

To estimate the length of the endmasses in the transducers, Equations 3.11 and 3.12 were initially used. Figure 3.20 illustrates iterations made using Equations 3.11 and 3.12 until the endmass lengths gave an optimal impedance ratio with a solution of 1. The estimated lengths from the analytical method were incorporated in to FEA models of the transducers. The model, similar to the model which predicted the 1^{st} longitudinal of the uniform slender bar (Section 3.2), used quadratic hexahedral elements (C3D20R) as well as utilising the Lanczos Eigensolver algorithm between 10kHz and 85kHz.

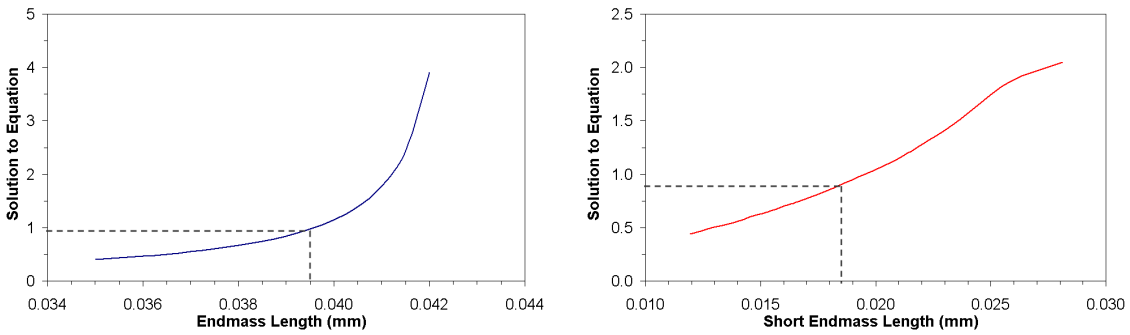

(a) Configuration A (b) Configuration B

Figure 3.20: Estimated endmass length with respect to acoustic impedance ratio

Meanwhile, experimental modal analysis (Section 3.3.7) was used to acquire the resonant frequencies and corresponding mode shapes of transducer configurations A and B. Figure

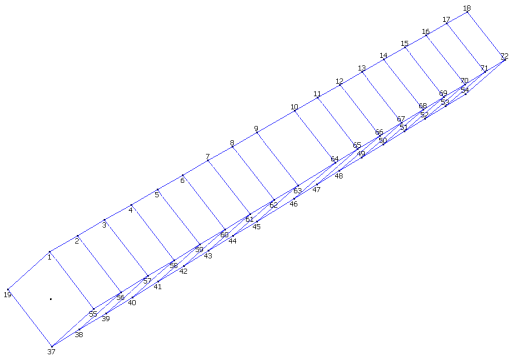

Figure 3.21: Undeformed 3D transducer geometry of transducer configuration A

3.21 illustrates the undeformed geometry of configuration A generated in the modal analysis software, ME'Scope, where a grid of 72 points was created along 4 paths of 18 equally spaced points positioned on the endmasses parallel to the axis of the transducer to match the locations of measured points. The 3D LDV measured the velocity response of configuration A at each of the 72 points and through the data acquisition software, Signal Calc ACE, produced 216 FRF files which corresponded with three different measurement axis; tangential, θ, radial direction, ϕ, and longitudinal direction, Z. This process was repeated for configuration B, where a grid of 68 points produced 204 FRF files. Figures 3.22(a) and 3.23(a) present all FRF traces from both transducer configurations on a single plot, however, these can be only be classified as 'raw data'. The curve fitted traces can be seen in Figures 3.22(b) and 3.23(b) and represent the modal response of each full structure.

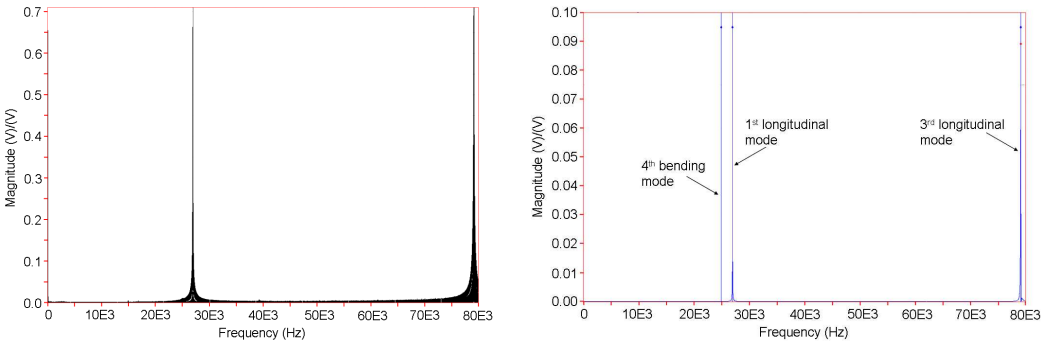

(a) Raw data: 216 overlaid traces

(b) Curve fitted trace

Figure 3.22: Configuration A: Experimental FRF's and curve fitted traces found through EMA

FEA predicted the presence of numerous mode shapes, however, only those which correspond with those found through EMA are presented in Figures 3.24 and 3.25. Three resonant frequencies were detected between 0-80kHz from the curve fitted data for both transducer configurations, Figures 3.22(b) and 3.23(b). Good correlation can be seen between the mode shapes while the percentage differences between the predicted resonant frequencies

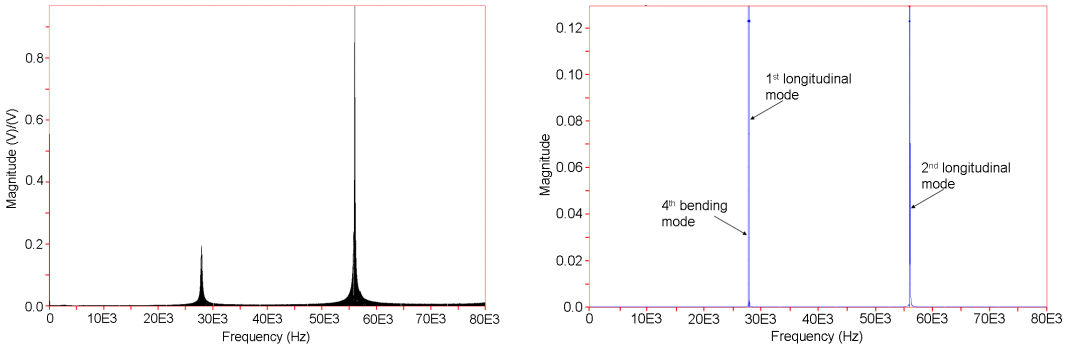

(a) Raw data: 204 overlaid traces

(b) Curve fitted trace

Figure 3.23: Configuration B: Experimental FRF's and curve fitted traces found through EMA

of the 4$^{\text{th}}$ bending mode, 1$^{\text{st}}$ and 3$^{\text{rd}}$ longitudinal modes and those found through EMA of configuration A were 0.20%, 5.62% and 4.02% respectively. The percentage difference between the 4$^{\text{th}}$ bending and 1$^{\text{st}}$ and 2$^{\text{nd}}$ longitudinal modes predicted through FEA and obtained through EMA for configuration B were 0.05%, 0.57% and 4.99% respectively.

A relatively high percentage difference between the frequency of the predicted and measured 1$^{\text{st}}$ longitudinal mode of configuration A, when compared to that of configuration B, may stem from suboptimal pre-loading of the piezoceramic stack during the manufacture of the transducers (Section 3.1.2). Literature discussing the effect of pre-loading, [186, 191], reported that insufficient pre-loading will lower the resonant frequency, while excessive will increase resonant frequency of a piezoceramic element, therefore it is likely that configuration A has had an insufficient pre-load applied during the manufacturing process. Furthermore, it is unclear why the 2$^{\text{nd}}$ longitudinal mode of configuration A was not measured experimentally, however the location of the piezoceramic stack in a longitudinal antinode combined with suboptimal pre-load could mean that not enough vibrational energy was available to excite it. Meanwhile the 3$^{\text{rd}}$ longitudinal mode of configuration B is likely to of lie outwith the frequency range of 0-80kHz and therefore was not excited.

3.4.2 Dynamic performance

Linear dynamic behaviour of the transducers has been simulated using finite element analysis. By estimating operating amplitudes, stress and strain levels within the transducer can be simulated ensuring that design parameters are fulfilled. To simulate linear operating conditions, the inverse piezoelectric effect of the piezoceramic elements within the model were utilised using 20 node quadratic piezoelectric elements (C3D20RE) while electrical boundary conditions of potential difference of 1V$_{\text{peak}}$ were applied across the poled direction of the elements. Two forms of damping were also utilised within the model. Rayleigh damping (material damping), is dependent on material used in the ultrasonic device as well as the frequency at which the device oscillates. Rayleigh damping consists of two damping constants

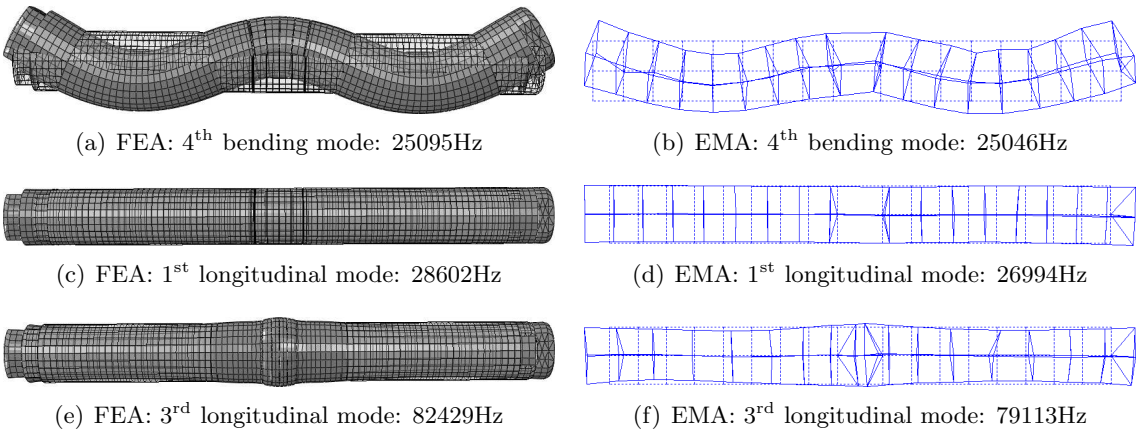

(a) FEA: 4th bending mode: 25095Hz

(b) EMA: 4th bending mode: 25046Hz

(c) FEA: 1st longitudinal mode: 28602Hz

(d) EMA: 1st longitudinal mode: 26994Hz

(e) FEA: 3rd longitudinal mode: 82429Hz

(f) EMA: 3rd longitudinal mode: 79113Hz

Figure 3.24: Resonant frequencies and mode shapes of configuration A found through FEA and EMA

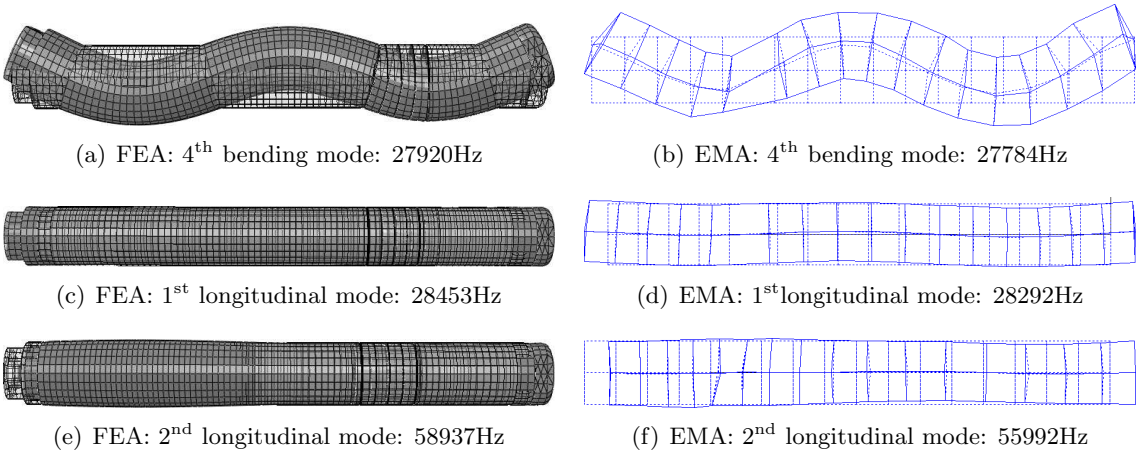

(a) FEA: 4th bending mode: 27920Hz

(b) EMA: 4th bending mode: 27784Hz

(c) FEA: 1st longitudinal mode: 28453Hz

(d) EMA: 1stlongitudinal mode: 28292Hz

(e) FEA: 2nd longitudinal mode: 58937Hz

(f) EMA: 2nd longitudinal mode: 55992Hz

Figure 3.25: Resonant frequencies and mode shapes of configuration B found through FEA and EMA

α and β and can be related to the damping ratio, ζ in the following expression;

$$\begin{aligned} [C] &= \alpha[M] + \beta[K] \\ \zeta &= \frac{\alpha}{2\omega} + \frac{\beta\omega}{2} \end{aligned} \tag{3.41}$$

where $[C]$, $[M]$ and $[K]$ are the structure damping matrix, structure mass matrix and structure stiffness matrix respectively and ω is the excitation frequency with relationship $\omega = 2\pi f$. The α component of the expression relates to viscous damping and its influence decreases as the frequency of vibration increases whilst the β component is the hysteresis or stiffness damping component and its influence increases as the frequency increases. At frequencies of concern in ultrasonic devices, the value of the α component is found to become insignificant and therefore can be classified as negligible. The second form of damping used with the FE model applies a uniform damping to the model and is referred to as 'global damping'.

Figure 3.26 illustrates the influence of different levels of global damping on the FE model of configuration A simulated to oscillate due to an applied voltage of $1V_{peak}$.

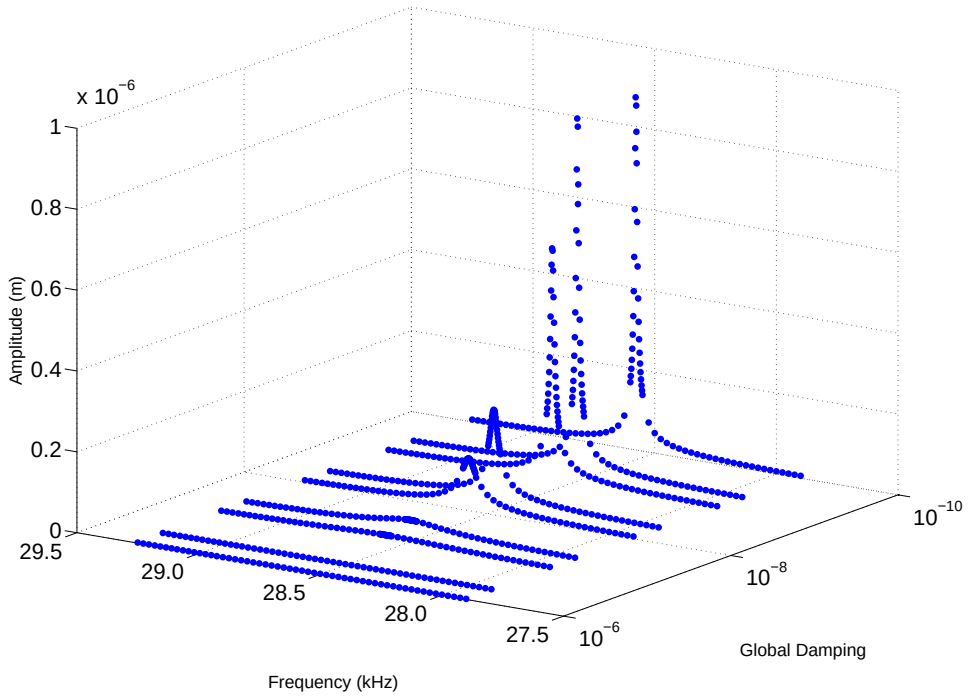

Figure 3.26: Influence of application of global damping on amplitudes of vibration on FE model of configuration A

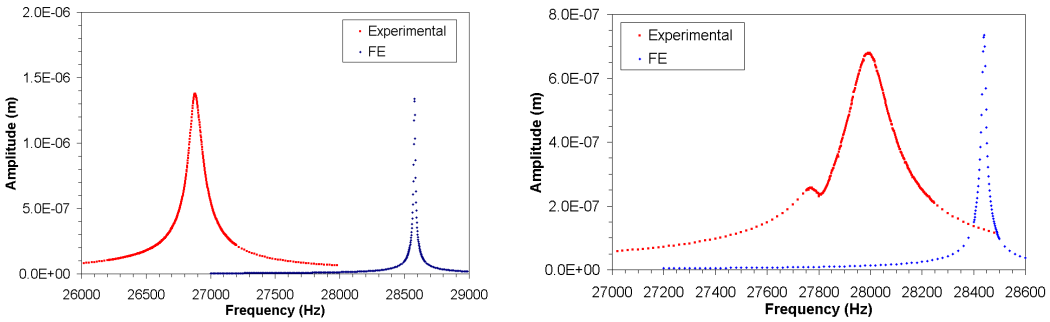

(a) Configuration A (b) Configuration B

Figure 3.27: Response of transducers excited at $1V_{peak}$ acquired from experimental and FE methods

Figure 3.27 contains experimentally measured responses of configurations A and B excited at $1V_{peak}$ around resonance as well as the most closely corresponding damped FE model. The damping value applied to the FE model (found through iteration, Figure 3.26) which predicted similar vibrational amplitudes as were measured experimentally, Figure 3.27 illustrates that not all properties of the transducers predicted through the FE model are in agreement with measurements. The Q_m of the simulated transducer configurations is significantly greater

than that of the actual transducers and this can be accredited to how damping has been applied. It is acknowledged that damping is not uniform throughout the transducer as locations of interfaces and joins will generate concentrations in damping. Furthermore, the value of Rayleigh or material damping has been calculated with respect to the resonant frequency, therefore it will decrease in accuracy further from resonance. It was also not possible to apply piezoelectric losses to the piezoceramic elements, and therefore the elements have been simulated as lossless. Figure 3.27(b) also illustrates a further difference between the predicted and measured amplitude response of configuration B. Experimentally, a second smaller resonance peak can be observed next to the principle resonance peak and corresponds with the frequency of the 4^{th} bending mode (Figures 3.23(b) and 3.25(b)). However the excitation of this mode was not predicted in the FE model simulating $1V_{peak}$ driving conditions, even though it was predicted in FE modal analysis.

3.5 Characterisation of medical ultrasonic devices

A selection of dental scaling and cutting devices designed to operate in conjunction with a surgical transducer designed by Mectron S.p.A has been characterised through a combination of FEA and EMA.

3.5.1 Characterisation of scaling inserts

Figure 3.28 shows the two scaling inserts investigated, known as S1 and S2. Designed for slightly different scaling applications, they differ slightly in geometry as the tip of the S1 insert consists of a relatively broad semi-circular cross-section allowing it to be applied to large tooth areas whilst the S2 insert has a narrower, triangular cross-sectional area with rounded surfaces and is utilised in interproximal scaling.

(a) S1 (b) S2

Figure 3.28: Mectron S.p.A scaling Inserts [70]

Experimental modal analysis provided good validation of the finite element models for the transducer assemblies containing the S1 and S2 inserts, as the percentage difference between the predicted and experimentally acquired tuned frequencies was 0.41% and 2.02%

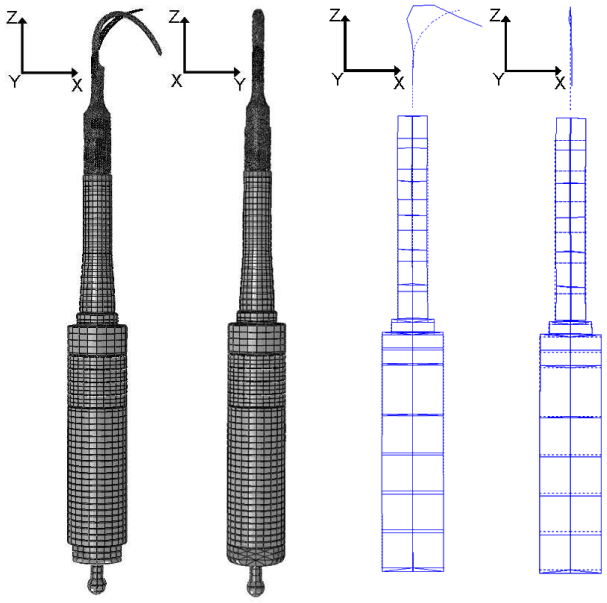

(a) FEA: 26996Hz (b) EMA: 27105Hz

Figure 3.29: S1 Insert: Deformed / undeformed 1st longitudinal mode

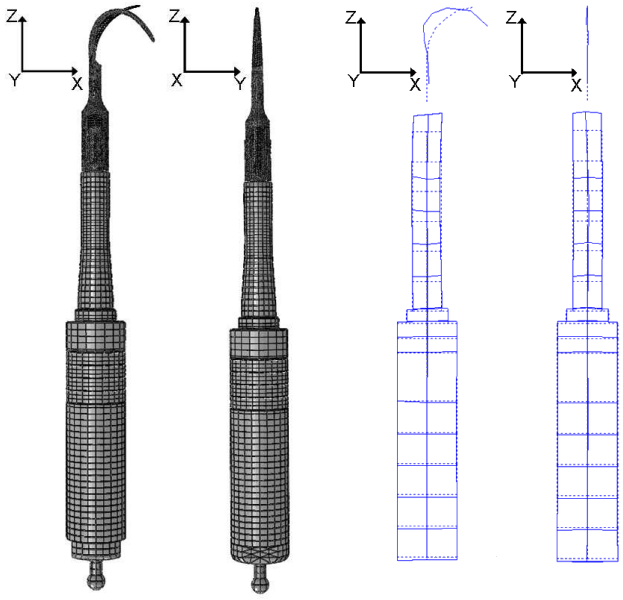

(a) FEA: 27151Hz (b) EMA: 27710Hz

Figure 3.30: S2 Insert: Deformed / undeformed 1st longitudinal mode

respectively, Figures 3.29 and 3.30. Using steady state simulated driving conditions, exciting the tuned assemblies with $25V_{peak}$ at the resonant frequency, it was predicted that the vibration amplitudes at the tip of the S1 and S2 inserts in the X-Z plane would reach 57 and 56μm, respectively. To validate amplitude responses predicted by the FE models, amplitudes of vibration across the tuned assemblies were measured using both 1D-LDV (Polytec, OFV

3001/OFV 303) and 3D-LDV (Section 3.3.7) under operational conditions. The highest stress values within the assembly were predicted to occur at the flexural nodal point of the insert tips, with peak values of 252MPa and 263MPa for S1 and S2 inserts respectively, Figure 3.31. The endurance stress limit of the type of steel used in the manufacture of the inserts is estimated at 664MPa [213] hence the values predicted in Figure 3.31 are well within the endurance limits of the steel and give a safety factor when operating free of load of around 60%.

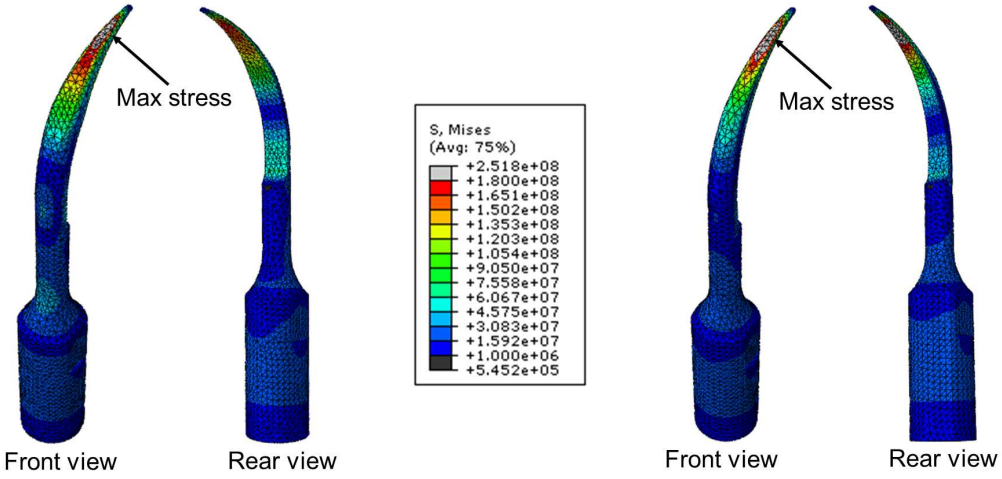

(a) S1 (b) Stress contour plot (Pa) (c) S2

Figure 3.31: Dynamic stress distributions in scaling inserts

3.5.2 Evolution of bone cutting device

Originally Mectron S.p.A solely manufactured scaling devices, however the first successful attempt at dissecting hard tissue using their device was reported during a sinus filling procedure [70, 72] and led to the evolution of the scaling device into a device specifically designed for bone cutting. The first prototype designs, OT1 and OT2, resembled the original scaling inserts, and can be seen in Figures 3.32(a) and 3.32(b). The OT1 and OT2 inserts are ultimately the same insert, however to assess which cutting edge finish would give the most efficient cut, two different edges were incorporated into the design and studied in parallel; a diamond coated cutting edge in the OT1 insert and a plain cutting edge similar to a traditional scalpel in the OT2 insert. Observations during the trials concluded that the OT1 insert was less efficient at cutting and also produced higher levels of heating within hard tissue, however, it is still used in medical procedures as a finishing tool on recently cut surfaces.

To enhance the cutting ability of the OT2 insert, larger vibrational amplitudes and a deeper cutting ability were necessary. To increase vibrational amplitudes a doubly curved shank was introduced and to further improve cutting efficiency a saw-like design was applied

(a) OT1 (b) OT2 (c) OT6 (d) OT7

Figure 3.32: Mectron cutting inserts [70]

to the cutting edge which resulted in the OT6 insert, Figure 3.32(c). To gain satisfactory cutting depth a longer blade length, which can be seen incorporated in the OT7 insert, was conceived, Figure 3.32(d). Due to dynamic stresses at the point at which the shank meets the blade, several prototype OT7 inserts failed, however stress concentrations were reduced through the introduction of a semi-conical connection.

Analysis of bone cutting devices

Figures 3.33, 3.34 and 3.35 show good correlation between the mode shapes and resonant frequencies predicted through FE models and obtained through experimental modal analysis of the OT2, OT6 and OT7 cutting assemblies. The percentage difference between the predicted and experimental acquired resonant frequencies was found to be 3.23%, 3.19% and 1.14% for the OT2, OT6 and OT7 cutting assemblies, respectively.

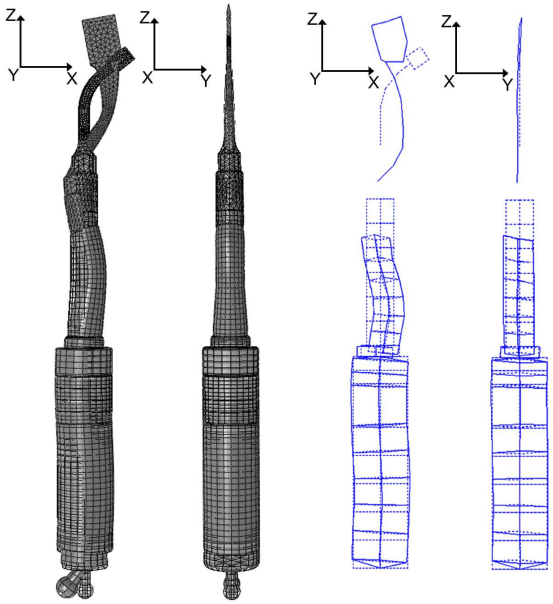

(a) FEA: 27024Hz (b) EMA: 26151Hz

Figure 3.33: OT2 Insert - deformed / undeformed 1st longitudinal mode

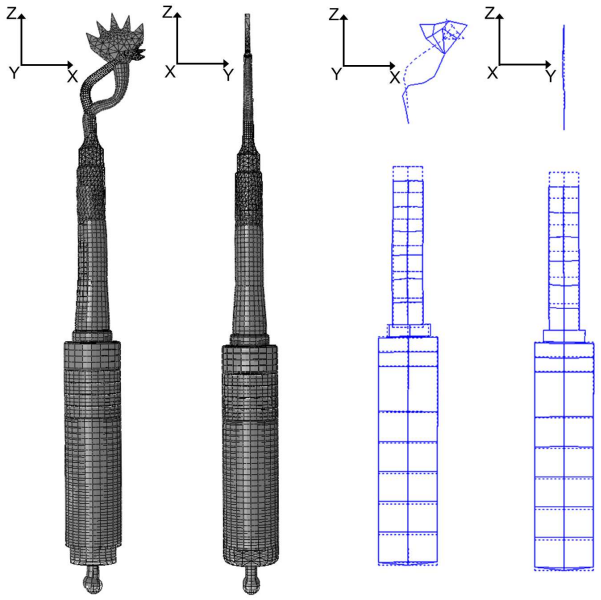

(a) FEA: 26474Hz (b) EMA: 25630Hz

Figure 3.34: OT6 Insert - deformed / undeformed 1st longitudinal mode

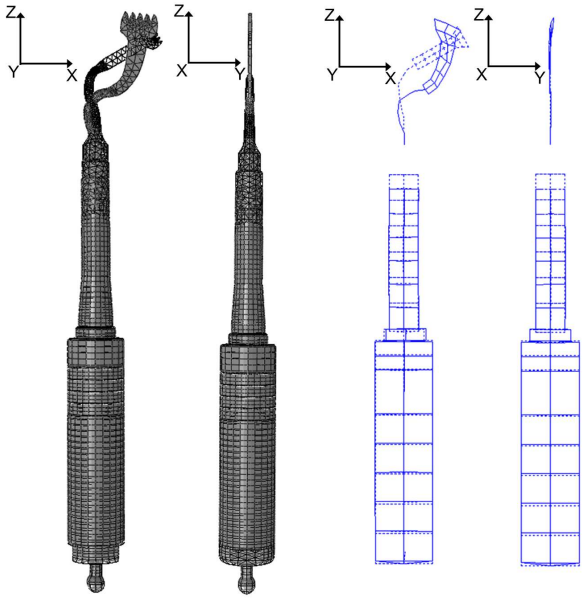

(a) FEA: 26880Hz (b) EMA: 27190Hz

Figure 3.35: OT7 Insert - deformed / undeformed 1st longitudinal mode

To investigate dynamic stress distribution throughout the tuned assemblies, the FE models were excited with a constant voltage of $40V_{peak}$ to simulate operational conditions at resonance. The vibrational amplitude, measured from the midpoint of the cutting edge, predicted that the OT2 would achieve 25μm while the amplitudes reached by the OT6 and OT7 inserts would be 35μm and 31μm, respectively. Comparing the predicted amplitudes of

the OT2, OT6 and OT7 inserts vindicates the proposition that the doubly curved shank does improve the achievable output amplitude, however it can also be observed that increasing the length of the cutting blade to enhance cutting depth sacrifices amplitude performance.

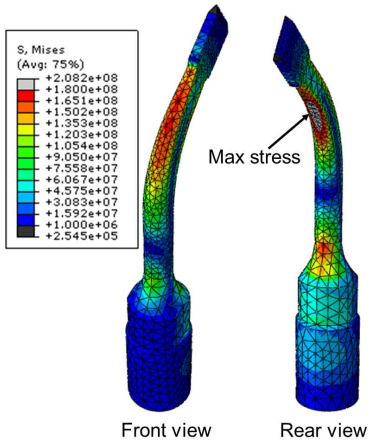

(a) OT2

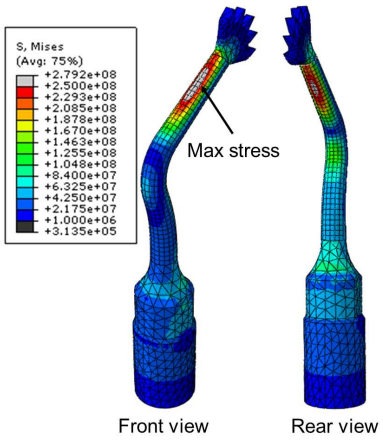

(b) OT6

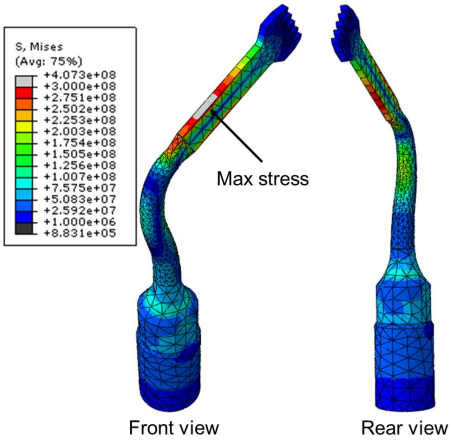

(c) OT7

Figure 3.36: Dynamic stress distributions in bone cutting inserts (Pa)

Figure 3.36 illustrates the stress distributions and locations of highest stress in the OT2, OT6 and OT7 inserts. The predicted values of highest stress in the OT2 and OT6 inserts were 223MPa and 274MPa and occurred at the flexural node in the shanks of the inserts. Meanwhile, the value of the highest predicted stress in the OT7 insert was 407MPa and occurred at the connection between the shank and blade. The values of highest stress predicted in the OT2, OT6 and OT7 inserts were found to be below the endurance limit of the steel and give factors of safety when operating free of load of 66%, 58% and 39% respectively [213]. Hence, as expected the inserts, if correctly manufactured, should not fail while in operation.

3.5.3 Optimisation of bone cutting devices

To investigate whether the blade length of the present OT7 insert design has been fully optimised to ensure maximum vibrational amplitude at the cutting face, the length of the blade in the original design was modified, by 1mm increments until it was either 4mm shorter or longer than the present insert, Figure 3.37.

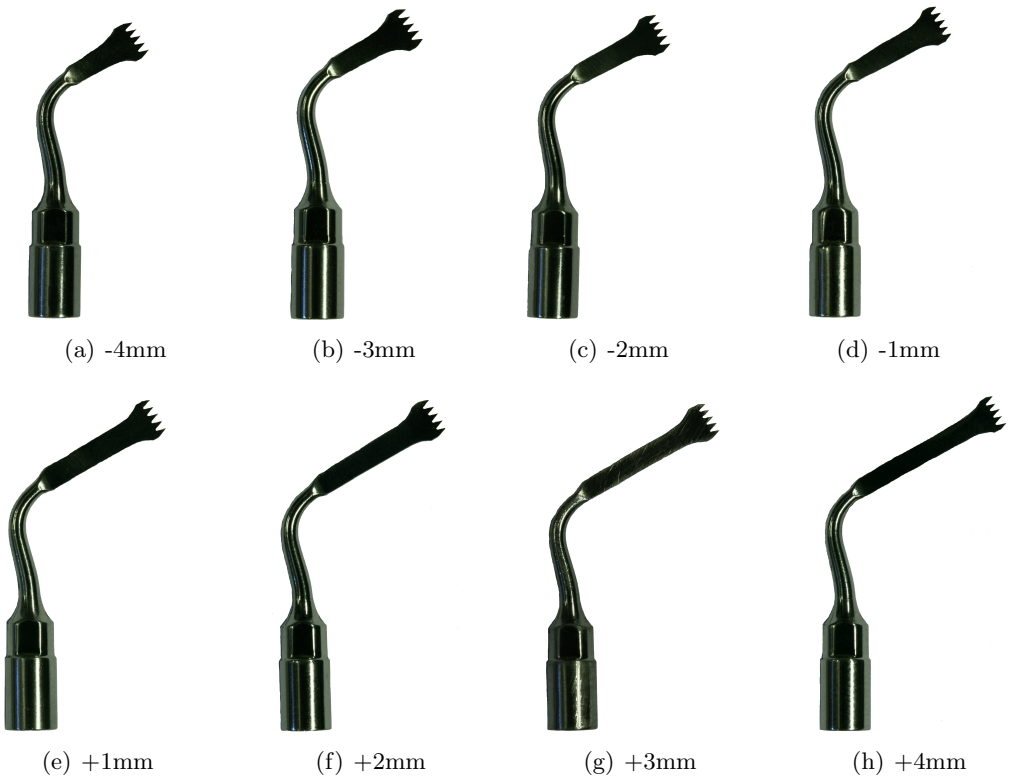

(a) -4mm (b) -3mm (c) -2mm (d) -1mm

(e) +1mm (f) +2mm (g) +3mm (h) +4mm

Figure 3.37: Modified OT7 cutting inserts

Modal analysis of modified bone cutting devices

Figures 3.38 and 3.39 illustrate good correlation between predicted and measured mode shapes of the tuned mode of vibration, while Table 3.8 presents that good correlation was also achieved between the predicted and measured frequencies of these modes. The position of the longitudinal antinode, seen in Figures 3.40 and 3.41 as red in the contour maps, moves location as the length of the blade in the modified inserts changes. As the blade increases in length, it can be observed that the position of the antinode moves from the shank, as seen in the insert with the shortest blade length Figures 3.40(a) and 3.41(a), to a location on the join between the shank and blade as seen with the insert with the blade extended by 2mm, Figures 3.40(f) and 3.41(f). The position of the antinode further moves, to a location on the blade, when the blade has been lengthening by 3mm and 4mm, respectively.

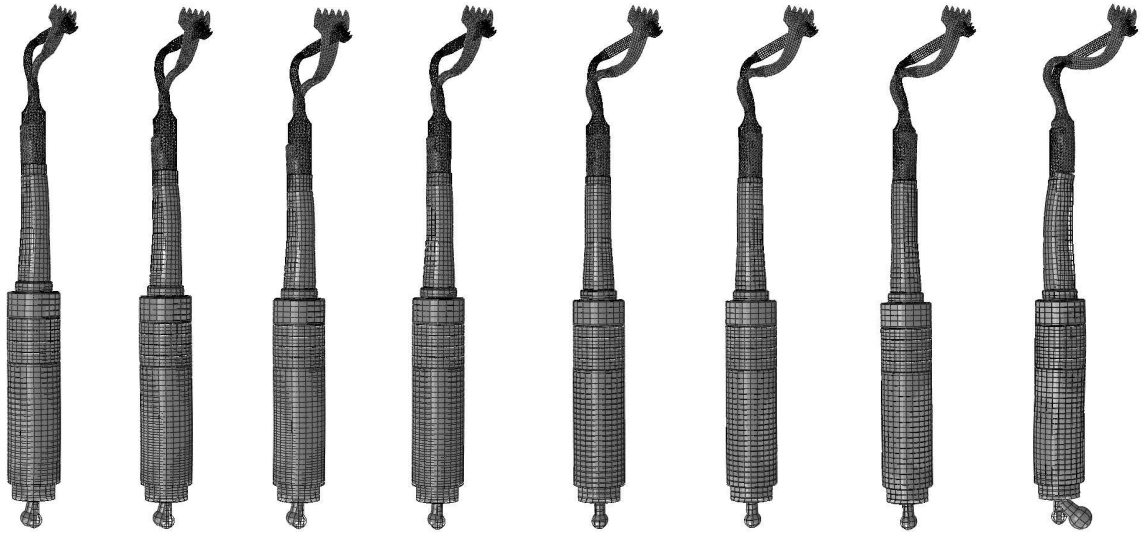

(a) -4mm (b) -3mm (c) -2mm (d) -1mm (e) +1mm (f) +2mm (g) +3mm (h) +4mm

Figure 3.38: Mode shapes predicted through FEA of modified OT7 inserts

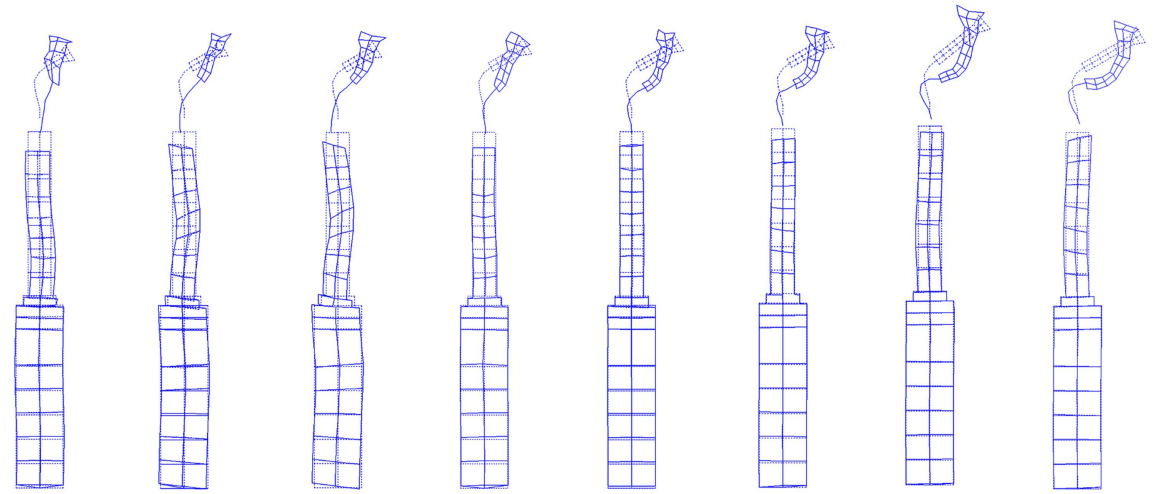

(a) -4mm (b) -3mm (c) -2mm (d) -1mm (e) +1mm (f) +2mm (g) +3mm (h) +4mm

Figure 3.39: Mode shapes extracted from EMA of modified OT7 inserts

Modified OT7 Insert	FEA (Hz)	EMA (Hz)	|%| Difference
-4mm	27300	25676	5.95
-3mm	27197	26338	3.16
-2mm	27084	25251	6.77
-1mm	26948	25948	3.71
+1mm	26478	25466	3.85
+2mm	25986	25365	2.39
+3mm	25123	24575	2.18
+4mm	23886	24191	1.26

Table 3.8: Predicted and measured frequencies of the tuned mode of vibration for the modified OT7 inserts

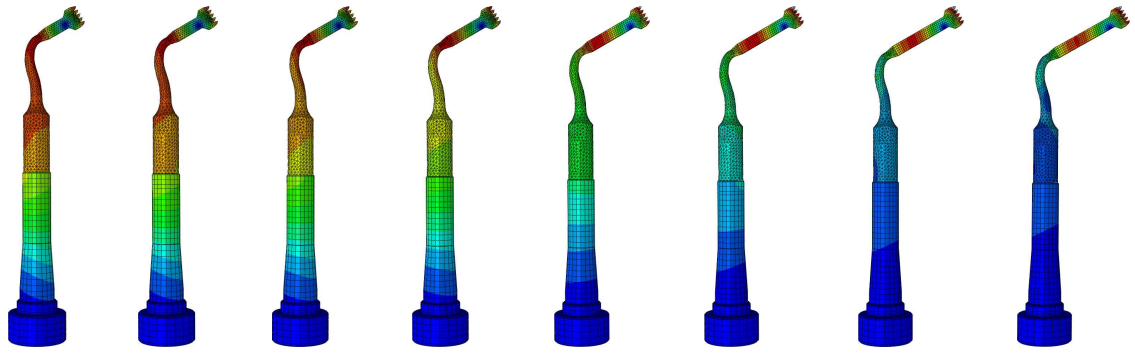

Figure 3.40: FEA - Modified OT7 insert assemblies normalised undeformed contour map of displacement

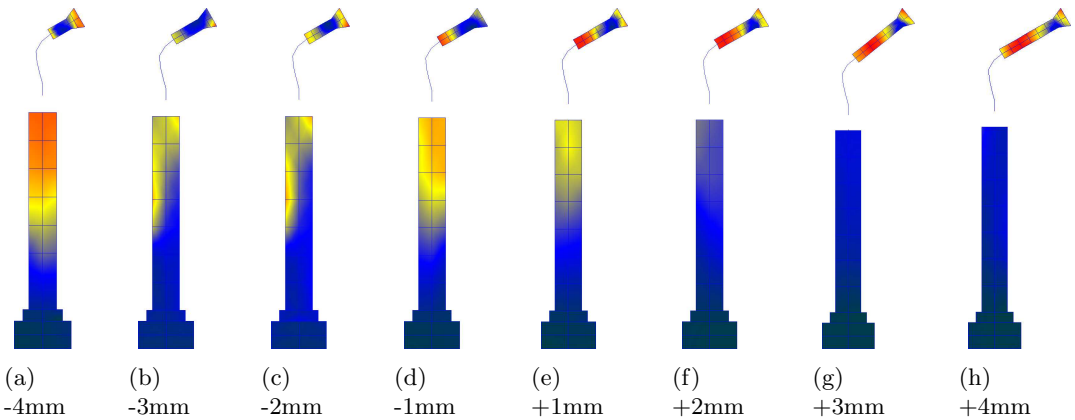

Figure 3.41: EMA - Modified OT7 insert assemblies normalised undeformed contour map of displacement

Stress analysis of modified bone cutting devices

As with Section 3.5.2, the stress distribution in the modified OT7 inserts was investigated under operational conditions using FEA. The simulated models were excited at a voltage of $80V_{peak}$ at the resonant frequency where the predicted stress distribution and displacement at the midpoint on the cutting edge was recorded.

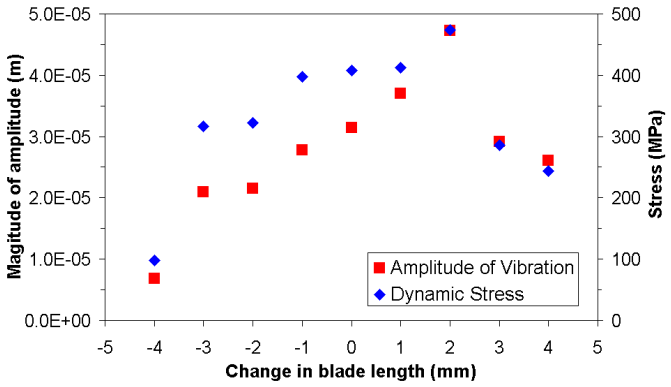

Figure 3.42: Amplitude of vibration and corresponding stress verses change in blade length

The vibrational amplitude of each of the modified inserts is presented in Figure 3.42 and it can be observed that the smallest vibrational amplitude, 7μm, was delivered by the insert with the shortest blade length, whilst the largest predicted amplitude, 47μm, was achieved by the insert with the blade extended by 2mm. Interestingly, the FE model predicted that inserts with blades elongated by 3mm and 4mm achieved similar vibrational amplitudes, 29μm and 26μm respectively, to the insert shortened by 1mm. The reduction in predicted vibrational amplitude in the inserts with the longest blade lengths can be accredited to the shifting of the longitudinal anti-node, seen in Figures 3.40 and 3.41, from the shank/blade interface to a location midway between the shank and cutting edge.

The peak dynamic stresses calculated in the FE models of the OT7 insert configurations followed the trend of the predicted values of the vibrational amplitude, as observed from Figure 3.42. As with the highest amplitude value, the value of highest predicted stress, 474MPa, occurred in the modified insert in which the blade had been extended by 2mm. This value is below the endurance stress limit of the steel alloy used in manufacture and gave a factor of safety of approximately 29% when vibrating under free loading conditions. However, it should be considered when designing cutting inserts for use in ultrasonic devices that previous research suggests that the highest values of dynamic stress within the cutting insert should not exceed 30% of the endurance limit of the material employed in manufacture of it [62], hence implying that, even though the insert in which the blade has been extended by 2mm provided the largest vibrational amplitude, it may not be suitable for use due to the possibility of failure once under load.

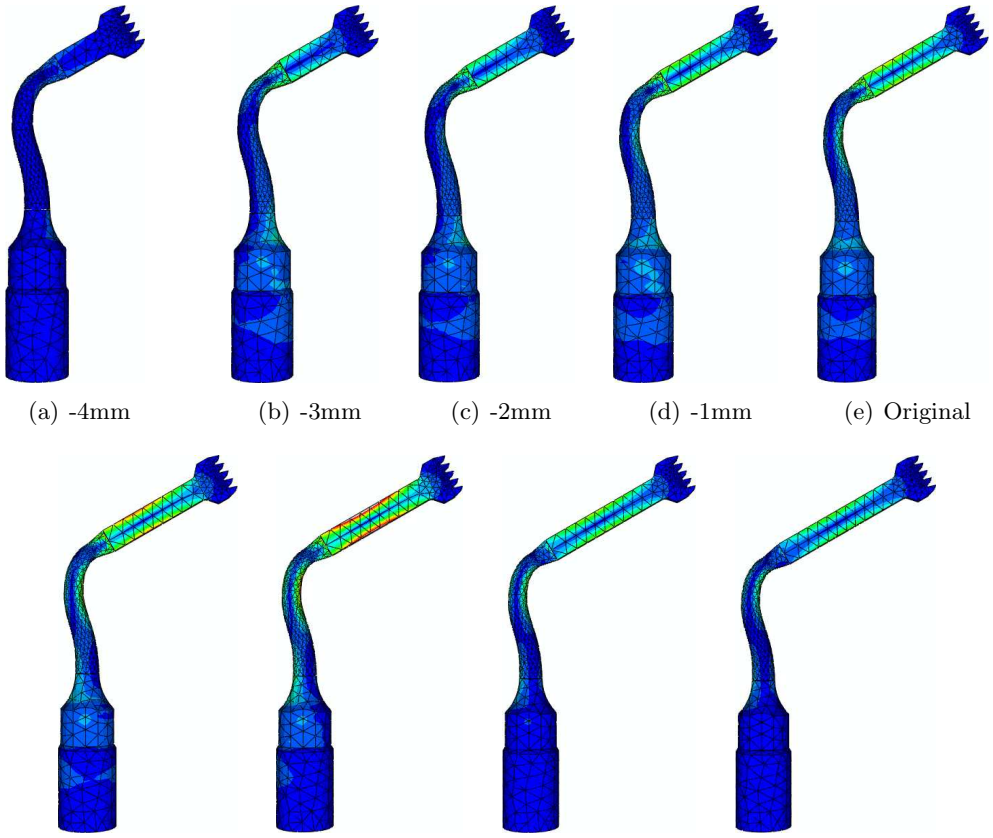

(a) -4mm (b) -3mm (c) -2mm (d) -1mm (e) Original

(f) +1mm (g) +2mm (h) +3mm (i) +4mm

Figure 3.43: Normalised stress distributions in modified OT7 cutting inserts

3.6 Chapter Summary

The design of ultrasonic devices has been investigated, initially from fundamental transducer and tool geometries, in which resonant frequencies can be predicted from straightforward analytical methods, to dental and surgical devices which rely upon finite element models to ensure tuning and reliability. Material selection for transducer and tool design has also been discussed and factors explored such as vibrational performance and operating environment which should be addressed before materials are selected. However, it has also been noted that economic factors may also be key to material selection. The selection of the material with the optimal material properties for a task may not always be paramount.

On the whole, good correlation between the predicted and measured resonant frequencies and mode shapes of the investigated devices was achieved and ensured validity of the FEA models, although it was observed that some devices achieved better correlation between predicted and measured resonant frequencies. However it could also be observed that the devices which achieved the closest correlation were commercially manufactured, while those with the worst correlation were prototype or uniquely manufactured. This may suggest that the manufacture of these components or devices may not be optimised, which could suggest that slight differences may exist between the components modelled and those experimentally

measured. Finally FE models which predict the vibrational response of a device by simulating the excitation voltage, Section 3.4.2, achieved good correlation between resonant frequency and amplitude of vibration and thus allowing stress analysis of the device whilst at resonant conditions. However, the simulated and measured response of the device away from the resonant frequency did not achieve good correlation. This is primarily due to the difficulty of correctly applying damping to the FE model.

Chapter 4

Characterisation of surgical devices

It has been widely reported over many decades that ultrasonic devices driven under high excitation levels at resonance inherently exhibit nonlinear behaviours which alter their operational performance [10, 146, 147, 150, 167, 189, 214]. It is therefore important that such behaviours can be characterised in order to set design rules for ultrasonic devices that help avoid their occurrence or aid with their control. Nonlinear behaviour can manifest in ultrasonic devices as;

- Increased mechanical loss
- Shift in resonant frequency
- Frequency hysteresis
- Harmonic response
- Modal energy transfer

The source of these behaviours within ultrasonic devices, partly discussed in Section 1.2.2 and Section 2.4, is to some extent a consequence of the device, or specifically the piezoceramic element, experiencing high vibrational strain when driven at or close to resonance. It is known that elastic properties of transducer materials, especially piezoceramics, do not behave linearly whilst oscillating at high amplitude levels and this has led to research to identify nonlinear material properties of piezoceramics [6, 27, 95, 150, 154, 159], and techniques to allow the accurate prediction and modelling of nonlinear behaviour [162, 168, 215, 216]. This work has allowed the determination of optimal operating limits of current piezoceramics or ultrasonic devices whilst also aiding in the enhancement of future piezoceramics and devices.

Nonlinear properties of piezoceramics and ultrasonic devices can be found through experimental characterisation. Various techniques have been developed over the years, all containing a fundamental similarity; an attempt to separate nonlinear behaviour stemming from temperature increases within the piezoceramic material from that stemming from elastic

and piezoelectric properties. The strategy most techniques utilise to remove any thermal effect is to take each measurement in the shortest possible time, then give enough time before the next measurement to allow any heat buildup to dissipate. More recently, strategies that excite the piezoceramic element for a short period of time through a burst have also been reported upon.

Through the characterisation at elevated vibrational amplitudes of ultrasonic surgical devices that differ geometrically and through material of manufacture, design guidelines that aid with the control or avoidance of nonlinear behaviours will ensue.

4.1 Experimental characterisation techniques

4.1.1 Harmonic response at constant voltage

The classical or traditional technique used to perform harmonic characterisation of piezoceramics and ultrasonic devices uses an impedance or network analyser. The analyser generates a frequency sweep at different voltage levels, obtaining the resonant frequency through measuring the current drawn by the piezoelectric device [152, 155, 164].

A limitation of this method is that to produce a single frequency response curve for a single excitation voltage, multiple frequency sweeps are required as each frequency sweep will only yield one data point. Therefore it is necessary to complete as many frequency sweeps as number of data points required to generate the response curve. This reveals a secondary problem concerning preventing temperature increases within the piezoceramics. To ensure there is no thermal effect, two options are available; either to complete each frequency sweep as quickly as possible, thus resulting in reduction of the accuracy of the measurement, or include a time delay between each frequency sweep, ensuring that any slight temperature rise dissipates before the measurement of the next data point [162]. This technique requires both upward and downward sweeps to be completed to ensure that the resonant frequency is obtained even if a hysteresis region occurs.

4.1.2 Harmonic response with constant current

Developed by Hirose *et al* [26, 162], harmonic response with constant current control has been extensively used to study the relationship between electromechanical characteristics and vibrational stress of various piezoceramics [159]. A feedback system compensates for the capacitance in the electrical branch of the resonant equivalent circuit, ensuring that a constant current flows through the piezoceramic. The main advantage of this characterisation technique is that any potential hysteresis region disappears thus allowing the direction of the sweep, low to high frequency or the reverse to become inconsequential.

However, this technique does have some limitations. The control system requires a sophisticated function generator, while, the overall power applied to the device for the

duration of the frequency sweep is greater than that of the constant voltage method. This is because the power delivered at resonance (where current flows with ease, thus power consumption is high) is at the same level as all frequencies away from resonance [162]. High power consumption throughout the whole of the frequency sweep, not just at resonance may also explain why controlling the temperature of the piezoceramics within a device, and thus removing any thermal effect, is difficult using this method [159].

4.1.3 Harmonic response: burst excitation

Characterisation methods discussed in Sections 4.1.1 and 4.1.2, generate a frequency sweep which delivers a constant excitation signal between the start and end frequencies. As previously discussed temperature increases can manifest in these techniques unless they are consciously dealt with. Temperature increases can be controlled through burst excitation. This method excites the ultrasonic device or piezoceramic element over a short period of time at a specified frequency through a burst of finite number of cycles. If required a time delay, which allows the dissipation of any heat, can be incorporated between measurements at sequential frequencies. Two methods using this technique are discussed in the following sections.

4.1.4 Burst excitation: measurement of transient response

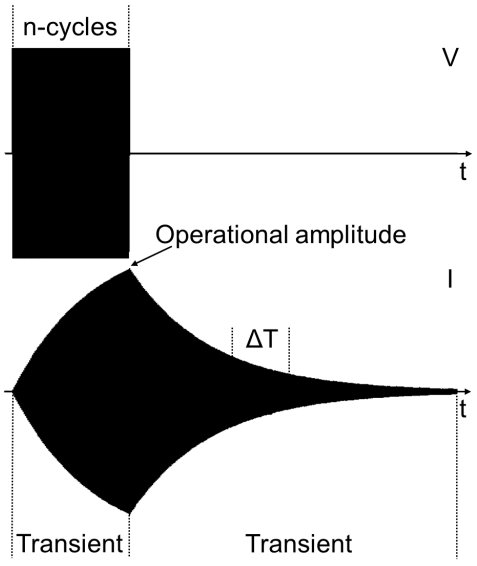

Figure 4.1: Transient response method: Voltage and current waveforms

Developed by Umeda *et al* [7, 8, 154, 163, 214], this characterisation method uses a burst signal to excite the piezoceramic or ultrasonic device at a constant voltage for a number of cycles, n (Figure 4.1). Once the operational amplitude of vibration has been reached, the voltage amplitude and frequency are measured before the electrical terminal is short

circuited [154]. The piezoceramic or ultrasonic device then experiences a transient interval of free vibration where the current and velocity response measurements are recorded at various time intervals during the transient response and are analysed to give the oscillation period, T, and frequency, f. These are then used to obtain the mechanical loss factor, Q_m^{-1}, and frequency shift, $\Delta f/f_o$.

The main advantage of this technique is its ability to separate a well known source of nonlinear behaviour in piezoceramics, the effect of high stress caused by high vibration amplitude, from two other sources of nonlinear behaviour; an increase in temperature and the effect of high electric fields [8]. However, Albareda *et al* [162], found limitations using this technique with 3-1 piezoceramic composites. Due to close proximity and excitation of different modal frequencies associated with thickness and lateral modes, the possibility arose for the manifestation of the beat phenomenon. This phenomenon is manifested in the transient response and results in making correct time constant measurements impossible.

4.1.5 Burst excitation: measurement of steady state response

Similar to the characterisation technique developed by Umeda *et al* in Section 4.1.4, this technique also controls the temperature of the piezoceramic by only supplying an excitation signal for a short time interval through a burst. However the crucial difference between the two techniques is that measurements of current and velocity are taken during steady state vibration.

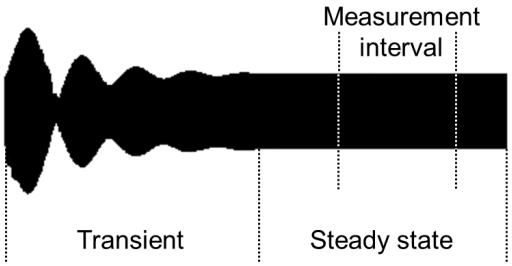

Figure 4.2: Burst response of current

Although nonlinear behaviour caused by the electric field is not separated from the effect that high stress has on piezoceramics, an advantage of this technique is that it allows the study of piezoceramics or ultrasonic devices under operating conditions. The beat phenomenon, which is induced by the transient behaviour of the technique described in Section 4.1.4, is also avoided because the piezoceramic element or device is excited to a steady state, preventing modes other than the desired from being excited [162]. The burst interval is generally longer in this technique than in the previous technique as steady state vibration is required to be reached. It is also advised to incorporate a suitable time delay between successive frequency bursts to ensure there is minimal increase in temperature within the piezoceramics.

4.2 Power harmonic characterisation: experimental setup

The characterisation technique used in measurements is essentially that described in Section 4.1.5, although it has evolved from a less complex setup.

4.2.1 Initial harmonic characterisation experimental setup

The experimental setup first used in this work to characterise nonlinear behaviour of ultrasonic devices through frequency sweeps can be seen in Figure 4.3. To generate an excitation signal a signal generator/analyser (Data Physics, Quattro) was utilised to produce a burst sine signal of a duration of approximately 1 second at a constant frequency. The signal was amplified by a power amplifier, QSC Audio RMX 4050HD, before exciting the ultrasonic device. A 1D laser Doppler vibrometer, Polytec, OFV 3001 control with OFV 303 sensor head, measured the vibration response of the ultrasonic device while Data physics, SignalCalc 240 software performed FFTs of the responses. Temperature increases occurred at high vibration amplitudes and thus suitable cooling periods were incorporated between successive increments of the frequency sweeps.

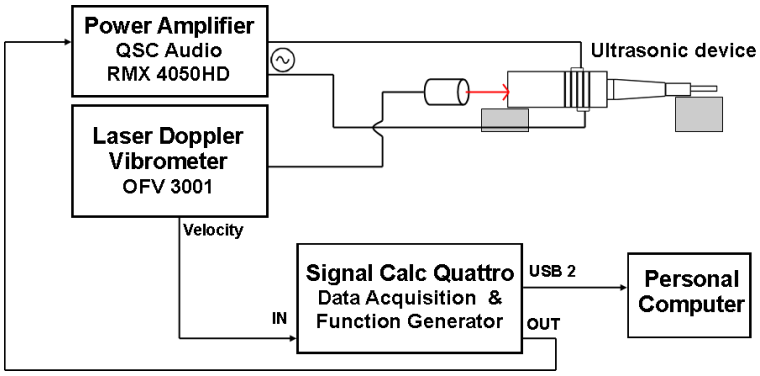

Figure 4.3: Schematic of initial experimental setup

To estimate a suitable time interval between successive increments of the frequency sweep a thermal imaging camera, Thermoteknix Miricle 110k, was used to identify temperature distributions in the ultrasonic devices. A reference image was taken at room temperature before the device was excited and was subtracted from images subsequently captured from the device immediately after excitation. Once one of the successive images cancelled with the reference image, leaving a blank frame, it could be assumed that initial temperature conditions had been reached thus allowing an estimation of a suitable delay time. After exciting the device at high vibration amplitudes, time between successive bursts could reach the order of several minutes. Images taken by the thermal imaging camera can be seen in Figure 4.4. This camera does not measure absolute temperature, but temperature gradients which show up as a gray scale colour band. Hottest parts are represented as the brightest spots in the image, Figure 4.4(b), and are located as expected at the piezoceramic stack.

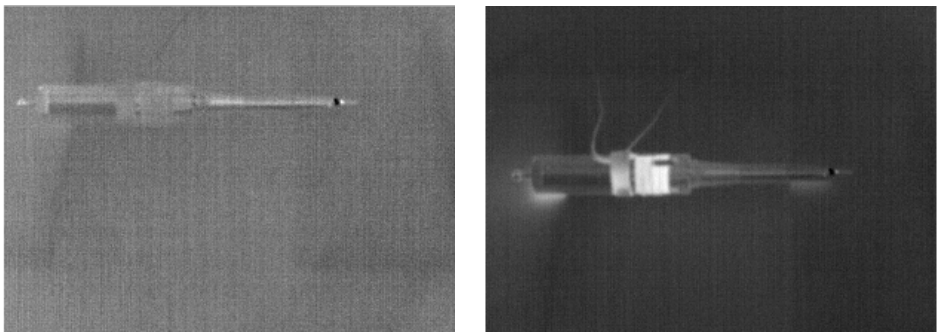

(a) Image captured at room temperature

(b) Image captured at resonance

(c) Subtraction ((b)-(a)) image captured at resonance

Figure 4.4: Thermal images of Mectron transducer with base insert - (b) & (c) are captured at the end of an excitation burst

4.2.2 Experimental harmonic characterisation setup developed at CSIC

Developed in the Power Ultrasonic laboratories at the Instituto de Acustica (CSIC), Madrid, Spain, the experimental method seen in Figure 4.5 is a more advanced experimental technique of nonlinear characterisation than that in the previous section. The ultrasonic device under test was excited by a signal (set in the Labview software as RMS voltage) generated by a function generator, Agilent 3322A, which was magnified by a power amplifier, QSC Audio RMX 4050HD, while the velocity response of the device was measured with a 1D laser Doppler vibrometer, Polytec OFV3001 with CFV055 sensor head. To measure the surface temperature of the bare piezoceramic stack, a custom infrared sensor was employed. National Instruments data acquisition hardware and interface in conjunction with Labview software coordinated the experimental protocol and data collection. Finally, to view the current and voltage responses and the frequency spectrum of the velocity response a Tektronic oscilloscope, DPO 7054, was used.

As with the experimental setup in Section 4.2.1, the ultrasonic devices were allowed to reach steady state conditions before measurements were taken, although with a significant difference in the burst length. To minimise temperature increases in the piezoceramic stack, the burst length was constricted to as few cycles as possible, usually in the region of a few thousand cycles. To ensure that a suitable number of cycles were incorporated in to the

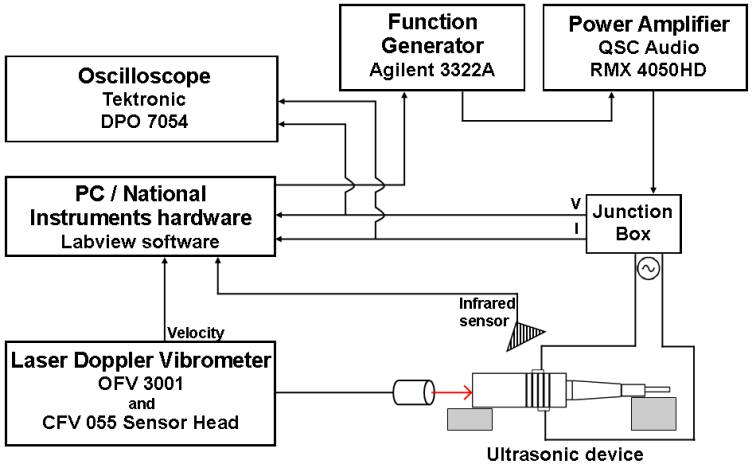

Figure 4.5: Schematic of CSIC experimental setup

burst, guaranteeing steady state vibration had been reached (constant level of vibration), the electrical quality factor of the device was found at low voltage levels (ensuring linear behaviour) and then compared to the Q-factor obtained from an impedance analyser (Hewlett Packard). If the values did not match, then the number of cycles within the burst was increased until they did. Figure 4.6, captured from the oscilloscope, illustrates the burst signal of both voltage and current. The transient regions of the current trace can be seen at the start and end of the burst.

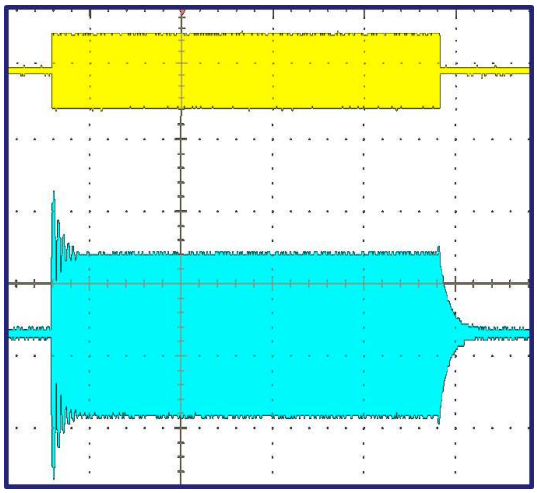

Figure 4.6: Burst voltage/current signal captured from the oscilloscope: Top trace; Voltage, Bottom trace; Current

4.3 Power harmonic characterisation of ultrasonic devices

Due to the broad range of processes and different conditions which ultrasonic devices operate in, their shape, size and the material they are manufactured from can vary considerably. To study the effect that geometric and material differences have on nonlinear behaviour, a selection of tuned inserts have undergone experimental characterisation at elevated voltage levels using the techniques discussed in Section 4.2. The tuned inserts consist of a combination of custom rod horns and commercial inserts utilised in bone surgery. Both custom and commercial horns are used in conjunction with the commercial Langevin transducer.

4.3.1 Commercial surgical insert: Half wavelength assembly

As part of the range of bone preparation and cutting devices known as the Piezosurgery® Device, the OT7 insert (Figure 4.8(a)) is specifically developed for bone cutting. The tuned device operates in a longitudinal-flexural mode, of which the transducer and base of the OT7 insert oscillate in a longitudinal motion and the shank and blade of the insert operate flexurally, Figure 4.7.

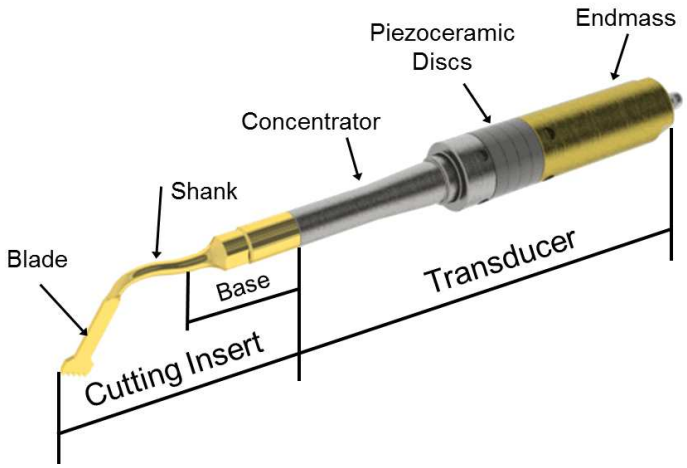

Figure 4.7: Transducer and OT7 insert assembly

All inserts used in the Piezosurgery® Device stem from a common base, hence to study the nonlinear effect of incorporating the shank and blade in to the assembly, two inserts are characterised, an OT7 insert and an insert which only contains the common base. This is referred to as the 'base insert', Figure 4.8(b). The mechanical quality factors for the assemblies containing the base insert and OT7 insert are 431.9 and 451.8 respectively.

(a) OT7 Insert (b) Base Insert

Figure 4.8: Piezosurgery® base and OT7 insert

FEA and EMA of Base and OT7 inserts

The dynamic behaviour of the two assemblies was studied through a combination of finite element and experimental modal analysis in order to find the natural frequency and mode shapes of the assemblies, Figures 4.9 and 4.10.

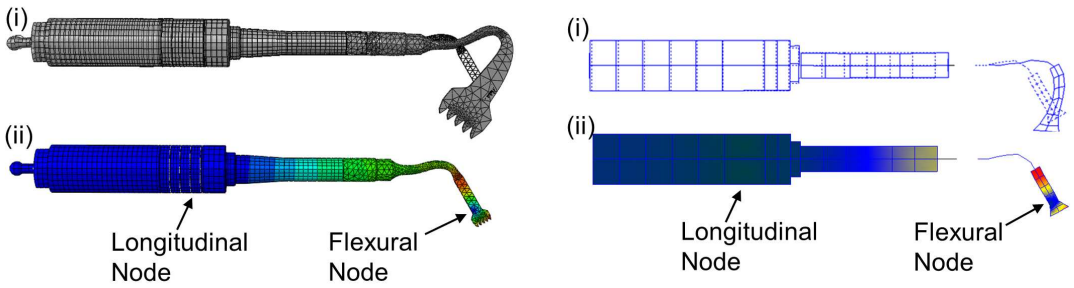

(a) FEA: 1st longitudinal mode $f = 26858$Hz (b) EMA: 1st longitudinal mode $f = 27190$Hz

Figure 4.9: Transducer with OT7 insert (i)Deformed/undeformed (ii)Undeformed normalised contour map of displacement

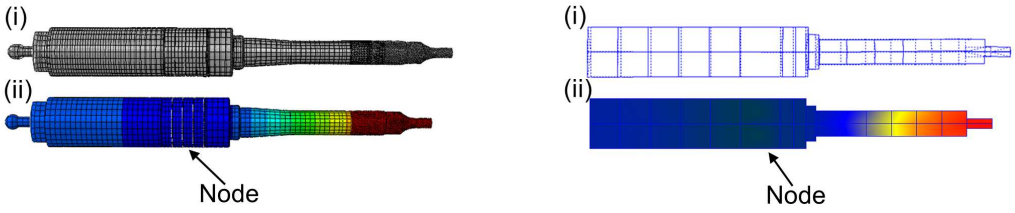

(a) FEA: 1st longitudinal mode $f = 28751$Hz (b) EMA: 1st longitudinal mode $f = 28761$Hz

Figure 4.10: Transducer with base insert (i)Deformed/undeformed (ii)Undeformed normalised contour map of displacement

Good correlation of modal parameters was achieved between finite element and experimental modal analysis methods. The percentage difference between the resonant frequency found through FEA and EMA for first longitudinal mode for the two assemblies containing

the OT7 and base insert was 1.22% and 0.03% respectively.

Power harmonic characterisation: Frequency sweep - Technique comparison

The assemblies containing the base insert and OT7 insert underwent characterisation using the techniques described in both Section 4.2.1 (experimental setup 1) and Section 4.2.2 (experimental setup 2). The resolution experimental setup 1 was 1Hz close to resonance and between 10Hz and 25Hz away from resonance, while the resolution of experimental setup 2 was 1Hz between excitation voltage of 2-10V_{rms} and 2Hz between 20-50V_{rms}.

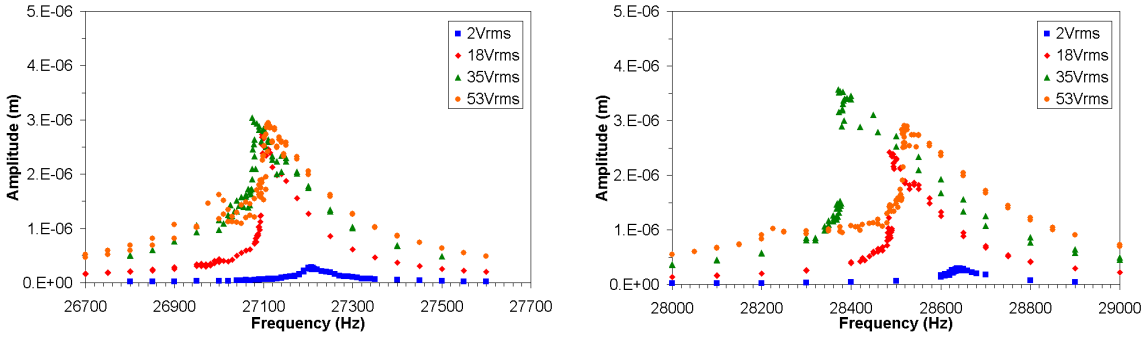

(a) Vibrational response of OT7 insert

(b) Vibrational response of base insert

Figure 4.11: Vibration response of OT7 and base insert assemblies - Experimental setup 1

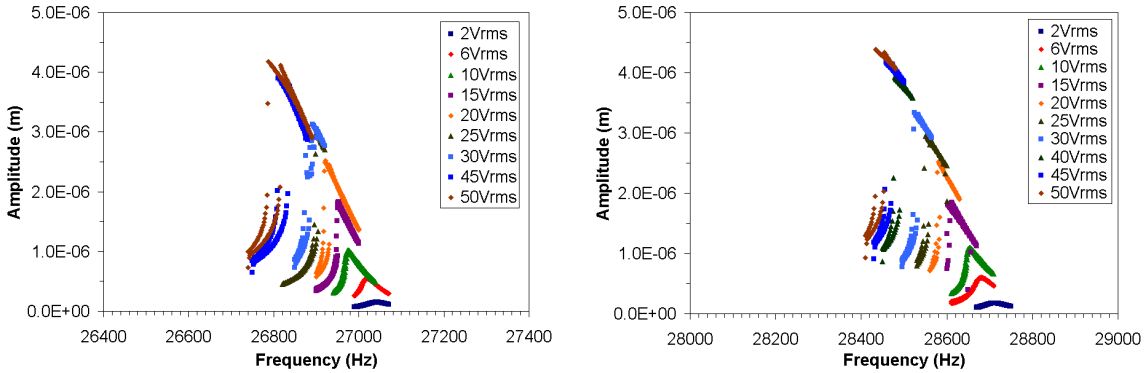

(a) Vibrational response of OT7 insert

(b) Vibrational response of base insert

Figure 4.12: Vibration response of OT7 and base insert assemblies - Experimental setup 2

The vibration response measurements were recorded from the free end of the endmass of the transducer (Figures 4.11 and 4.12) due to the difficult nature of acquiring measurements from the insert end. Initially at an excitation level of 2V_{rms} good correlation can be seen between the resonant frequencies, percentage difference of 0.24% and 0.61% (70Hz and 209Hz), and response amplitudes at these frequencies, a difference in vibrational amplitude of 0.05μm and 0.07μm, for the assemblies containing the base tip and OT7 inserts respectively. Good correlation was also seen at an excitation level of approximately 20V_{rms} between the

measurements taken by the two experimental setups, a percentage difference between the resonant frequencies of 0.73% and 0.57% (209Hz and 153Hz) was found while the amplitudes at these frequencies differed by 0.3μm and 0.1μm for the assemblies containing the base tip and OT7 inserts respectively.

However, the main variation between amplitude responses are in measurements taken at 53V_{rms} using experimental setup 1 and at 50V_{rms} using experimental setup 2. The amplitude response at 50V_{rms} measured by experimental setup 2 can be seen to have both the largest resonant frequency shift and maximum amplitude when compared to lower voltage levels. However it can be observed from measurements recorded at 53V_{rms} using experimental setup 1, the resonant frequency shift and maximum amplitude appear to be less than those measured an excitation level of 35V_{rms}. The saturation of vibrational amplitude at 53V_{rms} is probably due to temperature increases within the piezoceramic elements, however, the larger shift of resonant frequency at 35V_{rms}, where a larger vibrational amplitude was achieved may suggest that frequency shift is influenced more by amplitude of vibration rather than excitation voltage.

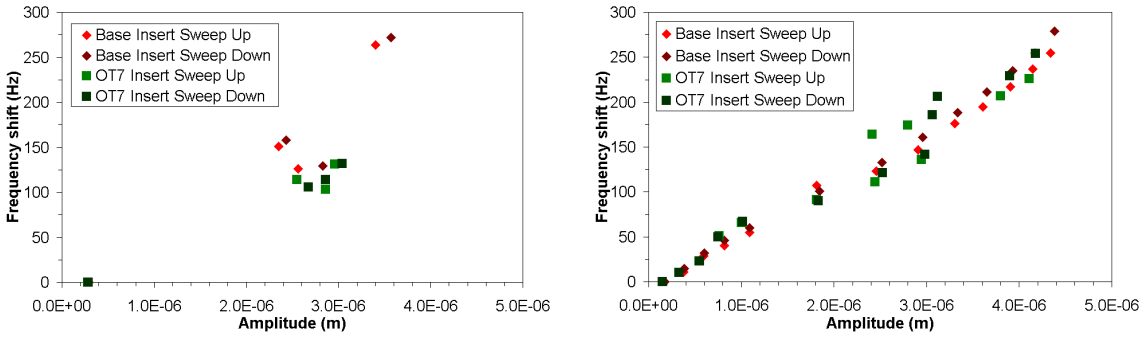

(a) Resonant frequency shift: Experimental setup 1 (b) Resonant frequency shift: Experimental setup 2

Figure 4.13: Comparison of resonant frequency shift found through experimental setup 1 & experimental setup 2

The resonant frequency shift (discussed in Section 1.5.1) found using experimental setups 1 and 2 can be seen in Figure 4.13. Figure 4.13(a) does not contain an abundance of data points and it is therefore difficult to state concrete conclusions, nevertheless at an amplitude of 2.8μm resonant frequency shifts of 129Hz and 114Hz were found using experimental setup 1 during the downward sweep, while at an amplitude of 2.9μm frequency shifts of 161Hz and 142Hz were found using experimental setup 2 during the downward sweep for the assemblies containing the base and OT7 inserts respectively. This is a resonant frequency shift of 0.021Hz and 0.025Hz per micron for the frequency shifts found using experimental setup 1 for the base and OT7 inserts, while a frequency shift of 0.018Hz and 0.020Hz per micron was found using experimental setup 2 for the base and OT7 inserts respectively. The similarity of frequency shift per micron strengthens the validity of the experimental setups. However, as previously discussed, temperature increases within piezoceramic elements can alter their dielectric and

elastic properties enough that they can significantly influence nonlinear behaviour, such as resonant frequency shift. This may suggest due to a smaller shift per micron exhibited in measurements found using experimental setup 2, that it is more successful at removing the thermal effect within the piezoceramic.

Amplitude jumps occurred in the responses of both OT7 and base insert assemblies when measured using both experimental techniques. In both cases they first appear in the response curves found using experimental setup 2 at a driving voltage of $15V_{rms}$ and amplitude of vibration of 1.8μm. This suggests that the presence of the blade and shank in the OT7 insert does not strongly affect this nonlinear behaviour.

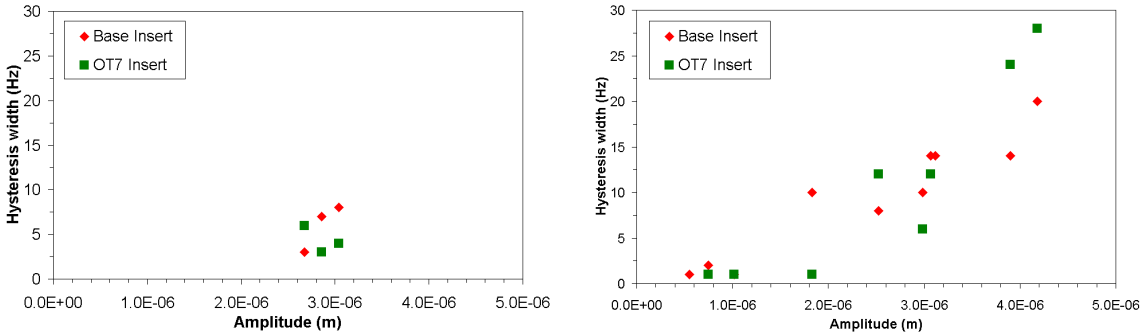

(a) Hysteretic width: Experimental setup 1

(b) Hysteretic width: Experimental setup 2

Figure 4.14: Comparison of hysteretic width found through experimental setup 1 & experimental setup 2

The width in the hysteretic regions between the resonant frequencies found during the upward and downward sweeps using experimental setups 1 and 2 can be seen in Figure 4.14. Again the number of data points found using experimental setup 1 is limited, however at an approximate amplitude of 3μm a hysteretic width of 8Hz and 4Hz was found using experimental setup 1, while hysteretic widths of 10Hz and 6Hz were found using experimental setup 2 for the assemblies containing the base and OT7 inserts respectively. Although the measured hysteresis widths are similar in both cases, the regions are smaller in the measurements taken with experimental setup 1. The source of this may be the difference in ambient air temperature between the measurements taken by the two experimental setups. Ambient air temperatures remained relatively constant during data collection using both experimental setups, however, whilst the air temperature during data collection using experimental setup 1 remained at approximately 20°C, the air temperature during measurements using experimental setup 2 was approximately 30°C. Literature [7, 154, 157], and experimental measurements in Section 4.4 suggest that a relatively small rise in temperature could change material properties of piezoceramics, thus causing an increase in hysteresis width, thus suggesting that hysteretic width is also partly dependent on the temperature of the piezoceramic stack.

Measurements of the current drawn through the piezoceramic stack of the transducer were

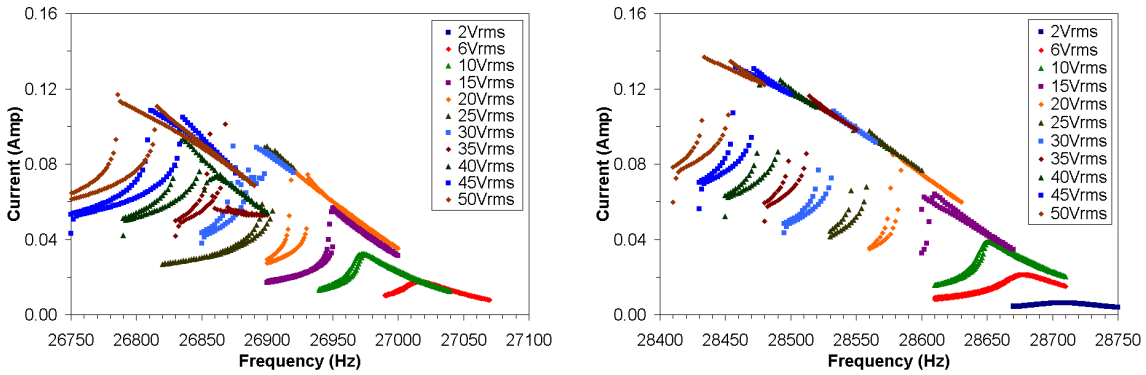

(a) OT7 insert assembly

(b) Base insert assembly

Figure 4.15: Current drawn by transducer during characterisation of OT7 and base insert assemblies - Experimental setup 2

recorded using experimental setup 2, Figure 4.15. The figures illustrate nonlinear behaviours which the tuned assemblies suffer from are consistent to those in Figure 4.12. Amplitude saturation seen in Figure 4.12 whose source lies in the nonlinear response of the tuned assemblies is also prevalent in the figure which plots the current drawn by the transducer against frequency. This allows both the amplitude of vibration and drawn current to be used to quantify the nonlinear behaviour of the tuned assemblies.

Harmonic responses

During measurements using experimental setup 2, an oscilloscope was used to view the vibration response of the tuned assemblies between 0-100kHz. Figures 4.16(a) and 4.16(b) are captured from the oscilloscope at frequencies close to resonance at an excitation voltage of $50V_{rms}$. Both images suggest the existence of nonlinear behaviour other than the resonant frequency shifts and hysteresis regions seen in Figures 4.11 and 4.12.

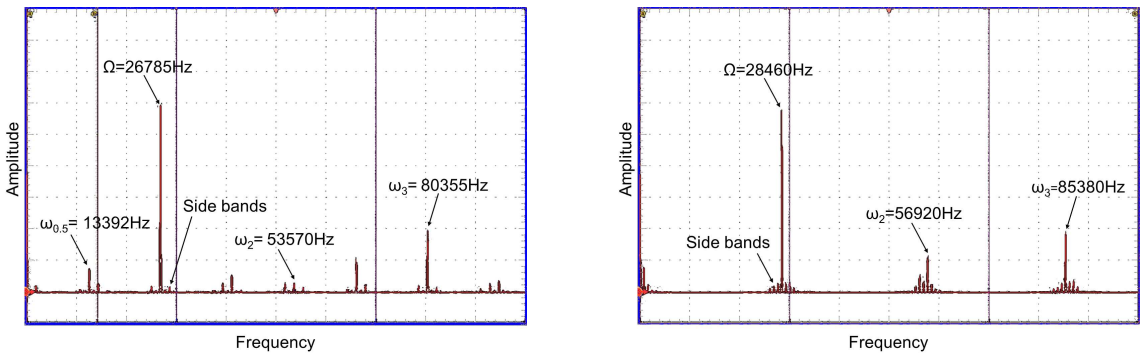

(a) OT7 Insert: Excitation frequency 26785Hz at $50V_{rms}$ (x-axis: 10kHz per block, y-axis: 100mV per block)

(b) Base Insert: Excitation frequency 28460Hz at $50V_{rms}$ (x-axis: 10kHz per block, y-axis: 100mV per block)

Figure 4.16: Oscilloscope images captured of OT7 and base inserts near resonance

Both oscilloscope traces (Figure 4.16) confirm that the tuned assemblies also experience harmonic responses at an excitation level of $50V_{rms}$. The fundamental frequency (Ω) as well as the 1^{st} and 2^{nd} harmonic frequencies (ω) are marked on the traces. Comparing Figure 4.16(a) to Figure 4.16(b) it is possible to observe that both assemblies suffer from harmonic responses as well as sidebands either side of the resonant and harmonic/subharmonic frequencies. However it can also be seen from Figure 4.16(a) that the assembly containing the OT7 insert contains a richer content of responses other than just the harmonic and subharmonics. This could indicate that the assembly with the OT7 insert could be exhibiting period doubling (Section 1.5.2), a condition which can lead to chaotic behaviour [81].

4.3.2 Commercial surgical insert: Full wavelength assemblies

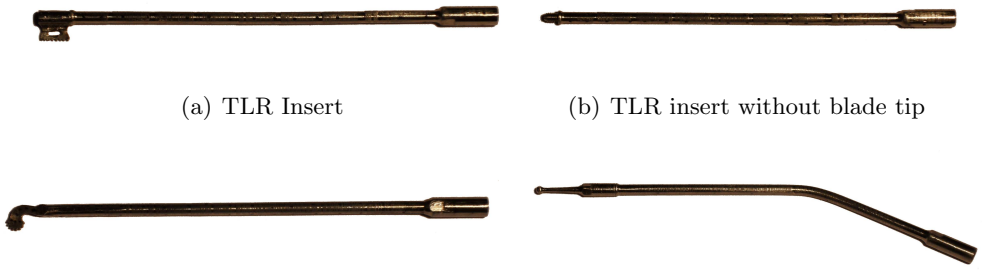

(a) TLR Insert (b) TLR insert without blade tip

(c) X15TR Insert (d) 420BR Insert

Figure 4.17: Photographs of half wavelength Mectron inserts

Three commercial surgical inserts designed to operate in conjunction with the Piezosurgery® Device have been analysed within their linear region using experimental modal analysis and characterised under high power driving conditions using experimental techniques discussed in Section 4.2.2. The inserts, Figure 4.17, are half wavelength and are designed to operate with the Piezosurgery® transducer as a full wavelength assembly, Figure 4.7, at the second longitudinal mode and are manufactured from three different alloys. The TLR insert, which possesses a removable blade tip, is manufactured from titanium and has been characterised with and without its blade tip. Both the X15TR insert and 420BR inserts are manufactured from stainless steel, although different alloys. The 420BR also contains a removable tip, however it was not removed during this study.

The mechanical quality factors of the surgical inserts can be seen in Table 4.1. It was found that the stainless steel inserts achieved the highest Q_m factors, while removing the blade tip from the TLR insert increased the Q_m factor.

	Q_m factor	Material of manufacture
TLR insert with blade tip	417.7	Titanium
TLR insert without blade tip	498.0	Titanium
X15TR insert	904.9	Stainless steel
420BR	723.3	Stainless steel

Table 4.1: Mechanical quality factors and material of manufacture of full wavelength surgical assemblies

Experimental modal analysis of full wavelength assemblies

The frequencies and mode shapes of the longitudinal modes between 0-80kHz of the surgical inserts found through experimental modal analysis can be seen in Figures 4.18 to 4.21. The frequencies of the longitudinal modes predicted through finite element methods were supplied by Mectron S.p.A (Table 4.2) and correlated well with those found through EMA.

	TLR (with tip)	X15TR	420BR
	(Hz)		
1^{st} Longitudinal mode	9568	10786	10984
2^{nd} Longitudinal mode	26910	28873	27386
3^{rd} Longitudinal mode	40056	43774	41560
4^{th} Longitudinal mode	48560	51594	49640
5^{th} Longitudinal mode	59648	68516	62024

Table 4.2: Longitudinal frequencies of full wavelength surgical assemblies predicted through FEA

Comparisons between Figures 4.18 and 4.19 illustrate the influence that the blade tip has on the natural frequency and shape of the longitudinal modes of the TLR insert. It can be seen that the resonant frequencies of the modes without the blade tip is higher than those with the blade tip, while its presence also induces a flexural motion in to each of the longitudinal modes of vibration. Figure 4.22 presents the percentage difference between the predicted frequencies of the longitudinal modes of vibration and those measured through EMA. Good correlation can be seen between the tuned mode of vibration (2^{nd} longitudinal) with a percentage difference of 3.62%, 2.70% and 2.79% between predicted and measured frequencies.

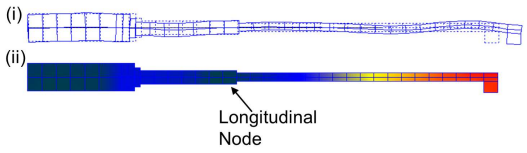

(a) FEA: 1st long. mode $f = 10159$Hz

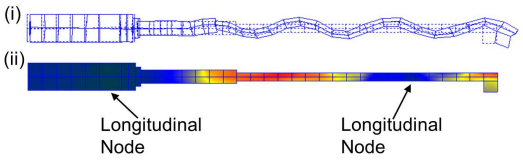

(b) EMA: 2nd long. mode $f = 25935$Hz

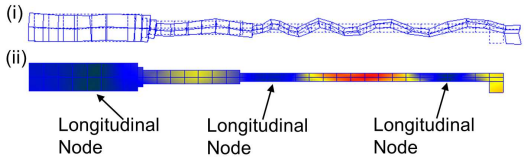

(c) EMA: 3rd long. mode $f = 39028$Hz

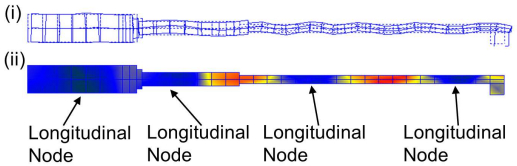

(d) EMA: 4th long. mode $f = 46248$Hz

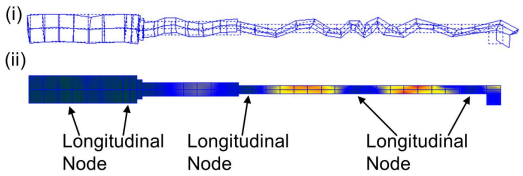

(e) EMA: 5th long. mode $f = 62427$Hz

Figure 4.18: Transducer with TLR insert and blade tip - (i)Deformed/undeformed (ii)Undeformed normalised contour map of displacement

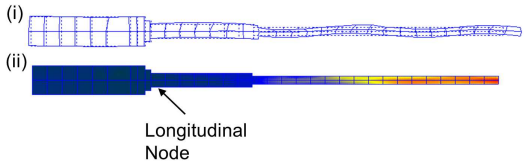

(a) EMA: 1st long. mode $f = 11649$Hz

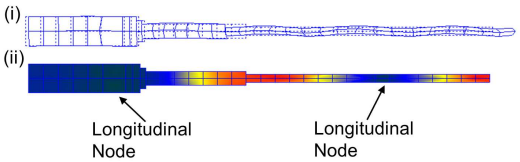

(b) EMA: 2nd long. mode $f = 28627$Hz

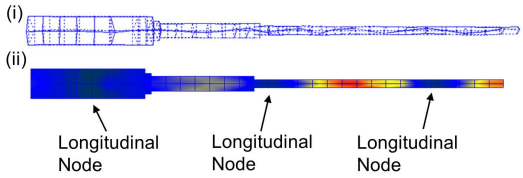

(c) EMA: 3rd long. mode $f = 43656$Hz

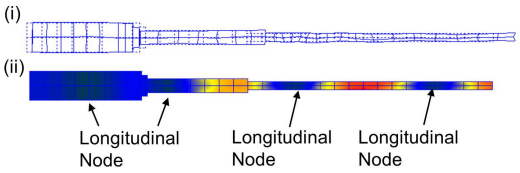

(d) EMA: 4th long. mode $f = 49470$Hz

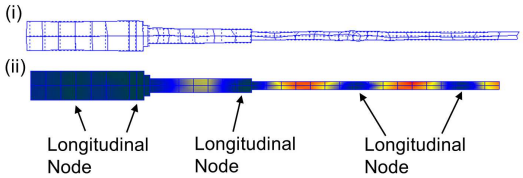

(e) EMA: 5th long. mode $f = 67966$Hz

Figure 4.19: Transducer with TLR insert without blade tip - (i)Deformed/undeformed (ii)Undeformed normalised contour map of displacement

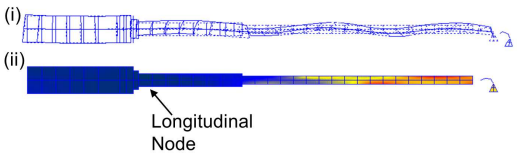

(a) EMA: 1st long. mode $f = 11642$Hz

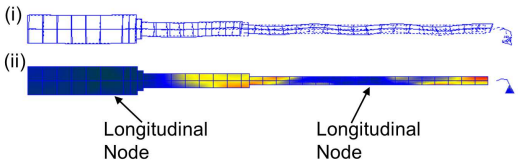

(b) EMA: 2nd long. mode $f = 28094$Hz

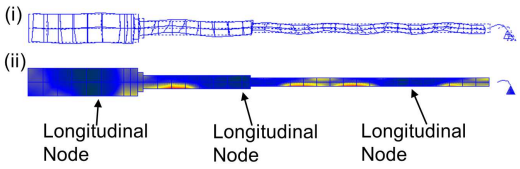

(c) EMA: 3rd long. mode $f = 43120$Hz

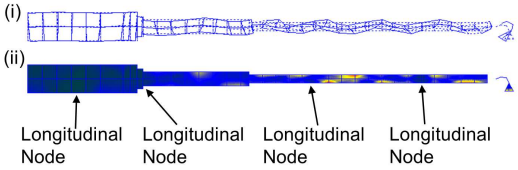

(d) EMA: 4th long. mode $f = 51232$Hz

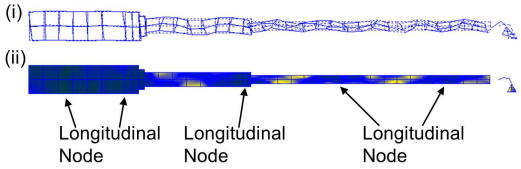

(e) EMA: 5th long. mode $f = 72315$Hz

Figure 4.20: Transducer with X15TR insert - (i)Deformed/undeformed (ii)Undeformed normalised contour map of displacement

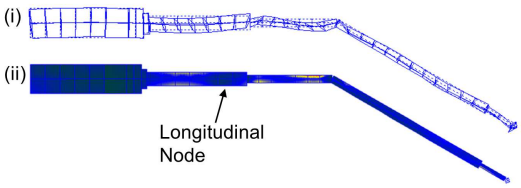

(a) EMA: 1st long. mode $f = 12742$Hz

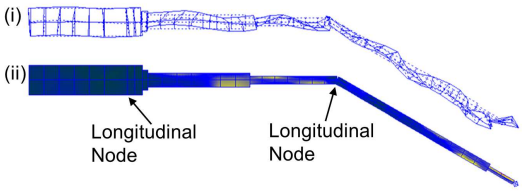

(b) EMA: 2nd long. mode $f = 26621$Hz

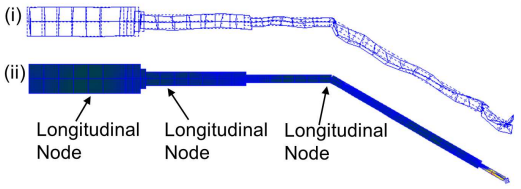

(c) EMA: 3rd long. mode $f = 43508$Hz

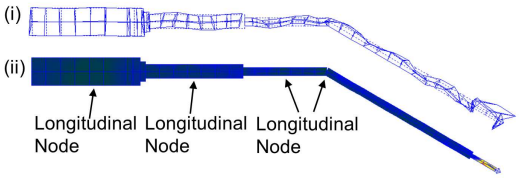

(d) EMA: 4th long. mode $f = 46986$Hz

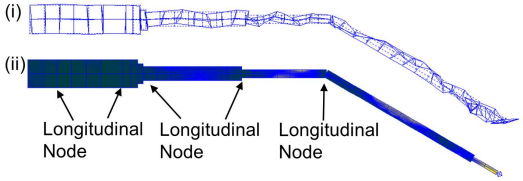

(e) EMA: 5th long. mode $f = 66157$Hz

Figure 4.21: Transducer with 420BR insert - (i)Deformed/undeformed (ii)Undeformed normalised contour map of displacement

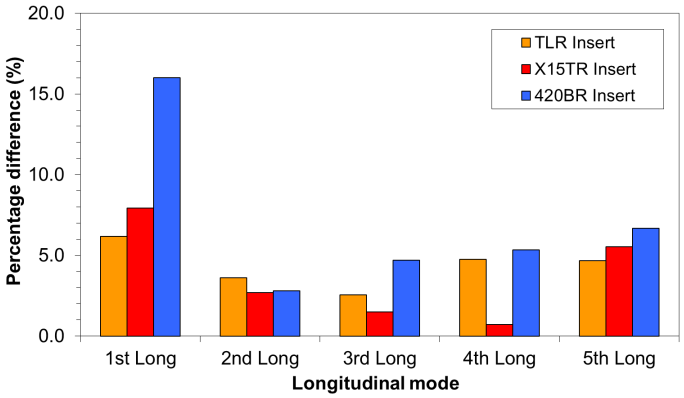

Figure 4.22: Percentage difference between frequencies of longitudinal modes found through FEA and EMA

Power harmonic characterisation of full wavelength surgical assemblies

The response measurements seen in Figure 4.23 represent the vibrational amplitude of the full wavelength surgical assemblies excited close to the second longitudinal mode of vibration. The measurements where taken from the free end of the base of the transducer and the ambient air temperature throughout data collection was approximately 30°C, while the frequency resolution was 1Hz between 1-10V_{rms} and 2Hz between 15-50V_{rms}.

As with previous transducer-horn assemblies studied in this chapter, the softening phenomenon is visible in the frequency response of each of the surgical insert assemblies, Figures 4.23 and 4.24. Over the range of vibrational amplitude, Figure 4.25, it can be seen that the assembly containing the TLR insert suffers from the largest shift in resonance frequency when compared to the X15TR and 420BR inserts. At an amplitude of vibration of approximately 0.25μm, the shift in resonant frequency in the assembly containing the TLR insert with the blade tip attached was 36Hz during the upward sweep and 41Hz for the downward sweep. Meanwhile, with the blade tip removed from the TLR insert a smaller shift in resonant frequency, 13Hz and 15Hz during the upward and downward sweeps, was observed. However, this was still larger than observed in the assemblies containing the X15TR and 420B inserts as the shift in resonant frequency during the upward and downward sweeps were 1Hz and 6Hz and 12Hz and 14Hz, respectively. At a vibrational amplitude of approximately 2.5μm the same trend can be seen. The TLR insert with the blade tip suffers from the largest resonant frequency shift, 118Hz during the sweep up and 120Hz during the sweep down, while the X15TR assembly suffers from the smallest shift in resonant frequency at this amplitude with shifts of 77Hz and 80Hz respectively.

Amplitude jumps appear in the responses, Figures 4.23 and 4.24, of the assemblies containing the TLR inserts, with and without the blade tip and the 420BR at an excitation voltage of 25V_{rms} and amplitude response of 1.97μm, 2.47μm and 1.60μm, respectively.

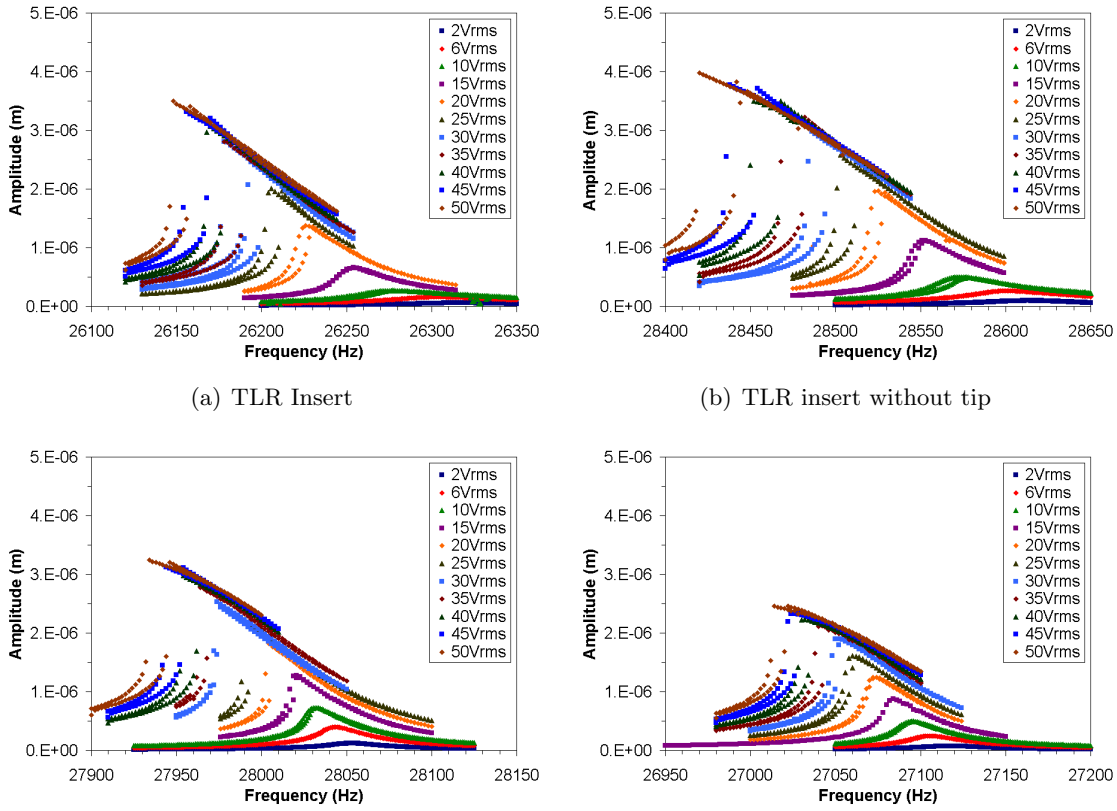

(a) TLR Insert

(b) TLR insert without tip

(c) X15TR Insert

(d) 420BR Insert

Figure 4.23: Vibrational response of full wavelength surgical assemblies between 2-50V_{rms}

However, they appear in the assembly containing the X15TR insert at a lower driving voltage of 15V_{rms} where the amplitude of vibration was 1.26μm.

The hysteretic width found in the assemblies containing the TLR, X15R and 420BR inserts can be seen in Figure 4.25(b). Below 2.0μm the width of the hysteretic regions are almost negligible, however, above 2.0μm as the amplitude of vibration increases so does the width of the hysteretic regions. The largest hysteretic width, 22Hz, is observed in the assembly (containing the TLR insert with the blade tip) that achieves the largest amplitude of vibration, 3.82μm.

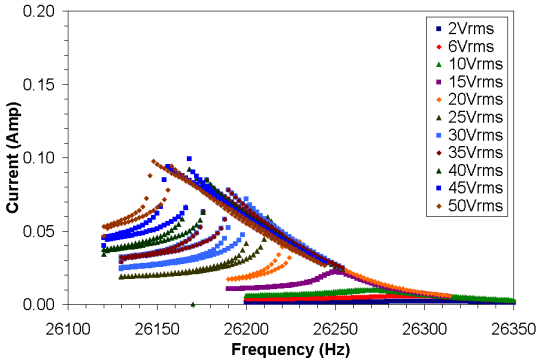

(a) TLR Insert

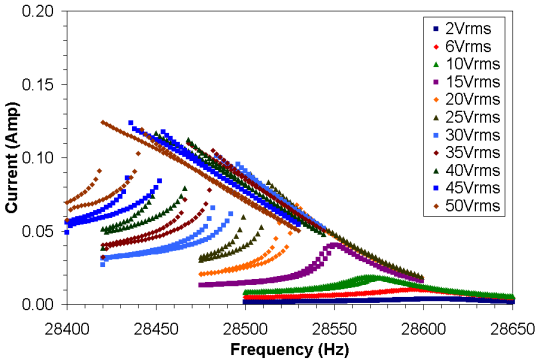

(b) TLR insert without tip

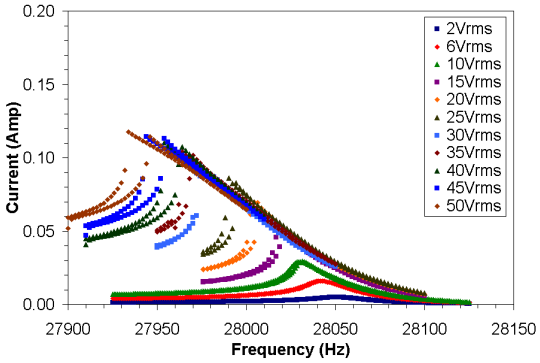

(c) X15TR Insert

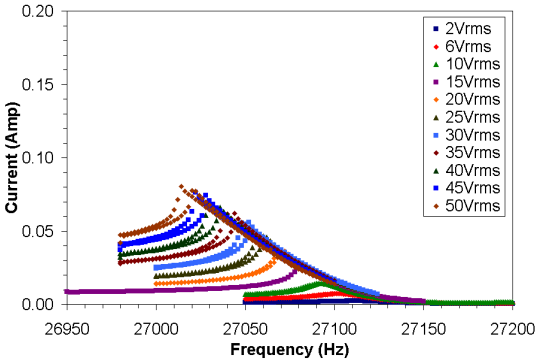

(d) 420BR Insert

Figure 4.24: Current drawn by transducer during response characterisation of full wavelength surgical assemblies

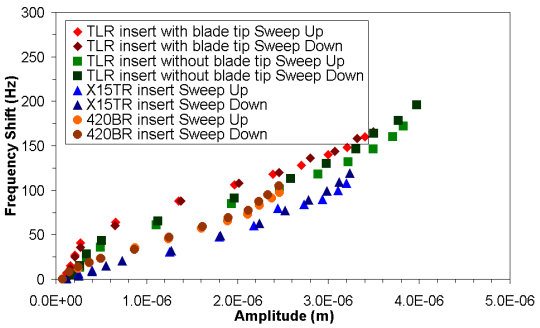

(a) Frequency shift against vibration amplitude

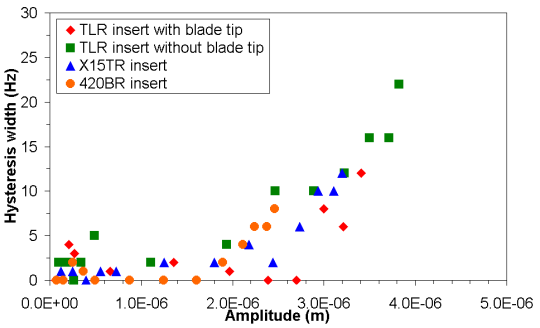

(b) Hysteresis width against vibration amplitude

Figure 4.25: Nonlinear behaviour of full wavelength surgical assemblies

Harmonic responses of full wavelength surgical assemblies

Images captured from the oscilloscope of the spectra response to an excitation close to the resonant frequency, Figures 4.26(a) and 4.26(b), suggest the existence of nonlinear behaviour other than the resonant frequency shifts and hysteresis regions as strong harmonic responses (ω) are visible the power spectra, Figures 4.23 to 4.24.

Under elevated excitation levels it can be seen that the assembly with the TLR insert without the blade tip, Figure 4.26(b), appears to suffer from sidebands around the fundamental and harmonic frequencies. Meanwhile, the TLR insert with the blade tip does not appear to suffer as strongly from sidebands, however, responses can be seen throughout the frequency spectrum that appear to have a relationship with the response seen at approximate 17kHz. The source of this response is unknown as no mode of vibration was found through EMA close to 17kHz nor at the first or second harmonic frequency, although, this spectrum response is similar to that seen in Figure 4.16(a), and again could indicate period doubling [81].

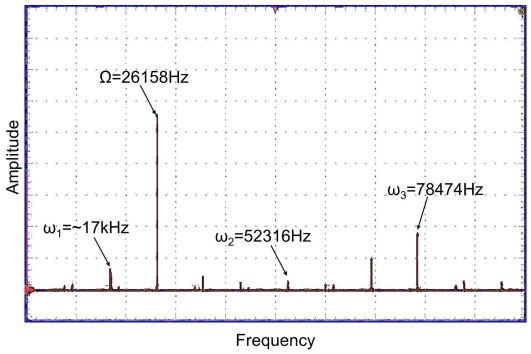

(a) TLR insert with blade tip: Excitation frequency 26158Hz at $50V_{rms}$ (x-axis: 10kHz per block, y-axis: 100mV per block)

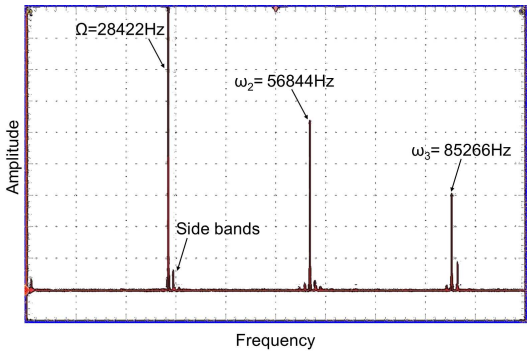

(b) TLR insert without blade tip: Excitation frequency 28422Hz at $50V_{rms}$ (x-axis: 10kHz per block, y-axis: 10mV per block)[1]

Figure 4.26: Power spectrum images captured of TLR insert with/without blade tip

4.3.3 Custom Inserts

Rod horns, tuned to operate with the surgical transducer as either half or full wavelength assemblies (Figure 4.27), were designed using methods discussed in Chapter 3 and manufactured from aluminium, brass and stainless steel alloys, Table 4.3. The half wavelength transducer-rod horn assemblies were tuned to oscillate in the first longitudinal mode within the range of 20-30kHz, while the full wavelength assemblies were tuned to oscillate in the second longitudinal mode within the range of 25-32kHz.

The mechanical quality factors of both the half and full wavelength rod horn-transducer assemblies were calculated using the $\sqrt{2}$ peak method (discussed Section 3.1.3) and data

[1]Captured image does not illustrate full amplitude of fundamental response, $\Omega = 28422$Hz

(a) Aluminium 6082 (b) Brass

(c) Stainless Steel AISI 316

Figure 4.27: Rod horns used in the half and full wavelength assemblies

	Density kgm^{-3}	Young's Mod MPa	Poisson's ratio	Length of rod horns mm	
				Assembly	
				Half λ	Full λ
Aluminium 6082	2628	69.50	0.346	16	95
Brass	8532	95.95	0.340	13	60
Stainless Steel AISI 316	7869	193.00	0.290	13	110

Table 4.3: Properties of rod horn material of manufacture

collected from their linear response when driven under low amplitudes of vibration, Table 4.4. The full wavelength assembly containing the aluminium rod had the greatest Q_m while the half wavelength assembly containing the stainless steel rod horn had the lowest Q_m. It can be observed that each of the full wavelength assemblies had a greater Q_m than the half wavelength assemblies of corresponding material.

	Q_m	
Rod horn	Half λ	Full λ
Aluminium 6082	492.3	1228.0
Brass	316.2	955.2
Stainless Steel AISI 316	311.1	337.3

Table 4.4: Mechanical quality factors of rod horn assemblies

4.3.4 Custom Insert: Half wavelength assemblies

Finite element and experimental modal analysis of custom half wavelength assemblies

The natural frequencies and mode shapes of the first, second and third longitudinal modes found through finite element analysis correlated well with the modal parameters found through experimental modal analysis, Figures 4.28, 4.29 and 4.30. Meanwhile, Figure 4.31 illustrates the percentage difference between the predicted and measured frequencies of each of the longitudinal modes of vibration, where it can be seen that the measured frequencies of the tuned mode (1^{st} longitudinal mode of vibration) achieved the smallest percentage difference for each of the half wavelength rod horn assemblies.

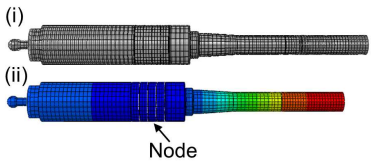

(a) FEA: 1^{st} longitudinal mode
$f = 29920$Hz

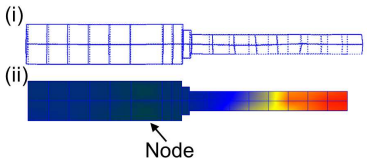

(b) EMA: 1^{st} longitudinal mode
$f = 29014$Hz

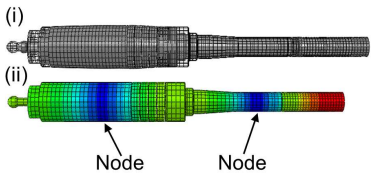

(c) FEA: 2^{nd} longitudinal mode
$f = 48920$Hz

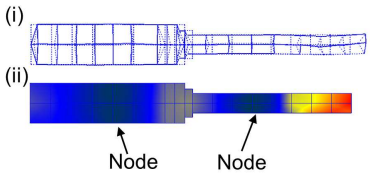

(d) EMA: 2^{nd} longitudinal mode
$f = 45582$Hz

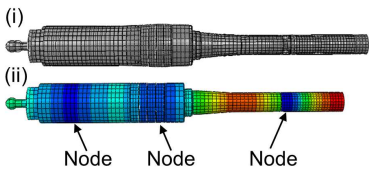

(e) FEA: 3^{rd} longitudinal mode
$f = 81454$Hz

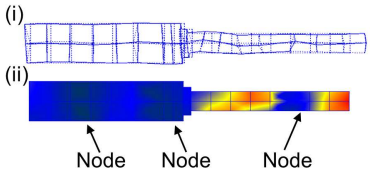

(f) EMA: 3^{rd} longitudinal mode
$f = 74784$Hz

Figure 4.28: Half wavelength aluminium rod horn assembly: Mode shapes of longitudinal modes of vibration found through FEA/EMA:
(i)Deformed/undeformed (ii)Undeformed normalised contour map of displacement

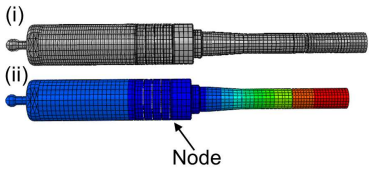

(a) FEA: 1st longitudinal mode
$f = 22693$Hz

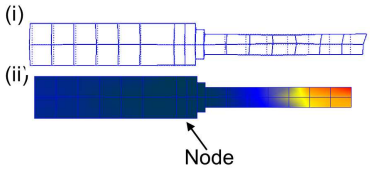

(b) EMA: 1st longitudinal mode
$f = 21657$Hz

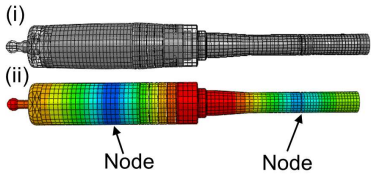

(c) FEA: 2nd longitudinal mode
$f = 47604$Hz

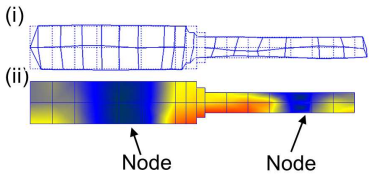

(d) EMA: 2nd longitudinal mode
$f = 43860$Hz

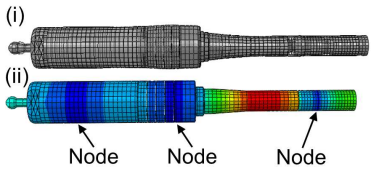

(e) FEA: 3rd longitudinal mode
$f = 78344$Hz

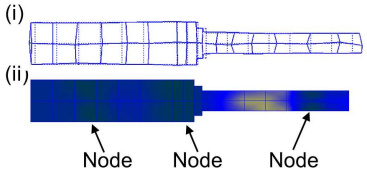

(f) EMA: 3rd longitudinal mode
$f = 72530$Hz

Figure 4.29: Half wavelength brass rod horn assembly: Mode shapes of longitudinal modes of vibration found through FEA/EMA:
(i)Deformed/undeformed (ii)Undeformed normalised contour map of displacement

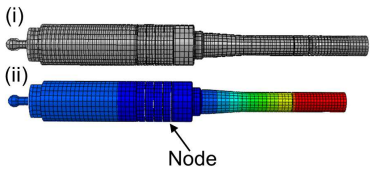

(a) FEA: 1st longitudinal mode
$f = 24957$Hz

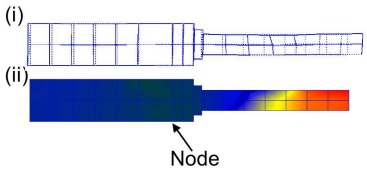

(b) EMA: 1st longitudinal mode
$f = 24868$Hz

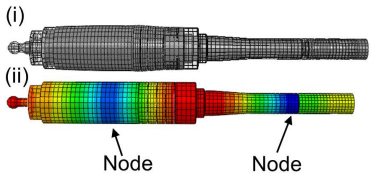

(c) FEA: 2nd longitudinal mode
$f = 48144$Hz

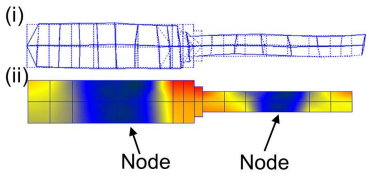

(d) EMA: 2nd longitudinal mode
$f = 45046$Hz

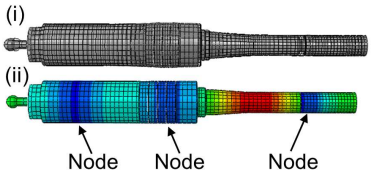

(e) FEA: 3rd longitudinal mode
$f = 82112$Hz

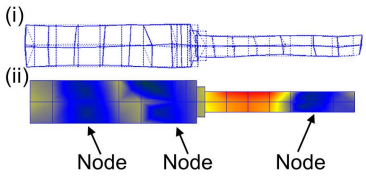

(f) EMA: 3rd longitudinal mode
$f = 77229$Hz

Figure 4.30: Half wavelength stainless steel rod horn assembly: Mode shapes of longitudinal modes of vibration found through FEA/EMA:
(i)Deformed/undeformed (ii)Undeformed normalised contour map of displacement

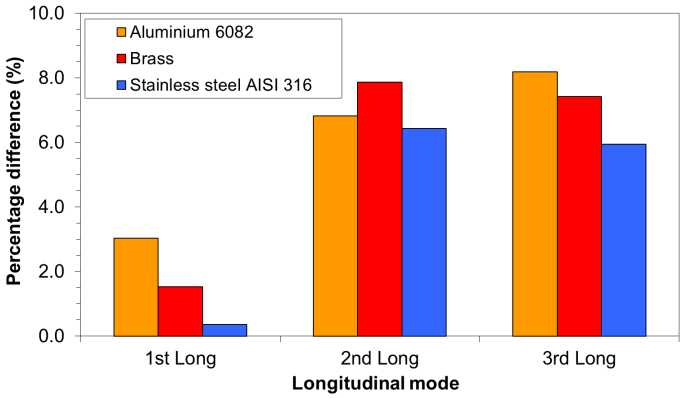

Figure 4.31: Percentage difference between frequency of longitudinal vibration of custom half wavelength assemblies

Power harmonic characterisation

Frequency response curves of the half wavelength assemblies excited close to the first longitudinal mode can be seen in Figure 4.32. The vibration response measurements were recorded from the free end of the rod horn and the ambient air temperature throughout the duration of the burst sine sweep characterisation remained around 30°C.

The manifestation of resonant frequency shift and hysteretic regions can be observed in Figures 4.32 and 4.33. From Figure 4.34(a) it can be seen that below an amplitude of vibration of approximately 12.5μm, the rod horn assemblies exhibit a similar shift in resonant frequency, while above 12.5μm the shift in resonant frequency of the rod horn assemblies appears to differ, increasingly with vibrational amplitude. At an amplitude of vibration of approximately 25μm, the frequency shift is largest in the assembly containing the stainless steel rod horn, where it is 341Hz, while in the assemblies containing the aluminium and brass rod horns, the frequency shift is 230Hz and 125Hz respectively.

The advent of amplitude jumps occurs initially only during the upward sweep at an excitation voltage of 15V_{rms} for the rod horn assemblies where the output amplitude of the aluminium, brass and stainless steel assemblies was 12.5μm, 11.5μm and 10.7μm respectively, Figure 4.32. However, above 15V_{rms}, amplitude jumps were found to occur during both upward and downward frequency sweeps. At an excitation voltage of 20V_{rms} the amplitude of vibration at the top of the jumps were 17.1μm (sweep up) and 16.7μm (sweep down) for the aluminium rod horn assembly, while the amplitude of vibration at the top of the jump for the brass and stainless rod horn assemblies was 18.1μm (sweep up) and 17.8μm (sweep down), and 14.1μm (sweep up) and 12.2μm (sweep down), respectively

The width of the hysteretic regions against amplitude of vibration response can be seen in Figure 4.34(b). Below a vibration amplitude of 12.5μm, the width of the region seen in each of the rod horn assemblies is insignificant, however, above an vibration amplitude 12.5μm the

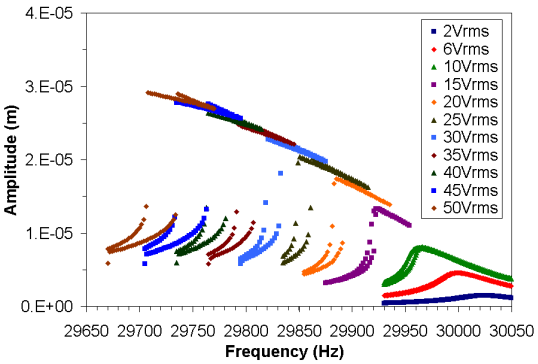

(a) Aluminium: 8062

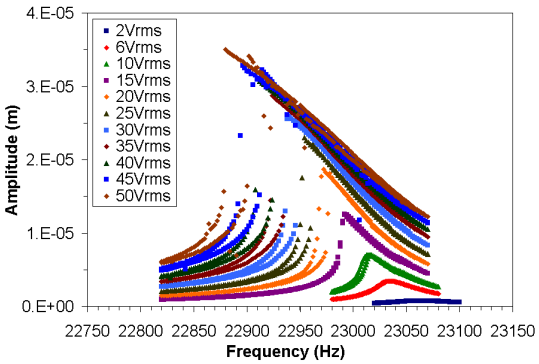

(b) Brass

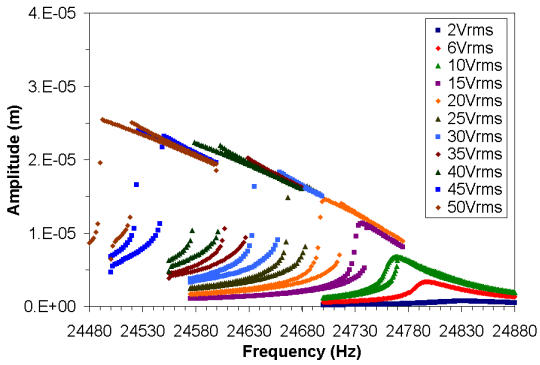

(c) Stainless steel: AISI 316

Figure 4.32: Vibrational response of half wavelength assemblies between 2-50V_{rms}

width of the hysteresis regions increase. At an amplitude response of approximately 25μm the hysteretic region are relatively small at 28Hz, 18Hz and 10Hz for the assemblies containing the stainless steel, aluminium and brass rod horns.

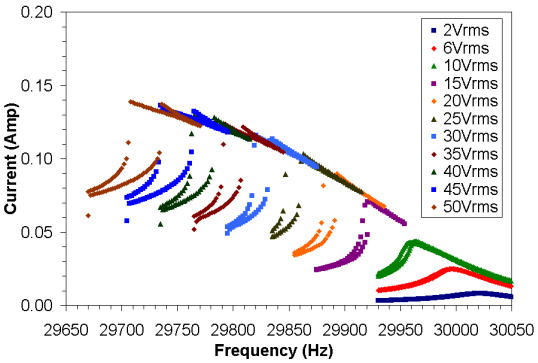

(a) Aluminium: 8062

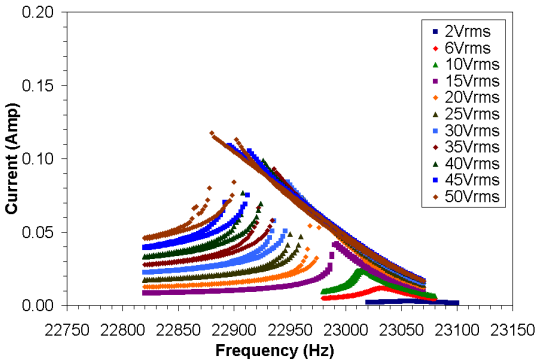

(b) Brass

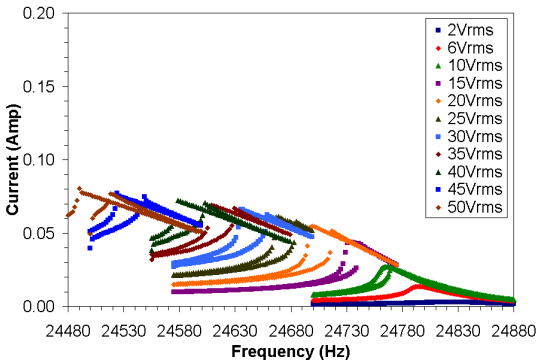

(c) Stainless steel: AISI 316

Figure 4.33: Current drawn by transducer during response characterisation of half wavelength assemblies

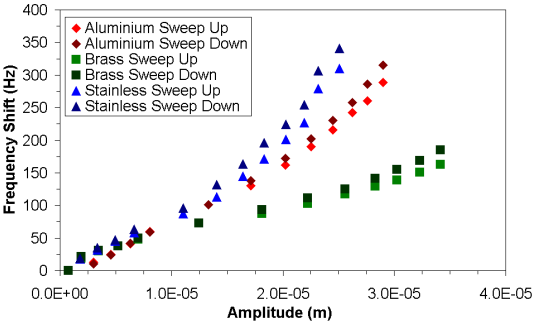

(a) Frequency shift against vibration amplitude

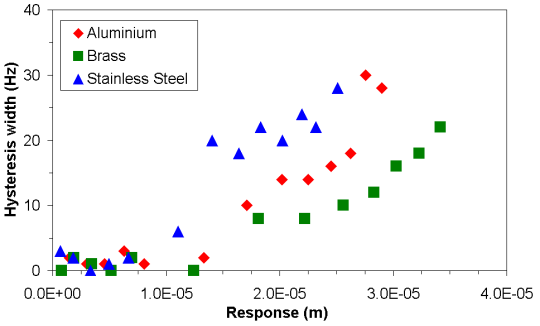

(b) Breadth of hysteresis region against vibration amplitude

Figure 4.34: Nonlinear behaviour of half wavelength assemblies

4.3.5 Custom Insert: Full wavelength assemblies

Finite element and experimental modal analysis of full wavelength assemblies

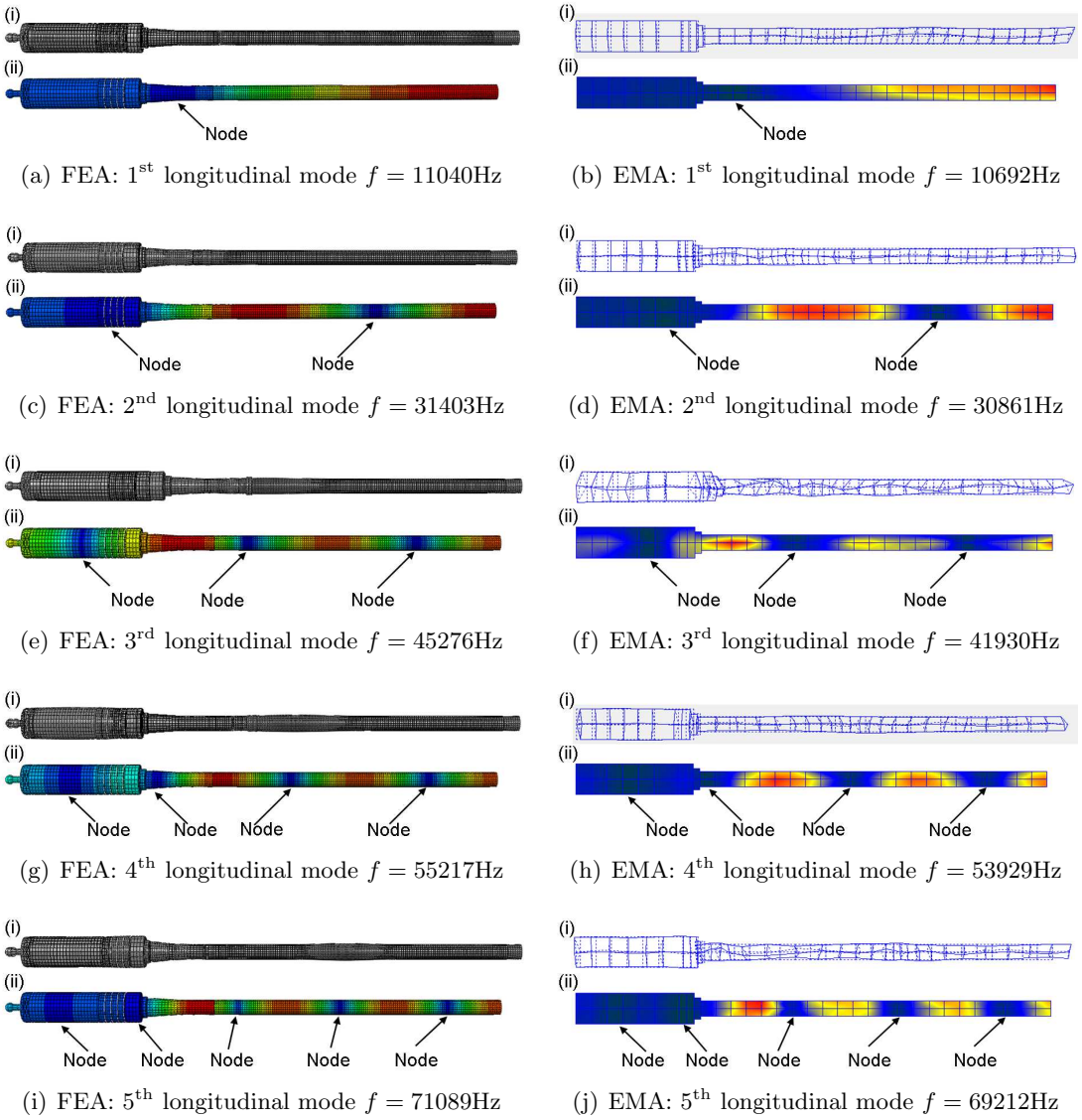

(a) FEA: 1st longitudinal mode $f = 11040$Hz

(b) EMA: 1st longitudinal mode $f = 10692$Hz

(c) FEA: 2nd longitudinal mode $f = 31403$Hz

(d) EMA: 2nd longitudinal mode $f = 30861$Hz

(e) FEA: 3rd longitudinal mode $f = 45276$Hz

(f) EMA: 3rd longitudinal mode $f = 41930$Hz

(g) FEA: 4th longitudinal mode $f = 55217$Hz

(h) EMA: 4th longitudinal mode $f = 53929$Hz

(i) FEA: 5th longitudinal mode $f = 71089$Hz

(j) EMA: 5th longitudinal mode $f = 69212$Hz

Figure 4.35: Full wavelength aluminium rod horn assembly: Mode shapes of longitudinal modes of vibration found through FEA/EMA:
(i)Deformed/undeformed (ii)Undeformed normalised contour map of displacement

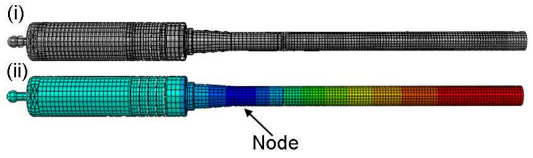

(a) FEA: 1st longitudinal mode $f = 10186$Hz

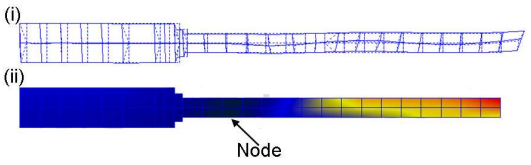

(b) EMA: 1st longitudinal mode $f = 9898$Hz

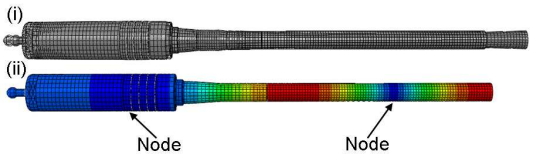

(c) FEA: 2nd longitudinal mode $f = 31906$Hz

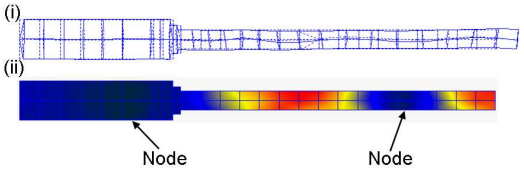

(d) EMA: 2nd longitudinal mode $f = 31754$Hz

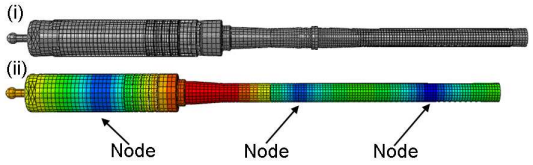

(e) FEA: 3rd longitudinal mode $f = 46127$Hz

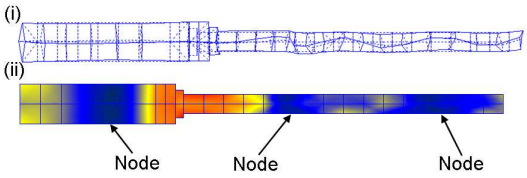

(f) EMA: 3rd longitudinal mode $f = 42975$Hz

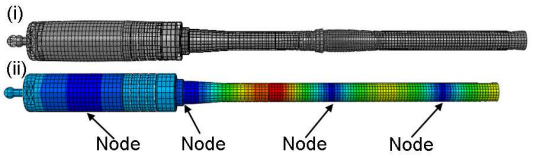

(g) FEA: 4th longitudinal mode $f = 57526$Hz

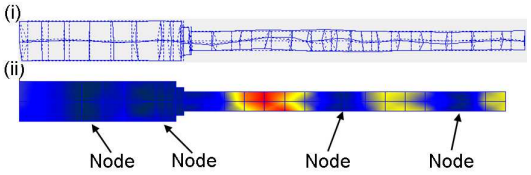

(h) EMA: 4th longitudinal mode $f = 56998$Hz

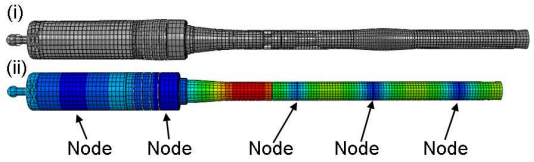

(i) FEA: 5th longitudinal mode $f = 74587$Hz

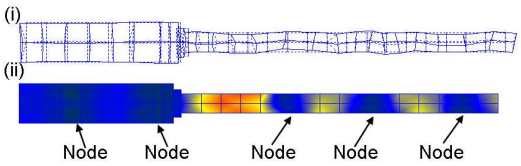

(j) EMA: 5th longitudinal mode $f = 73183$Hz

Figure 4.36: Full wavelength brass rod horn assembly: Mode shapes of longitudinal modes of vibration found through FEA/EMA:
(i)Deformed/undeformed (ii)Undeformed normalised contour map of displacement

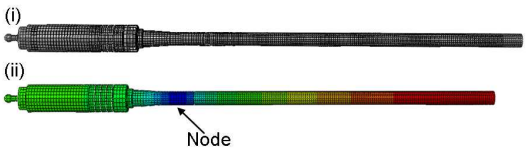

(a) FEA: 1st longitudinal mode $f = 8688$Hz

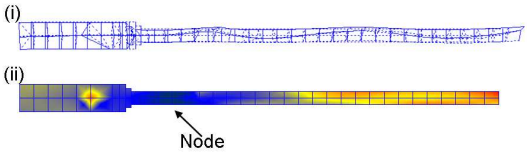

(b) EMA: 1st longitudinal mode $f = 8471$Hz

(c) FEA: 2nd longitudinal mode $f = 25404$Hz

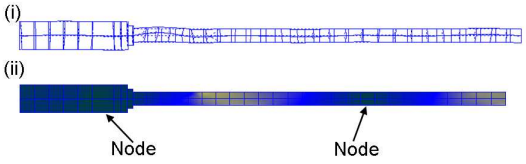

(d) EMA: 2nd longitudinal mode $f = 25250$Hz

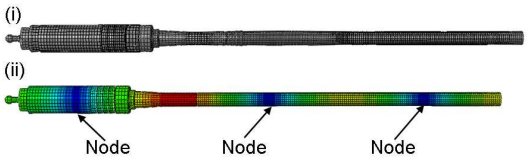

(e) FEA: 3rd longitudinal mode $f = 44298$Hz

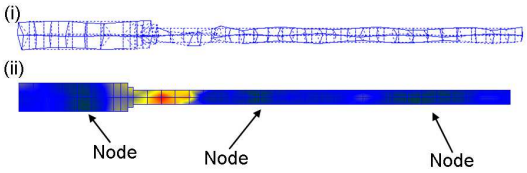

(f) EMA: 3rd longitudinal mode $f = 41957$Hz

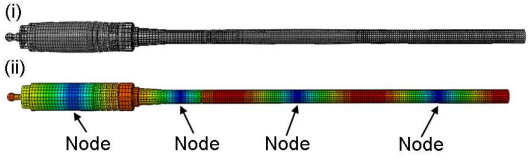

(g) FEA: 4th longitudinal mode $f = 49140$Hz

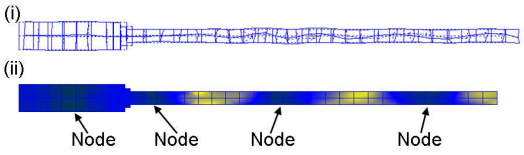

(h) EMA: 4th longitudinal mode $f = 47882$Hz

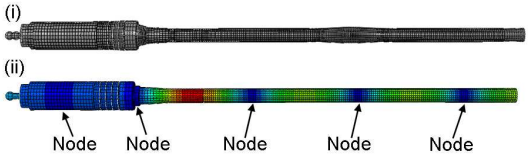

(i) FEA: 5th longitudinal mode $f = 66606$Hz

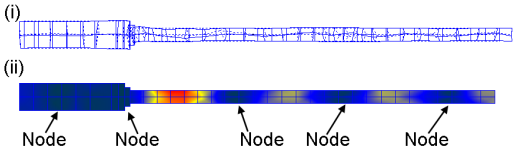

(j) EMA: 5th longitudinal mode $f = 66072$Hz

Figure 4.37: Full wavelength stainless steel rod horn assembly: Mode shapes of longitudinal modes of vibration found through FEA/EMA:
(i)Deformed/undeformed (ii)Undeformed normalised contour map of displacement

The natural frequencies and mode shapes of the first to fifth longitudinal mode found through finite element analysis and experimental modal analysis of the full wavelength assemblies can be seen in Figures 4.35, 4.36 and 4.37. A close match was found to exist between mode shapes and corresponding resonant frequencies obtained through FEA and EMA methods, the percentage difference between the frequencies can be seen in Figure 4.38.

Meanwhile, Figure 4.38 illustrates the percentage difference between the predicted and measured frequencies of each of the longitudinal modes of vibration. It can be seen that the measured frequencies of the tuned mode (2^{nd} longitudinal mode of vibration) achieved the smallest percentage difference for each of the full wavelength rod horn assemblies.

As with previous results, Section 4.3.4, the smallest percentage difference between the predicted and measured resonant frequencies was observed at the tuned longitudinal mode of vibration (2^{nd} longitudinal), Figure 4.38. Meanwhile, the largest percentage difference between predicted and measured longitudinal frequencies was found to be at the 3^{rd} longitudinal mode.

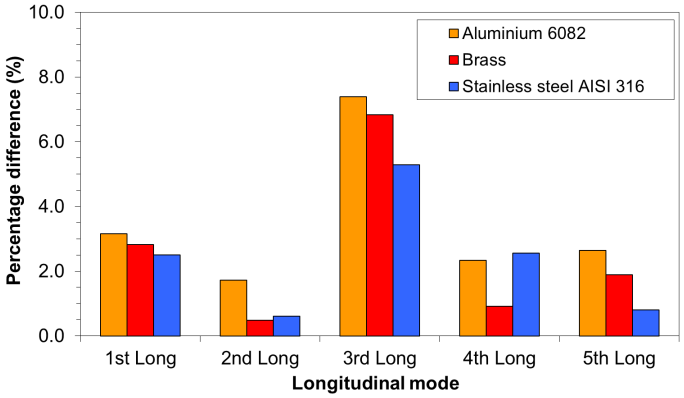

Figure 4.38: Percentage difference between frequency of longitudinal vibration of full wavelength assemblies found through FEA and EMA

Power harmonic characterisation

The frequency response measurements seen in Figure 4.39 represent the vibrational amplitude of the assemblies of the full wavelength assemblies excited close to the second longitudinal mode. The measurements were recorded from the free end of the rod horn and the ambient air temperature was approximately 30°C throughout data collection.

Figures 4.39 and 4.40 (showing current drawn by the transducer) confirm the presence of nonlinear behaviours, resonant frequency widths and hysteretic regions, in the frequency response measurements of the tuned assemblies, although they also suggest that the tuned assemblies do not equally suffer from nonlinear behaviours. Figure 4.41(a) plots resonant frequency shift against amplitude response of the free end of the rod horn. Between amplitudes of vibration of 0.42μm and 2.35μm the assembly containing the stainless steel

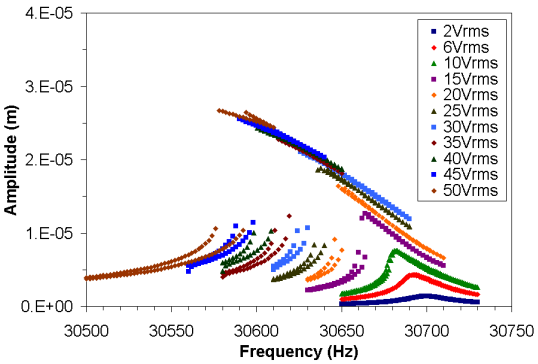

(a) Aluminium: 8062

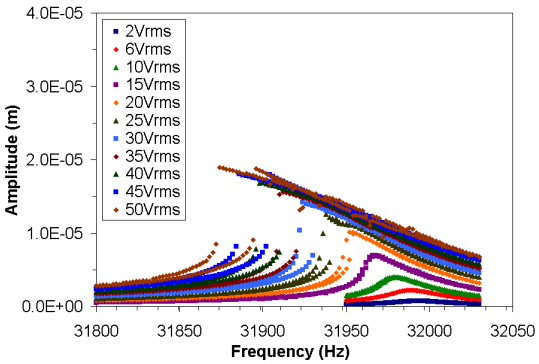

(b) Brass

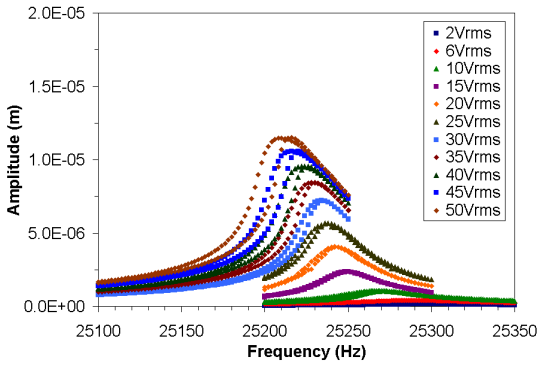

(c) Stainless steel: AISI 316

Figure 4.39: Vibrational response of full wavelength assemblies between 2-50V_{rms}

rod horn exhibits a stronger softening effect than those containing the aluminium and brass rod horns. At an output amplitude of around 2.4μm, the resonant frequency shifts found during upward and downward sweeps of the stainless steel rod horn assembly were 47Hz and 50Hz respectively, while the frequency shift exhibited by the aluminium and brass rod horn assemblies were 4Hz (both upward and downward sweeps) and 5Hz (both upward and downward sweeps) respectively. However above an amplitude of vibration of 2.4μm, a reduction in the influence of the softening effect in the response of stainless steel assembly can be seen, although with an increase in vibrational amplitude, an increase in frequency shift can also be seen. At an amplitude of vibration of approximately 12μm, the stainless steel assembly exhibits the largest shift in resonant frequency, 79Hz (upward sweep) and 92Hz (downward sweep), while the aluminium and brass rod horn assemblies exhibit frequency sweeps of 34Hz and 36Hz, and 49Hz and 56Hz respectively for upward and downward sweeps.

The occurrence of amplitude jumps is observed in Figures 4.39 and 4.40. The aluminium rod horn assembly first experiences amplitude jumps in both upward and downward sweeps at a driving voltage of 15V_{rms} and amplitude response level of 12.5μm, while the brass rod horn assembly experiences jumps from a driving voltage of 20V_{rms} and amplitude response of 9.86μm. However amplitude jumps are not observed in the frequency response of the stainless

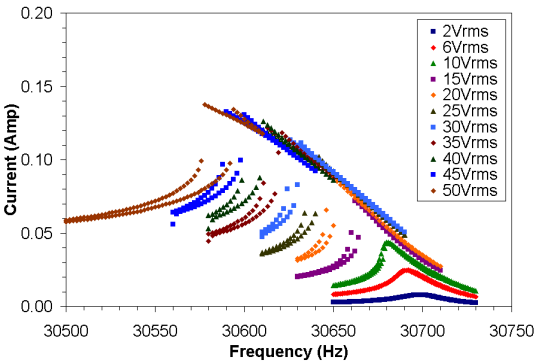

(a) Aluminium: 8062

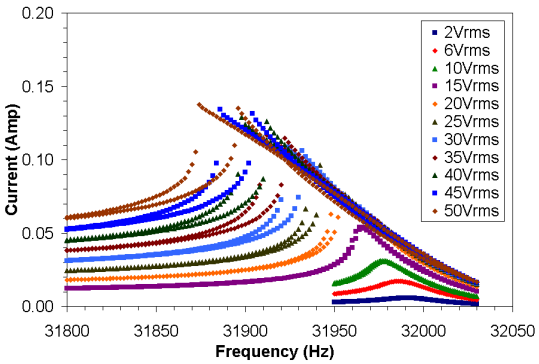

(b) Brass

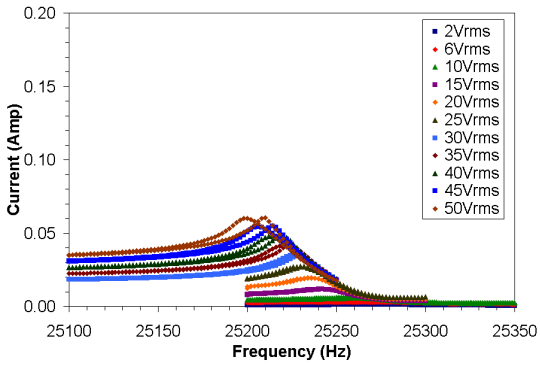

(c) Stainless steel: AISI 316

Figure 4.40: Current drawn by transducer during response characterisation of full wavelength assemblies

steel rod horn assembly even though the amplitude of vibration reached 11.5μm at a driving voltage of 50V_{rms}, Figures 4.39(c) and 4.40(c).

The hysteretic width found for each of the assemblies contain full wavelength assemblies are presented in Figure 4.41(b). Up to an amplitude of vibration of 7μm, the widths are no larger than 5Hz, however above 7μm, it can be seen that the hysteretic widths increase with amplitude of vibration, although amplitude of vibration influences each of the assemblies differently. The stainless steel rod horn assembly achieves a hysteretic width of 8Hz at an amplitude of response of 10.6μm, while the assemblies containing the aluminium and brass rod horns achieve a hysteresis region width of 8Hz at amplitude responses of 22.8μm and 14.2μm respectively.

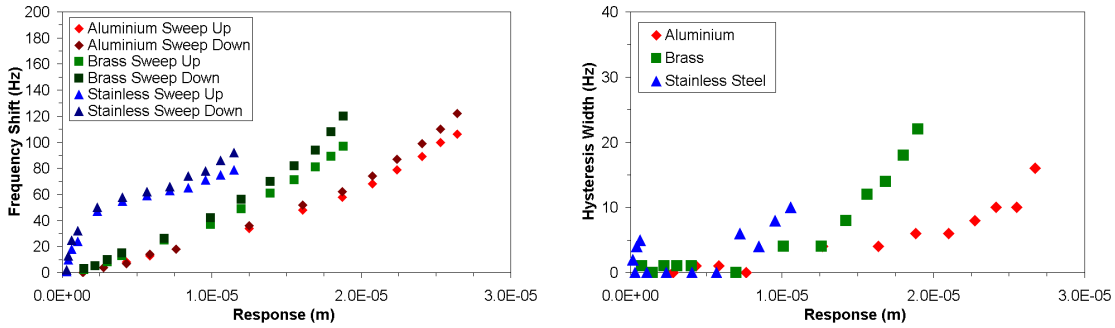

(a) Frequency shift against vibration amplitude

(b) Breadth of hysteresis region against vibration amplitude

Figure 4.41: Nonlinear behaviour of full wavelength assemblies with respect to amplitude

4.3.6 Discussion of custom and commercial inserts

Finite element and experimental modal analysis

Good correlation between mode shapes and resonant frequencies predicted through finite element analysis and acquired by experimental modal analysis gave validation to the finite element models. The percentage difference between the tuned resonant frequencies of the transducer-horn assemblies found using FEA and EMA methods did not rise above 5% although the frequencies of the longitudinal modes other than the tuned modes generally did not have as good accuracy.

The reason finite element models predicted some longitudinal modes with more accuracy than others is not fully understood, although, an interesting relationship with the location of the node in the device assemblies has been observed. In the cases where the highest accuracy was achieved, the location of a node was situated in the piezoceramic stack, whilst in the FE models with least agreement, the position of the piezoceramic stack corresponded with regions of higher vibrational amplitude. Furthermore, modes where the piezoceramic stack is situated away from a node, but in a region of lower vibration amplitude tend to have better accuracy than those where the piezoceramic stack is in a region of higher vibrational amplitude. Therefore it is possible that the mechanical properties, such as the elastic properties, of the piezoceramic elements are not optimally modelled, as elevated strain levels within these elements could reduce the accuracy of the modal analysis model.

Nonlinear behaviour

Figures which plot amplitude response and current drawn by the transducer at different driving voltages against excitation frequency in Sections 4.3.1, 4.3.2, 4.3.4 and 4.3.5 all highlight a saturation of amplitude response as excitation levels are increased. Amplitude saturation occurs due to the increase of mechanical and electrical losses within the piezoceramic materials and metal alloys which the tuned device is manufactured from.

Resonant frequency shift

The shift in resonant frequency with respect to amplitude of vibration of the assemblies containing the surgical inserts can be seen in Figures 4.13(b) and 4.25(a) while those of the rod horn assemblies can be seen in Figures 4.34(a) and 4.41(a). These suggest that both half and full wavelength assemblies exhibit an increase in frequency shift with increase in vibration amplitude. Table 4.5 presents the resonant frequency shift of the surgical assemblies at an amplitude of vibration of 2.5μm and rod horn assemblies at an amplitude of vibration 11μm. From the Table it can be observed that the half wavelength assemblies generally exhibit larger shifts in resonant frequencies than those seen in the comparative full wavelength assemblies.

	Half wavelength			Full wavelength		
	Frequency shift (Hz)			Frequency shift (Hz)		
	Sweep up	Sweep down	Q_m	Sweep up	Sweep down	Q_m
Surgical inserts [2]						
OT7 insert	111	121	451.8			
Base insert	123	133	429.2			
TLR with blade				118	120	417.7
TLR w/o blade				101	113	498.0
X15TR				80	77	904.9
420BR				97	105	723.3
Rod horn [3]						
Aluminium	101	101	492.3	34	36	1228.0
Brass	73	73	316.2	49	56	955.2
Stainless steel	87	96	311.1	75	86	337.3

Table 4.5: Frequency shift and Q_m of half and full wavelength surgical assemblies

A similar observation was seen in quarter and half wavelength blades used in the food industry [9, 176, 217]. Cardoni suggested that larger resonant frequency shifts seen in tuned devices containing quarter wavelength blades could be related to reaching a nonlinear elastic threshold in the tuned assembly material. Meanwhile, Mason and Wood [218], Mason and Wehr [170], Puškár [171], Campos-Pozuelo and Gallego-Juárez [173, 174], reported that elevated ultrasonic longitudinal strains in alloys of aluminium, titanium and stainless steel result in an increase in their mechanical loss factor, Q_m^{-1}. As viscous damping is dependent on Q_m^{-1}, and resonant frequency within a damped system is dependent on viscous damping, an increase in Q_m^{-1} will result in a lowering in resonant frequency.

However, in this study, the (shorter) half wavelength assemblies were studied at the same amplitude of vibration as the (longer) full wavelength assemblies, hence for the shorter assembly to achieve the same amplitude of vibration as the longer assembly, the strain induced will be larger. Furthermore, the Q_m for the half wavelength assemblies were found to be generally lower than those of the corresponding full wavelength assemblies. It is likely that at

[2] Measured at vibrational amplitude of 2.5μm
[3] Measured at vibrational amplitude of 11μm

a corresponding amplitude of vibration, a higher level of Q_m^{-1} and therefore viscous damping would exist in the half wavelength assemblies than full wavelength assemblies, thus inducing a larger shift in resonant frequency within the half wavelength assemblies.

It should also be mentioned that an increase in strain within the assembly could increase the influence of the nonlinear behaviour stemming from the electro-mechanical properties of the piezoceramic elements as it is well known in literature that piezoceramic materials have an elastic low nonlinear threshold [26, 158, 166]. A change in elastic properties of either the horn or piezoceramic material, or both will instigate a change in the dynamic response of an ultrasonic device which may manifest as a nonlinear behaviour such as a lowering in resonant frequency.

Amplitude jumps

Table 4.6 presents the amplitude of vibration and the excitation voltage at which amplitude jumps occur at in each of the ultrasonic devices discussed in this chapter. It can be seen that the jump phenomenon first occurs in all but one of the investigated devices within a voltage range of 15-30V_{rms}, although, it was not exhibited in the full wavelength assembly containing the stainless steel rod horn. Meanwhile, it can be observed that the jump phenomenon occurs in the surgical assemblies within a vibrational amplitude range of 1.23μm to 2.47μm (upward sweep) and 1.26μm to 2.35μm (downward sweep), the assemblies containing the TLR and X15TR first exhibiting jump phenomena at the largest and smallest vibrational amplitudes respectively. While the rod horn assemblies first exhibit the jump phenomenon between 10.1μm to 18.1μm (upward sweep) and 9.86μm to 17.4μm (downward sweep), the full wavelength assembly containing the brass rod horn and the half wavelength assembly also containing brass rod horn first exhibiting jump phenomena at the largest and smallest vibrational amplitudes. These observations suggest that the source of the jump phenomena is not dependent on the excitation voltage or the geometric shapes of the transducer-horn assembly but amplitude of vibration. Reports have found that the jump phenomenon occurs in both Langevin transducers [189] and single piezoceramic elements [7, 152, 166]. These investigated that at elevated vibrational amplitudes the elastic compliance, s^E, of the piezoceramic material is nonlinear, higher the vibrational amplitude, larger the value of s^E and this has been accredited to the jump phenomena.

	Sweep up (μm)	V_{rms}	Sweep down (μm)	V_{rms}
Surgical inserts				
OT7 insert	1.81	15	2.35	20
Base insert	1.82	15	1.84	15
TLR with blade	1.92	25	1.94	25
TLR w/o blade	2.47	25	2.58	25
X15TR	1.23	15	1.26	15
420BR	1.60	25	1.90	30
Rod horn				
Aluminium half λ	12.5	15	17.4	20
Aluminium full λ	12.5	15	12.7	15
Brass half λ	18.1	20	17.8	20
Brass full λ	10.1	20	9.86	20
Stainless steel half λ	14.1	25	12.2	25
Stainless steel full λ	n/a	n/a	n/a	n/a

Table 4.6: Amplitude of vibration and excitation voltage that amplitude jumps are first observed in tuned assemblies

Hysteretic regions

	Hysteretic width (Hz)	Q_m
Surgical inserts at 2.5μm		
OT7 insert	12	451.8
Base insert	8	431.9
TLR with blade	0	417.7
TLR w/o blade	10	498.0
X15TR	2	904.9
420BR	8	723.3
Rod horn at 11.5μm		
Aluminium half λ	2	492.3
Aluminium full λ	4	1228.0
Brass half λ	0	316.2
Brass full λ	4	955.2
Stainless steel half λ	6	311.1
Stainless steel full λ	10	337.3

Table 4.7: Hysteretic widths of tuned assemblies

The width of the hysteretic regions, seen in Figures 4.14, 4.25(b), 4.34(b) and 4.41(b), of the assemblies containing the surgical inserts were compared at an amplitude of vibration of 2.5μm, while those containing the rod horns were compared at 11.5μm, Table 4.7. From the Figures it can be observed that above a vibration threshold (2μm for surgical assemblies and 10μm for rod horn assemblies) that the hysteretic width is dependent upon amplitude of vibration, although, it can also be observed that at elevated amplitudes of vibration, the hysteretic width remains small. Meanwhile, from Table 4.7 the influence of geometry, material selection or Q_m of the tuned assemblies does not appear to significantly influence the width

of the hysteretic region.

Harmonic Responses

Similarities can be observed between frequency spectrum images captured by the oscilloscope of the surgical assemblies driven close to the resonant frequency at an excitation level of $50V_{rms}$, Figures 4.16 and 4.26. The spectrum responses seen in Figures 4.16(b) and 4.26(b) are of the assemblies which contain the base insert and TLR insert without blade tip. These inserts share a common geometric feature that removes flexural motion from the tuned mode of vibration. Both the assemblies containing the base insert and TLR insert without the blade tip are shown to have similar content; the presence of harmonics and side bands. On the other hand, the assemblies containing the OT7 insert and TLR insert with the blade tip both contain geometric features that induce flexural motion and also exhibit increased number of spectral responses when excited at elevated amplitudes close to resonance, Figures 4.16(a) and 4.26(a). As previously discussed, the response spectra of the OT7 insert and TLR with the blade tip appears to exhibit period doubling, a phenomenon which indicates a route to chaotic behaviour [81]. It could be suggested that the presence of a stronger flexural motion coupled with that of the longitudinal motion could combine to induce period doubling.

4.4 Effect of temperature on ultrasonic devices

The effect of temperature on the physical properties of piezoceramics was discussed previously, therefore any ultrasonic device relying on piezoceramics to generate mechanical motion from an electrical signal can experience a change in piezoceramic temperature which can alter the performance of the device. Moreover, nonlinear behaviour, which can also adversely affect performance, can manifest within ultrasonic devices if the correct conditions are reached. In order to understand the effect that dynamic operating conditions alone have on an ultrasonic device, the influence that temperature changes within the device must be removed from the characterisation.

4.4.1 Burst drive versus continuous drive

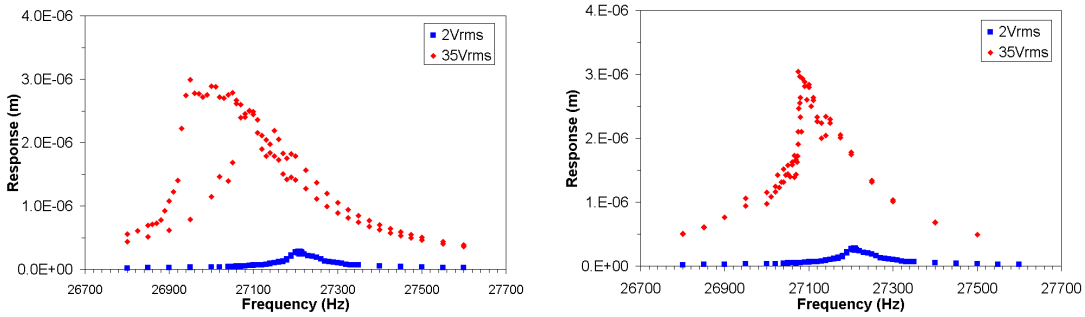

(a) Continuous excitation (b) Incremented frequency burst with time delay

Figure 4.42: Effect of temperature increases in OT7 insert assembly - Experimental setup 1

Measurements using experimental setup 1 (Section 4.2.1) were used to create Figure 4.42. The figure illustrates the difference between the frequency response of the OT7 insert assembly driven continuously through the frequency range, Figure 4.42(a), and the frequency response of the device driven by short bursts which incorporated a length of time allowing the piezoceramics to return to ambient temperature between frequency increments, Figure 4.42(b). At low excitation levels, $2V_{rms}$, both plots exhibit symmetric response curves, implying that the response of the tuned assembly operates linearly, independent from excitation type and temperature change. However, under a higher excitation voltage of $35V_{rms}$, both sets of measurements exhibit the softening effect. The shift in resonant frequency found during the sweep up were similar at 150Hz and 135Hz, although, in contrast, during the sweep down the resonant frequency shifts differed considerably, 270Hz and 136Hz for the continuous and burst drive respectively. Furthermore, this resulted in the formation of a wide hysteresis region of 120Hz in the response curve of the continuously driven device, Figure 4.42(a), while the hysteretic width was negligible in the response curve for the burst driven device, Figure 4.42(b).

4.4.2 Burst drive - Time delay study

In order to separate the effect of temperature change in piezoceramic elements from that of dynamic response, it has been concluded from Section 4.4.1 that the piezoceramic or ultrasonic device should be excited for as short as time interval as possible via a burst signal. However, a key component of the measurement process is the time delay between successive frequency increments which ensures any heat generated within the piezoceramics is dissipated to the surrounding environment. Figure 4.43 plots the response of the assembly containing the X15TR insert collected using experimental setup 2 (Section 4.2.2) incorporating a time delay of 1 second and a time delay of 10 seconds between frequency increments. During the measurements a burst length of 4000 cycles was used to drive the X15TR assembly, while ambient air temperature was approximately 28°C.

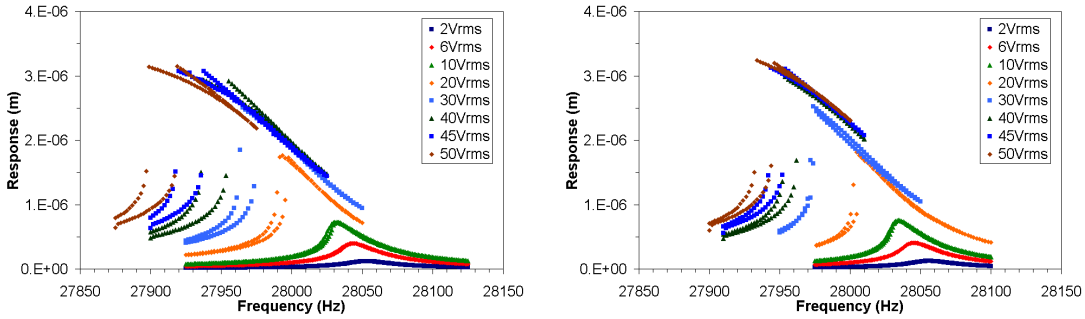

(a) 1 second time delay

(b) 10 second time delay

Figure 4.43: Response of assembly containing X15TR insert

From Figures 4.43, 4.44 and 4.45 it can be observed that below a vibrational amplitude of 1.75μm (achieved with an excitation voltage of 20V_{rms}) the responses of the X15TR assembly do not significant differ from each other, and the resultant hysteretic widths where found to be negligible. However, at an amplitude of vibration 1.75μm, the shift in resonant frequency begins to differ between the measurements incorporating a 1 second time delay and 10 second time delay, as does the hysteresis region. At this amplitude, the shift in resonant frequency were 59Hz and 52Hz, resulting in hysteretic widths of 4Hz and 2Hz, for the measurements incorporating a 1 second and 10 second time delay, respectively. Furthermore, at a vibrational amplitude of 2.95μm (achieved at an excitation voltage of 50V_{rms}), both the shift in resonant frequency, 154Hz and 112Hz, and the hysteretic region width, 19Hz and 10Hz, was larger than at smaller amplitudes of vibration for measurements incorporating a 1 second and 10 second time delay. However it can also be observed that for the shift in resonant frequency and hysteresis width are larger at vibrational amplitudes 1.75μm and 2.95μm in measurements incorporating a 1 second time delay.

The temperature of the surface of the piezoceramic stack during the frequency response measurements can be seen in Figure 4.46. From figure 4.46(b), it can be seen that a relatively

small temperature increase of 1.9°C occurs throughout the measurement interval utilising a 10 second time delay. Meanwhile in measurements featuring a 1 second time delay, Figure 4.46(a), above an excitation voltage of $20V_{rms}$, the temperature of the piezoceramics increases as the sweep (either upward or downward) approaches resonance. At resonance under an excitation voltage level of the $50V_{rms}$ the surface temperature of the piezoceramics was measured at 35.7°C, a 7.6°C increase over the temperature measured at the lowest excitation level of $2V_{rms}$. Although this increase in temperature is under 10°C, Umeda *et al* [6, 154] reported that mechanical loss factor, Q_m^{-1}, elastic compliance, s^E, dielectric constant, ε^T and piezoelectric constant, d, were all sensitive to changes in temperature between a range of 20°C to 50°C, therefore an increase in temperature of 7.6°C, increasing the temperature from 28.1°C to 35.7°C is likely to have an influence and thus behaviour of the piezoceramic elements.

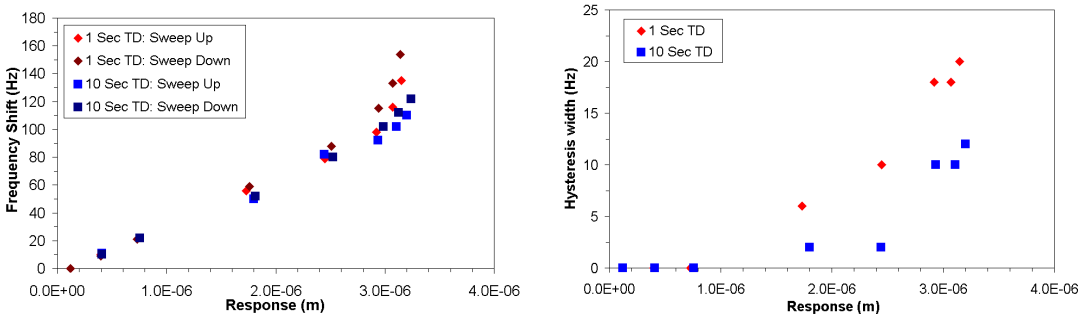

(a) Resonant frequency shift (b) Width of hysteresis region

Figure 4.44: Nonlinear behaviour of X15TR insert with respect to amplitude

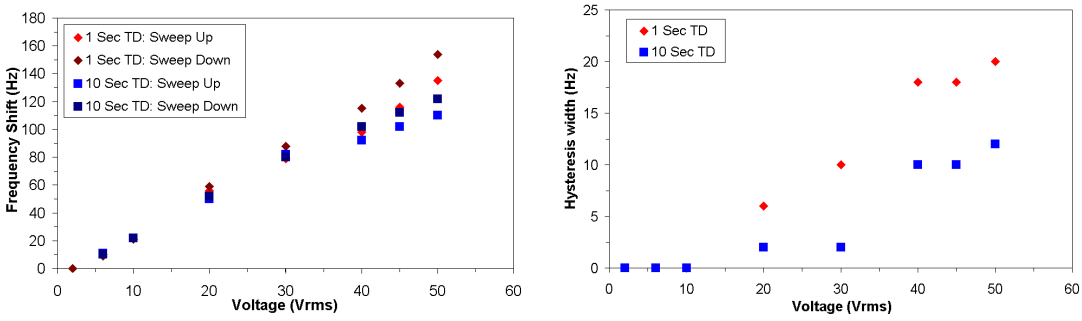

(a) Resonant frequency shift (b) Width of hysteresis region

Figure 4.45: Nonlinear behaviour of X15TR insert with respect to excitation voltage

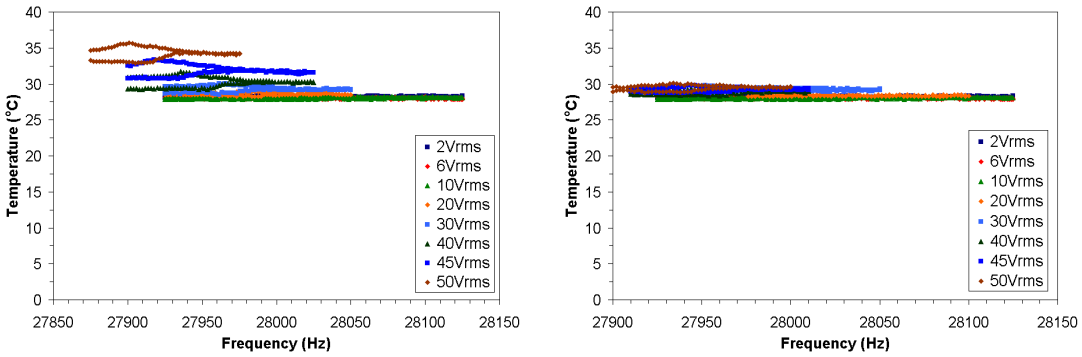

(a) 1 second time delay

(b) 10 second time delay

Figure 4.46: Temperature measurements from surface of piezoceramic stack: X15TR Insert

4.4.3 Discussion - Effect of temperature on ultrasonic devices

The cases discussed in the previous sections have reinforced the necessity of removing the effects of thermal change of the piezoceramic from those caused by dynamic response during nonlinear characterisation of piezoceramic and ultrasonic devices. Initially, measurements found at low levels of vibration suggest that the temperature of the piezoceramic elements do not appear to significantly change as the response of the ultrasonic device remains unaffected whether driven continuously or through a burst (either incorporating a short or long time delay). However, once a vibrational amplitude threshold has been surpassed (1.75μm in the case of the X15TR assembly), the temperature increase within the piezoceramic elements is significant enough to influence the response of the device.

Figures 4.42 and 4.43 illustrate that an increase in piezoceramic temperature increases the influence of nonlinear behaviours on the response of an ultrasonic device. Both resonant frequency shift and hysteretic regions where observed at vibrational amplitudes at which piezoceramic heating was minimal, hence it is evident that these initially stem from a source other than heating within the piezoceramics. However at higher amplitudes of vibration, Figures 4.42 and 4.43 both illustrate that the shift in resonant frequency shift as well as the width of the hysteretic region is larger in the responses where the temperature increases within the piezoceramic.

4.5 Effect of joint tightness

Ultrasonic devices are generally assembled from a number of components; transducer, booster and horn. To join each of these components, threaded fasteners such as bolts or studs are commonly used as they give the ability to replace or change assembly components or configurations with ease as well as giving a strong mechanical connection. Studies of joints in power ultrasonic devices are rare [179] but two studies by Kumehara *et al* [219, 220] investigating joints in relation to the reliability of a Langevin transducer revealed that better the surface finish of the joint bearing surfaces as well as high and uniform tightening forces (as is possible within allowable material stresses) will increase the acoustic efficiency as well as the reliability of the joint. A short study on the effect that torque has on the nonlinear characteristics of an ultrasonic device can be seen in the PhD thesis by Cardoni [9]. It reported that a joint with a low torque exhibits a stronger nonlinear response than that in a joint with a high torque.

On the other hand, properties of threaded joints such as tightness and contact conditions on bearing surfaces have been widely studied in basic dynamic systems through experimental, analytical and finite element methods. Understanding the dynamic response of a joint and energy dissipation through it allows the performance of the fastening to be quantified [221]. Esteban and Rogers [222], successfully used analytical and experimental methods to understand the relationship between energy dissipation through a joint versus its tightness using two overlapping aluminium beams fastened together by two steel bolts. A low power swept sine wave was propagated in to one of the aluminium beams on one side of the joint, while a receiver was located on the second beam on the other side of the joint. Two different torque cases were analysed experimentally, and the results, measured close to 17.4kHz (corresponding with a bending mode of vibration), showed that the case with the higher torque possessed the higher Q_m and provided a higher transmission of acoustic energy. Meanwhile a similar but more extensive study regarding torque and excitation level was completed by Rivière *et al* [223]. Using the technique of multimodal nonlinear resonance spectroscopy, a 1 second swept sine wave (1-24kHz) was propagated in to an aluminium plate containing a bolt at different levels of torque. It was reported that increased torque led to a reduction in damping and loss within the joint, while the resonant frequency shift of the bending mode of vibration seen to be reduced with respect to higher torque.

4.5.1 Characterisation of joint tightness

To study the effect that joint tightness has on the performance of an ultrasonic device, an ultrasonic assembly, previously discussed in Section 4.3.4, was studied. The half wavelength assembly containing a brass rod horn, Figure 4.27(b), was characterised at different excitation levels close to the resonant frequency of the first longitudinal mode. Unfortunately, it was not possible to quantify the torque with which the rod horn was connected to the transducer in the two measurements, although the difference in the response at low amplitude levels can be seen clearly in Figure 4.47. The resonant frequency of the tight joint assembly under linear excitation conditions was found to be 23065Hz while under the same conditions the assembly with the loose joint was found to have a lower resonant frequency of 22484Hz. The mechanical quality factors were also found to be different, the tight assembly having a Q_m of 316.2 while the Q_m of the assembly with the loose joint was almost half at 155.1.

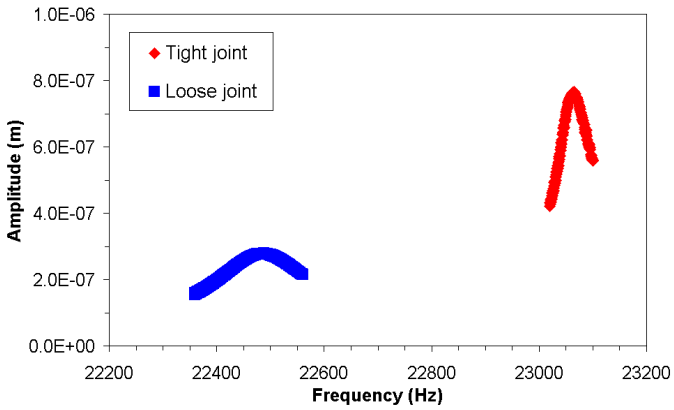

Figure 4.47: Frequency response of the half wavelength assembly containing a brass rod horn with tight and loose joints at an excitation of $2V_{rms}$

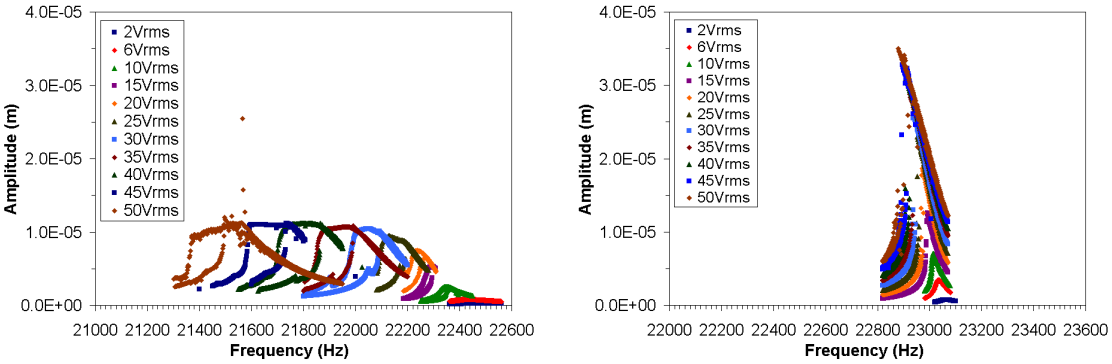

(a) Low Q_m: Loose joint

(b) High Q_m: Tight joint

Figure 4.48: Vibrational response of half wavelength assembly contain a brass rod horn

Figures 4.48, 4.49 and 4.50 illustrate that the assembly with the loose joint exhibits a larger shift in resonant frequency and hysteretic widths, while also exhibiting amplitude saturation at a considerably lower amplitude of vibration than the assembly containing the tight joint.

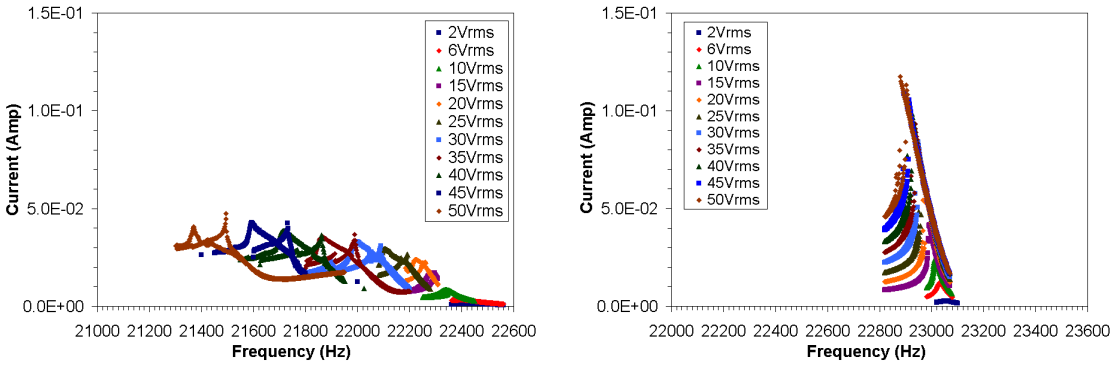

(a) Loose joint (b) Tight joint

Figure 4.49: Current drawn by transducer during nonlinear characterisation of half wavelength assembly containing a brass rod horn with tight and loose joints

At an amplitude response of 5.2μm the frequency shift exhibited by the assembly containing the tight joint during the upward and downward sweeps was 38Hz, while the frequency shift exhibited during the sweep up for the assembly with the loose joint was 184Hz and 195Hz during the sweep down. However at a larger amplitude of vibration of 12μm, the shift in resonant frequency for the assembly with the tight joint has increased to 73Hz, while the shift in resonant frequency exhibited in the assembly containing the loose joint is 984Hz.

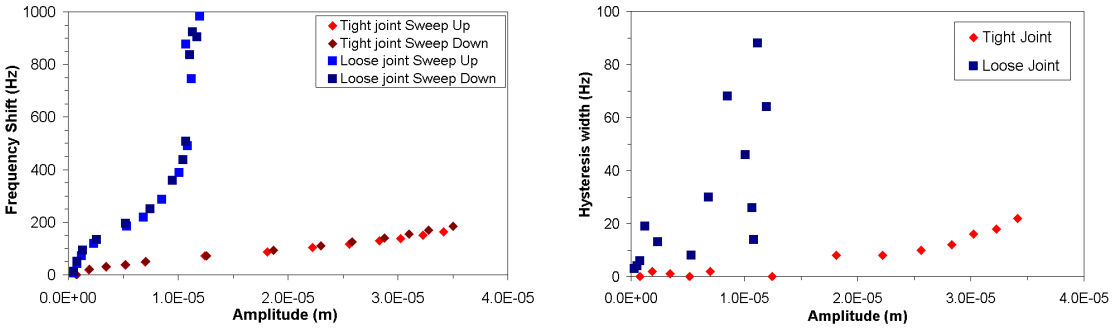

(a) Frequency shift against vibration amplitude (b) Breadth of hysteresis region against vibration amplitude

Figure 4.50: Nonlinear behaviour of half wavelength assembly containing a brass rod horn with tight and loose joints

A substantial difference in the widths of the hysteresis regions found for the assemblies containing the tight and loose joints can be seen in Figure 4.50(b). The hysteretic region for the assembly with the tight joint is negligible below 12.5μm, while above this amplitude,

it appears that the hysteretic width increases up to the final measurement at an amplitude of 34.1μm where the width is 22Hz. However, the assembly with the loose joint exhibits a different trend. The width of the hysteresis region increases to 19Hz at an amplitude of vibration of 1.23μm, then reduces to 8Hz at an amplitude of 5.33μm. Although, between an amplitude of 5.33μm and 12.0μm the width varies without any clear trend between 14Hz and 88Hz.

4.5.2 Discussion - Effect of joint tightness

It has been observed that nonlinear behaviours such as amplitude saturation, resonant frequency shift and hysteresis width are greater and are exhibited at lower amplitudes of vibration in the assembly containing the loose joint than the assembly with the tight joint. Although cases from literature [221–223] are studies of simple dynamic structures, the results and observations reported upon by the authors are not dissimilar to those presented in the previous section.

The Q_m and amplitude responses measured from the tuned assembly with the loose joint were seen to be significantly lower than those of the assembly with the joint with higher torque. This was consistent with literature [219–223] and suggests that the lower the torque, the lower the level of acoustic efficiency and thus higher the damping.

A difference in frequency shift can also be seen between the assemblies with tight and loose joints. The studies containing simple beam and plate structures [221–223] report the same nonlinear phenomenon. A lowering of resonant frequency with increasing excitation is exhibited by both ultrasonic assemblies, although it is larger in the assembly with the loose joint. Kumehara *et al* [219, 220] commented that the lower the joint tightness, the lower the global stiffness of the joint, while Rivière *et al* [223] also discussed the effect that joint stiffness has on the resonant frequency of a structure, explaining the phenomenon through a simple dynamic expression, Equations 4.1 and 4.2. These demonstrate that stiffness is proportional to frequency in relation to constant mass, implying that a lowering in stiffness will cause a lowering in resonant frequency.

$$f = \frac{1}{2\pi} \cdot \sqrt{\frac{k}{m}} \tag{4.1}$$

$$f \propto \sqrt{k} \tag{4.2}$$

The difference in width of the hysteretic regions seen in Figures 4.48, 4.49 and 4.50(b) illustrates the influence that joint tightness has on hysteretic nonlinearities. The presence of large hysteretic widths in the assembly containing the loose joint, when compared to the assembly with the tight joint, suggest the presence of a strong cubic nonlinearity [82]. Ouyang *et al* [224] also observed a strong cubic nonlinearity in a dynamic system containing

two beams connected together by a bolt joint at different torque levels. Initially, Ouyang *et al* states that a joint under high torque behaves similarly to a rigid joint, exhibiting basic viscous damping, however as the torque level lowers and amplitude of vibration increases the behaviour (and damping of the joint) becomes increasingly influenced by a softening cubic nonlinearity. Ouyang *et al* reported that as the influence of the cubic nonlinearity increases, microslip (a small relative tangential displacement in the contacting interface of the joint when the remaining interface of the joint is not relatively displaced tangentially) and friction within the joint becomes more influential to the behaviour of a dynamic system [224]. Therefore, from observations made from the responses of the tuned assemblies suggest that the joining conditions between the bearing surfaces evolve, as the torque within the joint decreases and vibrational amplitude increases, the influence of microslip and friction within the joint which in turn increases hysteretic behaviour.

4.6 Chapter Conclusion

It has been widely reported in literature that temperature increases within piezoceramic elements can influence their behaviour at high vibrational amplitudes, often masking the influence of other factors, such high strain and electric field strength. In order to discriminate the effect of strain and electric field strength from that of temperature, measurement techniques have been discussed which minimise temperature increase within the ultrasonic device during characterisation at high vibrational amplitudes.

To ensure validity of finite element models, all devices characterised at high amplitude levels were also characterised at low power in their linear response ranges through experimental modal analysis. Good correlation was generally achieved between resonant frequencies and mode shapes of the tuned mode and FE models, although some models achieved better correlation with measured resonant frequencies than others. A relationship between the position of the piezoceramic stack and locations of nodal points has been discussed.

A method of characterising ultrasonic devices at high amplitude levels has successfully minimised the effects of temperature increases in the piezoceramic stack of the transducer from those of vibrational stress and electrical field strength. Four categories of assemblies have been characterised; half and full wavelength assemblies containing surgical inserts and custom rod horns. It was noted that nonlinear phenomena, hysteretic regions and jump amplitudes are relatively unaffected by excitation voltage, geometric features or material choice of horns. However, it was discovered that geometry did influence the shift in resonant frequency as assemblies containing half wavelength assemblies generally had a larger shift in resonant frequency than the full wavelength assemblies. Furthermore it is observed that the presence of a blade on the inserts contained in either the half or full wavelength surgical assemblies increased the spectral density of the response. This suggests that inserts that contain a geometric feature that induces a flexural motion could be more susceptible to period doubling, a known route to chaos.

As expected, the response of the ultrasonic devices at elevated temperatures exhibited stronger nonlinear behaviours. Both larger shifts in resonant frequency and hysteretic widths were observed in devices which their piezoceramic stack was exposed to elevated temperatures. It was also observed that even when an ultrasonic device is excited through a burst, an adequate time delay is necessary between successive frequency increments to allow heat dissipation.

The join between two components of a tuned ultrasonic assembly can have a large effect on the performance and whether strong nonlinear behaviours are exhibited by the device. Important factors in achieving a stable and reliable ultrasonic joint are high accuracy between the bearing surfaces combined with as high a torque as allowable between the two joining parts.

Chapter 5

Characterisation of Langevin transducers

Langevin transducers, also known as stack or sandwich transducers, are generally constructed from four fundamental components; backmass, frontmass, piezoceramic stack and stud or bolt which hold the transducer together under a compressive pre-load [182,225]. It is traditionally proposed that the piezoceramic stack should be positioned at the node of the longitudinal mode of vibration of the transducer to ensure that the piezoceramic elements are kept under a constant compressive pre-load. However, in order to incorporate a support flange, it can be more advantageous to locate the flange at the longitudinal nodal point to minimise damping [226]. Meanwhile, the development of multi-frequency power ultrasonic transducers employed in sonochemistry and the advance of multi-mode ultrasonic motors has resulted in transducer designs which utilise multiple sets of piezoceramic stacks [38, 125, 227]. The architecture of some multi-mode motors incorporate two sets of piezoceramic stacks, as discussed in Section 1.3.2 and Figure 1.16(a). The first piezoceramic stack generates the longitudinal motion and is located close to the longitudinal nodal point, while the second piezoceramic stack, although carefully positioned to maximise the generation of either flexural or torsional motion, could be located at a position of elevated longitudinal vibrational amplitude and therefore could be exposed to variations of pre-load.

Investigating the effect of locating piezoceramic elements away from the longitudinal nodal point in power ultrasonic transducers was first explored in 1970. Shoh discussed the performance at high and low amplitude levels of two half wavelength Langevin transducers; the first consisted of a piezoceramic stack centrally located at the nodal point with endmasses of equal lengths while in the second the piezoceramic stack was shifted $\frac{1}{6}\lambda$ from the nodal point leaving endmasses of unequal lengths [226]. Meanwhile, Neppiras understood that to support a transducer with minimal damping, it may be necessary to position the piezoceramics away from the displacement nodal point [94]. He suggested that shifting the location of the piezoceramics potentially should not have an effect on the efficiency of the device; the

reduction in electro-mechanical coupling factor, k_{eff}, (due to a weakening in the coupling between the dielectric and elastic strain properties) would be cancelled out by an increase in Q_m due to a reduction in losses stemming from mechanical coupling between contacting surfaces of the piezoceramic elements and endmasses. Later that decade, LeMaster and Graff published a report investigating analytical models and experimental performance of Langevin transducers with ten different piezoceramic stack positions [228]. Experimental results collected included; tuned frequencies, amplitude of vibration, transducer quality factor and electrical impedance values. However, not all predicted values from the analytical models agreed with those collected experimentally, nevertheless they concluded that predicting the performance of the transducers was strongly influenced by nonlinear behaviour seen in the piezoceramic elements. More recently Shuyu [119, 183, 229] reported the effect that loading and unloaded conditions (air loaded) had on the resonant and antiresonant frequencies, electro-mechanical coefficient, and quality factor of power transducers used in sonochemistry.

To further investigate the consequence of shifting the piezoceramic stack from the longitudinal nodal position three custom transducers with differing stack positions have been manufactured and studied. Modal parameters and characterisation at both low and high excitation levels has been analysed to assess the impact on modal parameters and amplitude of vibration. Furthermore, finite element analysis has been utilised to predict stress levels throughout the transducers during simulated operative conditions.

5.1 Transducers

Three half wavelength transducers were manufactured with varied piezoceramic stack positions and are referred to as configuration I, II and III. Configuration I consists of a centrally located piezoceramic stack and two brass endmasses of equal length, while the position of the stacks in configurations II and III has been positioned away from the center of the transducer and thus the nodal point. The brass endmasses have length ratios of one quarter to three quarters and one eight to seven eights respectively, Figure 5.1.

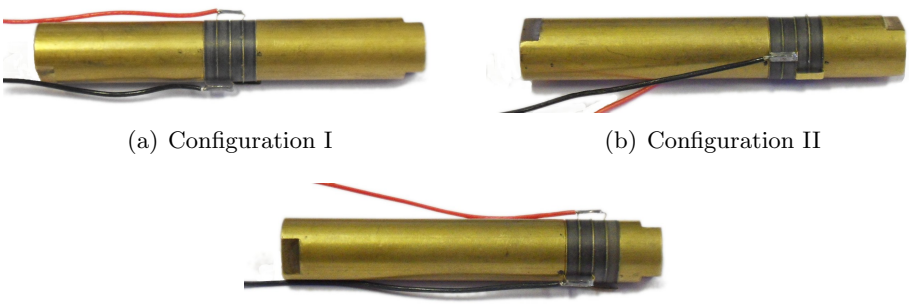

(a) Configuration I

(b) Configuration II

(c) Configuration III

Figure 5.1: Transducer Configurations

5.2 Resonant frequency and mode shape extraction

5.2.1 Finite element and experimental modal analysis

The transducers were designed using finite element analysis and tuned to operate in the 1st longitudinal mode of vibration. Experimental modal analysis validated the FE models, finding good correlation between the resonant frequencies and mode shapes of the first longitudinal mode of vibration predicted by FEA and measured through EMA, Figures 5.2 to 5.4. The percentage difference between the resonant frequencies of the 1st longitudinal mode found through FEA and EMA methods of configurations I, II and III was found to be 7.25%, 2.10% and 2.03% respectively. Meanwhile, the mode shapes and resonant frequencies of the 2nd longitudinal mode, also found through FEA and EMA methods, had percentage differences of 6.34%, 3.63% and 3.76% respectively, Figures 5.5, 5.6 and 5.7.

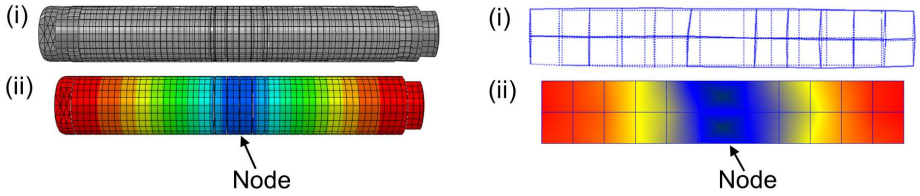

(a) FEA: 28831Hz (b) EMA: 26740Hz

Figure 5.2: Configuration I - 1st longitudinal mode
(i)Deformed/undeformed (ii)Undeformed normalised contour map of displacement

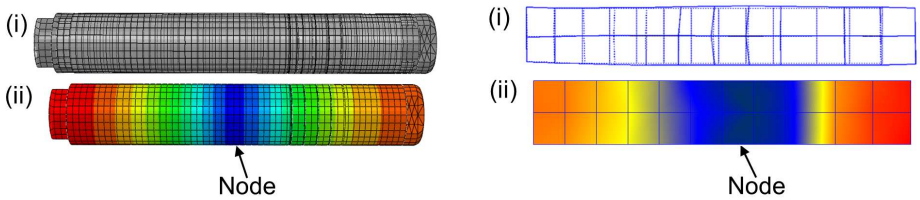

(a) FEA: 28770Hz (b) EMA: 28135Hz

Figure 5.3: Configuration II - 1st longitudinal mode
(i)Deformed/undeformed (ii)Undeformed normalised contour map of displacement

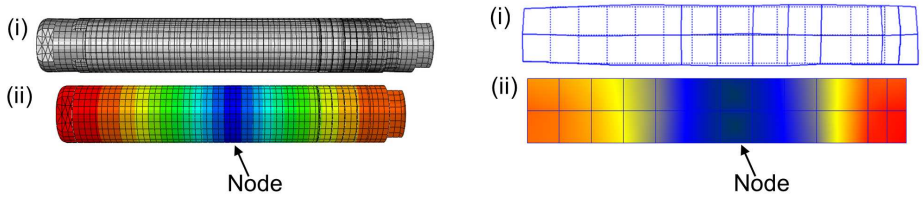

(a) FEA: 28582Hz (b) EMA: 29161Hz

Figure 5.4: Configuration III - 1st longitudinal mode
(i)Deformed/undeformed (ii)Undeformed normalised contour map of displacement

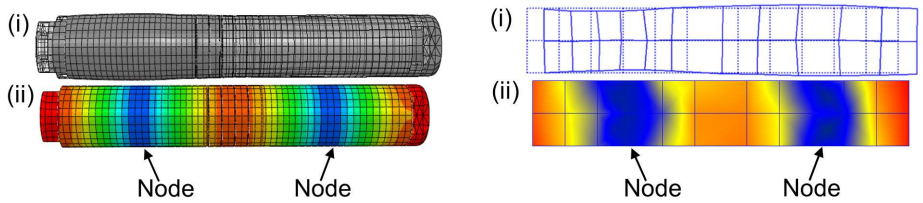

(a) FEA: 54576Hz (b) EMA: 58036Hz

Figure 5.5: Configuration I - 2nd longitudinal mode
(i)Deformed/undeformed (ii)Undeformed normalised contour map of displacement

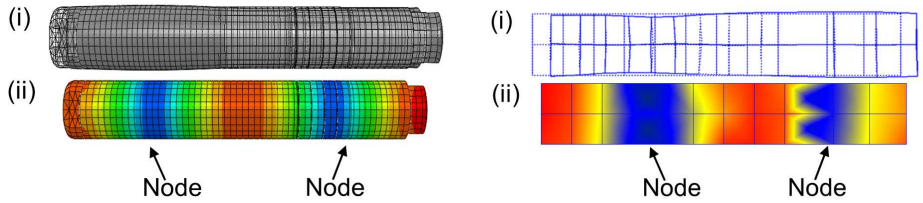

(a) FEA: 57569Hz (b) EMA: 55263Hz

Figure 5.6: Configuration II - 2nd longitudinal mode
(i)Deformed/undeformed (ii)Undeformed normalised contour map of displacement

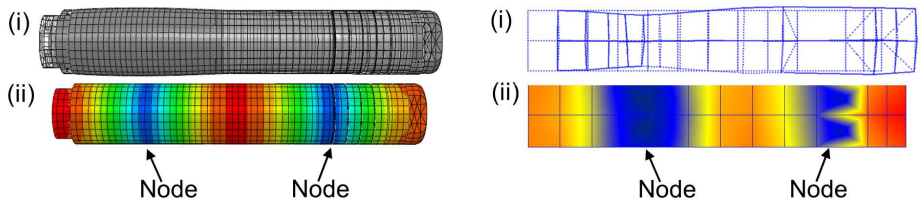

(a) FEA: 57948Hz (b) EMA: 55161Hz

Figure 5.7: Configuration III - 2nd longitudinal mode
(i)Deformed/undeformed (ii)Undeformed normalised contour map of displacement

5.2.2 Impedance Analyser measurements

The resonant frequency of the 3rd longitudinal mode of vibration of the transducer configurations lies above 80kHz and unfortunately outwith the operational frequency range of the data acquisition software and equipment used in EMA, however the predicted resonant frequencies and mode shapes can be seen in Figure 5.8. In order to measure the frequency of the 3rd longitudinal mode, an impedance analyser, Agilent 4294A, was used to excite the transducer configurations at a low excitation level ($0.5V_{p\text{-}p}$) and measure the electrical admittance and phase angle between the values of the maximum and minimum admittance, f_m and f_n, over a frequency range of 10kHz to 100kHz, Figure 5.9. To ensure the validity of the results, the impedance analyser was initially calibrated using two loads 0Ω (short load, Agilent HRM 504) and a 50Ω load (Agilent HRM 601), while measurement robustness was assessed through varying the excitation level and time duration of sweep to confirm measurement repeatability and reliability.

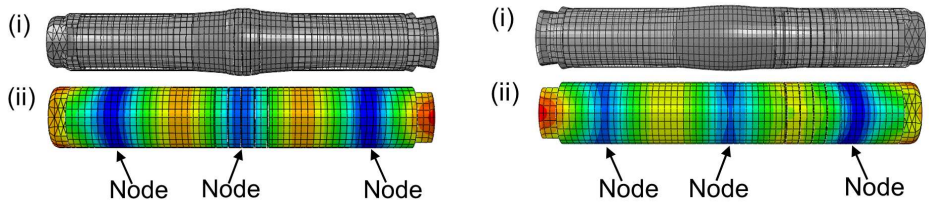

(a) Configuration I - 81615Hz

(b) Configuration II - 83637Hz

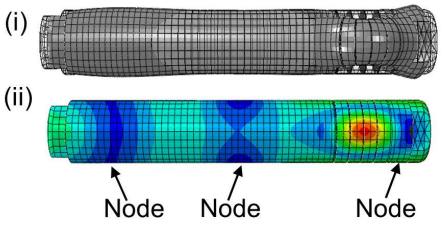

(c) Configuration III - 84000Hz

Figure 5.8: Mode shapes of 3rd longitudinal mode found through FEA
(i)Deformed/undeformed (ii)Undeformed normalised contour map of displacement

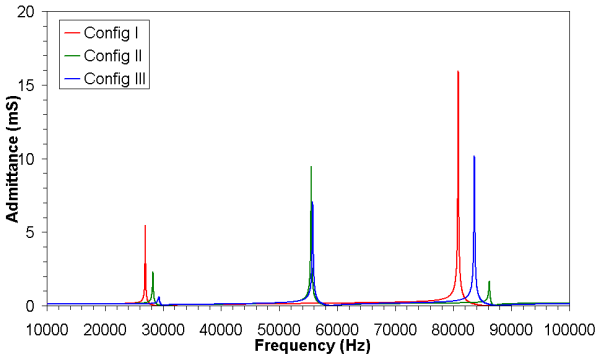

(a) Admittance

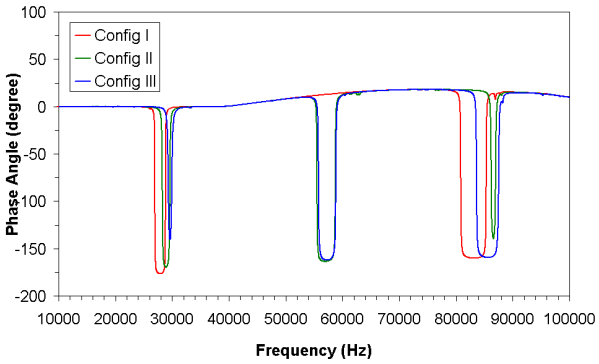

(b) Phase Angle

Figure 5.9: Admittance and impedance measurements of transducer configurations

As discussed in Section 1.2.2, when a tuned piezoelectric device is driven at resonance, it can be assumed that the relationship $f_m \approx f_r$ exists [22]. Therefore the points of maximum admittance found close to the frequencies of 1st and 2nd longitudinal modes can be assumed to be of those modes, Table 5.1 illustrating the small percentage difference between f_m and f_r of these modes. Hence, from Figure 5.9(a) it can also be assumed that the frequency of high admittance, which is measured close to the predicted frequency of the 3rd longitudinal mode of vibration are the resonant frequencies of that mode.

	Config I % difference	Config II % difference	Config III % difference
1st Longitudinal mode	0.030	0.114	0.024
2nd Longitudinal mode	N/A	0.387	1.104

Table 5.1: Percentage difference between resonant frequencies found through EMA and impedance analyser methods

To assess the accuracy of the finite element models, the percentage difference between the frequencies of the longitudinal modes predicted through FEA and those measured through EMA and from the impedance analyser are shown in Figure 5.10. The largest percentage difference between the predicted and experimentally acquired frequencies was to found to exist

in the tuned frequency of configuration I, 7.25%, while the smallest difference was found in the 3rd longitudinal mode, 0.99% for the same configuration. The 2nd longitudinal mode of vibration in configuration I was not excited by the impedance analyser (possibly due to the piezoceramic stack being located at a longitudinal antinode, an observation briefly discussed in Section 3.4.1) and therefore no data is present for it in Figures 5.9 and 5.10(b).

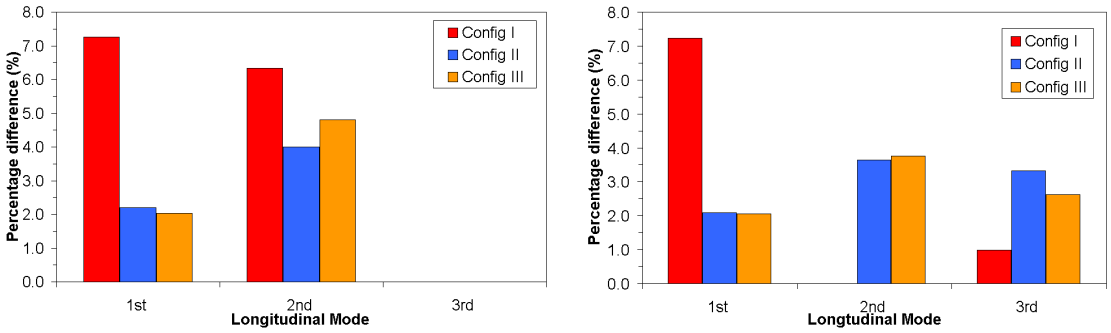

(a) FEA/EMA (b) FEA/IA

Figure 5.10: Percentage difference between frequencies of longitudinal modes of vibration of transducer configurations

The difference between the frequencies of maximum and minimum admittance, $\Delta f_{m,n}$, are presented in Table 5.2. The largest $\Delta f_{m,n}$ found at the 1st longitudinal mode was seen in configuration I, and the smallest was seen in configuration III, while, the largest difference between f_m and f_n for the 2nd and 3rd longitudinal modes was seen in configuration II. Finally configuration III achieved the smallest $\Delta f_{m,n}$ in each of the longitudinal modes.

	1st Longitudinal Mode (Hz)			2nd Longitudinal Mode (Hz)			3rd Longitudinal Mode (Hz)		
	f_m	f_n	$\Delta f_{m,n}$	f_m	f_n	$\Delta f_{m,n}$	f_m	f_n	$\Delta f_{m,n}$
Config I	26748	28568	1820	N/A	N/A	N/A	80805	85332	4527
Config II	28167	29484	1317	55477	58759	3282	80853	87011	6158
Config III	29168	29819	651	55770	58854	3084	86208	87533	1325

Table 5.2: Frequencies of maximum and minimum admittance of transducer configurations I, II & III

As reported in Section 1.2.2, the electro-mechanical coupling coefficient, k_{eff}, f_m and f_n are related through the Equation 1.8 when $f_m = f_r = f_s$ is assumed [22, 41, 95]. Therefore values of k_{eff} were calculated for each of the transducer configurations for each of the longitudinal modes and are presented in Table 5.3. Configuration I attained the largest value for $\Delta f_{m,n}$, hence also attaining the largest value for k_{eff}, whilst configuration III achieved the smallest values of k_{eff} at the 1st, 2nd and 3rd longitudinal modes of vibration.

Table 5.4 contains the electrical quality factors, Q_e, measured from the impedance analyser (Agilent 4294A). At the 1st longitudinal mode of vibration, configuration I achieves

	k_{eff}		
	1st Longitudinal Mode	2nd Longitudinal Mode	3rd Longitudinal Mode
Config I	0.351	N/A	0.321
Config II	0.295	0.330	0.370
Config III	0.207	0.319	0.173

Table 5.3: Values of k_{eff} for transducer configurations I, II & III

the largest value for Q_e, while the smallest value for Q_e is seen in configuration III. Configuration II achieves the largest value for Q_e at the 2nd longitudinal mode of vibration although it also attained the smallest value of Q_e at the 3rd longitudinal mode of vibration. Finally configuration I possesses the highest value of Q_e at the 3rd longitudinal mode.

	Q_e		
	1st Longitudinal Mode	2nd Longitudinal Mode	3rd Longitudinal Mode
Config I	393.4	N/A	841.7
Config II	225.3	577.7	525.0
Config III	116.7	442.1	695.9

Table 5.4: Values of Q_e for transducer configurations I, II & III

5.2.3 Discussion

Initially, it can be observed that good correlation can be seen between the resonant frequencies and mode shapes predicted by FEA and measured through EMA for the 1st and 2nd longitudinal modes of vibration. Furthermore, the resonant frequencies found experimentally through EMA and measured from the impedance analyser also show a high degree of correlation, however, it should be stated that to guarantee that the resonant frequency measured matches the expected mode shape, mode shape validation can only be sought through experimental modal analysis. Unfortunately, it is unclear why there is a relatively high percentage difference between the frequency of the predicted and measured 1st longitudinal mode of vibration for configuration I, when compared to configurations II and III, however as discussed in Chapter 3, the cause could be sub-optimal pre-loading during manufacture.

High values of k_{eff} and Q_e are desirable for efficient transduction; the greater these values are then the higher the efficiency of the tuned device will be [24, 94]. However from Tables 5.3 and 5.4 it can be observed that the longitudinal mode of vibration at which the highest value of k_{eff} for a transducer configuration is found does not necessary correspond with the longitudinal mode where the highest value of Q_e occurs. The highest value of k_{eff} for configuration I occurs at the 1st longitudinal mode of vibration, while the highest of Q_e is found at the 3rd longitudinal mode of vibration. Similarly with configuration II and III, the highest value of k_{eff} occurs at the 3rd and 2nd longitudinal modes of vibration, respectively,

while the highest value of Q_e is found at 2nd and 3rd.

The influence of the longitudinal mode of vibration on k_{eff} may be due to the position of the piezoceramic stack with reference to the nodal point. Shuyu [183], stated that for k_{eff} to achieve maximum and therefore optimal values, the piezoceramic stack should be located at the nodal point. This statement concurs with the findings for configurations I, II and III, as the highest value of k_{eff} occurs when the piezoceramic stack is located at or close to a nodal point of the respective longitudinal mode of vibration which it is occurs at. Meanwhile, the longitudinal mode of vibration appears to influence the value of Q_e. The values of Q_e found at the 2nd and 3rd longitudinal modes of vibration are considerably larger than those found at the 1st longitudinal mode of vibration, therefore it appears that, in general, a possible trend could be higher the longitudinal mode number, higher the value of Q_e. Again, it is unclear why this has occurred, but one possibility is that as the longitudinal mode number increases, vibrational amplitude decreases (for corresponding excitation level) and therefore Q_e lowers with elevated amplitudes of vibration.

5.3 Power harmonic characterisation

The transducer configurations were excited between 1V$_{rms}$ to 50V$_{rms}$ using the method described in Section 4.2.2 close to the resonant frequency of the first longitudinal mode of vibration. The mechanical quality factor, Q_m, was calculated for each transducer configuration using the $\sqrt{2}$ peak method from the frequency-responses at an excitation level of 1V$_{rms}$. The frequency increased and decreased by 1Hz during the sweeps, while a 10 second delay was incorporated between successive frequency increment, Figure 5.11.

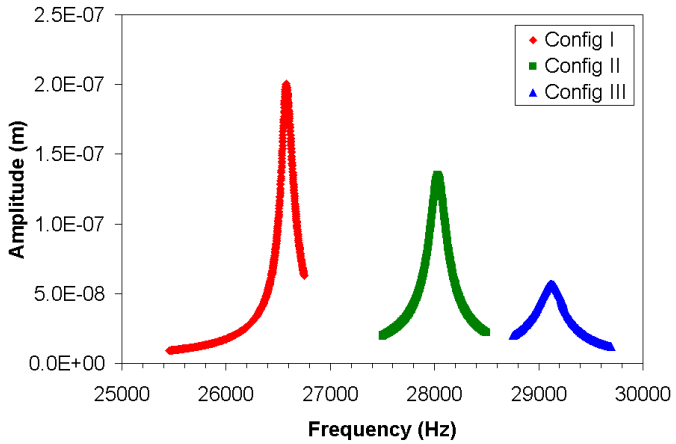

Figure 5.11: Amplitude response for 1st longitudinal mode under 1V$_{rms}$ excitation

The value of the mechanical quality factor varies over the transducer configurations, Table 5.3, and similar to Q_e, configuration I attained the largest value of Q_m.

	Q_m
Configuration I	255.1
Configuration II	186.5
Configuration III	111.7

Table 5.5: Mechanical quality factors of 1st longitudinal mode of transducer configurations I, II & III

5.3.1 Power harmonic characterisation of transducer configurations I, II & III

The response curves for the transducer configurations excited at frequencies close to the first longitudinal mode at voltages from $1V_{rms}$ to $10V_{rms}$ and from $1V_{rms}$ to $50V_{rms}$ can be seen in Figures 5.12, 5.13 and 5.14. The burst used to excite the transducers was 4000 cycles in length, while the duration of the time delay incorporated between successive frequency increments between excitation levels of $1V_{rms}$ to $10V_{rms}$ was 1 second, whereas for excitation levels between $10V_{rms}$ to $50V_{rms}$ the duration was 10 seconds. Vibrational responses recorded from configurations II and III were measured from the free end of the shorter endmass.

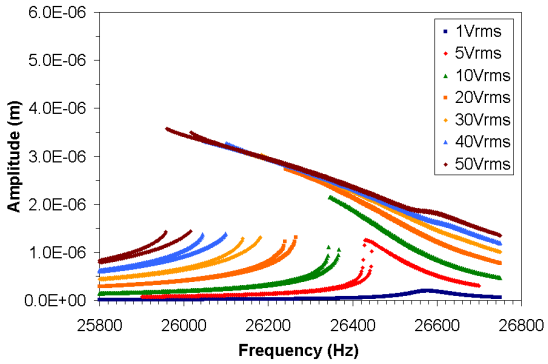

(a) 1 to $50V_{rms}$

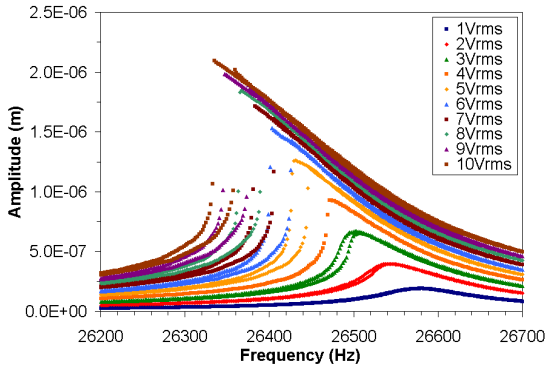

(b) 1 to $10V_{rms}$

Figure 5.12: Vibrational response of configuration I

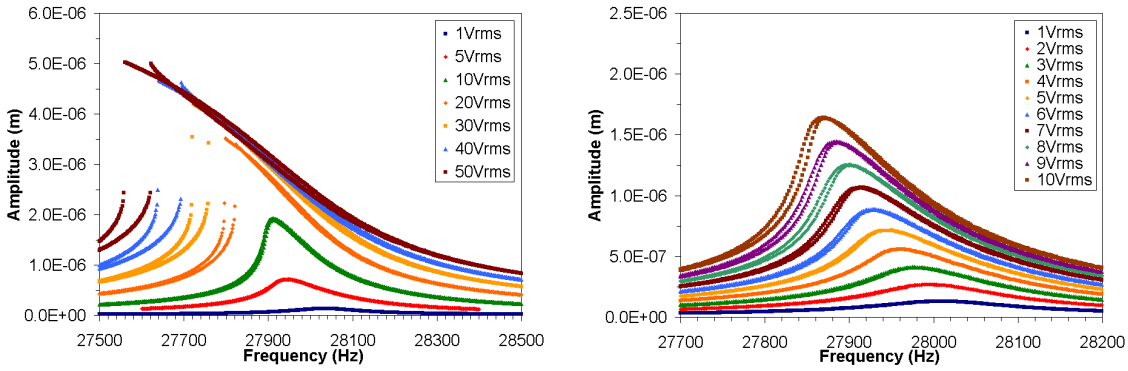

(a) 1 to 50V_{rms} (b) 1 to 10V_{rms}

Figure 5.13: Vibrational response of configuration II

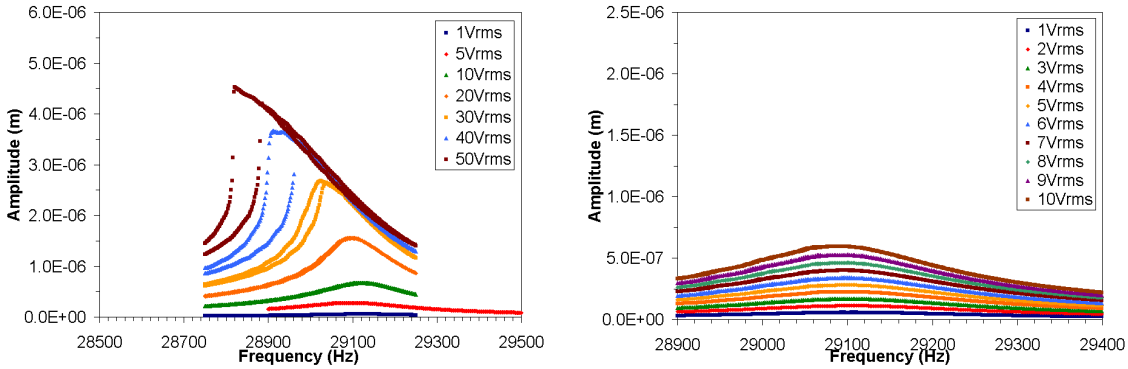

(a) 1 to 50V_{rms} (b) 1 to 10V_{rms}

Figure 5.14: Vibrational response of configuration III

Observations from Figures 5.12 5.13, 5.14, and Figure 5.15 initially show that between 1V_{rms} and 10V_{rms} configuration I delivers the largest output displacement per volt while configuration III produces the least. At a voltage level of 50V_{rms}, it can be seen that configuration II delivers the highest output amplitude, approximately 5μm, while at the same voltage level configuration I achieves the smallest output amplitude of the transducers, approximately 3.5μm.

A softening effect can also be observed in the amplitude response curves as well as in the measurement of the current drawn by the transducer configurations, Figures 5.12 to 5.14 and 5.16. The shift in resonant frequency is plotted for both upward and downward sweeps in Figure 5.17 and initially illustrates that configurations I and II exhibit a similar shift in resonant frequency at amplitudes below 1μm. At an amplitude of 0.4μm, the resonant frequency shift for upward and downward sweeps is 32Hz and 36Hz for configuration I, while configuration II exhibits frequency shifts of 40Hz and 38Hz respectively. However, the shift in resonant frequency exhibited below an amplitude of vibration of 1μm by configuration III is smaller, as it did not rise over 22Hz. Above an amplitude of vibration of 1μm, configuration

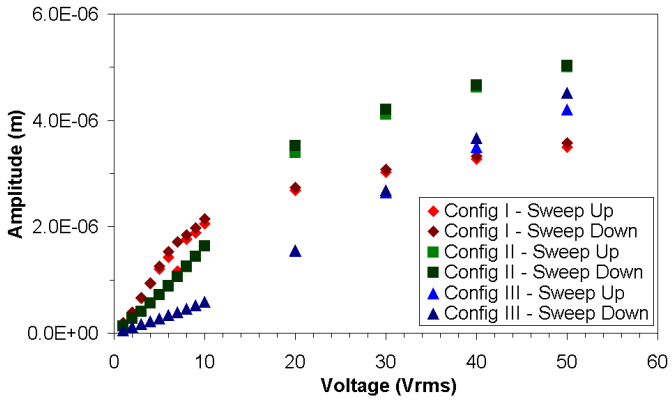

Figure 5.15: Vibrational response of transducer configurations against excitation voltage

I exhibits the largest shift in resonant frequency of the three transducer configurations. At an amplitude of vibration of 3.5μm, configuration I experiences resonant frequency shifts of 561Hz and 621Hz whereas configuration II suffers shifts of 194Hz and 216Hz during upward and downward sweeps, respectively. At the amplitude of vibration of 3.5μm configuration III exhibits the lowest shift in resonant frequency of the configurations, 146Hz and 186Hz during upward and downward sweeps.

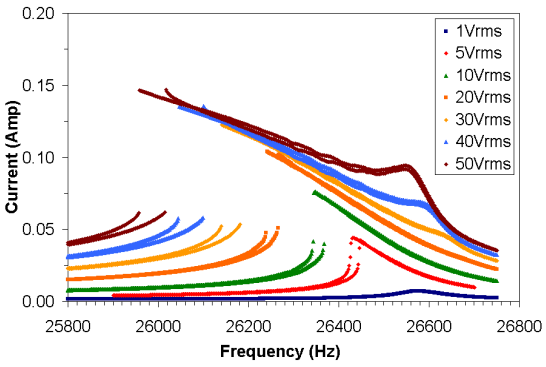

(a) Configuration I

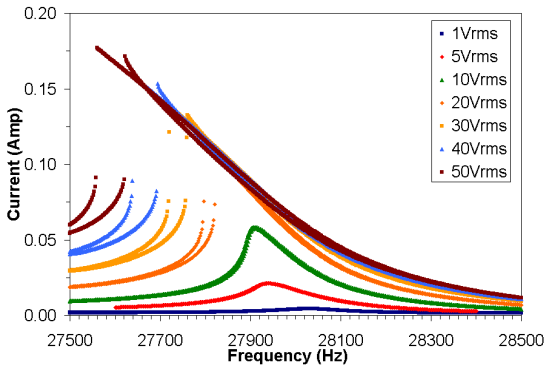

(b) Configuration II

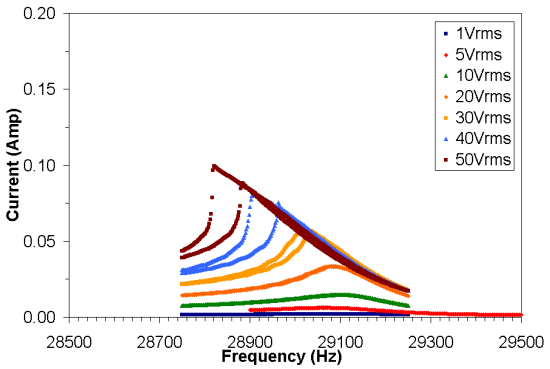

(c) Configuration III

Figure 5.16: Current drawn by transducer configurations

Amplitude jumps can also be observed in Figures 5.12 to 5.14 and 5.16. Configuration I amplitude exhibits jumps at the lowest excitation voltage, $5V_{rms}$, and vibration amplitude, 1.21μm. Meanwhile they are not exhibited in configuration II until a excitation voltage of $20V_{rms}$ and configuration III until an excitation voltage of $40V_{rms}$, although, the amplitude of vibration at which the amplitude jumps are exhibited in these configurations II and III is similar, 3.41μm and 3.50μm, respectively.

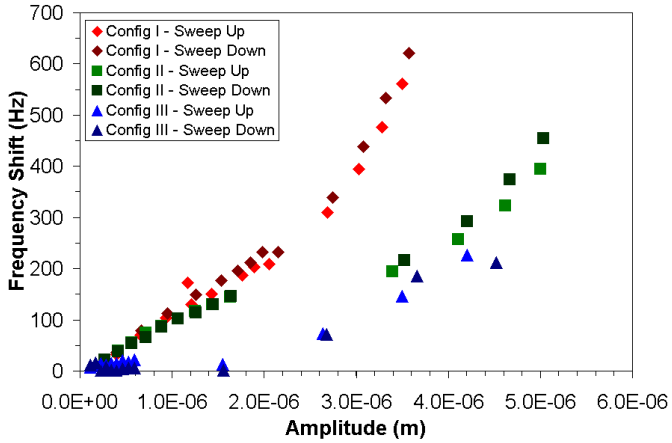

Figure 5.17: Resonant frequency shift versus vibrational response of transducer configurations

Figure 5.18 depicts the hysteretic width and the amplitudes at which they occur. Below an amplitude of approximately $2\mu m$ the largest hysteretic width that configurations I and II exhibit is 6Hz, while configuration III exhibits a width of 14Hz. Above 2μm, it can be observed that the hysteretic width of the transducer configurations increases, at an amplitude of vibration of 3.5μm the hysteresis widths are 22Hz, 24Hz and 54Hz for configurations I, II and III, respectively.

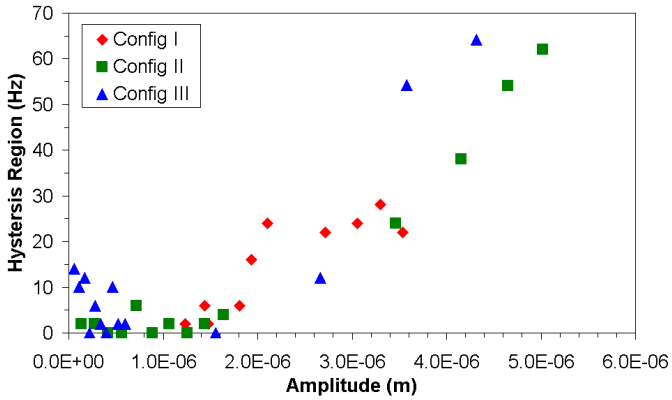

Figure 5.18: Hysteretic width and corresponding vibrational response of transducer configurations

The current drawn by the transducer configurations is plotted against vibrational amplitudes of the resonant frequencies found between driving voltages $1V_{rms}$ and 50_{rms},

Figure 5.19. It can be observed that the relationship between the current and amplitude of vibration is almost linear and as expected, the higher the amplitude of vibration, the higher the current drawn by the piezoceramic stack. Below a vibrational amplitude of 1μm, the current drawn by each of the transducer configurations is similar. However, above an amplitude of vibration of 1μm, it can be observed that configuration I draws more current per micron and configuration III, the least.

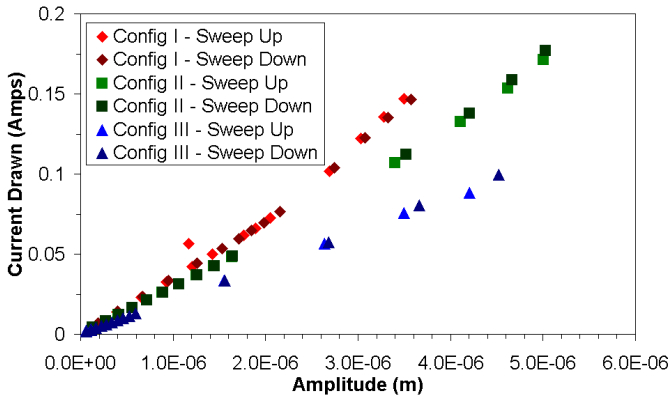

Figure 5.19: Current drawn by transducer configurations against vibrational response at first longitudinal mode

At an amplitude of vibration of 3.5μm, configuration I draws the largest current, 0.147Amps, during both upward and downward sweeps, whilst configuration III draws the least, 0.076Amps during the upward sweep, and 0.081Amps during the downward sweep. Unfortunately it is not possible to calculate the power consumption of the transducers as the phase angle between the voltage and current drawn by the transducer configurations is unknown. However, it can be concluded that if the transducers were driven under conditions of constant current then configuration III would deliver the highest output amplitude per Amp within the tested range.

5.3.2 Harmonic responses of configurations I, II and III

Configuration I

The response close to the 1st longitudinal mode of vibration of configuration I was captured from an oscilloscope (Section 4.2.2) during measurements and can be seen in Figure 5.20. First and second order harmonics are visible within the captured image and lie at frequencies with relationships of 2:1 or 3:1 to the fundamental frequency.

The vibration response of the second harmonic, ω_2, was recorded simultaneously as the response of the fundamental frequency, Figure 5.21. Between voltage levels of $1V_{rms}$ and $9V_{rms}$ no response was measured, Figure 5.21(b), however above an excitation voltage of $10V_{rms}$ a response can be seen at ω_2 which appears to imitate the response of the fundamental, Figure 5.21(a). Above an excitation level of $30V_{rms}$ a shallow trough or 'V' region can be observed between 26490Hz and 26660Hz on the fundamental response curve, Figure 5.12(a). This corresponds with the frequency range 79470Hz to 79980Hz of the response of the second harmonic, Figure 5.21(a), and contains a secondary peak. This suggests that a secondary mode of vibration could be energised between 79470Hz and 79980Hz. Furthermore this feature is more clearly observed in Figure 5.16(a), which illustrates that within the frequency range corresponding of the 'V' region seen in Figure 5.12(a), that the current drawn by the transducer increases.

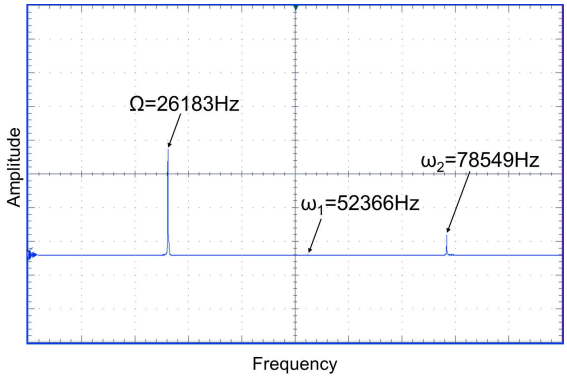

Figure 5.20: Configuration I - Power spectrum captured from oscilloscope, excitation $30V_{rms}$ at 26183Hz (x-axis: 500mV, y-axis: 10.0kHz per block)

Due to close proximity of ω_2 to the 3rd longitudinal mode of vibration, it is likely that this is the mode being energised. Figure 5.22 investigates whether exciting the 3rd longitudinal mode would result in excitation of the 1st longitudinal mode of vibration. Again the softening effect can be seen in Figures 5.22(a) and 5.23, however the response the subharmonic, $\omega_{0.333}$, Figure 5.21(b) between 26300Hz and 26500Hz (a frequency range that corresponds with that of the 'V' region in Figure 5.12(a)) that suggests that there is a path which energy is able to 'leak' from the 3rd longitudinal mode of vibration to a frequency which lies close to the 1st longitudinal mode of vibration.

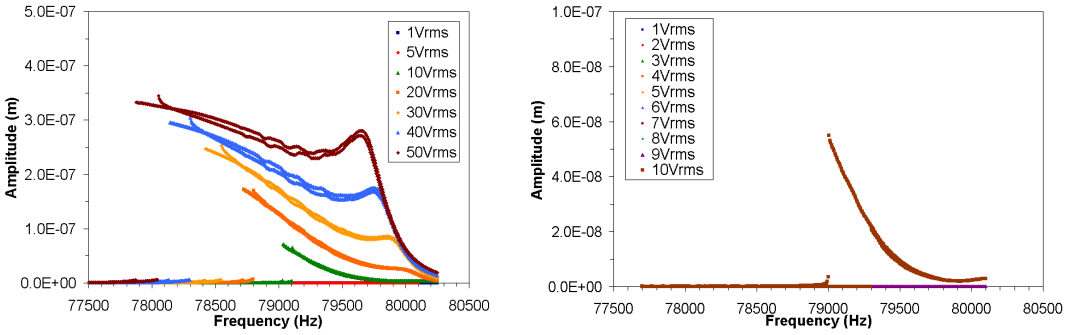

(a) 1 to 50V_{rms} (b) 1 to 10V_{rms}

Figure 5.21: Configuration I - Excitation of 1st longitudinal mode: Response of ω_2

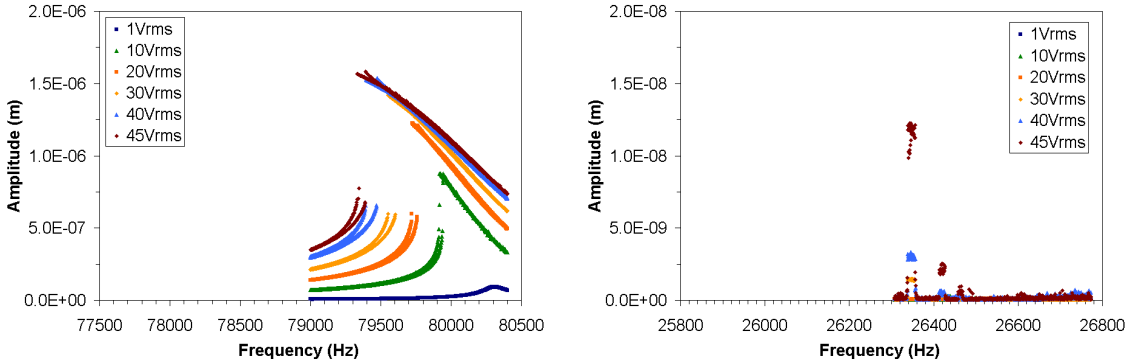

(a) Response of 3rd longitudinal mode of vibration (b) Response of $\omega_{0.333}$

Figure 5.22: Configuration I - Response of excitation at 3rd longitudinal mode of vibration

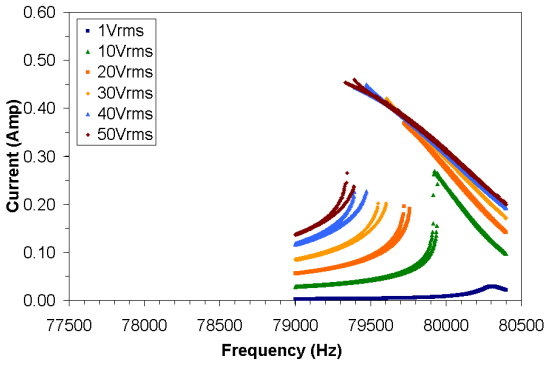

Figure 5.23: Configuration I - Current drawn by transducer at 3rd longitudinal mode

Configuration II

The fundamental, first and second harmonic, Ω, ω_1 and ω_2, responses of configuration II excited close to resonance at 50V_{rms} can be seen in Figure 5.24.

The frequency response of the second harmonic, recorded simultaneously can be seen in Figure 5.25. Whilst the response, Figure 5.25(a), shows similarities to that of the fundamental

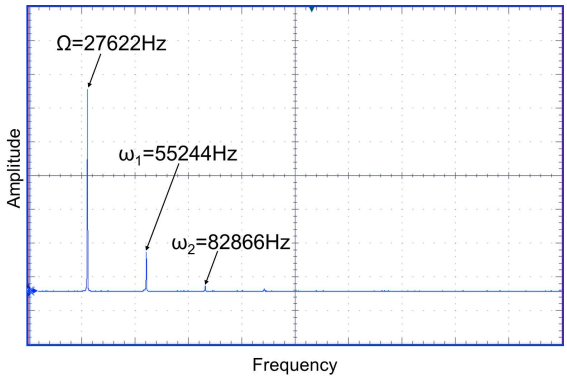

Figure 5.24: Configuration II - Power spectrum captured from oscilloscope, excitation $50V_{rms}$ at 27622Hz (x-axis: 600mV, y-axis: 25.0kHz per block)

response, there is no evidence of energy leaking from one mode of vibration to another as occurred with configuration I. However it should be noted that the location of the third longitudinal mode was found at 80853Hz, 1647Hz below the lowest frequency measured, and therefore any possible excitation of the 3rd longitudinal mode of vibration may lie outwith the measured range.

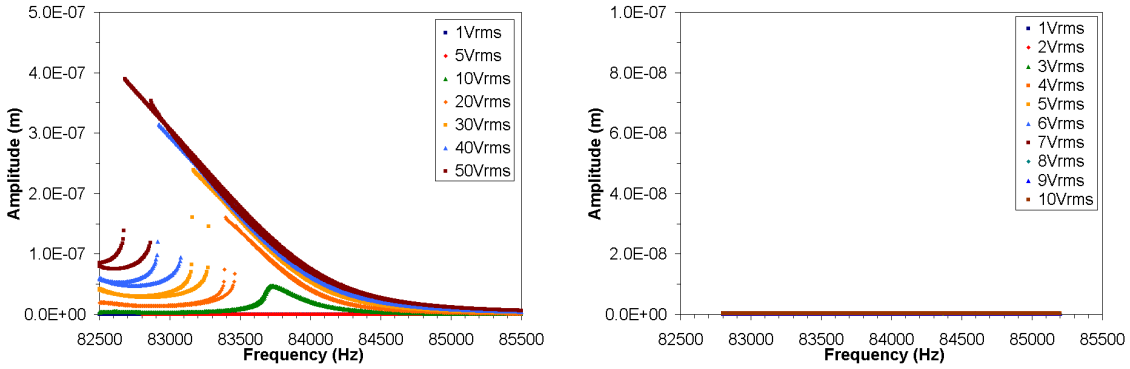

(a) 1 to $50V_{rms}$ (b) 1 to $10V_{rms}$

Figure 5.25: Configuration II - Frequency response of ω_2

Configuration III

Figure 5.26, a captured image from the oscilloscope, displays the power spectrum of configuration III excited with $30V_{rms}$ at the resonant frequency of the 1st longitudinal mode of vibration. Similarly to configurations I and II, the spectrum displays harmonic responses, ω_1 and ω_2 as well as the fundamental response Ω. The response of the ω_2 was recorded throughout characterisation of the 1st longitudinal mode due to the close proximity to the third longitudinal mode, Figure 5.27. Between excitation levels $1V_{rms}$ to $30V_{rms}$ the shape of the response of ω_2 was similar to that of Ω, Figure 5.14. However, the response of ω_2 at $40V_{rms}$ and $50V_{rms}$ significantly differ from those at previous voltage levels. Above 86790Hz

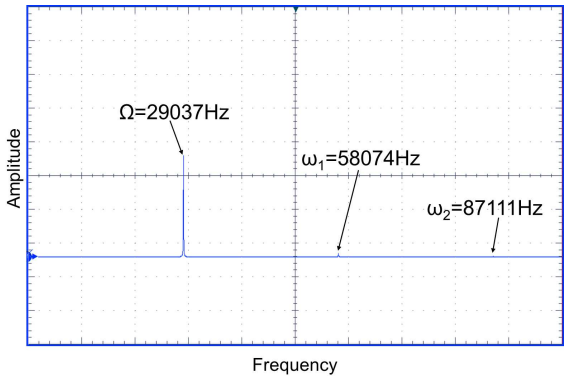

Figure 5.26: Configuration III - Power spectrum captured from oscilloscope, excitation 30V_{rms} at 29037Hz (x-axis: 500mV, y-axis: 10.0kHz per block)

the frequency responses of ω_2 at 40V_{rms} and 50V_{rms} appear to show similarities, although they are larger in amplitude than responses at lower excitation levels. However, below 86790Hz a large response, clearly seen when under an excitation of 50V_{rms}. It is likely that this is the result of the 3rd longitudinal mode of vibration becoming energised by the harmonic, as the highest vibrational amplitude achieved in Figure 5.27(a) occurred at 86421Hz, only 212Hz from the frequency of the 3rd longitudinal mode.

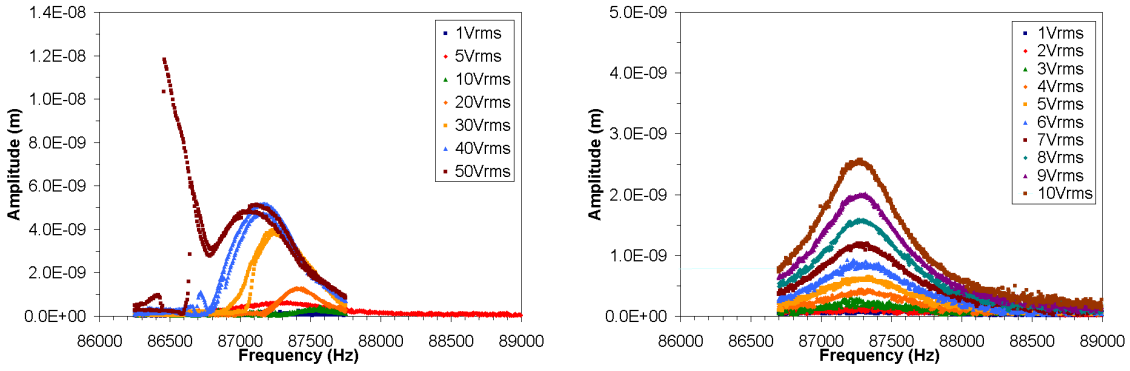

(a) 1 to 50V_{rms} (b) 1 to 10V_{rms}

Figure 5.27: Configuration III - Frequency response of ω_2

5.3.3 Discussion

At low excitation levels, the electrical and vibrational response of the transducer configurations are similar, configuration I achieves both the highest values for Q_e and Q_m and therefore at these excitation voltages configuration I achieves the highest response amplitude (per micron) with relation to excitation voltage. However, at the highest excitation voltage, 50V_{rms}, it is clear that both configuration II and III achieve higher ratios of output vibrational response to excitation voltage than configuration I. Furthermore, less current is drawn by configurations II and III at comparable amplitudes of vibration than by configuration I.

Although, due to (unknown) phase differences between voltage and current, the efficiency of the transducer configurations can not be calculated, however observations suggest that higher levels of vibrational amplitude may result from lower excitation voltages if the piezoceramic stack is situated from the nodal point. While contradicting with the findings of one article [183] this agrees with another and similar study, by Shoh [226]. Shoh's patent reports upon internal power dissipation (combination of electrical and mechanical heat loss) within sandwich transducers and describes that at low vibrational amplitudes the transducer with the stack positioned at the node dissipated less internal power when compared with a transducer with the stack moved $\frac{1}{6}\lambda$ from the node. However, at higher amplitude levels the reverse was found, the transducer with the stack at the node was found to have a higher level of internal power dissipation than that of the transducer with the stack moved $\frac{\lambda}{6}$ from the node. This could suggest that at higher amplitudes of vibration losses within the transducer could be reduced if the piezoceramic elements are moved from the nodal point. Thus, the level of vibrational amplitude can have an influential factor on the performance on each of the transducer configurations [228].

Nonlinear behaviour

The influence that the location of the piezoceramic stack has on the nonlinear behaviour; resonant frequency shifts, amplitude jumps and hysteretic widths, is varied. At lower amplitudes of vibration the resonant frequency shift found in configurations I and II appears to be similar, whilst the configuration III experiences a lesser shift in resonant frequency. However at higher amplitudes (Figure 5.17), it appears that configuration I suffers from the largest shift in resonant frequency, followed by configurations II and then III respectively. The shift in resonant frequency can be attributed to several sources, and is discussed in previous chapters, however in the case of these measurements, the location of the piezoceramic stack is the varying factor. It is known that the elastic properties of piezoceramics behave linearly only at relatively low levels of stress [26, 41, 158, 166]. Hence, moving the piezoceramic stack from the highest point of vibrational stress, the nodal point, to a position away from it, as it is in configurations II and III, suggests that through reducing vibrational stress levels within the piezoceramics elements may reduce the resonant frequency shift experienced by the transducer or tuned device.

Meanwhile, the location of the piezoceramic stack in the configurations also appears to have an effect on the appearance of jump amplitudes. Amplitude jumps first appear in configurations II and III at similar amplitudes, although at a slightly lower amplitude in configuration II, while in configuration I the first amplitude jump occurs at less than half of the amplitude than configurations in II and III. As discussed previously it is known that the jump phenomenon is related to nonlinear behaviour of the elastic constant of the piezoceramic material while at elevated vibrational amplitudes [7, 26, 152]. Therefore if the piezoceramic

elements are positioned in a location of lower stress, then it may be possible to achieve higher vibrational amplitudes before the jump phenomenon occurs.

Harmonic responses

Figure 5.12(a) and 5.21(a) exhibit features that suggest that autoparametric behaviour may be present in configuration I due to the presence of a shallow trough or 'V' region near the resonant frequency in the response curve. Meanwhile, a peak which can be observed in the response of the second harmonic suggests that a mode of vibration may be energised. This peak lies within 1kHz of the frequency of the 3rd longitudinal mode of vibration (measured under low excitation), however at an elevated excitation level, the resonant frequency of the 1st longitudinal mode of vibration lowers by 561Hz, and if it is assumed that the same occurs to the 3rd longitudinal mode of vibration, a relationship of approximately 3:1 would exist between the modes of vibration. Furthermore, an increase in current drawn by the transducer within the frequency range of the 'V' region, Figure 5.16(a), also indicates excitation of a mode of vibration.

Meanwhile, the responses of configuration III suggests that autoparametric behaviour did not occur due to the lack of a 'V' region in the fundamental response. However, it is still possible that with a significant enough amplitude of vibration and due to the proximity of the ω_2 to the 3rd longitudinal mode of vibration (within 300Hz), that ω_2 may correspond with the resonant frequency of this mode of vibration, which induces a relatively large response at this frequency and observed in Figure 5.27(a).

Finally, there is no evidence of modes other than the tuned becoming energised within configuration II. This may be that the frequency of the 3rd longitudinal modes lies outwith the range which may cause it be become energised through harmonic response of the fundamental, through autoparametric vibration. Table 5.2 demonstrates 3rd longitudinal mode lies approximately 1.5kHz below the lowest frequency of ω_2.

5.4 Stress in transducers

In two previous sections, Sections 5.2 and 5.3, similarities and differences in behaviour of the transducer configurations while excited at various levels of vibration amplitude has been investigated. As previously discussed, stress thresholds which piezoceramic elements behave linearly is relatively low, hence placing the piezoceramic stack at a nodal point (point of highest stress) could be detrimental and be at least partly responsible for inducing nonlinear behaviours.

5.4.1 Finite element model

To investigate stress distribution throughout the transducer configurations, finite element models have been used to model the vibrational behaviour of the transducer configurations whilst under steady state vibrational conditions while under a common amplitude of vibration. Figure 5.28 presents normalised stress distributions through each of the configurations, giving a guide to regions of highest and lowest stress concentration.

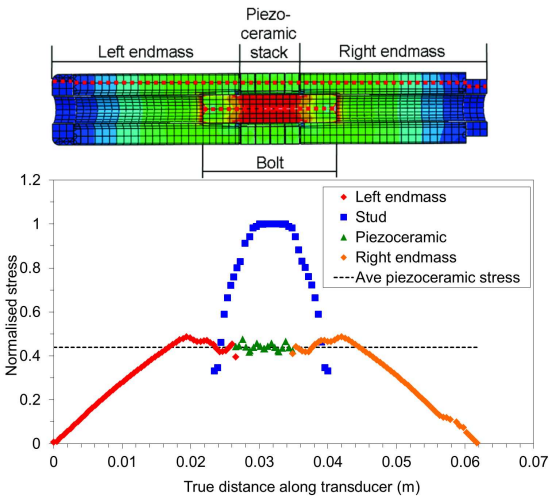

(a) Configuration I

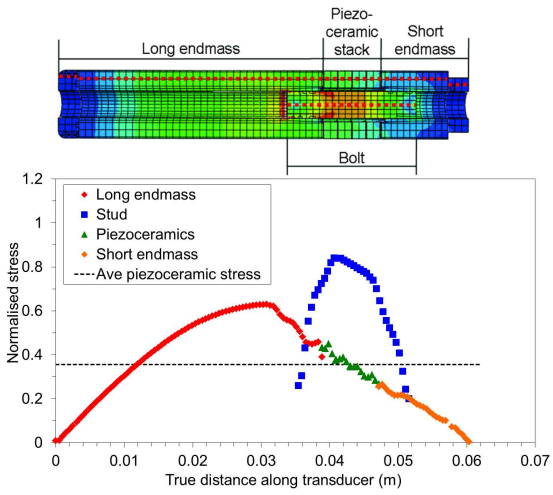

(b) Configuration II

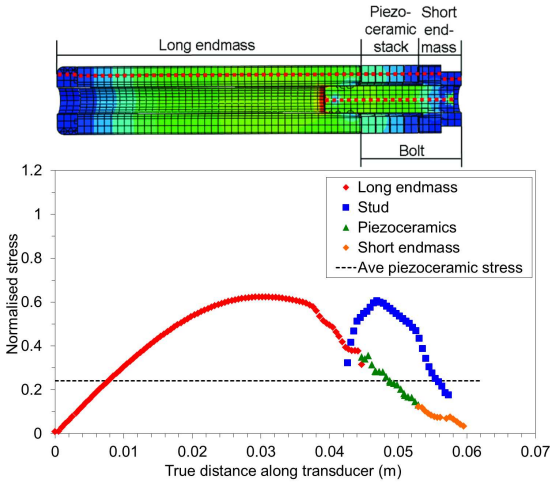

(c) Configuration III

Figure 5.28: Stress contour plots of transducer configurations - Normalised von Mises stress distribution

The normalised stress level was measured along a path and is marked as a dotted line on the sectioned image of the transducer, containing a colour contours illustrating the stress concentration (red: high stress, blue: low stress), Figure 5.28. It can be observed that highest levels of stress are seen in the bolts of the transducer configurations, while the level of stress

within the piezoceramics is significantly lower. Although, stress levels differ throughout the stacks in different configurations, the level of stress within a single stack is not constant, therefore to provide comparisons, the stress along the measured path in the piezoceramic elements has been averaged. Black dotted lines in Figures 5.28(a) to 5.28(c) depict the average stress within each of the piezoceramic stacks, and it can be observed that Configuration I attains the largest average stress concentration throughout the piezoceramic stack, while configuration III attains the lowest. On the other hand it can be observed that stress levels throughout the piezoceramic stack in configuration I are relatively constant when compared to configurations II and III where stress concentrations in each of the outer elements in the stack can differ.

5.4.2 Discussion

Results predicted through finite element analysis provide evidence that placing the piezoceramic stack in a location away from the nodal point reduces stress levels within piezoceramic elements. However, it also illustrates that positioning a stack consisting of multiple piezoceramic rings in a location away from the nodal point also leads to stress gradient within the stack. Hence, the piezoceramic positioned closest to the nodal point experiences a higher level of stress than one located furthest from the node. Whether this has a detrimental effect on the performance of the piezoceramics can not be concluded from current results.

Furthermore, positioning the piezoceramic elements in a location away from high stress inherently positions them in a location of higher strain. It is unknown whether in addition to strain induced by the inverse piezoelectric effect, increased levels of strain would cause the piezoceramic elements to experience increased physical deterioration such as delamination or depoling. Additionally it is also unknown whether high strain levels would induce the direct piezoelectric effect, generating an electrical field, which could lead to amplitude saturation or even the manifestation of further nonlinear behaviour once excitation levels higher than an those in this study were achieved [225].

5.5 Chapter conclusion

The performance of transducers with differing piezoceramic stack positions has been investigated at both low and high levels of vibrational amplitude. As with previous chapters, natural frequencies and mode shapes of the longitudinal modes predicted through FEA and experimentally measured by EMA have shown good correlation. Furthermore, resonant frequencies found through EMA also corresponded with resonant frequencies measured through an impedance analyser. To characterise the transducer configurations at high vibrational amplitudes, the experimental method described in Section 4.2.2 allowed the tuned devices to be studied under steady state conditions whilst removing the effect of temperature increases within the piezoceramic stack.

Experimental observations suggest that the level of vibrational amplitude is a significant factor with regards to performance (levels of achievable amplitude with respect to excitation and influence of nonlinear behaviour) of the transducer configurations. Nonlinear phenomena such as resonant frequency shifts, amplitude jumps and hysteretic regions have been proved to be present in all transducer configurations, although it has been observed that they do not appear to influence the configurations equally at the same excitation or amplitude levels. Under relatively low excitation levels ($1V_{rms}$) configuration I exhibited characteristics (highest values of Q_m, Q_e and k_{eff} at 1^{st} longitudinal mode) suggesting it would possess optimal performance (vibrational amplitude) over configurations II and III. However, at elevated vibrational levels, it can be observed (Figures 5.17 and 5.18) that configuration I exhibited stronger nonlinear behaviours than configurations II or III, while from Figure 5.19 it can be seen that configuration I draws the largest current per micron. Although it is not possible to conclude that at elevated amplitudes that configuration I is the least efficient transducer configuration, these observations may be sufficient to question conventional design rules that locating the piezoceramic stack at the longitudinal node will automatically provide the optimal performance.

Finally, finite element characterisation illustrated that at a similar amplitude of vibration, positioning the piezoceramic stack away from the nodal point reduced the average level of stress experienced by piezoceramic stack. However, it is also understood that locating the piezoceramic stack away from the nodal point and inducing a stress gradient through the stack may cause the introduction unforseen problems.

Chapter 6

Conclusions

The work presented in this thesis has focused on characterising linear and nonlinear behaviour of ultrasonic devices used in bone surgery through finite element and experimental methods. Through investigating a range of ultrasonic devices it has been possible to observe that some design features, such as geometry and mode of vibration, can influence the presence and strength of nonlinear behaviour. It has also been observed that other variables such as joint pre-loading can or piezoceramic heating can also strongly influence the the presence of nonlinear behaviour.

Although this work has characterised ultrasonic devices used in surgery, the methodology and the findings should be transferable to investigating other ultrasonic devices that exhibit similar nonlinear behaviours even if used in different applications.

6.1 Correlation between FEA and EMA

Under low vibrational amplitudes experimental modal analysis was used to measure the modal parameters of the ultrasonic devices under investigation as well as to validate the FE models. A high level of accuracy (less than a 4% difference) was mostly achieved between the predicted and measured resonant frequencies of the tuned mode of vibration, however it was found that lower correlation between predicted and measured tuned frequencies did occur in some of the investigated devices. The devices that exhibited the closest correlation between predicted and measured resonant frequencies were those under commercial production, while the devices which attained a lower correlation between predicted and measured resonant frequencies were prototypes or contained prototype inserts. The investigation involving the seven modified OT7 inserts highlights this, the percentage difference between the predicted and measured tuned frequencies for these inserts ranged from 1.26%, demonstrating good correlation between FEA and EMA, to 6.77%, showing not such good correlation. In this case, poorer correlation between FE models and EMA most likely stems from inaccuracies arising from manufacturing a ‘one off’ relatively complex component has resulted in slight

geometric or material property differences been those modelled and those measured.

Similarly, the percentage difference found between the predicted and measured frequencies of the tuned longitudinal mode of vibration of the Langevin transducers discussed in Section 3.4, Chapter 3 as well as those discussed in Chapter 5, illustrates that significant differences can occur in the predicted and measured tuned frequency. The percentage difference between the tuned longitudinal mode of vibration of the transducers discussed in Chapter 5 are 2.03%, 2.10% and 7.25%. Of the three transducers, two show a good level of correlation between FEA and EMA while one does not. The transducer which exhibits poorer correlation between FEA and EMA, could contain geometric differences with that of the modelled geometry, however, in this case it is likely that sub-optimal pre-loading has been applied during the transducer's assembly.

Overall, good correlation was achieved between modal parameters predicted by FEA and measured through EMA. FE models which attained lower correlation with EMA have been discussed and likely sources of errors reported upon.

6.2 Vibrational behaviour of ultrasonic devices

As with many studies investigating the behaviour of piezoceramic elements or ultrasonic devices [6, 9, 26, 27, 116, 146, 150–155, 158, 159], the strain and electrical thresholds at which behaviour changes from linear to nonlinear can be relatively low. It has been documented that mechanical and dielectric loss factors, Q_m^{-1} and δ, of piezoceramic materials are sensitive to both elevated electric field strength and temperature, while other properties, such as the elastic, dielectric and piezoelectric terms are more sensitive to elevated temperatures than elevated vibrational amplitudes. Hence, to investigate the influence that elevated driving conditions have on ultrasonic devices it is important to separate the influence of elevated vibrational amplitude and electric field strength from that of elevated temperatures.

Two methods of characterising ultrasonic devices at elevated driving conditions were discussed; burst excitation where either the transient or steady-state response of the ultrasonic device was measured. The steady-state burst technique was then selected for use in this work as it provided a closer representation of operational conditions.

6.2.1 Influence of tuned insert on vibrational behaviour

All half wavelength assemblies contained in the Piezosurgery® Device contain a common base from which usually stems a shank (to induce flexural motion) and a tool, such as a cutting blade. To investigate the influence of these features on the behaviour of the ultrasonic device the shank and tool were removed from one insert (base insert) and characterised in parallel with an unmodified insert (OT7 insert). The resultant vibrational responses of the tuned assemblies containing the base and OT7 inserts exhibited a response typical of a duffing

oscillator. Both a lowering in resonant frequency and hysteretic regions (between upward and downward frequency sweeps) where observed. However, it appears that the presence of the shank and cutting blade did not significantly influence the softening effect or the width of the hysteretic region.

Similar results were observed in the responses of the full wavelength assemblies containing half wavelength surgical inserts, which also stem from the common insert base. Again responses of the tuned inserts were typical of a softening duffing oscillator, exhibiting both a lowering in resonant frequency and hysteretic widths. Despite this, the difference in the various insert shapes did not appear to significantly influence these behaviours. However, when comparing the amplitude of vibration of assemblies containing the half and full wavelength assemblies containing surgical inserts, it can be observed that the highest vibrational amplitude attained by the assemblies was 4μm and, at this amplitude of vibration, the frequency shift observed in the half wavelength assemblies was greater (approximately 50Hz) than those exhibited by the full wavelength assemblies. Similarly, this observation was also seen in the responses of the half and full wavelength assemblies containing the rod horns. The half wavelength assemblies containing the rod horns also exhibited larger shifts in resonant frequency than those exhibited in the half wavelength assemblies containing the rod horns. Meanwhile, whether the half or full wavelength assemblies contained either surgical inserts or rod horns, this feature did not appear to strongly influence the width of the hysteretic regions.

However, if power spectrum plots captured at high amplitudes of vibration close to resonance of the half wavelength surgical assemblies (those containing either the base tip or OT7 insert) and full wavelength surgical assemblies (those containing the TLR insert, with and without the blade tip) are compared, clear similarities and differences can be observed between them. It can be observed that the spectrum response of the assemblies containing the base insert and TLR insert without the blade tip both only exhibit the fundamental response as well as the first and second harmonics. Nonetheless, from the power spectra of the assemblies containing the OT7 insert and TLR insert containing the blade tip, more than the fundamental and harmonic responses can be observed. It has been suggested that period doubling is present in the power spectrum when these assemblies are driven at elevated amplitudes of vibration which contain both flexural and longitudinal motions. Period doubling could lead to an unstable system as the phenomenon can indicate a route to chaotic behaviour.

From the tuned inserts studied, insert geometry has been found to have an influence on the behaviour of the tuned device. Regardless, it has been observed from other experimental work presented in this thesis that joint stiffness and elevated piezoceramic temperature potentially have much greater influence on the behaviour of ultrasonic devices than tuned inserts if they are not optimised or controlled.

6.2.2 Influence of location of piezoceramic stack on transducer behaviour

Traditionally, it has been proposed that the piezoceramic stack of a Langevin transducer should be located at the nodal point of the longitudinal mode of vibration. As this corresponds with the location of highest dynamic stress (it is well known that piezoceramic elements have a low linear threshold to stress) Langevin transducers were manufactured with different stack locations to investigate whether positioning the stack away from the nodal point influenced its behaviour.

At low levels of vibrational amplitude, properties which indicate high transducer efficiency, Q_m, Q_e and k_{eff}, were highest in transducer configuration I (piezoceramic stack located at longitudinal nodal point) and smallest in transducer configuration III (piezoceramic stack located furthest from longitudinal nodal point). At elevated vibrational amplitudes, all three transducer configurations exhibited responses similar to that of a softening duffing oscillator. However, it was observed that configuration I exhibited the largest shift in resonant frequency with respect to vibrational amplitude while configuration III exhibited the smallest. As configuration I exhibited the largest shift in resonant frequency, it could be suggested that the softening effect is directly related to elevated stresses within the piezoceramic stack. Although configuration I exhibited the largest shift in resonant frequency it also exhibited the smallest hysteretic width, while configuration III exhibited the largest. This again suggests that the position of the piezoceramic stack could influence nonlinear behaviour, although in this case locating the stack towards the nodal point would reduce the hysteretic width.

Jump amplitude responses can cause instability whilst driving at resonance due to the potential that the transducer can oscillate at either a high or low amplitude of vibration. Although amplitude jumps appear in the responses of configurations II and III at approximately the same amplitude, they occur in the response of configuration I at less than half this amplitude. This again suggests that this behaviour is related to the level of stress within the piezoceramic stack.

Meanwhile, characteristics of autoparametric vibration have been observed in the response of configuration I. It was observed that a mode of vibration (3^{rd} longitudinal mode of vibration) lay in close proximity to the frequency of the second harmonic and was becoming energised. Although there is no evidence that modes other than the tuned mode of vibration were energised when excited close to resonance in configuration II, the response of the second harmonic of configuration III suggests that the response of the harmonic is influenced by the close proximity of a mode of vibration (3^{rd} longitudinal mode of vibration). These observations suggest that if higher order longitudinal modes of vibration are located at frequencies close to harmonics, then there could be a significant chance that they become energised.

Although, traditional transducer design locates the piezoceramic stack at the nodal point, this study has reported that at elevated vibrational amplitudes benefits in transducer

behaviour exist if the piezoceramic stack is positioned away from the nodal point. However, from the completed work, it is has not been possible to prove whether benefits gained by locating the piezoceramic stack away from the nodal point outweigh those found by positioning the stack at the nodal point.

6.3 Summary of findings

Comparisons between the half and full wavelength assemblies investigated in this thesis has shown that nonlinear behaviours have been observed in these devices whilst excited at elevated amplitudes of vibration and that device geometry has higher influence on some nonlinear behaviours than others. It has also been observed that power spectrum responses of assemblies those inserts are tuned to operate in a longitudinal motion differed from those tuned to operate in a combined longitudinal-flexural motion. The power spectrum of the devices tuned to operate in a combined longitudinal-flexural motion exhibited responses suggesting that at elevated vibrational amplitudes the device would be unstable. Therefore it is important if combining longitudinal-flexural motions that the threshold at which the device begins to behave unstably should not be crossed whilst under operational conditions. Meanwhile, two other factors were found to significantly influence the behaviour of ultrasonic devices, heating within piezoceramic elements and torque within joints.

The design of Langevin transducers with differing piezoceramic stack locations has been presented. Measurements taken at low vibrational amplitudes have provided evidence that transducers with piezoceramic stacks located at the node have properties which indicate higher performance than those with a piezoceramic stack located away from the node. However, at elevated amplitudes of vibration it has been observed that the location of the piezoceramic stack can influence the nonlinear behaviour of the device. Locating the piezoceramic stack away from the nodal point saw lower levels in some nonlinear behaviours, but higher in another with respect vibrational amplitude. Finally, behaviour observed by two transducer configurations suggest that if higher order longitudinal modes of vibration are located at frequencies close to harmonics, then it is possible that these could become energised. This could have been prevented by ensuring that modes of vibration do not have frequencies in close proximity to harmonic frequencies.

6.4 Design guidelines

To briefly summarise the findings, and to assist in the design of ultrasonic devices, Table 6.1 briefly presents the findings of this thesis.

FEA & EMA	Guideline	Reasoning
Finite element analysis	i. Meshing geometry should preferably use hexahedral and wedge elements over tetrahedral elements. ii. Quadratic variations of these elements should also be used. iii. Ensure material properties applied to geometry are close to possible as actual values.	i. The use of the hexahedral and wedge elements over hexahedral elements will reduce output file size, reducing solve time. ii. Quadratic elements ensure real mode shapes are predicted by the solver. iii. Material properties strongly influence FE predictions, incorrect material properties will herald incorrect FE predictions.
Experimental modal analysis	i. The device should be preferably mounted at a nodal point of the tuned mode of vibration. ii. Excitation selection will depend upon the device under investigation, although it was found that using random excitation was best suited to slender structures.	i. Mounting a structure at the nodal point of the tuned mode of vibration should minimise the effect of damping on the mode most likely of interest. ii. Using random excitation, high noise levels (often seen in first few FRF averages) rapidly reduced. Resonant frequencies are also quickly found across the frequency range of interest.
Sources of nonlinear behaviour	**Observation**	**Guideline**
Shifts in resonant frequency	A lowering in resonant frequency (softening effect) was evident in each of the investigated devices when excited at elevated amplitudes of vibration. i.It was observed that half wavelength ultrasonic assemblies exhibited greater shifts in resonant frequency than full wavelength assemblies at comparable amplitudes of vibration. ii.It was also observed that heating within piezoceramic elements as well as the level of pre-loading of joints or Langevin transducers can dwarf the influence of inserts.	i.The presence of higher resonant frequency shifts in half wavelength assemblies has been accounted for higher levels of strain within the material and thus could be reaching nonlinear elastic thresholds. ii.Elevated temperatures should be avoided in piezoceramic elements as it is well known that properties are temperature dependent. Joint stiffness should be optimised to ensure joints are not under pre-loaded. Upper loading levels are dependent material properties of components being joined.
Hysteretic regions and amplitude jumps	i.Hysteretic regions are dependent upon piezoceramic temperature and joint tightness. ii.Amplitude jumps are dependent upon amplitude of vibration, piezoceramic temperature and joint tightness.	To attempt to control these behaviours; i.Control piezoceramic temperature. ii.Optimise joint tightness.
Period doubling	Difference in the spectral responses of surgical inserts (with and without cutting blades), excited close to resonance, were observed. The source of the period doubling was concluded as the the presence of the blade tips which induced a flexural motion into the tuned longitudinal motion.	Under current conditions of operation, chaotic motion was not detected. However the possibility of chaotic motion should be considered in during the design of future ultrasonic tools which combine both longitudinal and flexural modes of vibration.
Autoparametric vibration	Autoparametric vibration was observed in a half wavelength Langevin transducer. This was due to the frequency of the 3^{rd} longitudinal mode of vibration corresponded with the 2^{nd} harmonic and hence had a simple relationship of 3:1 with the frequency of the fundamental frequency.	The likelihood of exciting a mode other than the desired could be reduced by avoiding simple relationships (i.e 2:1 or 3:1) between the frequencies of different modes of vibration.

Table 6.1: General guidelines for the design and the control of common nonlinear behaviours observed in ultrasonic devices

Chapter 7

Future Work

The aim of this thesis was to characterise the linear and nonlinear behaviour of power ultrasonic devices utilised in bone surgery. However, to further the work several areas of research could be investigated;

Simulation and modelling Although good correlation was achieved between predicted and measured resonant frequencies and mode shapes, the FE model could be greatly improved by more closely representing damping in the system. The current model incorporates material damping and global (or uniform) damping. However, Ouyang *et al* [224] stated that up to 90% of the damping in a simple beam system containing a lap joint stems from the joint itself. Although most power ultrasonic components are joined using axial joints, it is still reasonable to assume that a significant percentage of damping will stem from the joint or joints in ultrasonic devices. To improve current models threaded joints could be more closely simulated by incorporating boundary conditions that acknowledge local frictional and compressive forces as well as damping.

Experimental The experimental setup used in the harmonic response measurements (incorporating sine sweep burst technique), although successful in characterising the behaviour of ultrasonic devices, could be improved by enhancing power transfer and thus efficiency between the power supply and ultrasonic device. To do this, a method of matching the electrical impedance of the power amplifier and ultrasonic device would be required. If impedance matched, a lower driving voltage would be required to achieve a corresponding amplitude of vibration than if not matched. This would therefore reduce the influence of the electric field on the piezoceramic stack within the ultrasonic device.

Optimal joining torque between ultrasonic components Although only briefly discussed, a more detailed investigation into the optimal level of torque required to join components together of ultrasonic devices could ensue design guidelines that promote a reduction in nonlinearities, increase vibrational performance and reliability.

Appendix A

List of publications

Journal Papers

1. M. Farrell, A. Mathieson, P. Chung, A. Heller, S. Clarke, M. McDonald and A. Cardoni. "In vitro performance testing of two arcuate oscillating saw blades designed for use during tibial plateau leveling osteotomy," *Veterinary Surgery*, vol. 40, pp. 694-707, 2011.

Conference Papers

1. A. Mathieson, A. Cardoni and N. Cerisola. "Nonlinear characterisation of a half and full wavelength ultrasonic devices," *Proceedings of 40th Annual Ultrasonic Industry Association Symposium*, 2011.

2. P. Harkness, A. Mathieson, C. Murray and M. Lucas. "Optimization of ultrasonic horns for momentum transfer and survivability in high-frequency/low frequency planetary drill tools," *Proceedings of AIAA Space 2011, Long Beach California*, AIAA-2011-7319, September 2011.

3. A. Cardoni, A. Mathieson and N. Cerisola. "Reducing the nonlinear vibration behaviour of power ultrasonic transducers for bone surgery," *Proceedings of Internoise 2010*, Lisbon, Portugal, June 2010.

4. A. Mathieson and A. Cardoni."A study into the vibration behaviour of power ultrasonic devices for bone surgery," *Physics Procedia*, vol. 3, no. 1, pp. 767-773, 2010.

5. A. Mathieson, A. Cardoni, P. Harkness and M. Lucas. "Characterisation of nonlinear behaviour of power ultrasonic drilling horns," *IEEE International Ultrasonics Symposium Proceedings*, pp. 2092-2096, 2009.

References

[1] *A Dictionary of Physics*. Oxford University Press: Oxford Reference Online, 2009. Accessed 10$^{\text{th}}$ January 2010.

[2] E. Neppiras, "Macrosonics in industry 1: Introduction," *Ultrasonics*, vol. 10, no. 1, pp. 9–13, 1972.

[3] J. Gallego-Juárez, "Macrosonics: Phenomena, transducers and applications," *Forum Acusticum Sevilla. Keynote Lectures: KL-05*, vol. 33, pp. 36–42, 2002.

[4] M. Lucas, A. Cardoni, E. McCulloch, G. Hunter, and A. MacBeath, "Applications of power ultrasonics in engineering," *Applied Mechanics and Materials*, vol. 13-14, pp. 11–20, 2008.

[5] M. Lucas, A. Gachagan, and A. Cardoni, "Research applications and opportunities in power ultrasonics," *Proceedings of the Institution of Mechanical Engineers, Part C: Journal of Mechanical Engineering Science*, vol. 223, no. 12, pp. 2949–2965, 2009.

[6] M. Umeda, S. Takahashi, Y. Sasaki, and S. U. Kentaro Nakamura, "Vibration stress and temperature dependence of piezoelectric resonators with lead-zirconate-titanate ceramics," *Electronics and Communications in Japan (Part II: Electronics)*, vol. 83, no. 9, pp. 762–768, 2000.

[7] M. Umeda, K. Nakamura, S. Takahashi, and S. Ueha, "An analysis of jumping and dropping phenomena of piezoelectric transducers using the electrical equivalent circuit constants at high vibration amplitude levels," *Japanese Journal of Applied Physics*, vol. 39, no. 9B, pp. 5623–5628, 2000.

[8] M. Umeda, K. Nakamura, S. Takahashi, and S. Ueha, "Waveforms of the vibration velocity and the current of a piezoelectric transducer in the transient state," *Japanese Journal of Applied Physics*, vol. 40, no. 9B, pp. 5735–5739, 2001.

[9] A. Cardoni, *Characterising the dynamic response of ultrasonic cutting devices*. PhD thesis, University of Glasgow, 2003.

[10] A. Cardoni, E. Riera, A. Blanco-Blanco, J. Gallego-Juárez, and V. Acosta-Aparicio, "On the nonlinear dynamics of plate-transducers," *IEEE Ultrasonics Symposium Proceedings*, pp. 2576–2579, 2009.

[11] A. Mathieson and A. Cardoni, "A study into the vibration behaviour of power ultrasonic devices for bone surgery," *Physics Procedia*, vol. 3, no. 1, pp. 767–773, 2010. International Congress on Ultrasonics, Santiago de Chile, January 2009.

[12] A. E. Clark and M. Wun-Fogle, "Modern magnetostrictive materials: classical and nonclassical alloys," *Proceedings SPIE*, vol. 4699, pp. 421–436, 2002.

[13] A. Olabi and A. Grunwald, "Design and application of magnetostrictive materials," *Materials & Design*, vol. 29, no. 2, pp. 469–483, 2008.

[14] R. E. Newnham, *Properties of materials: Anisotropy, symmetry, structure.* Oxford, UK: Oxford University Press, 2008.

[15] J. Gallego-Juárez, "Piezoelectric ceramics and ultrasonic transducers," *Journal of Physics E: Scientific Instruments*, vol. 22, no. 10, pp. 804–816, 1989.

[16] D. Berlincourt, *Ultrasonic Transducer Materials: Chapter 2 Piezoelectric crystals and ceramics.* Plenum Press, 1971.

[17] *Piezoelectric ceramics: Booklet.* Morgan Electro-Ceramics, 2007.

[18] D. Damjanovic, "Ferroelectric, dielectric and piezoelectric properties of ferroelectric thin films and ceramics," *Reports on Progress in Physics*, vol. 61, no. 9, pp. 1267–1324, 1998.

[19] L. Brown and G. Harris, "Introduction to the special issue on the 30^{th} anniversary of the discovery of piezoelectric PVDF," *IEEE Transactions on Ultrasonics, Ferroelectrics and Frequency Control*, vol. 47, no. 6, pp. 1275–1276, 2000.

[20] E. Fukada, "History and recent progress in piezoelectric polymers," *IEEE Transactions on Ultrasonics, Ferroelectrics and Frequency Control*, vol. 47, no. 6, pp. 1277–1290, 2000.

[21] P. Ueberschlag, "PVDF piezoelectric polymer," *Sensor Review*, vol. 21, no. 2, pp. 118–126, 2001.

[22] D. Berlincourt, D. Curran, and H. Jaffe, "Piezoelectric and piezomagnetic materials and their function in transducers," *Physical Acoustics, Principles and Methods*, vol. 1A, pp. 169–270, 1964.

[23] *IEEE Standard on Piezoelectricity: An American National Standard (ANSI/IEEE Std 176-1987).* The Institute of Electrical and Electronics Engineers, Inc, 1987.

[24] "Guide to piezoelectric-dielectric ceramics," http://www.morganelectroceramics.com/resources. Accessed 30$^{\text{th}}$ Nov 2009.

[25] K. Ng, H. Chan, and C. Choy, "Piezoelectric and pyroelectric properties of PZT/P(VDF−TrFE) composites with constituent phases poled in parallel or antiparallel directions," *IEEE Transactions on Ultrasonics, Ferroelectrics and Frequency Control*, vol. 47, no. 6, pp. 1308–1315, 2000.

[26] S. Takahashi and S. Hirose, "Vibration-level characteristics of lead-zirconate-titanate ceramics," *Japanese Journal of Applied Physics*, vol. 31, no. 9B, pp. 3055–3057, 1992.

[27] S. Takahashi, S. Hirose, K. Uchino, and K. Oh, "Electro-mechanical characteristics of lead-zirconate-titanate ceramics under vibration-level change," *Proceedings of the 9th IEEE International Symposium on Applications of Ferroelectrics*, pp. 377–382, 1994.

[28] K. Graff, "Ultrasonics: Historical aspects," in *Ultrasonics Symposium*, pp. 1–10, 1977.

[29] K. Graff, "Macrosonics in industry 5: Ultrasonic machining," *Ultrasonics*, vol. 13, no. 3, pp. 103–109, 1975.

[30] T. Thoe, D. Aspinwall, and M. Wise, "Review on ultrasonic machining," *International Journal of Machine Tools and Manufacture*, vol. 38, no. 4, pp. 239–255, 1998.

[31] A. Cohan, "New method machines: sintered carbides, sintered borides, hardened tool steels," *Joural of Metals*, vol. 3, pp. 219–217, 1951.

[32] S. Kelley, "Hard, brittle materials machined using ultrasonic vibrations," *Materials and Methods*, vol. 34, pp. 92–94, 1951.

[33] A. Shoh, "Welding of thermoplastics by ultrasound," *Ultrasonics*, vol. 14, no. 5, pp. 209–217, 1976.

[34] J. Tsujino, "Recent developments of ultrasonic welding," vol. 2, pp. 1051–1060, 1995.

[35] A. Hulst, "Macrosonics in industry 2: Ultrasonic welding of metals," *Ultrasonics*, vol. 10, no. 6, pp. 252–261, 1972.

[36] F. Rawson, *Ultrasound in food processing - Chapter 14: An introduction to ultrasonic food cutting*. London, UK: Blackie Academic & Professional, 1998.

[37] E. McCulloch, *Experimental and finite element modelling of ultrasonic cutting of food*. PhD thesis, University of Glasgow, 2008.

[38] Y. Watanabe, Y. Tsuda, and E. Mori, "A longitudinal-flexural complex-mode ultrasonic high-power trasnducer system with one-dimensional construction," *Japanese Journal of Applied Phyics*, vol. 32, no. 5B, pp. 2430–2434, 1993.

[39] J. Tsujino, T. Ueoka, T. Kashino, and F. Sugahara, "Transverse and torsional complex vibration systems for ultrasonic seam welding of metal plates," *Ultrasonics*, vol. 38, pp. 67–71, 2000.

[40] P. Harkness, A. Cardoni, and M. Lucas, "Ultrasonic rock drilling devices using longitudinal-torsional compound vibration," *IEEE International Ultrasonics Symposium Proceedings*, pp. 2088–2091, 2009.

[41] K. Uchino and J. R. Giniewicz, *Micromechatronics*. New York, United States: Marcel Dekkar Inc, 2003.

[42] K. Uchino, "Piezoelectric ultrasonic motors: Overview," *Smart Materials and Structures*, vol. 7, no. 3, pp. 273–285, 1998.

[43] T. Ide, J. Friend, K. Nakamura, and S. Ueha, "A non-contact linear bearing and actuator via ultrasonic levitation," *Sensors and Actuators A: Physical*, vol. 135, no. 2, pp. 740–747, 2007.

[44] S. Ueha, Y. Hashimoto, and Y. Koike, "Non-contact transportation using near-field acoustic levitation," *Ultrasonics*, vol. 38, no. 1-8, pp. 26–32, 2000.

[45] P. Liu, J. Li, H. Ding, and W. Cao, "Modeling and experimental study on near-field acoustic levitation by flexural mode," *IEEE Transactions on Ultrasonics, Ferroelectrics and Frequency Control*, vol. 56, no. 12, pp. 2679–2685, 2009.

[46] Y. Hashimoto, Y. Koike, and S. Ueha, "Transporting objects without contact using flexural traveling waves," *Journal of the Acoustical Society of America*, vol. 103, pp. 3230–3233, 1998.

[47] K. Nakamura, "Ultrasonic levitation for transporting particle / plates," Invited presentation, University of Glasgow, 7$^{\text{th}}$ October 2009.

[48] G. T. Clement, "Perspectives in clinical uses of high-intensity focused ultrasound," *Ultrasonics*, vol. 42, no. 10, pp. 1087–1093, 2004.

[49] K. D. Evans, B. Weiss, and M. Knopp, "High-intensity focused ultrasound (HIFU) for specific therapeutic treatments: A literature review," *Journal of Diagnostic Medical Sonography*, vol. 23, no. 6, pp. 319–327, 2007.

[50] T. J. Mason, "Therapeutic ultrasound an overview," *Ultrasonics Sonochemistry*, vol. 18, no. 4, pp. 847–852, 2011.

[51] D. E. Brooks, "Phacoemulsification cataract surgery in the horse," *Clinical Techniques in Equine Practice*, vol. 4, no. 1, pp. 11–20, 2005.

[52] E. J. Linebarger, D. R. Hardten, G. K. Shah, and R. L. Lindstrom, "Phacoemulsification and modern cataract surgery," *Survey of Ophthalmology*, vol. 44, no. 2, pp. 123–147, 1999.

[53] J. Tan, D. Newman, C. Klunker, S. Watts, and R. Burton, "Phacoemusification cataract surgery: Is routine review necessary on the first post-operative day?," *Eye*, vol. 14, pp. 53–55, 2000.

[54] M. Boukhny and J. Chon, *Phacoemulsification cutting tip.* US Patent 5,676,649, 1997.

[55] M. Boukhny, *Torsional ultrasonic handpiece.* US Patent 6,077,285, 2000.

[56] D. Wuchinich, *Longitudinal-torsional ultrasonic tissue dissection.* US Patent 7,762,976, 2007.

[57] W. Bethke, "Phaco: New tech, new techniques," *Review of Ophthalmology: Online Review*, vol. 11, no. 33, Accessed August 15$^{\text{th}}$ 2011. http://www.revophth.com.

[58] J. F. Amaral, "The experimental development of an ultrasonically activated scalpel for laparoscopic use," *Surgical Laparoscopy & Endoscopy*, vol. 4, no. 2, pp. 92–99, 1994.

[59] http://www.ethiconendosurgery.com/. Accessed 15$^{\text{th}}$ August 2011.

[60] *EES Product Catalog 2010.* http://www.ethiconendosurgery.com/, Accessed 15$^{\text{th}}$ August 2011.

[61] B. O'Daly, E. Morris, G. Gavin, J. O'Byrne, and G. McGuinness, "High-power low-frequency ultrasound: A review of tissue dissection and ablation in medicine and surgery," *Journal of Materials Processing Technology*, vol. 200, no. 1-3, pp. 38–58, 2008.

[62] A. MacBeath, *Ultrasonic bone cutting.* PhD thesis, University of Glasgow, 2006.

[63] S. Jablonski, *Illustrated Dictionary of Dentistry.* Eastbourne, United Kingdom,: W.B. Saunders Company, 1982.

[64] W. Johnson and J. Wilson, "The application of the ultrasonic dental unit to scaling procedures," *Journal of Periodontology*, vol. 28, pp. 264–271, 1957.

[65] L. Balamuth, "Ultrasonics and dentistry," *Sound: Its Uses and Control*, vol. 2, no. 2, pp. 15–19, 1963.

[66] N. Suppipat, "Ultrasonics in periodontics," *Journal of Clinical Periodontology*, vol. 1, pp. 206–213, 1974.

[67] M. Dragoo, "A clinical evaluation of hand and ultrasonic instruments," *The International Journal of Periodontics and Restorative Dentistry*, vol. 12, pp. 310–323, 1992.

[68] T. Arabaci, Y. Çiçek, and C. Çanakçi, "Sonic and ultrasonic scalers in periodontal treatment: A review," *International Journal Dental Hygiene*, vol. 5, pp. 2–12, 2007.

[69] F. van der Weijden, *The power of ultrasonics*. Paris, France: Quintessence International, 2005.

[70] http://www.mectron.com. Accessed 5$^{\text{th}}$ March 2011.

[71] B. Felver, D. C. King, S. C. Lea, G. J. Price, and A. D. Walmsley, "Cavitation occurrence around ultrasonic dental scalers," *Ultrasonics Sonochemistry*, vol. 16, no. 5, pp. 692–697, 2009.

[72] J.-L. Beziat, J.-C. Bera, B. Lavandier, and A. Gleizal, "Ultrasonic osteotomy as a new technique in craniomaxillofacial surgery," *International Journal of Oral Maxillofacial Surgery*, vol. 36, pp. 493–500, 2007.

[73] A. Cardoni, "P3C-6 power ultrasonics in oral implantology," *IEEE Ultrasonics Symposium*, pp. 1780–1783, 2007.

[74] D. Hoigne, S. Stübinger, O. V. Kaenel, S. Shamdasani, and P. Hasenboehler, "Piezoelectric osteotomy in hand surgery: first experiences with a new technique," *BMC Musculoskeletal Disorders*, 2006.

[75] T. Vercellotti, M. L. Nevins, D. M. Kim, M. Nevins, K. Wada, R. K. Schenk, and J. P. Fiorellini, "Osseous response following resective therapy with Piezosurgery," *The International Journal of Periodontics and Restorative Dentistry*, vol. 25, pp. 543–549, 2005.

[76] M. Robiony, F. Polini, F. Costa, T. Vercellotti, and M. Politi, "Piezoelectric bone cutting in multipiece maxillary osteotomies," *Journal of Oral and Maxillofacial Surgery*, vol. 62, no. 6, pp. 759–761, 2004.

[77] S. Schaeren, C. Jaquiry, M. Heberer, M. Tolnay, T. Vercellotti, and I. Martin, "Assessment of nerve damage using a novel ultrasonic device for bone cutting," *Journal of Oral and Maxillofacial Surgery*, vol. 66, no. 3, pp. 593–596, 2008.

[78] G. Pavlíková, R. Foltán, M. Burian, E. Horká, S. Adámek, A. Hejcl, T. Hanzelka, and J. Sedý, "Piezosurgery prevents brain tissue damage: an experimental study on a new rat model," *International Journal of Oral and Maxillofacial Surgery*, vol. In Press, Corrected Proof, 2011.

[79] T. Vercellotti, "Technological characteristics and clinical indications of piezoelectric bone surgery," *Minerva Stomatologica*, vol. 53, no. 5, pp. 207–214, 2004.

[80] J. Horton, T. Tarpley, and L. Wood, "The healing of surgical defects in alveolar bone produced with ultrasonic instrumentation, chisel, and rotary bur," *Oral Surgery*, vol. 39, pp. 536–546, 1975.

[81] J. J. Thomsen, *Vibrations and stability: Order and chaos*. London, UK: McCraw-Hill, 1997.

[82] M. Cartmell, *Introduction to linear, parametric and nonlinear vibrations*. London, UK: Chapman and Hall, 1st ed., 1990.

[83] S. Dostrovsky, "Early vibration theory: Physics and music in the seventeenth century," *Archive for the History of Exact Sciences*, vol. 14, pp. 169–218, 1975.

[84] H. Raghuram and G. Marimuthu, "Donald redfield griffin: The discovery of echolocation," *Resonance: Indian Journal of Science Education*, vol. 10, no. 2, pp. 20–32, 1995.

[85] K. Graff, "Historical highlights in ultrasonics - 2," *Proceedings of the IEEE International Frequency Control Symposium and Exposition*, pp. 5–10, 2004.

[86] R. G. Goldman, *Ultrasonic Technology: Basic Theory and Modern Practices*. Reinhold Publishing Corporation, 1962.

[87] W. Mason, "Sonics and ultrasonics: Early history and applications," *Sonics and Ultrasonics, IEEE Transactions*, vol. 23, no. 4, pp. 224–231, 1976.

[88] W. Cady, "The piezo-electric resonator," *Proceedings of the Institute of Radio Engineers*, vol. 10, no. 2, pp. 83–114, 1922.

[89] J. R. Frederick, *Ultrasonic Engineering*. London, UK: John Wiley and Sons, 1965.

[90] K. Van Dyke, "The piezo-electric resonator and its equivalent network," *Proceedings of the Institute of Radio Engineers*, vol. 16, no. 6, pp. 742–764, 1928.

[91] J. H. Vincent, "Experiments on magnetostrictive oscillators at radio frequencies," *Proceedings of the Physical Society*, vol. 41, no. 1, pp. 476–486, 1928.

[92] G. W. Pierce, "Magnetostriction osillators," *Proceedings of the American Academy of Arts and Sciences*, vol. 63, pp. 1–47, 1928.

[93] E. Neppiras, "New magnetostrictive materials and transducers - I," *Journal of Sound and Vibration*, vol. 8, no. 3, pp. 408–430, 1968.

[94] E. A. Neppiras, "The pre-stressed piezoelectric sandwich transducer," *Ultrasonics International conference proceedings*, pp. 295–302, 1973.

[95] H. Jaffe and D. A. Berlincourt, "Piezo transducer materials," *Proceedings of the IEEE*, vol. 53, no. 10, pp. 1375–1386, 1965.

[96] A. Crawford, "Lead zirconate-titanate piezoelectric ceramics," *British Journal of Applied Physics*, vol. 12, no. 10, pp. 529–534, 1961.

[97] Y. Saito, H. Takao, T. Tani, T. Nonoyama, K. Takatori, T. Homma, T. Nagaya, and M. Nakamura, "Lead-free piezoceramics," *Nature*, vol. 432, pp. 84–87, 2004.

[98] J. Rödel, W. Jo, K. Seifert, E. Anton, T. Granzow, and D. Damjanovic, "Perspective on the development of lead-free piezoceramics," *Journal of the American Ceramic Society*, vol. 92, pp. 1153–1177, 2009.

[99] "http://www.morganelectroceramics.com," Accessed 13$^{\text{th}}$ April 2011.

[100] O. Söderberg, A. Sozinov, and V. Lindroos, *Giant magnetostrictive materials The Encyclopedia of Materials: Science and Technology*. Amsterdam, Netherlands: Elsevier Science, 2005.

[101] R. W. Wood and A. L. Loomis, "The physical and biological effects of high frequency sound-waves of great intensity," *Philosophical Magazine and Journal of Science*, vol. 4, no. 22, pp. 417–436, 1927.

[102] K. Söllner and C. Bondy, "The mechanism of coagulation by ultrasonic waves," *Transactions of the Faraday Society*, vol. 32, pp. 616–623, 1936.

[103] T. Bulat, "Macrosonics in industry: 3. ultrasonic cleaning," *Ultrasonics*, vol. 12, no. 2, pp. 59–68, 1974.

[104] P. Chendke and H. Fogler, "Macrosonics in industry: 4. chemical processing," *Ultrasonics*, vol. 13, no. 1, pp. 31–37, 1975.

[105] A. Shoh, "Industrial applications of ultrasound: A review I. High-power ultrasound," *IEEE Transactions on sonics and ultrasonics*, vol. su-22, no. 2, pp. 60–71, 1975.

[106] L. Balamuth, "Mechanical impedance transformers in relation to ultrasonic machining," *Transactions of the IRE Professional Group on Ultrasonic Engineering*, vol. 2, no. 1, pp. 23–33, 1954.

[107] L. Merkulov, "Design of ultrasonic concentrators," *Soviet Physical Acoustics*, vol. 3, pp. 230–238, 1957.

[108] L. Merkulov and A. Kharitonov, "Theory and analysis of sectional sconcentrators," *Soviet Physical Acoustics*, vol. 5, pp. 183–190, 1959.

[109] P. Derks, *The design of ultrasonic resonators with wide output cross-sections.* PhD thesis, Eindhoven University of Technology, 1984.

[110] K. Adachi, S. Ueha, and E. Mori, "Modal vibration analysis of ultrasonic plastic welding tools using the finite element method," *Proceedings - Ultrasonics International*, pp. 727–732, 1985.

[111] Y. Koike and S. Ueha, "A finite-element analysis of transient vibration of an ultrasonic welding tool," *Japanese Journal of Applied Physics*, vol. 32, no. 5B, pp. 2426–2429, 1993.

[112] G. Chapman and M. Lucas, "Frequency analysis of an ultrasonically excited thick cylinder," *International Journal of Mechanical Sciences*, vol. 32, no. 3, pp. 205–214, 1990.

[113] F. Rawson and P. Morris, *Ultrasonic cutting apparatus.* US Patent 5,226,343, 1993.

[114] F. Hamilton, *Ultrasonic cutting device.* US Patent 5,437,215, 1995.

[115] A. Cardoni and M. Lucas, "Enhanced vibration performance of ultrasonic block horns," *Ultrasonics*, vol. 40, no. 1-8, pp. 365–369, 2002.

[116] A. Cardoni, M. Lucas, M. Cartmell, and F. Lim, "A novel multiple blade ultrasonic cutting device," *Ultrasonics*, vol. 42, no. 1-9, pp. 69–74, 2004.

[117] A. Cardoni and M. Lucas, "Strategies for reducing stress in ultrasonic cutting systems," *Strain*, vol. 41, pp. 11–18, 2005.

[118] W. P. Mason, *Methods and apparatus employing torsionally vibratory energy.* US Patent 3,131,515, 1964.

[119] L. Shuyu and Z. Fucheng, "Study of vibrational characteristics for piezoelectric sandwich ultrasonic transducers," *Ultrasonics*, vol. 32, no. 1, pp. 39–42, 1994.

[120] J. Tsujino, T. Ueoka, K. Hasegawa, Y. Fujita, T. Shiraki, T. Okada, and T. Tamura, "New methods of ultrasonic welding of metal and plastic materials," *Ultrasonics*, vol. 34, no. 2-5, pp. 177–185, 1996.

[121] T. Asami and H. Miura, "Vibrator development for hole machining by ultrasonic longitudinal and torsional vibration," *Japanese Journal of Applied Physics*, vol. 50, no. 7, p. 07HE31, 2011.

[122] W. Xu, X. Lu, G. Pan, Y. Lei, and J. Luo, "Effects of the ultrasonic flexural vibration on the interaction between the abrasive particles; pad and sapphire substrate during chemical mechanical polishing (CMP)," *Applied Surface Science*, vol. 257, no. 7, pp. 2905–2911, 2011.

[123] P. Leclercq, C. Zenati, S. Amr, and D. M. Dohan, "Ultrasonic bone cut part 1: State-of-the-art technologies and common applications," *Journal of Oral and Maxillofacial Surgery*, vol. 66, no. 1, pp. 177–182, 2008.

[124] S. Trenter, A. Walmsley, G. Landini, and J. Shippen, "Assessment of the ultrasonic dental scaler insert," *Medical Engineering and Physics*, vol. 24, no. 2, pp. 139–144, 2002.

[125] Y. Tomikawa, K. Adachi, M. Aoyagi, T. Sagae, and T. Takano, "A rod-type ultrasonic motor using longitudinal and torsional vibration modes," *IEEE 7^{th} International Symposium: Applications of Ferroelectrics*, pp. 229–232, 1990.

[126] K. Nakamura, M. Kurosawa, and S. Ueha, "Characteristics of a hybrid transducer-type ultrasonic motor," *IEEE Transactions on Ultrasonics, Ferroelectrics and Frequency Control*, vol. 38, no. 3, pp. 188–193, 1991.

[127] K. Nakamura and S. Ueha, "Performances of a hybrid transducer-type ultrasonic motor as a function of the size," *IEEE Proceedings of Ultrasonics Symposium*, vol. 1, pp. 557–560, 1994.

[128] J. Tsujino, R. Suzuki, and H. Yasojima, "Load characterisatics of ultrasonic rotart motor using a longitudinal-torsional vibration converter," *IEEE Proceedings of Ultrasonics Symposium*, pp. 377–382, 1996.

[129] M. Takano, K. Hirosaki, M. Takimoto, S. Ichimura, and K. Nakamura, "Improvements in controllability of ultrasonic linear motors by longitudinal-bending multilayered transducers with independent electrodes," *Japanese Journal of Applied Physics*, vol. 50, no. 7, p. 07HE25, 2011.

[130] R. Whymark, "Acoustic field positioning for containerless processing," *Ultrasonics*, vol. 13, no. 6, pp. 251–261, 1975.

[131] H. Hatano, Y. Kanai, Y. Ikegami, T. Fujii, and K. Saito, "Ultrasonic levitation and positioning of samples," *Japanese Journal of Applied Physics*, vol. 21 S3, no. Supplement 21-3, pp. 202–204, 1982.

[132] M. C. Catuna, "Sonic energy: A possible dental application," *Annals of density*, vol. 12, pp. 100–101, 1953.

[133] L. Balamuth, "Ultrasonic cutting tool," *US Patent 2990616*, July 4$^{\text{th}}$ 1961.

[134] D. Zinner, "Recent ultrasonic dental studies, inceeding periodontia, without the use of an abrasive," *Jorunal of Dental Research*, vol. 34, no. 5, pp. 748–749, 1955.

[135] M. J. Richman, "The use of ultrasonics in root canal therapy and root resection," *Journal of Dental Medicine*, vol. 12, no. 1, pp. 12–18, 1957.

[136] A. Walmsley, W. Laird, and P. Lumley, "Ultrasound in dentistry. Part 2–Periodontology and endodontics," *Journal of Dentistry*, vol. 20, no. 1, pp. 11–17, 1992.

[137] H. Martin, "Ultrasonic disinfection of the root canal," *Oral Surgery, Oral Medicine, Oral Pathology*, vol. 42, no. 1, pp. 92–99, 1976.

[138] H. Mararow, "Bone repair after experimentally produced defects," *Journal of Oral Surgery*, vol. 18, pp. 107–114, 1960.

[139] T. McFall, G. Yamane, and G. Burnett, "Comparison of the cutting effect on bone of an ultrasonic cutting device and rotary burs," *Journal of Oral Surgery*, vol. 19, pp. 200–209, 1961.

[140] H. H. Postle, "Ultrasonic cavity preparation," *The Journal of Prosthetic Dentistry*, vol. 8, no. 1, pp. 153–160, 1958.

[141] H. Aro, H. Kallioniemi, A. Aho, and P. Kellokumpu-Lehtinen, "Ultrasonic device in bone cutting: A histological and scanning electron microscopical study," *Acta orthopaedica Scandinavica*, vol. 52, pp. 5–10, 1982.

[142] M. Schlee, M. Steigmann, E. Bratu, and A. Garg, "Piezosurgery: Basics and possibilities," *Implant dentistry*, vol. 15, no. 4, pp. 334–340, 2006.

[143] G. Preti, G. Martinasso, B. Peirone, R. Navone, C. Manzella, G. Muzio, C. Russo, R. A. Canuto, and G. Schierano, "Cytokines and growth factors involved in the osseointegration of oral titanium implants positioned using piezoelectric bone surgery versus a drill technique: A pilot study in minipigs," *Journal of Periodontology*, vol. 78, no. 4, pp. 716–722, 2007.

[144] M. Labanca, F. Azzola, R. Vinci, and L. F. Rodella, "Piezoelectric surgery: Twenty years of use," *British Journal of Oral and Maxillofacial Surgery*, vol. 46, no. 4, pp. 265–269, 2008.

[145] M. F. McKneally, "Ethical problems in surgery: Innovation leading to unforeseen complications," *World Journal of Surgery*, vol. 23, no. 8, pp. 786–788, 1999.

[146] K. Negishi, "Jump phenomenon in resonance curve of ferroelectric ceramics," *Journal of the Physical Society of Japan*, vol. 15, no. 3, pp. 534–534, 1960.

[147] R. Woollett and C. Leblanc, "Ferroelectric nonlinearities in transducer ceramics," *IEEE Transactions on Sonics and Ultrasonics*, vol. 20, no. 1, pp. 24–31, 1973.

[148] H. Hagemann, "Loss mechanisms and domain stabilisation in doped $BiTiO_3$," *Journal of Physics C: Solid State Physics*, vol. 11, no. 15, pp. 3333–3344, 1978.

[149] P. Gerthsen, K. Hardtl, and N. Schmidt, "Correlation of mechanical and electrical losses in ferroelectric ceramics," *Journal of Applied Physics*, vol. 51, no. 2, pp. 1131–1134, 1980.

[150] H. Beige, "Elastic and dielectric nonlinearities of piezoelectric ceramics," *Ferroelectrics*, vol. 52, no. 1, pp. 113–119, 1983.

[151] S. Hirose, M. Aoyagi, and Y. Tomikawa, "Dielectric loss in a piezoelectric ceramic transducer under high-power operation; increase of dielectric loss and its inflence on transducer efficieny," *Japanese Journal of Applied Physics*, vol. 32, no. 5B, pp. 2418–2421, 1993.

[152] P. Gonnard, V. Perrin, R. Briot, D. Guyomar, and A. Albareda, "Characterization of the piezoelectric ceramic mechanical nonlinear behavior," *Proceedings of the 11^{th} IEEE International Symposium on Applications of Ferroelectrics*, pp. 353–356, 1998.

[153] V. Perrin, M. Troccaz, and P. Gonnard, "Non linear behavior of the permittivity and of the piezoelectric strain constant under high electric field drive," *Journal of Electroceramics*, vol. 4, pp. 189–194, 1999.

[154] M. Umeda, K. Nakamura, and S. Ueha, "Effects of vibration stress and temperature on the characteristics of piezoelectric ceramics under high vibration amplitude levels measured by electrical transient responses," *Japanese Journal of Applied Physics*, vol. 38, no. 9B, pp. 5581–5585, 1999.

[155] A. Albareda, J. Casals, R. Perez, and F. Montero de Espinos, "Nonlinear measurements of piezocomposite transducers with burst excitation," *Proceedings of the 12^{th} IEEE International Symposium on Applications of Ferroelectrics*, vol. 2, pp. 979–982, 2000.

[156] B. K. Mukherjee, W. Ren, S.-F. Liu, A. J. Masys, and G. Yang, "Nonlinear properties of piezoelectric ceramics," vol. 4333, pp. 41–54, SPIE, 2001.

[157] S. Sherrit, X. Bao, D. Sigel, M. Gradziel, S. Askins, B. Dolgin, and Y. Bar-Cohen, "Characterization of transducers and resonators under high drive levels," *IEEE Ultrasonics Symposium*, vol. 2, pp. 1097–1100, 2001.

[158] A. Albareda, P. Gonnard, V. Perrin, R. Briot, and D. Guyomar, "Characterization of the mechanical nonlinear behavior of piezoelectric ceramics," *IEEE Transactions on Ultrasonics, Ferroelectrics and Frequency Control*, vol. 47, no. 4, pp. 844–853, 2000.

[159] S. Takahashi, Y. Sasaki, N. K. Umeda, M, and S. Ueha, "Nonlinear behavior in piezoelectric ceramic transducers," *Proceedings of the 12th IEEE International Symposium Applications of Ferroelectrics*, vol. 1, pp. 11–16, 2000.

[160] U. von Wagner and P. Hagedorn, "Nonlinear effects of piezoceramics excited by weak electric fields," *Nonlinear Dynamics*, vol. 31, no. 2, pp. 133–149, 2003.

[161] R. Sabat, B. Mukgerjee, W. Ren, and G. Yang, "Temperature dependence of the complete material coefficients matrix of soft and hard doped piezoelectric lead zirconate titanate ceramics," *Journal of Applied Physics*, vol. 101, pp. 064111–064111–7, 2007.

[162] A. Albareda, R. Perez, J. Casals, J. Garcia, and D. Ochoa, "Optimization of elastic nonlinear behavior measurements of ceramic piezoelectric resonators with burst excitation," *IEEE Transactions on Ultrasonics, Ferroelectrics and Frequency Control*, vol. 54, no. 10, pp. 2175–2188, 2007.

[163] M. Umeda, K. Nakamura, and S. Ueha, "The measurement of high-power characteristics for a piezoelectric transducer based on the electrical transient response," *Japanese Journal of Applied Physics*, vol. 37, no. 9B, pp. 5322–5325, 1998.

[164] D. Guyomar, N. Aurelle, C. Richard, P. Gonnard, and L. Eyraud, "Nonlinearities in Langevin transducers," *Proceedings of IEEE Ultrasonics Symposium*, vol. 2, pp. 925–928, 1994.

[165] K. Uchino, "Materials issues in design and performance of piezoelectric actuators: An overview," *Acta Materialia*, vol. 46, no. 11, pp. 3745–3753, 1998.

[166] J. F. Blackburn and M. G. Cain, "Nonlinear piezoelectric resonance: A theoretically rigorous approach to constant I - V measurements," *Journal of Applied Physics*, vol. 100, no. 11, pp. 114101:1–114101:10, 2006.

[167] J. F. Blackburn and M. G. Cain, "Non-linear piezoelectric resonance analysis using burst mode: a rigorous solution," *Journal of Physics D: Applied Physics*, vol. 40, no. 1, pp. 227–233, 2007.

[168] D. Guyomar, B. Ducharne, and G. Sebald, "High nonlinearities in Langevin transducer: A comprehensive model," *Ultrasonics*, vol. 51, no. 8, pp. 1006–1013, 2011.

[169] W. Mason, "Internal friction and fatigue in metals at large strain amplitudes," *Journal of the Acoustical Society of America*, vol. 28, pp. 1207–1218, 1956.

[170] W. Mason and J. Wehr, "Internal friction and ultrasonic yield of the alloy 90Ti6Al4V," *Journal of Physics and Chemistry of Solids*, vol. 31, no. 8, pp. 1925–1933, 1970.

[171] A. Puškár, "Cyclic stress-strain curves and internal friction of steel at ultrasonic frequencies," *Ultrasonics*, vol. 20, no. 3, pp. 118–122, 1982.

[172] V. Kuz'menko, "Fatigue strength of structural materials at sonic and ultrasonic loading frequencies," *Ultrasonics*, vol. 13, no. 1, pp. 21–30, 1975.

[173] C. Campos-Pozuelo and J. Gallego-Juárez, "Nonlinear effects in aluminium alloys subjected to high intensity ultrasound," *Procedings of World Congress on Ultrasonics*, pp. 191–194, 1995.

[174] C. Campos-Pozuelo and J. Gallego-Juárez, "Limiting strain of metals subjected to high-intensity ultrasound," *Acta Acustica*, vol. 82, pp. 823–828, 1996.

[175] M. Lucas, J. Petzing, A. Cardoni, L. Smith, and J. McGeough, "Design and characterisation of ultrasonic cutting tools," *CIRP Annals - Manufacturing Technology*, vol. 50, no. 1, pp. 149–152, 2001.

[176] F. Lim, M. Cartmell, A. Cardoni, and M. Lucas, "A preliminary investigation into optimising the response of vibrating systems used for ultrasonic cutting," *Journal of Sound and Vibration*, vol. 272, pp. 1047–1069, 2004.

[177] A. Cardoni, F. Lim, M. Lucas, and M. Cartmell, "Characterising modal interactions in an ultrasonic cutting system," *Forum Acusticum paper ULT-02-003-IP, Seville, Spain*, 2002.

[178] A. Mathieson, A. Cardoni, P. Harkness, and M. Lucas, "Characterisation of nonlinear behaviour of power ultrasonic drilling horns," *IEEE International Ultrasonics Symposium Proceedings*, pp. 2092–2096, 2009.

[179] L. Han and J. Zhong, "Experimental observations on nonlinear phenomena in transducer assembly for thermosonic flip-chip bonding," *Microelectronic Engineering*, vol. 85, no. 7, pp. 1568–1576, 2008.

[180] J. Gallego-Juárez, E. Riera, and V. M. Acosta-Aparicio, "Modal interactions in high-power ultrasonic processing transducers," *AIP Conference Proceedings*, vol. 1022, no. 1, pp. 595–604, 2008.

[181] P. Gatti and V. Ferrari, *Applied Structural and Mechanical Vibrations, theory, methods and measuring instrumentation.* London, UK: E & FN Spon, 1^{st} ed., 1999.

[182] H. M. Minchenko, "Electromechanical transducer." US Patent 3,396,285, 1968.

[183] L. Shuyu, "Optimization of the performance of the sand piezoelectric ultrasonic transducer," *Joural of acoustical society of America*, vol. 114, no. 1, pp. 182–186, 2004.

[184] D. DeAngelis and G. Schulze, "Optimizing piezoelectric ceramic thickness in ultrasonic transducers," in *39th Annual Ultrasonic Industry Association Symposium (UIA)*, pp. 1–9, 2010.

[185] D. Chacón, G. Rodríguez-Corral, L. Gaete-Garretón, E. Riera, and J. Gallego-Juárez, "A procedure for the efficient selection of piezoelectric ceramics constituting high-power ultrasonic transducers," *Ultrasonics*, vol. 44, no. Supplement 1, pp. e517–e521, 2006.

[186] D. DeAngelis and G. Schulze, "Optimizing piezoelectric crystal preload in ultrasonic transducers," in *38th Annual Ultrasonic Industry Association Symposium (UIA)*, pp. 1–6, 2009.

[187] A. Abdullah, M. Shahini, and A. Pak, "An approach to design a high power piezoelectric ultrasonic transducer," *Journal of Electroceramics*, vol. 22, pp. 369–382, 2009.

[188] G. Bradfield, "Ultrasonic transducers: 1. Introduction to ultrasonic transducers - part B," *Ultrasonics*, vol. 8, no. 3, pp. 177–189, 1970.

[189] N. Aurelle, D. Guyomar, C. Richard, P. Gonnard, and L. Eyraud, "Nonlinear behavior of an ultrasonic transducer," *Ultrasonics*, vol. 34, no. 2-5, pp. 187–191, 1996. Proceedings of Ultrasonics International 1995.

[190] "The design of piezoelectric sandwich transducers. tp-235," http://www.morganelectroceramics.com/ resources. Accessed 30th Nov 2009.

[191] J. Qiao and F. Wang, "Effect of tightening torque on the frequency of the sandwich piezoelectric ceramic transducer vibrator," *11th International Conference on Electronic Packaging Technology High Density Packaging (ICEPT-HDP)*, pp. 893–896, 2010.

[192] S. Hirose, M. Aoyagi, Y. Tomikawa, S. Takahashi, and K. Uchino, "High power characteristics at antiresonance frequency of piezoelectric transducers," *Ultrasonics*, vol. 34, no. 2-5, pp. 213–217, 1996.

[193] A. Puškár, "The thermal activation of cummulative fatigue damage at ultrasonic frequencies," *Ultrasonics*, vol. 15, no. 3, pp. 124–128, 1977.

[194] M. Adithan, "Tool wear characteristics in ultrasonic drilling," *Tribology International*, vol. 14, no. 6, pp. 351–356, 1981.

[195] J. Kumar, J. Khamba, and S. Mohapatra, "Investigating and modeling tool-wear rate in the ultrasonic machining of titanium," *The International Journal of Advanced Manufacturing Technology*, vol. 41, pp. 1107–1117, 2009.

[196] *Materials handbook Volume 3 - Properties and selection: Stainless steels, tool materials and special purpose metals.* Ohio, United States: American Society for Metals, 9 ed., 1980.

[197] N. A. Waterman and M. F. Ashby, eds., *The materials selector: Volume 2*. London, UK: Chapman and Hall, 2 ed., 1997.

[198] W. D. C. Jr, *Materials science and engineering: An introduction*. John Wiley & Sons, Inc., 4 ed., 1997.

[199] S. Kalpakjian and S. R. Schmid, *Manufacturing processes for engineering materials*. Person Education, Inc. Upper Saddle River, NJ, United States: Prentice Hall, 4 ed., 2003.

[200] http://www.acoustics.co.uk/static/pdf/PVdF-properties.pdf. Accessed 15$^{\text{th}}$ December 2011.

[201] N. Murayama, K. Nakamura, H. Obara, and M. Segawa, "The strong piezoelectricity in polyvinylidene fluroide (PVDF)," *Ultrasonics*, vol. 14, no. 1, pp. 15–24, 1976.

[202] Quotation: 317139. Righten: Glasgow service centre, 1$^{\text{st}}$ April 2011.

[203] C. Chong, H. Chan, M. Chan, and P. Liu, "Resonances in 1-3 piezocomposite rings," *Applied Physics A: Materials Science & Processing*, vol. 80, pp. 1793–1799, 2005.

[204] M. W. Kehoe, "Historical overview of flight flutter testing," *NASA Technical Memorandum, 4720*, 1995.

[205] C. Kennedy and C. Pancu, "Use of vectors in vibration measurement and analysis," *Journal of the Aeronautical Sciences*, vol. 14, no. 11, pp. 603–625, 1947.

[206] R. E. D. Bishop and G. M. L. Gladwell, "An investigation into the theory of resonance testing," *Philosophical Transactions of the Royal Society of London. Series A, Mathematical & Physical Sciences*, vol. 255, no. 1055, pp. 241–280, 1963.

[207] F. J. Harris, "On the use of windows for harmonic analysis with the discrete fourier transform," *Proceedings of the IEEE*, vol. 66, no. 1, pp. 51–83, 1978.

[208] D.J.Ewins, *Modal Testing - Theory, Practice and Application*. Baldock, Hertfordshire England: Research Studies Press Ltd, 2nd ed., 2000.

[209] K. G. McConnell, "Modal testing," *Philosophical Transactions of the Royal Society of London. Series A, Mathematical, Physical & Engineering Sciences*, vol. 359, pp. 11–28, 2001.

[210] *Signal Calc. 240V 4.2.207 User's manual, Data Physics Corporation*, 2007.

[211] http://www.polytec.com. Accessed 19$^{\text{th}}$ Oct 2010.

[212] *ME'Scope Version 4.0.0.92 User's manual, Vibrant Technology Inc.*, 2005.

[213] J. Woolman and R. Mottram, *The mechanical and physical properties of the British standard En Steels (B.S. 970-1955)*. London, UK: Pergamon Press, 3^{rd} ed., 1969.

[214] M. Umeda, K. Nakamura, and S. Ueha, "Effects of a series capacitor on the energy consumption in piezoelectric transducers at high vibration amplitude level," *Japanese Journal of Applied Physics*, vol. 38, no. 5B, pp. 3327–3330, 1999.

[215] R. Lerch, "Simulation of piezoelectric devices by two and three-dimensional finite elements," *IEEE Transactions on Ultrasonics, Ferroelectrics and Frequency Control*, vol. 37, no. 3, pp. 233–247, 1990.

[216] R. Simkovics, H. Landes, M. Kaltenbacher, and R. Lerch, "Nonlinear finite element analysis of piezoelectric transducers," in *Ultrasonics Symposium Proceedings*, vol. 2, pp. 1057–1060, 1999.

[217] M. P. Cartmell, F. C. N. Lim, A. Cardoni, and M. Lucas, "Optimisation of the vibrational response of ultrasonic cutting systems," *IMA Journal of Applied Mathematics*, vol. 70, no. 5, pp. 645–656, 2005.

[218] W. Mason and W. A. Wood, "Fatigue mechanism in fcc metals at ultrasonic frequencies," *Journal of Applied Physics*, vol. 39, no. 12, pp. 5581–5584, 1968.

[219] H. Kumehara, K. Morimura, K. Marauyama, and I. Yoshimoto, "Characteristics of threaded joints in ultrasonic vibrating system," *Bulletin of JSME*, vol. 27, no. 223, pp. 117–123, 1984.

[220] H. Kumehara, M. Mori, and H. Suda, "Failure of threaded joints in ultrasonic vibration system," in *Bull. Japan Society of Precision Engineering*, vol. 20, pp. 39–40, 1986.

[221] R. Ibrahim and C. Pettit, "Uncertainties and dynamic problems of bolted joints and other fasteners," *Journal of Sound and Vibration*, vol. 279, no. 3-5, pp. 857–936, 2005.

[222] J. Esteban and C. A. Rogers, "Energy dissipation through joints: Theory and experiments," *Computers and Structures*, vol. 75, no. 4, pp. 347–359, 2000.

[223] J. Rivière, G. Renaud, S. Haupert, M. Talmant, P. Laugier, and P. A. Johnson, "Nonlinear acoustic resonances to probe a threaded interface," *Journal of Applied Physics*, vol. 107, no. 12, pp. 124901:1–124901:9, 2010.

[224] H. Ouyang, M. Oldfield, and J. Mottershead, "Experimental and theoretical studies of a bolted joint excited by a torsional dynamic load," *International Journal of Mechanical Sciences*, vol. 48, no. 12, pp. 1447–1455, 2006.

[225] D. Zhou and M. Kamlah, "Dielectric and piezoelectric performance of soft pzt piezoceramics under simultaneous alternating electromechanical loading," *Journal of the European Ceramic Society*, vol. 25, no. 12, pp. 2415–2420, 2005.

[226] A. Shoh, *Sonic Transducer*. US Patent 3,524,085, 1970.

[227] L. Shuyu and X. Chunlong, "Analysis of the sandwich ultrasonic transducer with two sets of piezoelectric elements," *Smart Materials and Structures*, vol. 17, no. 6, p. 065008, 2008.

[228] R. LeMaster and K. Graff, "Influence of ceramic location on high power transducer performance," *Ultrasonics Symposium*, pp. 296–299, 1978.

[229] L. Shuyu, "Load characteristics of high power sandwich piezoelectric ultrasonic transducers," *Ultrasonics*, vol. 43, pp. 365–373, 2005.